

CO₂ Hydrogenation to Methanol in Different Reactor Concepts Using Metal-doped Indium-based Catalysts

Faculty of Mathematics, Informatics and Natural Sciences

Department of Chemistry

Institute of Technical and Macromolecular Chemistry

University of Hamburg

Doctor rerum naturalium (Dr. rer. nat.)

submitted to the Universität Hamburg by

Philipp Kampe

born on 18.12.1995 in Magdeburg

Hamburg 2025

accepted on the recommendation of

Reviewer 1: Prof. Dr.-Ing. Jakob Albert

Reviewer 2: Prof. Dr. Raimund Horn

Date of the Disputation: 07.03.2025

Examiner 1: Prof. Dr.-Ing. Jakob Albert

Examiner 2: Prof. Dr. Michael Steiger

Examiner 3: Dr. Charlotte Ruhmlieb

This work was conducted between October 2020 and September 2023 at the Institute of Technical and Macromolecular Chemistry, University of Hamburg, Hamburg, Germany under the supervision of Prof. Dr.-Ing. Jakob Albert.

List of publications originating from this work

P. Kampe, A. Wesner, P. Schühle, F. Hess, J. Albert. “Effect of Conversion, Temperature and Feed Ratio on $\text{In}_2\text{O}_3/\text{In}(\text{OH})_3$ Phase Transitions in Methanol Synthesis Catalysts: A Combined Experimental and Computational Study”, *ChemPlusChem*, 2023, 88, e202300425, DOI: doi.org/10.1002/cplu.202300425

Published under a Creative Commons license.

A. Wesner, **P. Kampe**, N. Herrmann, S. Eller, C. Ruhmlieb, J. Albert. “Indium-based Catalysts for CO_2 Hydrogenation to Methanol: Key Aspects for Catalytic Performance”, *ChemCatChem*, 2023, 15, e202301125, DOI: doi.org/10.1002/cctc.202301125

Published under a Creative Commons license.

P. Kampe, N. Herrmann, C. Ruhmlieb, M. Finsel, O. Korup, R. Horn, J. Albert. “Spatially Resolved Reaction Profiles of CO_2 Hydrogenation to Methanol Using In-Based Catalysts in a Compact Profile Reactor”, *ACS Sustainable Chemistry & Engineering*, 2024, 12, 25, 9541-9549, DOI: doi.org/10.1021/acssuschemeng.4c03279

Published under a Creative Commons license.

P. Kampe, N. Herrmann, A. Wesner, C. Ruhmlieb, J. Albert. “Catalyst and Parameter Optimization Study for Slurry-Phase Methanol Synthesis Using Ni-Doped Indium-Based Catalysts”, *ACS Sustainable Chemistry & Engineering*, 2023, 11, 14633-14644, DOI: doi.org/10.1021/acssuschemeng.3c05584

Reprinted (adapted) with permission from ACS Sustainable Chem. Eng. 2023, 11, 14633–14644. Copyright 2023 American Chemical Society.

List of conference contributions

P. Kampe, A. Wesner, J. Albert: "CO₂-hydrogenation to methanol with indium based catalysts in a fixed-bed reactor", NaWuReT Summer School, Ulm, 2022, poster.

P. Kampe, A. Wesner, J. Albert: "Development of a novel Ni-In₂O₃/ZrO₂ for methanol synthesis via CO₂ hydrogenation", 56. Jahrestreffen Deutscher Katalytiker, Weimar, 2023, poster and pitch presentation.

P. Kampe, N. Herrmann, A. Wesner, C. Ruhmlieb, J. Albert: "Catalyst and parameter optimization study for slurry phase methanol synthesis using Ni-doped indium-based catalysts", International Congress on Catalysis, Lyon, 2024, poster.

P. Kampe, N. Herrmann, A. Wesner, C. Ruhmlieb, J. Albert: "Catalyst and parameter optimization study for slurry phase methanol synthesis using Ni-doped indium-based catalysts", Annual Meeting on Reaction Engineering and Electrochemical Processes, Wuerzburg, 2024, poster.

Table of contents

I.	List of publications originating from this work	I
II.	Table of contents	II
III.	List of abbreviations and symbols	VI
1	Zusammenfassung	1
2	Abstract	4
3	Introduction	6
3.1	Methanol as promising Power-to-X hydrogen carrier	7
3.1.1	Synthesis of Methanol from CO vs. CO ₂ (kinetics and thermodynamics)	13
3.1.2	Industrial applications	23
3.2	Catalysts for methanol synthesis	24
3.2.1	Commercial Cu-based catalyst	24
3.2.2	In-based catalysts as promising alternative	27
3.3	Reactor concepts	29
3.3.1	Two-phase reactors	29
3.3.2	Three-phase reactors	36
3.3.3	Design of Experiments	37
4	Objective of the present work	40
5	Materials and methods for experimental evaluation	42
5.1	Used chemicals and materials	42
5.2	Catalyst preparation	43
5.3	Different reactor setups	44
5.3.1	Fixed bed reactor setup (two-phase)	44
5.3.2	Compact Profile Reactor setup (two-phase)	45
5.3.3	Three-phase Stirred-tank reactor setup in batch mode	46
5.4	Experimental Details	47
5.4.1	Two-phase Methanol Synthesis Using the Fixed Bed Reactor setup	47
5.4.2	Two-phase Methanol Synthesis Using the CPR setup	48
5.4.3	Three-phase Methanol Synthesis Using the Batch Reactor setup	49
5.5	Applied analytics	50
5.5.1	Online Gas Chromatography	50
5.5.2	Fourier-transform infrared spectroscopy	50
5.5.3	Thermogravimetric Analysis	50

5.5.4	Powder X-ray Diffraction	51
5.5.5	Inductively Coupled Plasma Optical Emission Spectroscopy	51
5.5.6	X-ray Photoelectron Spectroscopy	51
5.5.7	Nitrogen Physisorption	51
5.5.8	CO ₂ -Temperature-Programmed Desorption	51
5.5.9	H ₂ -Temperature-Programmed Reduction	52
5.5.10	Scanning Electron Microscopy and Energy-Dispersive X-ray Spectroscopy	52
5.5.11	High-Resolution Transmission Electron Microscopy	52
5.5.12	Nuclear Magnetic Resonance Spectroscopy	52
5.6	Calculations	52
5.6.1	Calculations for the Two-Phase Continuous Methanol Synthesis	53
5.6.2	Calculations for the Three-Phase Batch Methanol Synthesis	56
6	Cumulative part of the dissertation	57
6.1	Influence of the phase transition of pure In ₂ O ₃ in two-phase methanol synthesis	58
6.2	Investigations of supported In ₂ O ₃ catalysts in a fixed bed reactor	73
6.3	Spatially resolved study of supported In ₂ O ₃ catalysts in a Compact Profile Reactor	87
6.4	Investigations of supported In ₂ O ₃ in a slurry reactor	98
7	Comprehensive discussion	112
8	Bibliography	120
9	Appendix	132
9.1	Characterization of the setup	132
9.1.1	GC calibration curves for all setups	132
9.1.2	MFC calibration curves	133
9.1.3	Fixed bed reactor	133
9.1.4	Compact Profile Reactor	135
9.2	List of hazardous substances used according to GHS	136
9.3	Supporting Information of 1 st publication (available online)	138
9.4	Supporting Information of 2 nd publication (available online)	144
9.5	Supporting Information of 3 rd publication (available online)	165
9.6	Supporting Information of 4 th publication (available online)	174
10	Danksagung	189
11	Curriculum Vitae	191
12	Declaration on oath	192

Abbreviations and Symbols

Abbreviation	Definition
AA	Alfa Aesar
AE	Alkaline Electrolysis
ARC	Advanced Reactor Concept
atm	Standard atmosphere
BET	Brunauer-Emmett-Teller
BJH	Barrett-Joyner-Halenda
CCS	Carbon Capture and Storage
CCU	Carbon Capture and Utilization
CMD	Collect-Mix-Distribute reactor
CP	Co-Precipitation
CPR	Compact Profile Reactor
CZA	CuO-ZnO-Al ₂ O ₃
DC	Direct Current
DFT	Density Functional Theory
DME	Dimethyl ether
DMFC	Direct Methanol Fuel Cell
DoE	Design of Experiments
e.g.	For example
EDX	Energy-dispersive X-ray spectroscopy
EQ	Equilibrium
Eq.	Equation
EU	European Union
FGD	Fuel-gas desulfurization
FID	Flame ionization detector
FTIR	Fourier transform infrared spectrometer
GC	Gas chromatography
GHS	Globally Harmonized System
GHSV	Gas hourly space velocity
HAADF	High angle annular dark-field
HER	Hydrogen evolution reaction
HRTEM	High resolution transmission electron microscopy
H-ZSM5	Zeolite Socony Mobil-5
ICI	Imperial Chemical Industries
ICP	Inductively coupled plasma
IMC	Isothermal Methanol Converter
LH ₂	Liquefied hydrogen
LHHW	Langmuir-Hinshelwood-Hougen-Watson
M	Martin

MeOH	Methanol
MFC	Mass flow controller
MGC	Mitsubishi Gas Chemical
MHI	Mitsubishi Heavy Industry
MRF-Z [®]	Multi-stage radial flow and intermediate Cooling reactor
MS	Mean square
MTBE	Methyl <i>tert</i> -butyl ether
MTG	Methanol-to-Gasoline
MTO	Methanol-to-Olefines
NG	Natural Gas
NMR	Nuclear magnetic resonance
NO _x	Nitrogen oxide
OER	Oxygen evolution reaction
OES	Optical emission spectrometry
PEM	Proton exchange membrane electrolysis
ppm	Parts per million
PtC	Power-to-Chemicals
PtG	Power-to-Gas
PtH	Power-to-Heat
PtL	Power-to-Liquid
PtX	Power-to-X
RDS	Rate determining step
Ref	Reference
rWGS	Reverse water-gas shift
S	Schühle
SAPO 34	Silicoaluminophosphate 34 zeolite
SEM (ger. REM)	Scanning electron microscope (ger. Raster- elektronenmikroskop)
SG	Saint-Gobain
SN	Stoichiometric number
SOEC	Solid oxide electrolysis
SO _x	Sulfur oxide
SR	Suspension reactor
SRK	Soave-Redlich-Kwong
STY	Space time yield
syngas	Synthesis gas
t	Tonne
TCD	Thermal conductivity detector
Tech	Technology
TEM	Transmission electron microscopy
TGA	Thermal gravimetric analysis

TOS	Time-on-stream
TPD	Temperature programmed desorption
TPR	Temperature programmed reduction
USD	US-Dollar
V _o	Oxygen vacancy
WGS	Water-gas shift
WI	Wetness impregnation
XPS	X-ray photoelectron spectroscopy
XRD	X-ray diffraction

Symbol	Definition	Unit
a	Specific external surface	m ⁻¹
Ca	Carberry number	-
D	Diffusions coefficient	m ² s ⁻¹
d _p	Particle diameter	m
ΔG_R°	Standard Gibbs free energy of reaction	J mol ⁻¹
ΔH_R°	Standard enthalpy of reaction	J mol ⁻¹
<i>f</i>	Fugacity	bar
c	Concentration	g mol ⁻¹
E	Residence time distribution	s ⁻¹
K	Equilibrium constant	-
k	Reaction rate constant	(L mol ⁻¹) ^{order of reaction-1} s ⁻¹
M	Molare Mass	g mol ⁻¹
N	Number of responses	-
P	Productivity	g _i g _{reference} ⁻¹ h ⁻¹
p	Pressure	bar
R	Universal gas constant	J mol ⁻¹ k ⁻¹
r	Reaction rate	mol s ⁻¹
Re	Reynolds number	-
S	Selectivity	%
S _{BET}	BET Surface area	m ² g ⁻¹
Sc	Schmidt number	-
Sh	Sherwood number	-
STY	Space-time-yield	g _{MeOH} g _{cat} ⁻¹ h ⁻¹
T	Temperature	K
t	Time	s
u	Superficial velocity	m s ⁻¹
v	Diffusions volume	
\dot{V}	Volume flow	mL min ⁻¹

X	Conversion	%
y	Molar fraction	-
Y	Yield	%

Greek symbols	Definition	Unit
α	Probability threshold	-
ε	Porosity	-
μ	Gas viscosity	Pa s
ν	Stoichiometric number	-
ρ	Density	kg m ⁻³
φ	Fugacity coefficient	-

Indices	Definition
bed	Catalyst bed
f	Formation
i	Reference to a component
in	Inlet
cat (ger. Kat.)	Catalyst (ger. Katalysator)
LHV	Lower heating value
N	At standard temperature and pressure
obs	Observed
out	Outlet
R	Reaction

1 Zusammenfassung

Die Hydrierung von CO_2 mit H_2 aus der Wasserelektrolyse zu Methanol (MeOH) ist eine Schlüsselstrategie zur chemischen Energiespeicherung und zur Nutzung von CO_2 . MeOH verfügt über ein breites Anwendungsspektrum und gilt als wichtige Plattformchemikalie in der chemischen Industrie. Diese Arbeit untersucht die Anwendung von Indium-basierten Katalysatoren in der Methanolsynthese durch die Hydrierung von CO_2 in unterschiedlichen Reaktorkonzepten. Im Fokus stehen die Reaktionsbedingungen und die Katalysatoreigenschaften, die für eine hohe Aktivität und Selektivität benötigt werden.

Die industrielle Methanolproduktion verwendet hauptsächlich Zweiphasen- (gas-fest) oder Dreiphasenreaktoren (gas-fest-flüssig). Zweiphasenreaktoren sind anhand der Wärmeabfuhr in der katalytischen Schüttung in adiabatische und isotherme Reaktoren unterteilt. Dreiphasenreaktoren, wie Suspensions- und Wirbelschichtreaktoren ermöglichen eine effizientere Wärmeabfuhr und minimieren Massentransportlimitierungen.

Zunächst wurde die katalytische Performance von In_2O_3 und $\text{In}(\text{OH})_3$ in einem gas-fest-Reaktorsystem (Festbettreaktor) untersucht. Dabei wurden die Auswirkungen der Position des Thermoelements in der katalytischen Schüttung untersucht (oben, mittig oder unten). Ein katalytischer Modellzyklus bezüglich der Phasenumwandlung von $\text{In}_2\text{O}_3/\text{In}(\text{OH})_3$ wurde simuliert und mit den katalytischen Daten für 200, 250 und 300 °C und der Materialcharakterisierung (XRD und TGA) nach der Reaktion validiert. Bei der CO_2 Hydrierung entsteht Wasser als Nebenprodukt, wodurch In_2O_3 zu $\text{In}(\text{OH})_3$ degradieren kann. Bei hohen CO_2 Umsätzen und niedrigen Temperaturen (200 °C) postuliert das Modell stabiles $\text{In}(\text{OH})_3$. Bei höheren Temperaturen (> 275 °C) hingegen ist In_2O_3 stabil. Der Einfluss auf die Phasenumwandlung wurde jeweils bei 200, 250, 275 und 300 °C untersucht, indem $\text{In}(\text{OH})_3$ in zwei identische Segmente, getrennt durch eine Schicht Glaswolle, im Reaktor gepackt wurde. Durch das obere Segment strömt frisches Reaktionsgas, das dort teilweise zu MeOH , CO und H_2O umgesetzt wird und durch das untere Segment strömt. XRD und TGA zeigten eine Inversion des Trends der Phasenumwandlung zwischen 250 °C und 275 °C, das Modell prognostiziert dies bei 285 °C. Abschließend wurden mit dem validierten Modell die Auswirkungen von Wasserstoffarmut im Zustrom aufgrund der fluktuierenden Produktion aus erneuerbaren Energien auf die Katalysatorstabilität vorhergesagt. Für weitere Untersuchungen im Festbettreaktor wurde In_2O_3 mit unterschiedlichen Synthesemethoden auf zwei verschiedenen ZrO_2 -Trägern beladen. Im Detail, zeigte die Kombination der Nassimprägnierung nach Martin et al. (M) und dem

ZrO₂ (SG) mit einer größeren BET-Oberfläche und CO₂ Adsorptionskapazität die beste katalytische Performance. Maximal wurde 4,25 g_{MeOH} g_{In}⁻¹ h⁻¹ bei 300 °C, 75 bar, CO₂/H₂ = 1/3 und 8600 h⁻¹ produziert. Um die MeOH-Produktivität zu steigern, wurden verschiedene Metalle (Cu, Ni, Mg, Ce) als Promotoren für In₂O₃/ZrO₂ (M-SG) untersucht. NiO-In₂O₃/ZrO₂ (M-SG) steigerte die katalytische Aktivität von purem In₂O₃/ZrO₂ (M-SG). Durch erhöhte H₂-Aufnahme wird der H₂-Spillover-Effekt gesteigert, wodurch die Dissoziation und Migration zur Trägeroberfläche verbessert wird und die Bildung der Sauerstoffstellen, den aktiven Zentren für die CO₂ Hydrierung, begünstigt werden. Dies wurde durch chemisorptive Analysen (H₂-TPR und CO₂-TPD) bestätigt. Die Nassimprägnierung (WI) von NiO auf In₂O₃/ZrO₂ führte zu katalytisch aktiveren Katalysatoren. 0,76 Gew.% Nickel im NiO-In₂O₃/ZrO₂ (WI) Katalysator steigerte die Methanolproduktivität auf 4,42 g_{MeOH} g_{In+Ni}⁻¹ h⁻¹ im Vergleich zu purem In₂O₃/ZrO₂ (M-SG) mit 4,25 g_{MeOH} g_{In}⁻¹ h⁻¹ bei 300 °C, 75 bar, CO₂/H₂ = 1/3 und 8600 h⁻¹. Die Methanisierung wurde vollständig unterdrückt. Während der Reaktionszeit von 100 h war NiO-In₂O₃/ZrO₂ (WI) durchgängig stabil und aktiv.

Unter der Verwendung eines Compact Profile Reactors (CPR) wurden die Reaktionsprofile der In₂O₃/ZrO₂-basierten Katalysatoren im Vergleich mit dem industriell verwendeten Cu/ZnO/Al₂O₃ Katalysator untersucht. Das Reaktordesign erlaubt die räumlich aufgelöste Untersuchung der Reaktionsprofile einzelner Spezies und der Temperatur in der katalytischen Schüttung während der Hochdruck MeOH-Synthese. Der Einfluss der Reaktionsbedingungen, wie Gesamtdruck, Raumgeschwindigkeit (GHSV) und Temperatur wurden mit dem aktivsten Katalysator, Ni-In₂O₃/ZrO₂, untersucht. In dieser Studie führten höhere Drücke, Temperaturen und GHSVs zu einer Steigerung der MeOH Produktivität. Kürzere Verweilzeiten erhöhen die MeOH-Selektivität. Bei 50 bar, 275 °C, CO₂/H₂ = 1/3 und 63.000 h⁻¹ produzierte Ni-In₂O₃/ZrO₂ 4,90 g_{MeOH} g_{In+Ni}⁻¹ h⁻¹ mit einer MeOH-Selektivität von 73 %. Der restliche Kohlenstoff wurde durch die rWGS zu CO umgesetzt. Die Synthese von MeOH benötigt eine geringere Aktivierungsenergie (49 kJ mol⁻¹) als die reverse Wassergas-Shift-Reaktion (71 kJ mol⁻¹).

In einem Suspensionsreaktor (SR) wurde pures In₂O₃ und In₂O₃/ZrO₂ mit Ni durch unterschiedliche Synthesemethoden dotiert und für die dreiphasige MeOH-Synthese eingesetzt. Durch Co-Fällung (CP) synthetisiertes Ni-In₂O₃/ZrO₂ suspendiert in Mineralöl erzielte die höchste Aktivität und Selektivität sowohl für die Hydrierung von CO₂ als auch für die Hydrierung von CO. Unter Verwendung von Synthesegas mit industrieller Zusammensetzung (H₂/CO/CO₂) und einem

Zusammenfassung

Molverhältnis von 70/28/2 konnte eine sehr hohe Produktivität ($6,84 \text{ g}_{\text{MeOH}} \text{ g}_{\text{Kat}}^{-1} \text{ h}^{-1}$) erreicht werden. Der Katalysator ist bezogen auf den Aktivmetallgehalt im SR deutlich effizienter als der kommerzielle Cu/ZnO/Al₂O₃ Katalysator ($1,25 \text{ g}_{\text{MeOH}} \text{ g}_{\text{Cu}}^{-1} \text{ h}^{-1}$). Abschließend blieb der Katalysator und das Mineralöl in einer Rezyklierungsstudie mit vier Wiederholungen stabil.

Intensive Materialcharakterisierung mittels ICP-OES, XRD, XPS, N₂-physisorption, CO₂-TPD, H₂-TPR und TEM bzw. REM-EDX Aufnahmen begründen die unterschiedliche katalytische Aktivität der Katalysatoren in den verschiedene Reaktorkonzepten.

2 Abstract

CO₂ hydrogenation with H₂ from water electrolysis to methanol (MeOH) is a key strategy for chemical energy storage and for CO₂ utilization. MeOH serves various applications and is an important feedstock for the chemical industry as well. This work investigates the application of indium-based catalysts for MeOH synthesis via the hydrogenation of CO₂ in various reactor concepts focusing on the reaction conditions and catalyst properties necessary to achieve high activity and selectivity.

Industrial methanol production mainly uses two-phase (gas-solid) or three-phase reactors (gas-solid-liquid). Two-phase reactors are categorized into adiabatic and isothermal reactors based on the heat dissipation in the catalyst bed. Three-phase reactors, such as slurry and trickle bed reactors, enable more efficiency in heat removal and minimize mass transport limitations.

First, the catalytic performance of In₂O₃ and In(OH)₃ was studied in a fixed bed reactor. The impact of thermoelement positioning in the catalyst bed (top, middle or bottom position) was studied. Using catalytic data received at 200, 250 and 300 °C, along with material characterization (XRD and TGA) after the reaction, a catalytic model cycle was defined concerning the phase transition. CO₂ hydrogenation produces water as a by-product, leading to the degradation of In₂O₃ to In(OH)₃. The model postulates stable In(OH)₃ at low temperatures and higher conversions. In contrast, In₂O₃ remains stable at higher conversions and temperatures. The separation of In(OH)₃ into two identical segments, with a layer of glass wool between the segments, investigated the influence of the phase transition at 200, 250, 275 and 300 °C. Fresh gas flows through the top segment, being partially converted into MeOH, CO and water and flowing through the bottom segment. XRD and TGA analyses revealed an inversion of the trend between 250 °C and 275 °C, while the computational model predicts this occurrence at 285 °C. Lastly, the validated model was employed to predict the effects of hydrogen drop out in the feed due to fluctuating production from renewable energies on catalyst stability. In further studies within the fixed bed reactor, two different ZrO₂ were used as catalyst support and impregnated with In₂O₃ using different synthesis methods. In detail, the combination of wetness impregnation according to Martin et al. (M) and the ZrO₂ (SG) with a larger BET surface area and CO₂ adsorption capacity exhibited the best catalytic performance. At 300 °C, 75 bar, CO₂/H₂ = 1/3 and 8600 h⁻¹ the maximum MeOH production reached 4.25 g_{MeOH} g_{In}⁻¹ h⁻¹. To increase the MeOH productivity, various metals (Cu, Ni, Mg, Ce) were investigated as promoters for the In₂O₃/ZrO₂ (M-SG) catalyst. NiO-In₂O₃/ZrO₂ (M-SG) demonstrated an enhanced catalytic

activity. Due to enhanced H₂ uptake the H₂ spillover effect increases, which promotes H₂ dissociation and migration to the carrier surface and favors the formation of oxygen vacancies, the active centers for CO₂. This was confirmed by chemisorptive analyses (H₂-TPR and CO₂-TPD). NiO on In₂O₃/ZrO₂ prepared by wetness impregnation (WI) resulted in catalysts that were catalytically more active. NiO-In₂O₃/ZrO₂ (WI) with 0.76 wt.% Ni produced with 4.42 g_{MeOH} g_{In+Ni}⁻¹ h⁻¹ more MeOH than pure In₂O₃/ZrO₂ (M-SG) with 4.25 g_{MeOH} g_{In}⁻¹ h⁻¹ at 300 °C, 75 bar, CO₂/H₂ = 1/3 and 8600 h⁻¹. No methanation was observed. Over 100 h time on stream the NiO-In₂O₃/ZrO₂ (WI) remains stable and active.

In the Compact Profile Reactor (CPR), the reaction profiles of In₂O₃/ZrO₂-based catalysts were investigated and compared with the industrially used Cu/ZnO/Al₂O₃ catalyst. The reactor design enables spatially resolved analysis of the reaction profile for every species and temperature inside the catalytic bed during high-pressure MeOH synthesis by the hydrogenation of CO₂. The influence of reaction conditions, including total pressure, gas hourly space velocity (GHSV), and temperature, was studied using the most active catalyst, Ni-In₂O₃/ZrO₂. In this study, higher pressures, temperatures, and GHSVs led to increase the MeOH productivity. Shorter residence times enhance MeOH selectivity. At 50 bar, 275 °C and 63,000 h⁻¹, Ni-In₂O₃/ZrO₂ produced 4.90 g_{MeOH} g_{In+Ni}⁻¹ h⁻¹ with 73 % selectivity of MeOH. The remaining carbon is converted into CO via the rWGS. MeOH synthesis requires a lower activation energy (49 kJ mol⁻¹) compared to the reverse water-gas shift reaction (71 kJ mol⁻¹).

In a suspension (slurry) reactor (SR), pure In₂O₃ and In₂O₃/ZrO₂ was doped with nickel using different synthesis methods and used for three-phase MeOH synthesis. Ni-In₂O₃/ZrO₂ prepared by co-precipitation (CP) and suspended in mineral oil achieved the highest catalytic activity and selectivity for MeOH for both CO and CO₂ hydrogenation. Using synthesis gas with industrial combustion (H₂/CO/CO₂) and a molar ratio of 70/28/2, a very high productivity of MeOH (6.84 g_{MeOH} g_{Kat}⁻¹ h⁻¹) was achieved, which is significantly more efficient than the productivity of the commercial Cu/ZnO/Al₂O₃ catalyst (1.25 g_{MeOH} g_{Cu}⁻¹ h⁻¹) in the SR related to the quantities of active metals. Finally, the catalyst and the mineral oil remained stable in a recycling study with four replicate runs.

Intensive catalyst material characterization using ICP-OES, XRD, XPS, N₂-physisorption, CO₂-TPD, H₂-TPR and TEM or SEM-EDX mappings provide insights in the difference in catalytic activity of the catalysts in the various reactor concepts.

3 Introduction

Since the industrial revolution, the carbon dioxide (CO₂) emissions have been increasing and acting as a greenhouse gas for global warming [1]. Industries with high energy demand such as cement, iron and steel, nonferrous metals manufacturing (e.g. copper), refineries, pulp and paper emit substantial amounts of CO₂ [2,3]. A promising strategy to reduce the emissions involves the carbon capture and storage (CCS) and utilization (CCU) approach directly from industry exhaust gas or from the atmosphere into commercial products such as methanol [3].

To mitigate the CO₂ emissions, traditional fossil fueled power plants must be replaced with renewable energy alternatives. Renewable energy from wind and solar are highly intermittent sources, resulting in additional strain on the existing grid power generation and transmission infrastructure.[4] Excess renewable energy is either stored by generation of heat (Power-to-Heat, PtH) or used by technologies that are capable of converting abundant molecules such as water or CO₂ to energy holding chemicals (Power-to-Chemicals, PtC). During electrolysis, water is split into oxygen and hydrogen. Hydrogen and CO₂ from CCS react to methane or synthesis gas (Power to Gas, PtG) or to liquids such as methanol (Power-to-Liquid, PtL). [5,6]

Figure 3.1 shows the schematics of Power-to-X (PtX), which is defined by the different pathways for storage and utilization technologies of surplus electricity from renewable sources and for reducing greenhouse gas emissions [7].

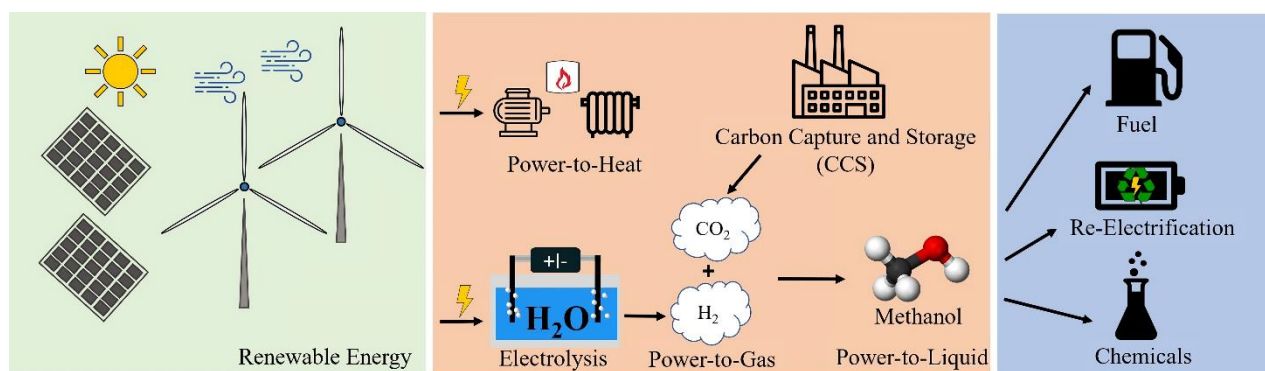


Figure 3.1. Schematics of Power-to-X infrastructure focused on methanol.

In 2022 the global production capacity of methanol reached approximately 172 million metric tons [8]. It is mainly used as a raw material for the synthesis of olefines and formaldehyde. Methanol is discussed as a potential energy carrier due to its higher volumetric energy density (4.2 kWh L⁻¹) than hydrogen (0.003 kWh L⁻¹, atm) and its liquid state at ambient conditions. Energy recovery can

be accomplished by methods such as direct burning, steam reforming or use in direct methanol fuel cells (DMFCs) for re-electrification. [9,10]

Commercially, methanol is produced at 50–100 bar and 200–300 °C using syngas (CO, H₂) derived from fossil sources such as natural gas or crude oil. The reaction is accelerated by a copper-based catalyst and the addition of small amounts of CO₂ [11,12]. The reactors for industrial synthesis of methanol are classified into adiabatic (e.g. the ICI converter) or isothermal (e.g. Lurgi reactor) reactors according to their strategy of heat removal [13]. This is significant because otherwise, the state-of-the-art Cu/ZnO/Al₂O₃ catalyst deactivates by thermal sintering above 300 °C [14]. For pure CO₂ hydrogenation, Cu/ZnO/Al₂O₃ deactivates due to segregation of Cu/ZnO [15].

Indium-based catalysts have demonstrated to be highly selective and stable catalysts for hydrogenation of CO₂ to methanol [16]. Under methanol synthesis reaction conditions, In₂O₃ creates oxygen vacancies that activate CO₂ for formate (HCOO⁻) formation. The combination with ZrO₂ as a support increases the catalytic activity due to a synergistic effect between the oxygen vacancy defects of the oxides at the interface [16,17].

This thesis “CO₂ Hydrogenation to Methanol in Different Reactor Concepts using Metal-doped Indium-based Catalysts” aims to improve the understanding of these catalysts and continues to develop their catalytic activity. The experimental work can be divided in three distinctive reactor setups: a continuously operated fixed bed reactor (integral operation, two-phase reactor), a continuously operated compact profile reactor (differential operation, two-phase reactor) and a slurry stirred-tank reactor (batch operation, three-phase reactor) for the CO₂ hydrogenation to methanol. This thesis includes four publications [18–21] as the cumulative part.

3.1 Methanol as promising Power-to-X hydrogen carrier

Governments worldwide are accelerating the expansion of renewable energies, particularly solar and wind power to achieve the goals set by the Paris Climate Agreement in 2015 to limit global warming [22]. Due to the increasing share of renewable energies in power generation and the associated fluctuations, the storage of excess power generated is very important. Especially on sunny or windy days, a negative residual load is present in the power grid. [4] Residual load is defined as the difference between electricity demand and electricity from renewables [23]. To ensure that generators do not need to be disconnected from the grid, energy consumers are required,

preferably in form of energy storage solutions [24]. Energy storage can be categorized into short-, medium- and long-term options [4,9,25]. Flywheels or supercapacitors are considered very short-duration storage options, typically providing storage for less than 5 minutes [25]. Electrochemical batteries are commonly used between seconds and hours [26]. Medium-term storage options, lasting from 4 to 200 hours, include thermo-mechanical storage systems, e.g. pump-storage hydroelectricity, pumped thermal energy storage or compressed air energy storage [25,27]. Long-term storage with a duration exceeding 200 hours is primarily accomplished by storing fuels such as hydrogen, ammonia, or bio-gas [25]. Another classification for a range of technologies that convert electrical energy, typically from renewable sources, into other forms of energy or energy carriers is Power-to-X (PtX). This includes PtG e.g. hydrogen or methane, PtH e.g. using a heating element, and PtL e.g. methanol or ammonia applications. [5,6]

Hydrogen from water electrolysis/ Water electrolysis technologies

Electrical energy (preferably excess from renewables) is transformed into hydrogen by electrolysis of water. In this process, a direct current (DC) is used in an electrolyzer to produce a difference in electric potential (voltage) between anode to cathode. Water is supplied and electrochemically decomposed to oxygen and hydrogen [28]. At the cathode (negative electrode) hydrogen is formed via the hydrogen evolution reaction (HER) whilst at the anode (positive electrode) oxygen is produced via the oxygen evolution reaction (OER). The main relevant technologies are the solid oxide electrolysis (SOEC), alkaline electrolysis (AE) and the proton exchange membrane electrolysis (PEM) [29,30].

SOEC is a high temperature electrolyzer operating between 600 °C and 1000 °C [31–33], up to 30 bar and at current densities between 0.2-1.3 A cm⁻² [34]. Gaseous water is introduced at the cathode side and is reduced to hydrogen (HER). The oxide anions cross the solid electrolyte (e.g. yttria-stabilized zirconia) to form O₂ by oxidation at the anode side (Figure 3.2, Table 3.1, tech. SOEC) [32]. Due to a stack lifetime of 40,000-50,000 hours [31,34], and an energy efficiency up to 100 % [35], SOECs have garnered significant attention. The hydrogen purity is 99.9 % [36]. The SOECs operating flexibility allows for electrolysis of CO₂ to CO and the co-electrolysis of H₂O/CO₂ to H₂/CO (syngas) as well [35]. The technology is mostly still at lab-scale, but studies like the EU-funded GrInHy2.0 project (2022) mark the first implementation of SOEC in an industrial environment. 18 kg h⁻¹ hydrogen will be produced using waste heat from an iron-and-steel factory

with a nominal input of 720 kW and an electrical efficiency of 84 %_{el,LHV} [37]. The drawbacks are associated with material durability due to high temperatures. Moreover, SOECs are hardly compatible to be coupled with fluctuating renewable energy generated electricity [38].

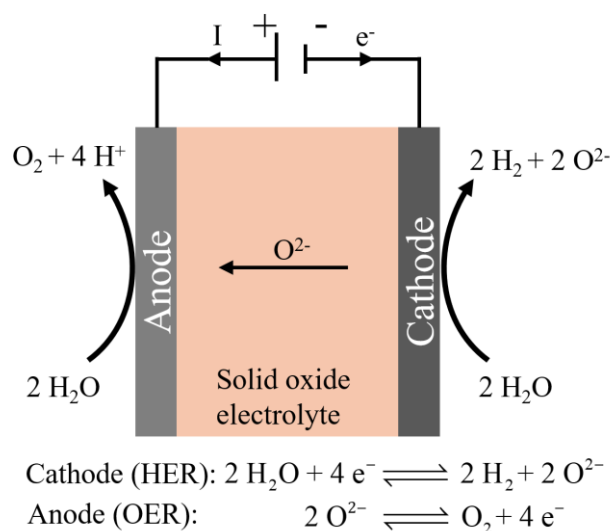


Figure 3.2. Schematic SOEC and the corresponding electrode reactions (HER,OER), adapted from [34,39].

For AEs, typically a 20–40 wt% potassium hydroxide solution is used as a liquid electrolyte operating at low current densities (0.2–0.5 A cm⁻²). The operating pressure is up to 30 bar and typical operating temperatures are between 50 °C and 100 °C [34,40]. This system utilizes nickel as the cathode catalyst, and either nickel or copper coated with metal oxides (Mn, Ru, or W) as the anode catalyst. [41] Water is split at the cathode (HER) using electrons into hydrogen and hydroxide ions. The latter migrate through the electrolyte and the diaphragm to be converted at the anode (OER) into water and oxygen while releasing electrons (see Figure 3.3). [42] The gas purities are 99.3–99.9998 % for H₂ and 99.2 % for O₂ [34,42]. A long lifetime (60,000–100,000 h), a relatively cheap liquid electrolyte and a low content of noble metals favor the AE [31,34]. Problems related to the crossover of oxygen to the cathode reduces the efficiency due to recombination. The energy efficiency is up to 84 % [43]. Hydrogen diffusion into the OER chamber can also occur. A drawback is the low maximum current density because of high ohmic losses across the diaphragm and the liquid electrolyte.[35] The specifications of AE are summarized in Table 3.1.

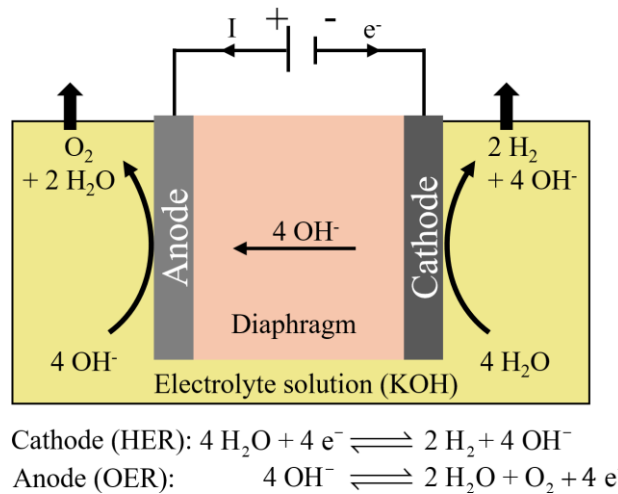


Figure 3.3. Schematic AE and the corresponding electrode reactions (HER,OER), adapted from [34,39].

For water electrolysis with intermittent renewable power sources, PEMs are most suitable [41]. PEMs operated at temperatures up to 170 °C [44] and pressures up to 180 bar [45]. Noble metals such as Platinum serve as electrocatalyst at the cathode for HER and IrO₂/RuO₂ at the anode for OER. A thin solid polymer electrolyte or proton exchange membrane (20–300 μm) separates cathode and anode (see Figure 3.4) [46]. The proton-conducting polymer (usually perfluorosulfonic acid or Nafion) is impermeable to electrons and gases, which minimize electron short circuit and gas crossover [47]. PEMs can achieve a high rate of hydrogen production while maintaining the purity of gases at 99.999 % [31], a life time of stack up to 100,000 h [34] and an energy efficiency of 83 %. With a compact design, high current densities up to 10 A cm⁻² can still be achieved as well [34], summarized in Table 3.1. The high costs of cell/electrolyzer components, noble metal electrocatalysts and an acidic corrosive environment are the main disadvantages [35,36,46].

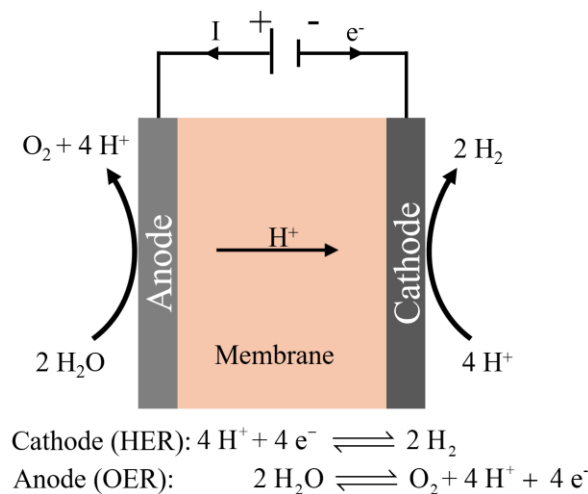


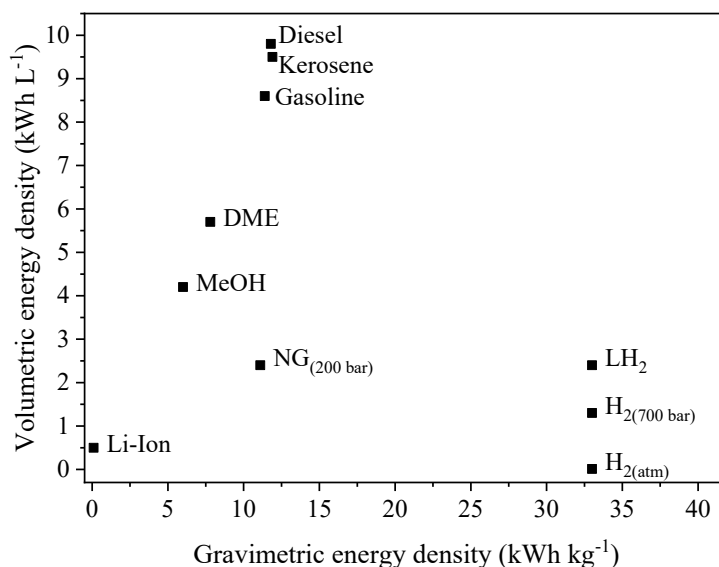
Figure 3.4. Schematic PEM and corresponding reactions at the electrodes, adapted from [34,39].

Table 3.1. Comparison of the water electrolyzer technologies.

Specification	SOEC	AE	PEM
Cell temperature (°C)	600-1000	50-100	<170
Cell pressure (bar)	30	30	<180
Current density (A cm ⁻²)	0.2-1.3	0.2-0.5	<10
Hydrogen purity (vol.%)	99.9	99.3-99.9998	99.999
Stack lifetime (h)	40,000-50,000	60,000-100,000	<100,000
Energy efficiency (%)	100	84	83
Charge carrier	O ²⁻	OH ⁻	H ⁺
Electrolyte	Yttria-stabilized zirconia	20-40 wt.% KOH	Perfluorosulfonic acid, Nafion
HER catalyst	Ni/Yttria-stabilized zirconia	Ni	Pt
OER catalyst	Perovskite-type	Ni, Cu	IrO ₂ , RuO ₂
Reference	[31–34,36,39]	[34,36,39,40,42]	[34,39,41,46,48]

Hydrogen as a chemical energy storage molecule

Electricity can be converted into chemical energy via hydrogen through the process of water electrolysis, enabling the storage of excess power. The replacement of fossil fuels with hydrogen, is the key aspect for a “green hydrogen economy” to reduce or eliminate CO₂ emissions in the sectors of power generation, heating, industry and transportation. John Bockris [49] created the concept of a “hydrogen economy” with hydrogen as a principle energy carrier in the 1970s. In fuel cells, hydrogen is converted back to water to generate electricity. It can also be used in internal combustion engines or jet engines to generate power for transportation or heat, as a chemical feedstock or as a reagent for synthetic fuel production [50,51]. The gaseous form of hydrogen from electrolysis of water has a high gravimetric energy density of 33.0 kWh kg⁻¹ compared to diesel with 11.8 kWh kg⁻¹ or gasoline with 11.4 kWh kg⁻¹ (see Figure 3.5) [52].

**Figure 3.5.** Comparison of different fuels and Li-Ion batteries. Volumetric versus gravimetric energy density, adapted from [9,52].

The hydrogen economy is significantly impacted by the major challenge of hydrogen storage. Gaseous hydrogen is typically stored in pressure tanks, as hydrides (metal hydrides, boron- and nitrogen-based hydrides), converted to a liquid organic hydrogen carrier (LOHC) or adsorbed on the surface of carbon nanotubes, microspheres or capillaries [53,54]. Due to the low volumetric energy density of gaseous hydrogen (0.003 kWh L^{-1} , Figure 3.5), pressurized hydrogen (1.3 kWh L^{-1} , 700 bar) and liquefied hydrogen (2.4 kWh L^{-1} , LH_2) require large tanks, special materials and energy-intensive compression or cooling [53]. The challenges associated with hydrogen storage include transportation, safety concerns, low storage density, boil-off losses and high costs. Due to the numerous disadvantages, the chemical conversion of gaseous hydrogen into a liquid, such as methanol with a high volumetric energy density (4.2 kWh L^{-1}), is a viable option.

Methanol as a hydrogen carrier

Methanol, sometimes called methyl alcohol or wood alcohol with the formula CH_3OH ($M_{\text{MeOH}} = 32.04 \text{ g mol}^{-1}$), is often abbreviated as MeOH. It is a colorless liquid under normal temperature and pressure ($20 \text{ }^\circ\text{C}$, 1.013 bar) with a melting point of $-97.8 \text{ }^\circ\text{C}$. Methanol is the simplest aliphatic alcohol and mixes completely with water. The boiling point of methanol is $64.7 \text{ }^\circ\text{C}$ at 1.013 bar with $37.34 \text{ kJ mol}^{-1}$ heat of vaporization at $25 \text{ }^\circ\text{C}$ [55]. It is an ideal hydrogen carrier with an amount of 12.6 wt.% hydrogen per methanol molecule [56]. Methanol as an energy carrier has a volumetric energy density of 4.2 kWh L^{-1} and a gravimetric energy density of 6.0 kWh kg^{-1} (see Figure 3.5). Electricity can be generated via an electrochemical reaction using a mixture of liquid methanol and water with a direct-methanol fuel cell (DMFC). One advantage of the DMFC, compared to other fuel cells, is its ability to utilize liquids instead of gases, making fuel handling easier. This is highly suitable for portable power generation with the drawback of lower efficiency ($< 30 \%$) due to a methanol cross-over across the membrane. [10]

Methanol is already traded as a base chemical and does not have to be compressed or liquefied in an energy intensive cryogenic process. Current crude infrastructure e.g. pipes or tankers could transport methanol with minor modifications. [57] Due to the simple handling, the potential to integrate methanol into the existing infrastructure and having a diverse range of applications (see Chapter 3.1.2) the “methanol economy” was proposed by Olah [58]. However, a carbon source is necessary for methanol synthesis, besides hydrogen.

3.1.1 Synthesis of Methanol from CO vs. CO₂ (kinetics and thermodynamics)

Conventionally, methanol is produced from syngas. The raw materials for syngas production are fossil fuels such as natural gas, coal and oil or biomass. Natural gas containing methane or light hydrocarbons as feedstock can be successfully converted into syngas by reforming technologies (dry and steam reforming). Heavy oil, coal and biomass containing hydrocarbons produce syngas via gasification and pyrolysis technologies [11,59]. The interaction of carbon dioxide with methane at temperatures up to 800 °C over Ni-based catalysts results to dry reforming [60–62]. A great challenge with dry reforming is the catalyst deactivation by coking [63]. While the dry reforming process utilizes CO₂ as the co-reactant, steam reforming is an endothermic reaction between natural gas feed and steam at similar temperatures. For steam reforming of natural gas, a desulfurization step is required to attain purified methane. For example, small amounts of sulfur in the form of H₂S are filtered out with the reaction of ZnO to ZnS. Higher amounts of sulfur are removed by absorption (scrubbing) with aqueous amine solutions. Organic sulfur compounds (e.g. thiophene) need to be hydrotreated before removal, at first [11]. The main reaction of the natural gas steam reforming technology is to convert methane with steam into hydrogen:



The high endothermic reaction produces a high H₂/CO ratio of 3/1 [64]. High operating temperatures of 700–900 °C [65] and pressures of about 30 bar are required for the reaction inside a reformer [11]. Nickel supported on ceramic oxides are the most common heterogeneous catalyst used for methane steam reforming (Eq. (3.1)) [64].

Gasification or partial oxidation converts carbon compounds such as biomass, coal or heavy oils into a syngas with oxygen (Eq. (3.2)) or steam (Eq. (3.3)).



The kind of the gasifier used depends on the impurity, water and ash content of the carbon compound [66]. A fixed bed gasifier, for example, can only process non-coking coals, since other coals can form agglomerates leading to an elevated pressure drop or potential blockage of the reactor/catalyst. In the gasification process, CO₂, formed by the water-gas shift reaction (WGS, see Eq. (3.4)), can partly gasify carbon by the Boudouard reaction (Eq. (3.5)) at temperatures of 900 °C [11]. The hydrogen content of the produced syngas is deficient and can be enhanced through the WGS reaction. Impurities such as tar, ash, soot (solid carbon) have to be removed by filtration from the raw syngas [11]. The clean syngas may be pressurized using a compressor, combined with unconverted recycled syngas, preheated and then be directly used as raw material for methanol synthesis. The blended gases, featuring a H₂/CO ratio ranging from 3/1 to 5/1, are fed into the reactor. [66]

Pyrolysis, a thermochemical process, decomposes organic materials at higher temperatures in the absence of oxygen. The products of e.g. biomass pyrolysis are bio-oil, biochar and syngas derived from their composition of cellulose, lignin, hemicellulose and extractives. In comparison to the partial oxidative gasification process, the inert pyrolysis of biomass exhibits a lower process efficiency. However, it has the advantage of producing fuel gas with a high heating value. [67] At first, the transient heating of the solid biomass particles causes a local temperature increase, leading to the evaporation of moisture (drying step). This is followed by the progressive release of pyrolytic volatiles (primary pyrolysis step) from the thermal cleavage (T < 500 °C) of chemical bonds to permanent gas species (e.g. CO, CH₄, CO₂). The devolatilization step is the chemical decomposition during heating in the absence of oxygen to char, non-condensable gases (CO, CH₄, CO₂, H₂), water vapor and tar [67]. After the successful production, the purified syngas is utilized as a cost-effective feedstock for the synthesis of methanol.

Methanol synthesis from syngas

The production of methanol from syngas involves the WGS (Eq. (3.4)) and the following reactions [13]:



Due to the parallel WGS reaction (Eq. (3.4)), the produced CO₂ and CO can be stoichiometrically converted into methanol:



The by-product water (see Eqs. (3.7) and (3.8)) has a detrimental effect on the traditional Cu-based catalyst by deactivating the active species (refer to Chapter 3.2.1) [68]. Furthermore, the formation of water reduces the overall efficiency and hydrogen utilization.

Compared with the CO hydrogenation to methanol (Eq. (3.6)), the CO₂ hydrogenation (Eq. (3.7)) generates less reaction heat. The endothermic reverse water-gas shift reaction (rWGS, Eq.(3.8)) weakens the overall heat release likewise:



The reaction network, including endothermic and exothermic reactions, influences the methanol synthesis and selectivity. For exothermic reactions, the equilibrium shifts towards the product side (methanol) according to Le Chatelier's [69] principle with lower temperatures. The opposite applies to endothermic reactions. The reaction pressure influences the methanol synthesis as well. A volume-reducing reaction, like the methanol synthesis, is favored at higher pressure. Assuming an ideal gas, the rWGS (Eq. (3.8)) is constant in volume and therefore not influenced by pressure. In conclusion, methanol production from CO or CO₂ is favorable at low temperatures and high pressures (see Figure 3.6). [70]

Syngas produced from various carbon sources and through the WGS (Eq. (3.4)) contains a certain proportion of CO₂. Klier et al. [12] investigated the effects of CO₂ on catalytic performance of MeOH synthesis using the CuO/ZnO catalyst. With a syngas composition ratio of CO/CO₂/H₂ = 28/2/70 a maximum reaction rate was observed. The stoichiometric number (SN) determined the ratio between molar fraction (y_i) of H₂ and CO₂ (Eq. 3.9):

$$SN = \frac{y_{\text{H}_2} - y_{\text{CO}_2}}{y_{\text{CO}} + y_{\text{CO}_2}} \quad (3.10)$$

For industrial processes a stoichiometric mixture $SN > 2$ with an excess of H₂ is adjusted to prevent the formation of side products [71]. For example, the equilibrium yield of methanol (calculated with Aspen Plus V12 using the equation-of-state by Soave-Redlich-Kwong ((SRK) [72]) is $Y_{\text{MeOH}} = 72 \%$ at 250 °C and 75 bar for pure CO hydrogenation (Figure 3.6 a)). With the addition

of 2 % CO₂ into the feed, the yield increases slightly ($Y_{\text{MeOH}} = 74\%$, Figure 3.6 b)) at the same conditions.

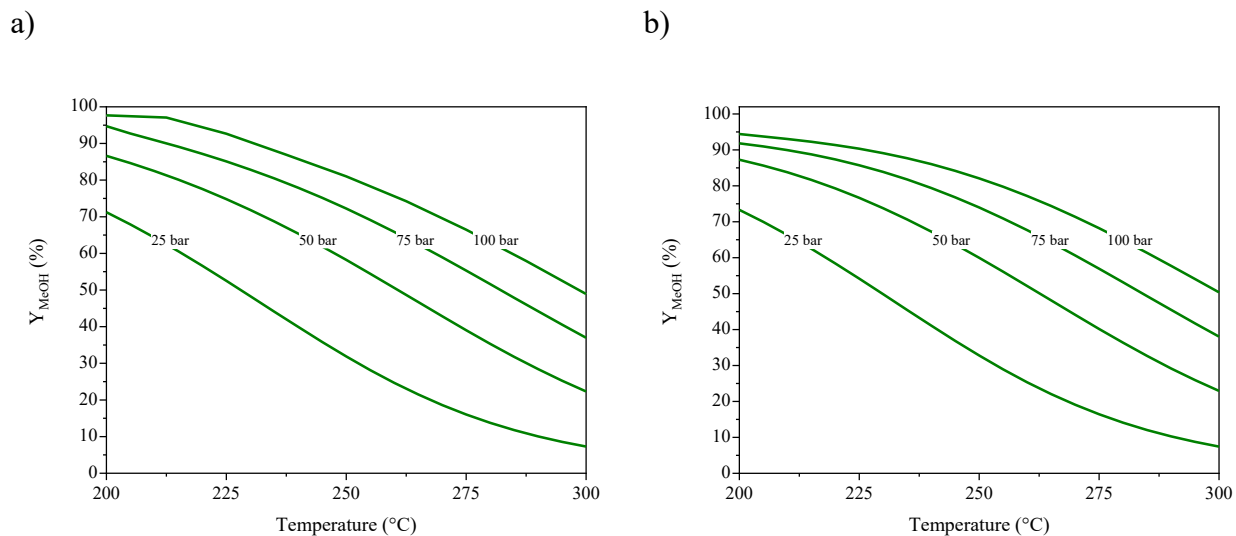


Figure 3.6. Equilibrium yields of methanol calculated with Aspen Plus V12 using equation-of-state by SRK [72]. a) Pure CO hydrogenation to methanol with $\text{CO}/\text{H}_2 = 33/67$, b) max. reaction rate composition $\text{CO}/\text{CO}_2/\text{H}_2 = 28/2/70$ [12].

Methanol synthesis from CO₂

The combustion of fossil fuels for energy generation leads to a significant emission of anthropogenic greenhouse gases, mostly in the form of CO₂, to the atmosphere. CO₂ undeniably plays a crucial role in the greenhouse effect. The substantial emissions are leading to issues of global warming and climate change [3]. In 2022, the global CO₂ emissions reached 37.5 Gt [73], and the concentration of atmospheric CO₂ has increased to 418.6 ppm in 2022 [74] (see Figure 3.7). Before the industrial revolution, the concentration of CO₂ in the atmosphere was about 280 ppm [3].

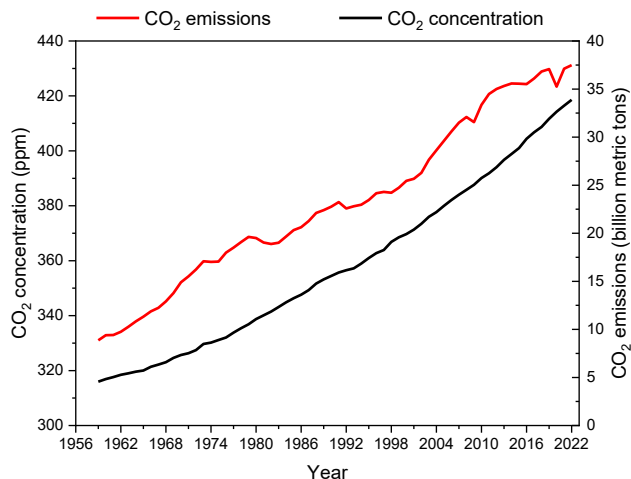


Figure 3.7. CO₂ emissions and concentration in the atmosphere from 1959 to 2022, data out of [73,74].

This aspect underlines the significance of advancing alternative technologies and achieving CO₂-free power generation. In comparison to CCS technology, CCU technology, involving electrocatalytic, thermocatalytic and photocatalytic processes, goes beyond merely mitigating greenhouse gas emissions and conserving fossil resources. [75] It involves recycling CO₂ as a building block (C1) to produce chemicals, materials and high-value fuels. The direct utilization of CO₂ as a feedstock in the chemical industry is a promising approach. [76] Depending on the CO₂ source in industry, different contaminants such as NO_x, SO_x, aromatics, dust and much more can occur in the syngas. If those are not removed, they could lead to catalyst poisoning for example. In a typical cement manufacturing process, CO₂ is generated from de-carbonation of limestone in the kiln (535 kg t⁻¹ clinker), fuel combustion in the kiln (335 kg t⁻¹ cement) and use of electricity (50 kg t⁻¹ cement). [77] To remove the impurities (see Table 3.2) specialized equipment is required, e.g. a selective catalytic reduction (SCR) system to reduce NO_x, a fuel-gas desulfurization (FGD) system to reduce SO_x and filter systems to remove particles. To further separate CO₂, a post combustion capture system using an amine scrubbing system with monoethanolamin is used. The pure CO₂ is then stripped from the amine, dried, and pressurized, typically to 110 bar and ready to be used as a raw material [77]. Other potential sources of CO₂ from industry and their impurities are shown in Table 3.2.

Table 3.2. Potential CO₂ sources from industry processes and their impurities.

CO ₂ source	CO ₂ concentration	Impurities	Ref.
Cement industry	14–33 %	NO ₂ , NO _x , SO ₂ , O ₂ , dust	[77–79]
Traditional Iron and steel	15–42 %	NO _x , SO _x , BTX, phenol, hydrocarbons, PAH, dust, heavy metal compounds, HCl	[79–81]
Ammonia production	98–100 %	H ₂ , O ₂ , CH ₄	[81]
Ethylene production	7–12 %	H ₂ O, CO, NO _x , SO _x , O ₂ , N ₂	[81]
Coal power plant	10–15 %	NO _x , SO _x , O ₂ , N ₂ , CO, Hg, As, Se	[81]
Petroleum power plant	3–8 %	NO _x , SO _x , O ₂ , N ₂	[81]
Natural gas power plant	3–5 %	NO _x , SO _x , O ₂ , N ₂ , CO, Hg, As, Se	[81]
Ethanol production	98–99 %	H ₂ S, methanol, ethanol, acetaldehyde, dimethyl sulphide, ethyl acetate	[81]

A renewable carbon source is crucial for the sustainable production of methanol through electrolytic hydrogen from renewables (PtX). The fixation of industrial emissions containing CO₂ producing methanol is a promising option. The stoichiometric conversion with hydrogen using a Cu-based or In-based catalyst produces methanol and water (Eq.(3.7)). CO is a by-product of the rWGS (Eq.(3.8)). The CO₂ hydrogenation to methanol (-49 kJ mol⁻¹) is less exothermic than CO hydrogenation (-91 kJ mol⁻¹). Coupled with the endothermic rWGS (+41 kJ mol⁻¹) the CO₂ hydrogenation to methanol produces less reaction heat and thus, a more homogeneous temperature profile is expected in a catalytic bed. The equilibrium yields of MeOH and CO calculated using Aspen Plus V12 and the equation-of-state by SRK [72] are shown in Figure 3.8. For pure CO₂ hydrogenation the equilibrium yields are much lower than for pure CO hydrogenation. At 250 °C and 75 bar, the equilibrium yield of methanol is $Y_{\text{MeOH}} = 28\%$ for a stoichiometric ratio of $\text{CO}_2/\text{H}_2 = 25/75$.

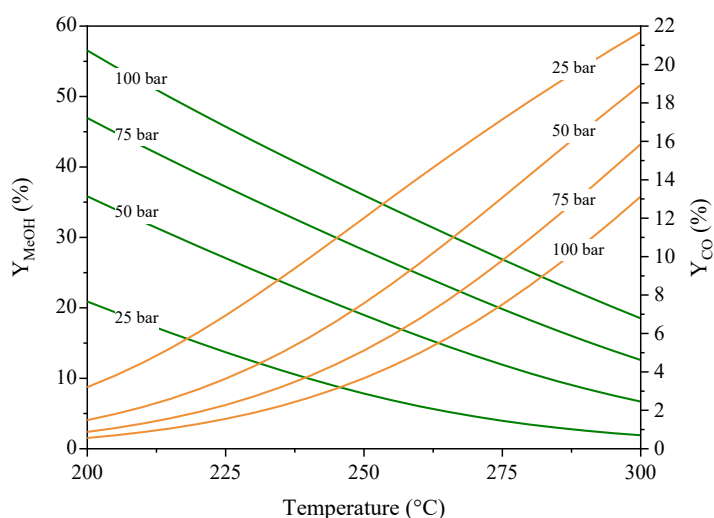


Figure 3.8. Equilibrium Yield of methanol for pure CO₂ hydrogenation with $\text{CO}_2/\text{H}_2 = 25/75$.

Kinetic models

The pressure affinity of the methanol synthesis can be explained with the law of mass action. It is described as the relationship between the activities of the reactants in a chemical reaction at equilibrium. The equilibrium constant determines the distribution of reactants in the equilibrium state. For ideal gases the equilibrium constants K and its change in temperature can be calculated using the following equations (Eq. (3.11), Eq. (3.12)) [82]:

$$K = e^{\left(\frac{-\Delta G_R^\circ}{RT}\right)} \quad (3.11)$$

$$\ln K(T_2) = \frac{1}{R} \left[\frac{-\Delta G_R^\circ(298.15 \text{ K})}{298.15 \text{ K}} + \int_{298.15 \text{ K}}^T \frac{\Delta H_R^\circ(T)}{T^2} dT \right] \quad (3.12)$$

The standard enthalpy ΔH° is a function of temperature involving the heat capacities of the components c_p as follows (Eq. (3.13)):

$$\Delta H_R^\circ(T) = \Delta H_R^\circ(298.15 \text{ K}) + \int_{298.15 \text{ K}}^T \Delta c_p^\circ(T) dT \quad (3.13)$$

Industrial methanol synthesis is conducted at elevated temperatures and pressures ($T > 200 \text{ }^\circ\text{C}$, $p > 50 \text{ bar}$). Hence, corrections for non-ideal gas behavior are required. The fugacity of real gases is a function of partial pressures p_i and component fugacity coefficient ϕ_i (Eq. (3.14)):

$$f_i = \phi_i \cdot p_i \quad (3.14)$$

In general, the equilibrium state K_f for real gases is calculated under consideration of the stoichiometric coefficient ν_i as follows (Eq. (3.15)):

$$K_f = K_p \cdot K_\phi = \prod_i (p_i)^{\nu_i} \prod_i \phi_i^{\nu_i} \quad (3.15)$$

For the Eq. (3.6)–(3.8) the equilibrium states $K_{f,1}$ (CO hydrogenation), $K_{f,2}$ (rWGS) and $K_{f,3}$ (CO₂ hydrogenation) are calculated using Eq. (3.15) [83]:

$$K_{f,1} = K_{p,(3.6)} \cdot K_{\phi,(3.6)} = \frac{p_{\text{MeOH}} \cdot p_0^2}{p_{\text{CO}} \cdot p_{\text{H}_2}^2} \cdot \frac{\phi_{\text{MeOH}}}{\phi_{\text{CO}} \cdot \phi_{\text{H}_2}^2} \quad (3.16)$$

$$K_{f,2} = K_{p,(3.8)} \cdot K_{\phi,(3.8)} = \frac{p_{\text{CO}} \cdot p_{\text{H}_2\text{O}}}{p_{\text{CO}_2} \cdot p_{\text{H}_2}} \cdot \frac{\phi_{\text{CO}} \phi_{\text{H}_2\text{O}}}{\phi_{\text{CO}_2} \cdot \phi_{\text{H}_2}} \quad (3.17)$$

The CO₂ hydrogenation Eq. (3.8) is the stoichiometric sum of reactions Eq. (3.6) and Eq. (3.7) and the equilibrium constant is the result of multiplication:

$$K_{f,3} = K_{f,1} \cdot K_{f,2} \quad (3.18)$$

Graaf et al. [84] postulate a kinetic model based on the adsorption of CO₂ and CO on two active sites and their stepwise hydrogenation already in 1988. This kinetic model was refurbished by Henkel [85] using a micro fixed bed and Berty-type reactor. For the following kinetic model adopted from Graaf's [84] model, the CO hydrogenation refers to (1), CO₂ hydrogenation to (2) and rWGS to (3). Graaf and Henkel [84,85] formulated the kinetic rate equation, using a Langmuir-Hinshelwood-Hougen-Watson type mechanism (LHHW). The LHHW approach assumes energetically equivalent adsorption sites on the surface, whereby adsorbate-adsorbate interactions are not considered. In addition, it is postulated that all reactants and products are in equilibrium with the surface species and a clearly identifiable reaction rate determining step (RDS) exists. The surface coverages are related to partial pressures through Langmuir adsorption isotherms [86]. The general term for the LHHW rate equation is defined as follows (Eq.(3.19)):

$$r = \frac{\text{rate factor} \times \text{driving force}}{\text{inhibition term}} \quad (3.19)$$

Henkel [85] also considers the fugacities f_i of the reactants relevant for the forward chemical reaction and modified the numerator term using the *EQ* number (Eq. (3.20)-(3.22)):

$$EQ_1 = 1 - \frac{f_{\text{MeOH}}}{f_{\text{CO}} \cdot f_{\text{H}_2}^2 \cdot K_{f,1}} \quad (3.20)$$

$$EQ_2 = 1 - \frac{f_{\text{CO}} \cdot f_{\text{H}_2\text{O}}}{f_{\text{CO}_2} \cdot f_{\text{H}_2} \cdot K_{f,2}} \quad (3.21)$$

$$EQ_3 = 1 - \frac{f_{\text{MeOH}} \cdot f_{\text{H}_2\text{O}}}{f_{\text{CO}_2} \cdot f_{\text{H}_2}^3 \cdot K_{f,3}} \quad (3.22)$$

The model postulated the existence of two different types of active centers. It is assumed that dissociative H₂ and H₂O adsorption takes place at one center (*) while the other active center (#) serves as an adsorption site for CO and CO₂. Two parallel pathways were assumed for the formation of methanol: one via the stepwise hydrogenation of CO and secondly via stepwise hydrogenation of

CO₂. For the rWGS, it is assumed that the mechanism takes place via a formate species. This results in a reaction network (see Figure 3.9) with three independent elementary step combinations accordingly. [84]

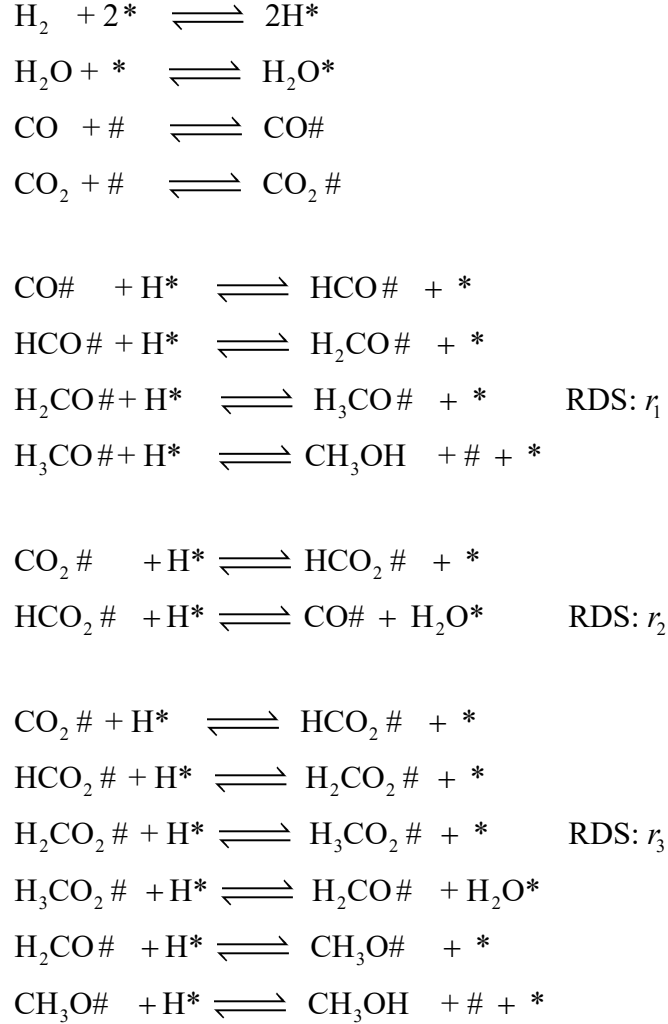


Figure 3.9. Surface reactions according to Graaf et al. [70] with two different types of active centers * and #.

For the formation of methanol from CO, according to the model, the hydrogenation of a formaldehyde species is postulated to be the RDS r_1 and for the rWGS reaction this is the hydrogenation of a formate species r_2 . The assumed RDS (r_3) for the formation of methanol from CO₂ is the hydrogenation of a created dioxomethylene species. The mentioned reaction rates can each be calculated by the following equations: [85]

Introduction

$$r_1 = \frac{k_1 \cdot K_1 \cdot f_{\text{CO}} \cdot f_{\text{H}_2}^{1.5} \cdot EQ_1}{(1 + K_1 \cdot f_{\text{CO}} + K_2 \cdot f_{\text{CO}_2}) \cdot (f_{\text{H}_2}^{0.5} + K_3 \cdot f_{\text{H}_2\text{O}})} \quad (3.23)$$

$$r_2 = \frac{k_2 \cdot K_2 \cdot f_{\text{CO}_2} \cdot f_{\text{H}_2} \cdot EQ_2}{(1 + K_1 \cdot f_{\text{CO}} + K_2 \cdot f_{\text{CO}_2}) \cdot (f_{\text{H}_2}^{0.5} + K_3 \cdot f_{\text{H}_2\text{O}})} \quad (3.24)$$

$$r_3 = \frac{k_3 \cdot K_2 \cdot f_{\text{CO}_2} \cdot f_{\text{H}_2}^{1.5} \cdot EQ_3}{(1 + K_1 \cdot f_{\text{CO}} + K_2 \cdot f_{\text{CO}_2}) \cdot (f_{\text{H}_2}^{0.5} + K_3 \cdot f_{\text{H}_2\text{O}})} \quad (3.25)$$

The kinetic parameters fitted by Henkel [85] are listed in Table 3.3. The component fugacities are calculated using the SRK equation [72]. The equilibrium constants $K_{\text{eq},2}$ and $K_{\text{eq},3}$ were calculated by Graaf and Winkelman [82].

Table 3.3. Kinetic parameters for the micro fixed bed and Berty reactor fitted by Henkel [85] and summarized by Nestler et al. [85,87].

Parameter	Micro fixed bed reactor	Berty	Unit
k_1	$2.021 \cdot 10^6 \cdot \exp \frac{-112,322}{R \cdot T}$	$12.975 \cdot \exp \frac{-60,609}{R \cdot T}$	$\text{mol} \cdot \text{kg}^{-1} \cdot \text{s}^{-1} \cdot \text{Pa}^{-0.5}$
k_2	$3.172 \cdot 10^{-4} \cdot \exp \frac{-45,893}{R \cdot T}$	$4.629 \cdot 10^{-4} \cdot \exp \frac{-47,472}{R \cdot T}$	$\text{mol} \cdot \text{kg}^{-1} \cdot \text{s}^{-1} \cdot \text{Pa}^{-1}$
K_1	$1.040 \cdot 10^{-8} \cdot \exp \frac{-61,856}{R \cdot T}$	$5.797 \cdot 10^{-14} \cdot \exp \frac{-112,322}{R \cdot T}$	Pa^{-1}
K_2	$1.000 \cdot 10^{-4}$	$1.935 \cdot 10^{-4}$	Pa^{-1}
K_3	$2.420 \cdot 10^{-14} \cdot \exp \frac{81,976}{R \cdot T}$	$2.743 \cdot 10^{-17} \cdot \exp \frac{108,082}{R \cdot T}$	$\text{Pa}^{-0.5}$

3.1.2 Industrial applications

In addition to being used as an energy source, hydrogen carrier and possibly for CO₂ fixation, methanol is mainly used as a platform chemical. In 2022, 172 Mt of methanol undergo conversion into downstream end products through a variety of chemical processes (see Figure 3.10) [8,88].

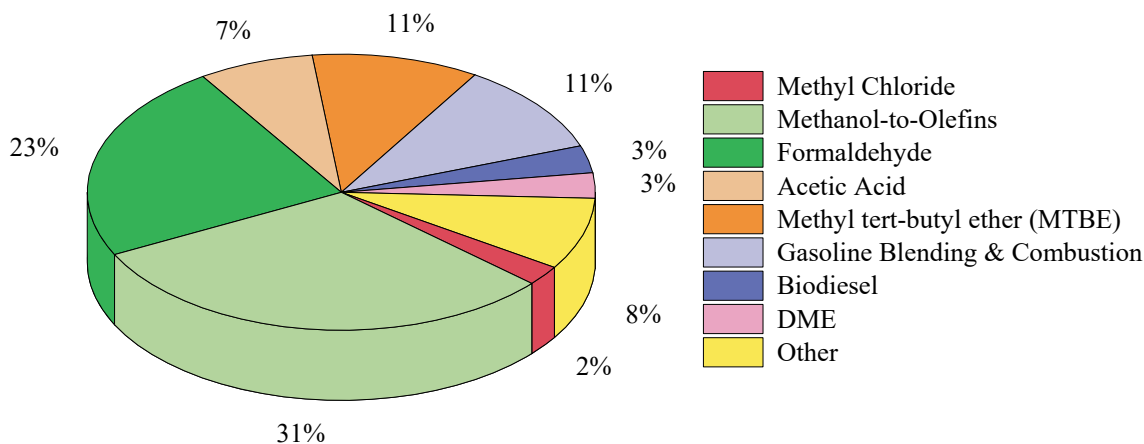


Figure 3.10. The areas of application and downstream products resulting from the industrial processing of methanol, along with the products percentage distribution in 2022, data out of [88].

31 % of methanol was utilized in Methanol-to-Olefins (MTO) processes [88]. With specially adapted zeolites, such as SAPO-34, a silicoaluminophosphate zeolite with a unique geometry and pore size (3.5 Å), limits the diffusion of branched and heavy hydrocarbons with high selectivity to light olefins (C₂–C₄). A milder acidity reduces the hydrogen transfer reactions, that lowers paraffinic product yields. Ethylene and propylene are extracted from this fraction and employed in the production of plastics. With an acidic zeolite such as H-ZSM-5, methanol is first condensed into dimethyl ether and water. Subsequently, catalytic conversion takes place into a mixture of olefins, aliphatics and aromatics, up to C₁₀ at 350–400 °C under atmospheric pressure in the methanol-to-gasoline (MTG) process. [89] 11 % of the global methanol capacity was used for gasoline blending & combustion in 2022 [88]. Formaldehyde, comprising 23 % of the global methanol capacity ranks as the second most common methanol product. Commercially, formaldehyde is produced from air and methanol using a molybdenum oxide catalyst, which is inside the tubes of a “tube and shell reactor” or using a silver oxide catalyst in a fixed bed reactor. Formaldehyde is the primary component in the production of resins, phenols, urea, and melamine and is used in glue production, the manufacturing of plastics, vaccines and carpets. [88,90] Around 11 % of the global methanol demand is used in the synthesis of methyl tert-butyl ether (MTBE) [88]. In this process, methanol reacts with isobutene by an acidic sulphonic ion-exchange catalyst (e.g. Amberlyst-15) to

MTBE [91]. MTBE is used as an additive to gasoline to provide oxygen for the combustion and decrease carbon monoxide emissions [92]. Other resulting products of methanol are acetic acid (7 %), biodiesel (3 %), dimethyl ether (DME, 3 %) or methyl chloride (2 %) (see Figure 3.10) [88].

Annually, less than 0.2 Mt of renewable methanol are produced in a price range of USD 320–770 per tonne. Under current trends, annual production could increase to 500 Mt of methanol by 2050 in a range of USD 100–250 per tonne, resulting in the release of 1.5 Gt CO₂ per year if exclusively derived from fossil fuels [93]. To augment the production of renewable methanol and to reduce production costs, it is a viable option to overhaul the existing catalysts structure and develop better performing catalysts.

3.2 Catalysts for methanol synthesis

From the initiation of industrial methanol synthesis in the 1920s, methanol was produced from synthesis gas under conditions of 300–450 °C and 250–350 bar using a catalyst system comprising of ZnO/Cr₂O₃. During that period a more active copper-based catalyst was available already, but the ZnO/Cr₂O₃ catalyst exhibited higher stability against chlorine and sulfur compounds present in syngas at that time. With a higher purity of syngas achieved in the 1950s, the ZnO/Cr₂O₃ catalyst was replaced in the 1960s by a more active and selective copper-based catalyst in a low-pressure process [94,95]. Similar to numerous industrial catalytic processes, the practical implementation of methanol synthesis came before a full understanding of its underlying chemistry. Consequently, the process was operated for decades relying on empirical observations [96]. There is an increasing focus on the utilization of Cu/ZnO-based catalysts for CO₂ hydrogenation (see Chapter 3.2.1). Recent studies showed that In-based catalysts are promising due to their high activity and stability for CO₂ hydrogenation and are discussed in detail in Chapter 3.2.2.

3.2.1 Commercial Cu-based catalyst

Industrially, the Cu/ZnO/Al₂O₃ catalyst is used for the WGS reaction to produce high-purity H₂ and CO₂ from CO and H₂O (reverse Eq. (3.8)), for methanol steam reforming (reverse Eq.(3.7)) and for methanol synthesis via CO hydrogenation (Eq. (3.6)) [97]. The usual molar ratio of the commercial Cu/ZnO/Al₂O₃ (CZA) catalysts is Cu/Zn/Al = 60/30/10. On an industrial scale, the catalyst is produced through co-precipitation. During this preparation, metal nitrates are dissolved and precipitated with sodium carbonate. After drying and calcination in air at 300–500 °C the CuO/ZnO/Al₂O₃ is obtained. The final CZA catalyst is received in-situ due to subsequent reduction

under a diluted hydrogen flow at 250 °C. Figure 3.11 illustrates a typical CZA catalyst using transmission electron microscopy (TEM) [98,99].

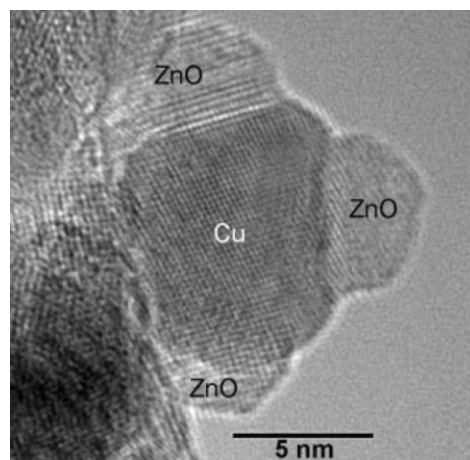


Figure 3.11. High-resolution TEM image illustrates the typical microstructure of CZA catalysts, adapted from Kasatkin et al. [98].

For the WGS reaction of Cu/ZnO-based catalysts, it is discussed whether the ZnO stabilized copper phase, the well dispersed metallic copper [100,101] or the Cu-ZnO interface, which is dissociating H_2O [102], acts as the active site. The addition of aluminum to the Cu/Zn precursor enhances the catalytic activity due to the formation of hydrotalcite [100]. Three distinct mechanisms have been suggested: the surface redox mechanism via formyl path, the carboxyl intermediate path and the formate intermediate path [103].

The transformation of methanol into hydrogen-rich gaseous mixtures can be achieved either through methanol decomposition (reverse Eq.(3.6)) or methanol steam reforming (reverse Eq.(3.7)) using the CZA catalyst. Alternatively, methanol reacts to methyl formate. This step has been demonstrated to be the RDS for methanol steam reforming [104].

Figure 3.12 illustrates the pathways of methanol formation. For CO hydrogenation, methanol is produced using the CZA catalyst in the process of formyl species creation (formyl pathway). Through stepwise hydrogenation of formaldehyde with dissociated hydrogen, a progressive reduction occurs, achieving formaldehyde initially, followed by a methoxy intermediate, and finally methanol. However, another proposed mechanism is the formation of the carboxyl intermediate from CO (Figure 3.12, labeled B) or from CO_2 (Figure 3.12, labeled A). The hydrogenation of CO_2 over the CZA catalyst leads to the formation of CO due to the rWGS reaction (see Eq.(3.8)). This can generate a Cu-O-Cu species on the catalyst surface through the carboxyl (H-O-C-O)

intermediate pathway in which the O–CO bond is activated. After hydrogenation to a carbene diol, split-off the hydroxy (–OH) and renewed hydrogenation, methanol is formed. [105]

In the proposed formate pathway for methanol synthesis by CO₂ hydrogenation, CO₂ is initially hydrogenated to the HCOO intermediate (monodentate or bidentate ligand) on the Cu surface. The formate intermediate is being gradually hydrogenated to formalin and then to H–formalin. After the decomposition of hydroxy (–OH), formaldehyde is formed and hydrogenated to methanol. [105]

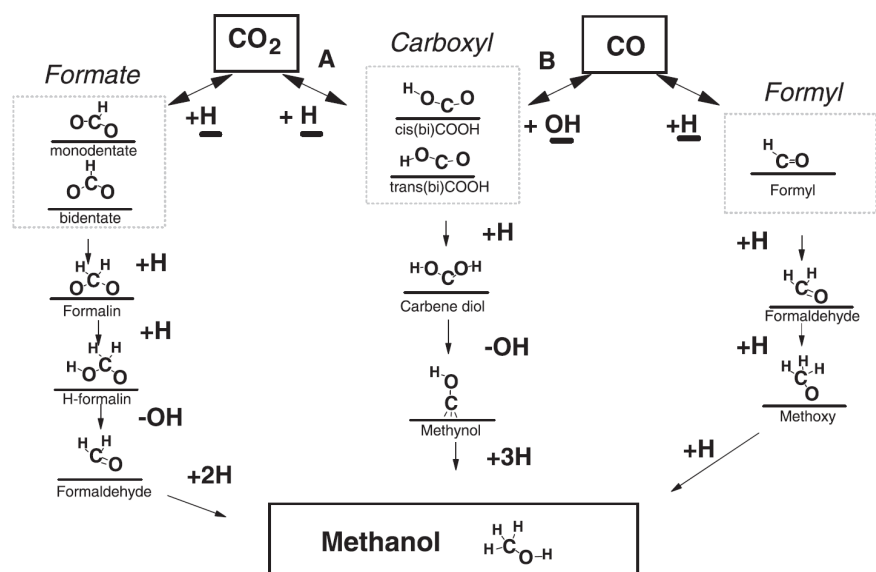


Figure 3.12. Pathways of methanol synthesis for CO and CO₂ hydrogenation over Cu-based catalysts. Direct CO₂ conversion due to formate pathway is shown in the left column. Direct CO conversion due to formyl pathway is shown in the right column. The middle column shows the carboxyl pathway, adapted from [105].

The CZA catalysts consistently exhibits deactivation behavior in industrial applications. For methanol synthesis from syngas or CO₂ sources from industry processes (refer to Table 3.2) the trace impurities e.g. sulphur-based components such as H₂S or SO₂ in the feed gas can poison the catalyst [106]. Reducing the sulfur concentration of the feed gas to 0.5 ppm or below is essential to avoid catalyst deactivation [107,108]. Further CZA catalyst poisons are NH₃, metals (carbon source from steel-work off-gases) such as Na, Ca and Fe and halogen compounds [109,110]. Higher reaction temperatures (above 300 °C) cause Cu particle sintering [14,111] and carbon deposition [112] which, in addition to the thermodynamic properties of methanol synthesis, limits the reaction temperature for CZA catalysts. During methanol synthesis via CO₂ hydrogenation, in-situ water formation is an additional reason for the deactivation of CZA. Water blocks the hydrogen adsorption sites leading to changes of Cu morphology and the oxidation of the active Cu-phase [68]. Caused by the water, an increased sintering tendency and crystallization of the Cu and ZnO components

might occur [113,114]. Liang et al. [115] showed that the methanol space-time-yield was decreased by 34.5 % during 720 h time-on-stream (TOS) at 200 °C, 30 bar and $H_2/CO_2 = 3/1$. Consequently, after a TOS of 720 h, the ZnO species agglomerated, and the metallic Cu was oxidized [115].

In-based materials have emerged as promising alternative catalysts for CO_2 hydrogenation to methanol showcasing less deactivation behavior and higher selectivity [16].

3.2.2 In-based catalysts as promising alternative

Research of the last decade focused on In-based catalysts for methanol synthesis via CO_2 hydrogenation. At low reaction temperatures (200–300 °C) the competing rWGS reaction is not catalyzed and completely avoided by In_2O_3 resulting in a methanol selectivity of 100 % [16]. The density function theory (DFT) studies of Ye et al. [116] revealed high activity of defective $In_2O_3(110)$ surface for adsorption and activation of CO_2 . The perfect $In_2O_3(110)$ surface consists of In–O–In chains. Each chain consists of two O–In squares linked by O_3 – In_3 – O_4 exhibiting symmetry with respect to In_3 (Figure 3.13 a)).

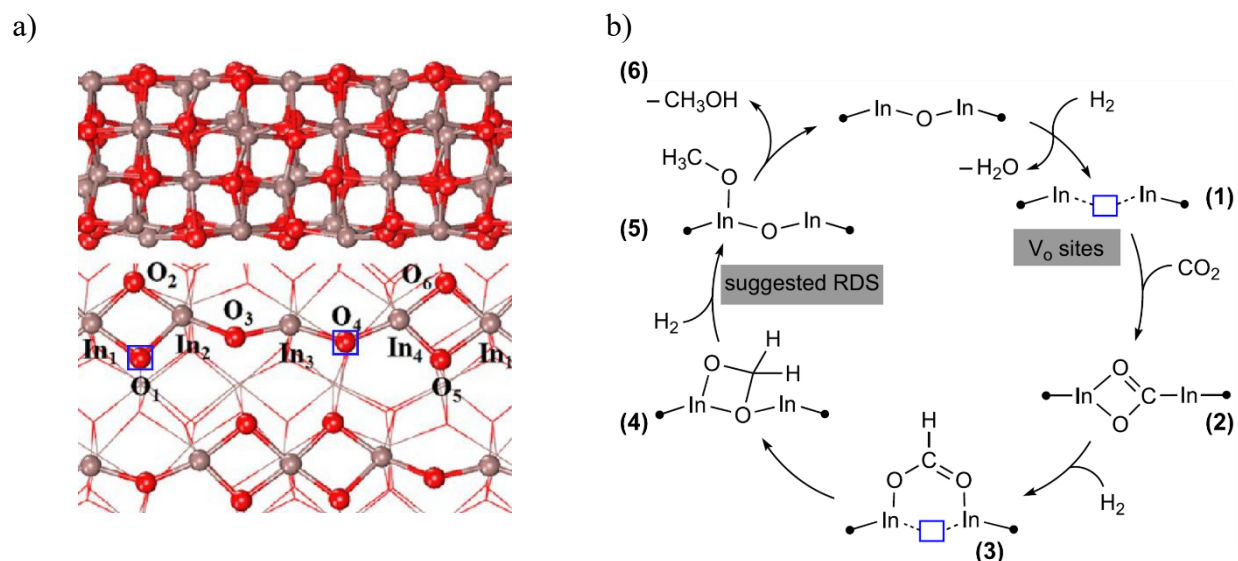


Figure 3.13. a) $In_2O_3(110)$ surface from the side (upper) and top (below) view with framed lattice oxygens O_1 or O_4 , adapted from [116], b) The proposed catalytic mechanism of CO_2 hydrogenation to methanol on V_o sites over $In_2O_3(110)$, adapted from [117].

Under methanol reaction conditions, DFT calculations attribute the active sites of In_2O_3 catalysts to the created oxygen vacancies V_o . The oxygen vacancy formation is more readily achieved by H_2 or CO reduction than by thermal desorption. The V_{O1} defective site is identified as the most thermodynamically favorable, whereas the V_{O4} defective site is characterized as the least stable and more preferred for CO_2 activation [116].

The DFT studies expect hydrogenation to be the primary reaction at the V_{O4} defective site where methanol is formed via the formate pathway. According to this, the generation of surface oxygen vacancy occurs through reduction with H_2 . Figure 3.13 b) illustrates the proposed catalytic mechanism of CO_2 hydrogenation to methanol on V_O sites over $In_2O_3(110)$. The dissociative adsorption of H_2 forms one hydroxyl group with a lattice oxygen and a H–In bond. A subsequent condensation desorbs water from the surface under the formation of an oxygen vacancy **(1)**. CO_2 adsorbs at the In_2O_{3-x} surface sites **(2)** and forms mono–HCOO with atomic H on In. Mono–HCOO is very instable and quickly converts to a more stable bidentate configuration (bi–HCOO) under oxygen vacancy formation **(3)**. The C=O of bi–HCOO breaks, binds with a H-atom and the O fills the oxygen vacancy to form H_2COO **(4)**. Then the direct hydrogenation to CH_3O is favored over the protonation to H_2COH for methanol formation **(5)**. The hydrogenation to CH_3O is the expected RDS, due to highest activation barrier. After the protonation of CH_3O methanol is formed **(6)**. [116,117]

Studies of Sun et al. [118] showed that In_2O_3 produced $3.69 \text{ mol}_{MeOH} \text{ h}^{-1} \text{ kg}_{cat}^{-1}$ methanol at $330 \text{ }^\circ\text{C}$ and 40 bar with a selectivity of 40 % using a fixed bed reactor. The introduction of transition metals on In_2O_3 such as Pt, Pd or Ni could enhance the hydrogen adsorption and dissociation compared to pure In_2O_3 [119–122]. The resulting hydrogen spillover contributes to higher hydrogen availability on the catalyst surface and further improves the catalytic activity [123].

Another strategy to improve the catalytic activity is the combination with metal oxides as a carrier. Martin et al. [16] showed an increase in the space-time-yield (STY) using ZrO_2 compared to other metal oxide carriers (TiO_2 , ZnO , SiO_2 , Al_2O_3 , SnO_2 , MgO). With an optimum In loading of 9 % on ZrO_2 the study demonstrated no deactivation over 1000 h TOS. DFT results by Dou et al. [124] proved that ZrO_2 and TiO_2 enhance the activity and stability of In_2O_3 . On monoclinic ZrO_2 an epitaxial alignment of In_2O_3 ensures a high dispersion of the active In_2O_3 . Also an unfavorable lattice matching of monoclinic ZrO_2 results in tensile strain, promoting the formation of more and potential diverse oxygen vacancies on In_2O_3 [125]. The study of Schühle et al. [106] investigated the performance of In_2O_3/ZrO_2 under a $H_2/CO_2 = 3:1$ flow added with typical impurities of CO_2 sources from industry such as H_2S , SO_2 , NH_3 , NO_2 or hydrocarbons. The In_2O_3/ZrO_2 catalyst was deactivated by the formation of indium sulphate and indium sulfide. NH_3 , NO_2 or hydrocarbon impurities showed no deactivation effects on the methanol production [106]. Latest research introduced Pd or Pt to In_2O_3/ZrO_2 to boost the catalytic activity for CO_2 hydrogenation to methanol [126,127].

3.3 Reactor concepts

The reactor is the key equipment within a chemical plant. Today's industrial methanol plants are categorized in Mega, Giga or Jumbo plants producing 2,000 t d⁻¹ to 10,000 t d⁻¹ of methanol. The maximum capacity of the methanol reactor is energetically constrained by both, the pressure drop and by the manufacturing and transportation limitations of the pressure vessel. The reaction heat of syngas-based methanol production is much higher than for pure CO₂ hydrogenation (Chapter 3.1.1). The primary challenge in reactor design is to economically manage the removal of the reaction heat, providing temperature control, preventing by-product formation, and attaining high conversion rates through low outlet temperatures. Additionally, ensuring good energy efficiency due to internal heat recovery is important as well [9]. The existing reactor technologies can be broadly categorized into two main categories: two-phase and three-phase reactors [66].

3.3.1 Two-phase reactors

The industrial synthesis of methanol is usually done with a two-phase reactor wherein the reactant mixture is present in the gas/vapor phase and overflows a solid catalyst for reaction. There are two types of reactor, classified into adiabatic or isothermal reactors according to the strategy of heat removal within the catalyst bed [128]. Also, two-phase reactors in a laboratory scale are used for methanol synthesis for catalyst testing [129].

Adiabatic reactors

The adiabatic reactor, also called quench converter, consists of one or more (up to five) adiabatic catalyst beds positioned in series inside a single pressurized shell. After each bed, cooling gas is introduced (quenching) using distributors, called lozenges. These are located horizontally across the converter with a central pipe for feeding the cold quenching gas (see Figure 3.14 a)). Quenching relieves the reaction temperature by adding fresh and recycled syngas, shifting the equilibrium to higher methanol yields (see Figure 3.14 b)). The most applied low-pressure quench converter is from Imperial Chemical Industries, ICI (now Johnson Matthey) [128,130]. The ICI converter operates between 50–100 bar at 270 °C using the CZA catalyst in each single bed [9,131]. The methanol production capacity for the ICI is up to 3,000 t d⁻¹. One of the drawbacks is an irregular flux distribution through various catalyst pellet sizes and voids between the pellets. This leads to a temperature influx inside the bed with cold spots having a low reaction rate and hot spots where

byproducts are formed, or the reaction is thermally deactivated by sintering of the catalyst particles. Due to less effective heat recovery and lower conversion rates, a higher recycle stream is necessary [66].

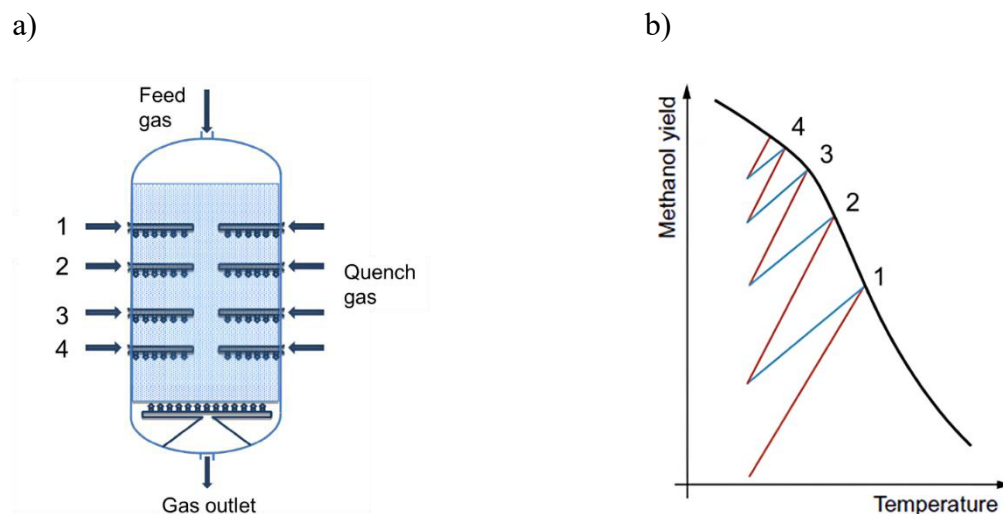


Figure 3.14. a) Simplified adiabatic reactor with gas quenching (ICI) due to four lozenges and b) the corresponding temperature profile: the red lines represent the increase of temperature along the catalyst beds, the blue lines shows the quenching zones due to fresh and recycled feed gas and the black line represents the equilibrium yield of methanol as a function of temperature, adapted from [66,132].

The Advanced Reactor Concept ARC from Casale in collaboration with ICI differs from the ICI by the deployment of distribution plates in different sections. The revamping increases the methanol production up to 20 %. The ARC operates at 80–90 bar and 240–290 °C [133].

The solution from Toyo Engineering Corporation comprises of a reactor with a multi-stage radial flow and intermediate cooling, called MRF-Z[®] (see Figure 3.15 a)). The catalyst is loaded in concentric beds where the blade boiler tubes remove the reaction heat. Across the catalyst bed the radial flow configuration enables a reduction of pressure drops. The catalyst volume is about 30 % lower compared to the ICI with the same product capacity and operating close to its maximum viable reaction temperature. Efficient heat recovery is used for steam production, which can be utilized in synthesizing the syngas feedstock. The MRF-Z[®] reactor produces up to 5,000–6,000 t d⁻¹ methanol at 100 bar and 240–260 °C [131,133].

Another adiabatic reactor was designed by Kellogg, Brown and Root (see Figure 3.15 b)), which incorporates multiple adiabatic fixed bed reactors in series. The reactor is shaped spherically, and the catalyst is positioned between the inner spherical shell and the external wall of the reactor. The reactant flows from the outer to the inner sphere radially passing through the catalyst. This results

in lower pressure drops compared to tubular reactors. The generated reaction heat is dissipated by intercoolers. Thinner reactor walls are required for constructing this reactor setup, reducing costs for manufacturing, transport, and installation. Kellogg, Brown and Root ensure higher methanol yields compared to ICI, thereby less recycling of the reaction stream is necessary. The methanol production capacity is up to 10,000 t d⁻¹ [131,133].

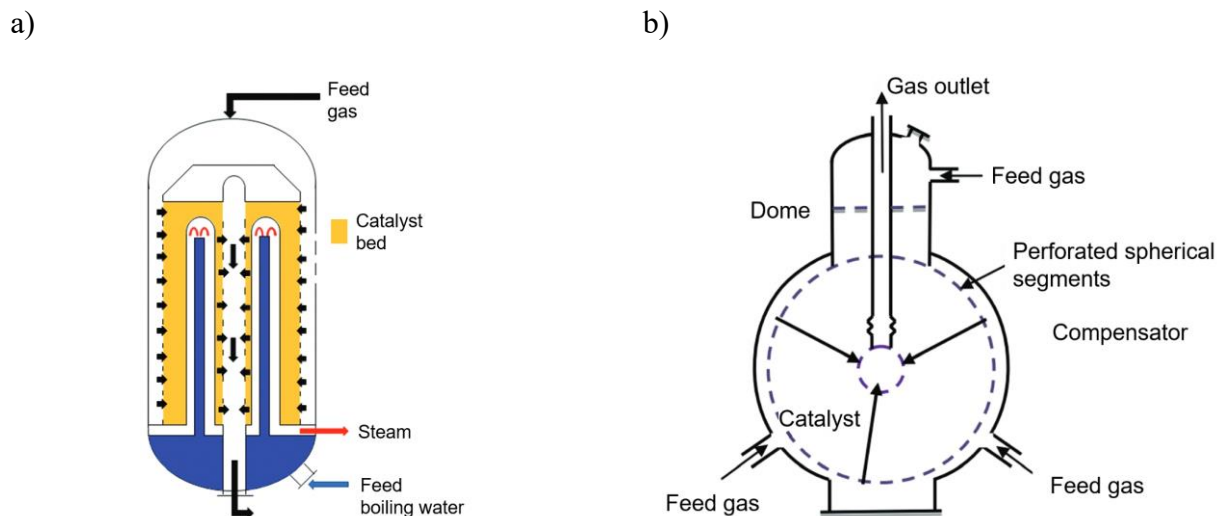


Figure 3.15. Schematic reactor setups: a) Toyo MRF-Z[®] reactor b) Spherical Kellogg, Brown and Root reactor, adapted from [133].

Haldor Topsøe (now Topsoe) modified the quench reactor and designed a collect-mix-distribute reactor (CMD). Vertical support beams separate the catalyst beds. The feed of fresh syngas is at the bottom of the reactor, flowing radially across the catalyst to the top of the bed. Cold quench gas is introduced and mixed in the reaction stream before being forced to flow radially downwards through a second catalyst bed. This configuration produces up to 10,000 t of methanol per day at 50–100 bar and 290 °C [131,133].

Isothermal reactors

The main objective of an isothermal reactor is to regulate the reaction temperature by employing cooling instruments and maintaining a quasi-isothermal process. In comparison to adiabatic reactors, the isothermal reactors cool itself, the catalyst, and the reaction gas. They are categorized in gas-assisted cooling and heat removal by steam generation reactors. The main benefits of these reactor types include an extended catalyst lifetime, higher conversions, and methanol selectivity. The energy is recovered by steam generation, which is utilized for syngas feed generation [133].

The Lurgi reactor (now part of Air Liquide) was introduced at the beginning of the 1970s. The fixed bed reactor is basically a shell and tube design. The feed gas flows across the catalyst-filled tubes in axial direction. Boiling water is pumped through the outer shell of the reactor, cooling the catalyst indirectly. The excess reaction heat is used either to produce a medium pressure steam for the compression section or for the methanol distillation process. The Lurgi reactor operates in the range of 50–100 bar and 230–265 °C. The methanol capacity for a single-train is restricted to 1,500–2,200 t d⁻¹. [131,133] In combination with a second Lurgi methanol converter (two-stage), it is called Lurgi MegaMethanol™ (see Figure 3.16). The first stage operated at high space velocities and high temperature to partially convert syngas to methanol and to generate high pressure steam. The outlet gas of the first converter is fed to the shell side of the second reactor. In countercurrent to the feed, the cold fresh syngas circulates inside the tubes. This configuration enables efficient heat recovery to reduce production costs and to maintain the reaction driving force. This set-up enables a methanol productivity up to 10,000 t d⁻¹. [131,133,134]

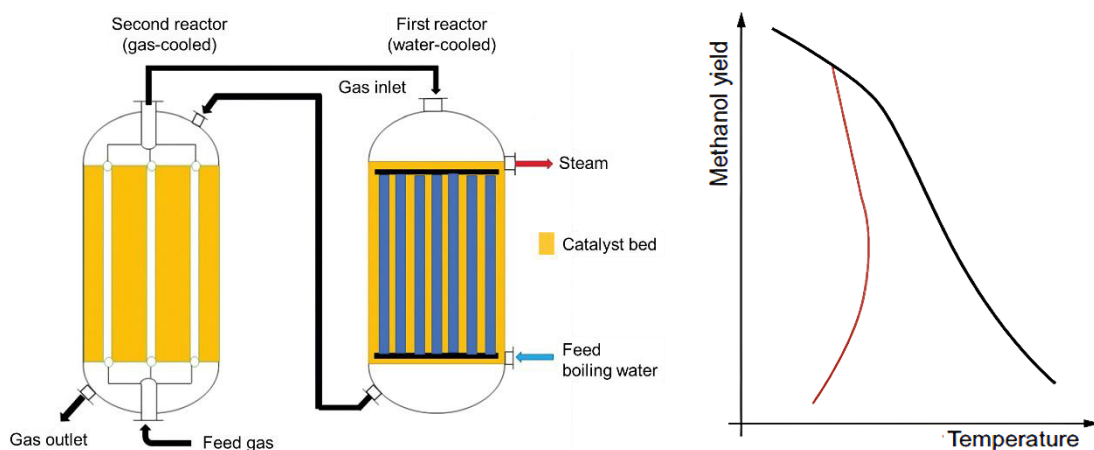


Figure 3.16. Schematic configuration of the Lurgi MegaMethanol™ process and the corresponding temperature profile in the first (water-cooled) reactor, adapted from [132,133].

Another reactor, the Linde isothermal reactor, is equipped with helical tubes inside the catalyst bed. The tube bundle is fed by cooling or boiling water, providing an indirect heat exchange. The boiling water flows axially from the bottom upwards due to natural draft and is converted to steam at the reactors top. The catalyst can work at an optimum temperature, thus resulting in higher productivity, less by-products, longer catalyst lifetime as well as efficient heat recovery and lower operating costs. This configuration can be used for both exothermic and endothermic catalytic reactions and for gas to gas, gas to liquid or liquid to liquid systems (see Figure 3.17 a)). Linde reactors produce up to 4,000 t d⁻¹ of methanol. [131,135]

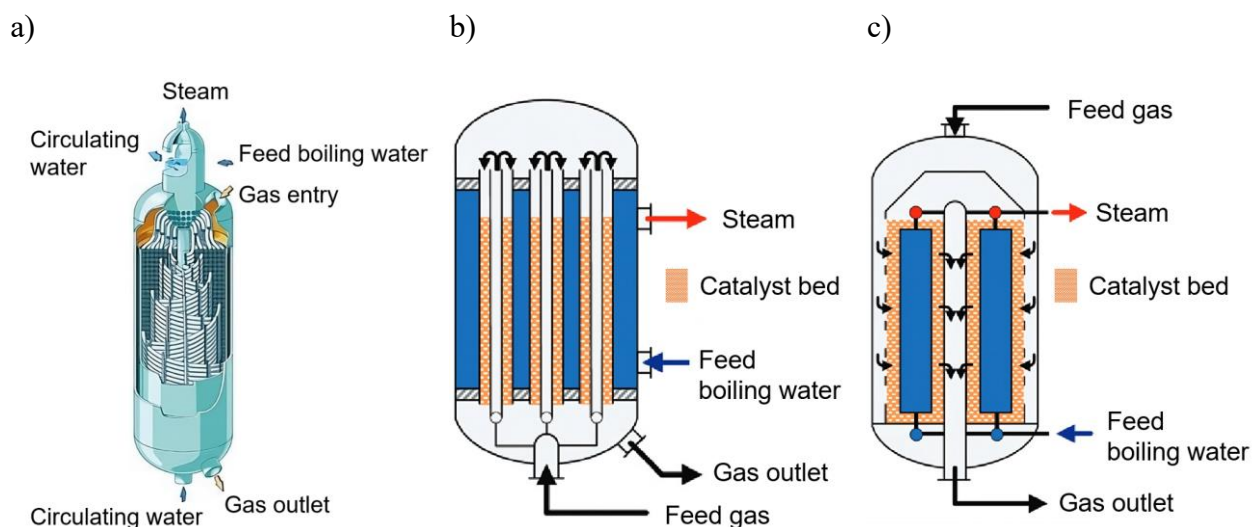


Figure 3.17. Simplified reactor configuration of a) Linde isothermal reactor, b) MGC/MHI Superconverter and c) Isothermal Methanol Converter (IMC), adapted from [9,135].

Mitsubishi Gas Chemical and Mitsubishi Heavy Industry developed an isothermal converter called MGC/MHI Superconverter. The reactor includes double-walled tubes with the catalyst bed inserted between the outer and inner tubes in a boiling water vessel. The boiling water around the tubes helps to remove the reaction heat. The fresh syngas is fed upwards from the bottom of the converter and preheated inside the tubes. The gas is then channeled downwards, overflowing the catalyst bed in the outer tube (see Figure 3.17 b)). To reach the desired temperature profile along the catalyst bed a slightly higher temperature at the reactor inlet of 250–260 °C for preheating the fresh syngas is required. The temperature gradually decreases as it exits the reactor (240–250 °C). At 55–100 bar the MGC/MHI Superconverter produces up to 2,500 t d⁻¹ of methanol [133,136].

The Isothermal Methanol Converter (IMC) by Casale SA contains hollow plates for heat exchange embedded in the catalyst bed. Inside the plates, fluids such as feed gas, boiling water or other coolants are used for temperature control. The plates can be independently supplied with coolant by adjusting the coolant flow at different heights (see Figure 3.17 c)). The quasi-isothermal temperature profile of the IMC can be controlled and adjusted to operate at the maximum reaction rate [9]. The good temperature control prolongs the catalyst lifetime and reaction heat can be recovered to produce stream. The design of the reactor can include a mixed axial-radial flow configuration [66]. The axial flow configuration can reach methanol capacities up to 2,000 t d⁻¹. However, for larger capacities ranging from 7,000–10,000 t d⁻¹ methanol in a single converter, an axial-radial flow configuration is employed resulting in a pressure drop of less than one bar [9]. The reactor operates at 225–280 °C and 65–80 bar [132]. There is virtually no limit to the size of the IMC and its

construction is straightforward, because a conventional vessel that includes the catalyst bed and plates is manufactured [66].

Laboratory scale two-phase reactors

Two-phase reactors for laboratory scale are categorized in packed bed reactors and gradient-less recycle reactors. The simplest reactor for investigating heterogeneous catalytic reactions is a fixed bed reactor. Usually, the catalyst bed is positioned in the center of the reactor tube and held in place by quartz wool on both sides to prevent fluidization in up-flow direction. In many cases, inert beads are mixed with the catalyst to dilute and to disperse the gas flow. A thermocouple is installed in the middle of the catalyst bed and the fixed bed tubular reactor is placed in a furnace as shown in Figure 3.18 a). The fixed bed reactor can be operated in differential or in integral form (Figure 3.18 b)). [129]

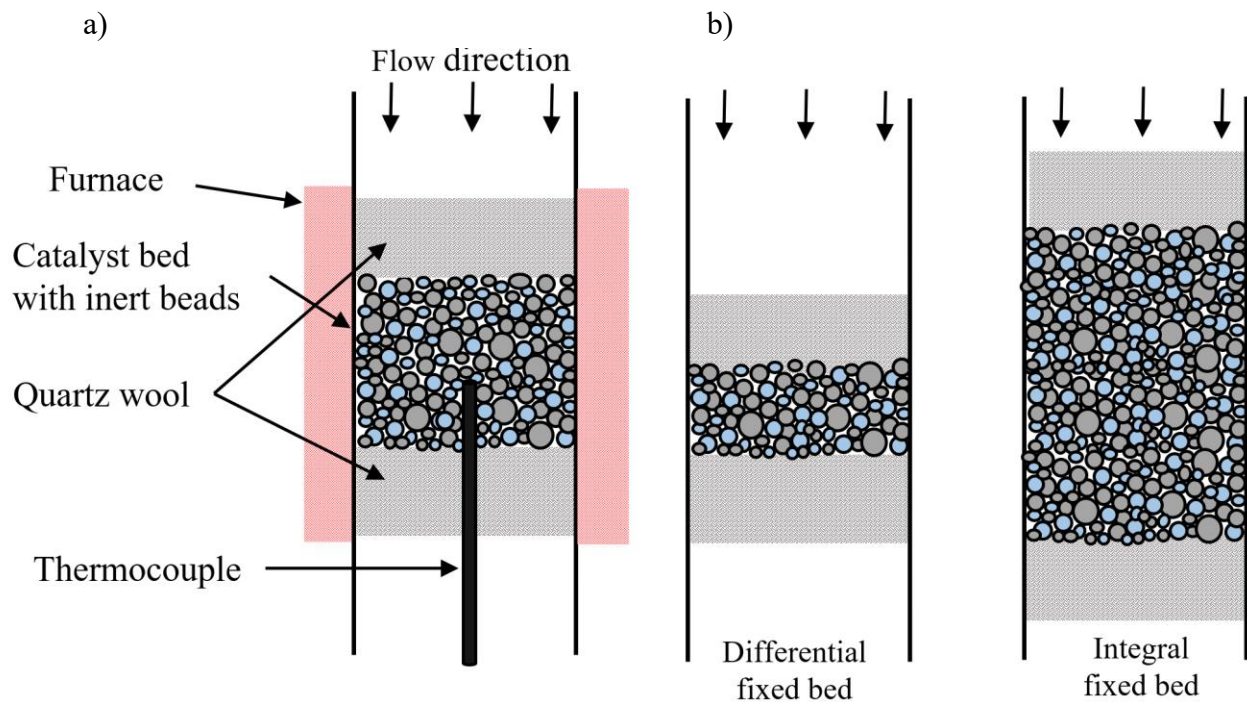


Figure 3.18. a) Schematic configuration of a laboratory scale fixed bed reactor. b) Operation opportunities of laboratory scale fixed bed reactor, adapted according [129].

Less catalyst in the differential reactor leads to a higher reactant concentration and a lower conversion than in the integral reactor [129]. The smaller fixed bed largely eliminates internal temperature gradients [137]. Geikwad et al. [138] split the catalyst bed of CZA in three parts, which

were separated by empty spaces for gas analysis. This study demonstrated that methanol is synthesized at low temperatures by direct high-pressure CO₂ hydrogenation. Above 260 °C, methanol formation is favored by hydrogenation of CO via the rWGS reaction (Eq.(3.8)) [138].

The Compact Profile Reactor (CPR) by REACNOSTICS GmbH enables both integral and differential operation modes for laboratory scale fixed bed reactors. In the setup, the catalyst is filled in a reactor tube and fixated by quartz wool plugs. A capillary with four orifices in the wall passes through the catalyst bed for gas sampling. At these four bores a thermocouple is positioned inside the capillary for temperature measurement. The reactor is movable along the capillary in axial direction through a guide rail (see Figure 3.19 a)). This enables spatially resolved reactant compositions and temperature profiles. The CPR is already established for various heterogeneously catalyzed reactions. [139–143]

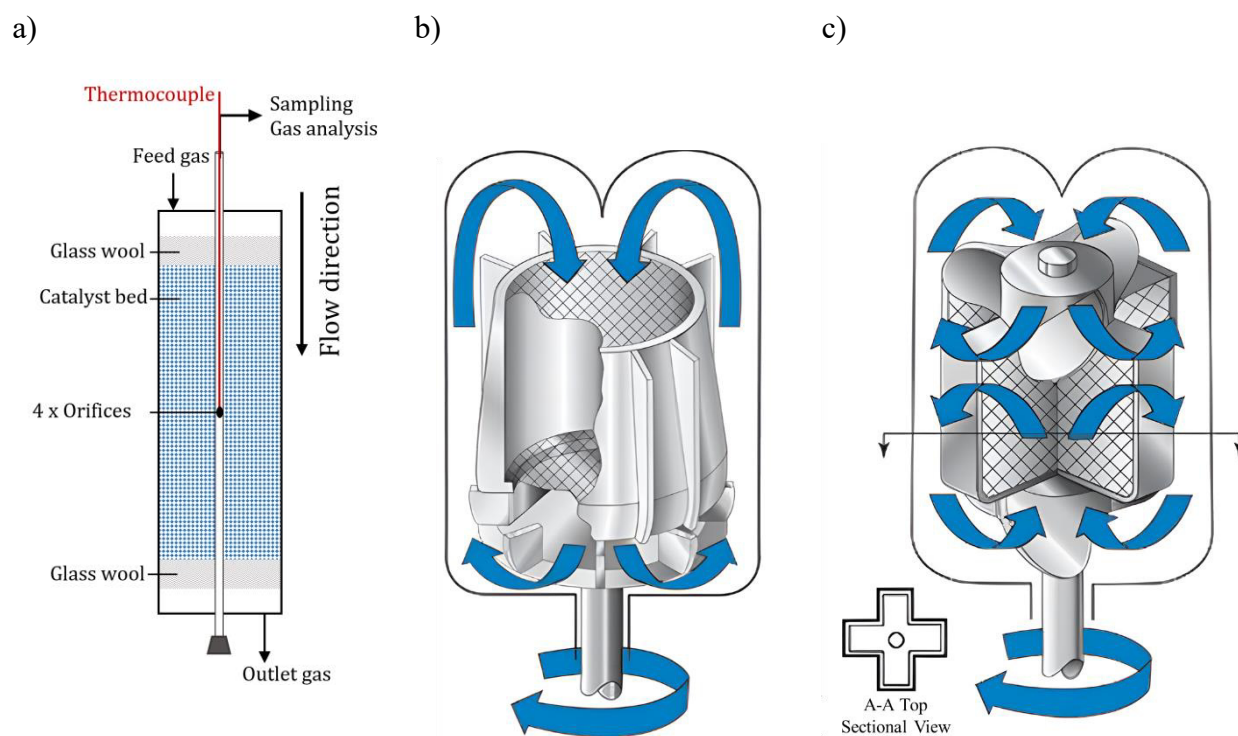


Figure 3.19. Laboratory reactor concepts. a) Schematic design of the CPR by REACNOSTICS GmbH, adapted from [143]. b) Simplified diagram of a Bertly stationary catalyst basket reactor and c) a Carberry spinning catalyst basket reactor, adapted from [129].

Typical gradient-less recycle reactors for gas-solid reaction system are the Bertly and Carberry reactor for determining reaction kinetics [129]. The Bertly reactor features a fixed circular catalyst bed and a bottom-mounted blower, see Figure 3.19 b) [129]. The reaction gas mixture is passing through the catalyst bed and forced up the draft tube by the impeller. The gas is directed upwards

along the wall of the vessel and flows down through the catalyst bed again[129]. The turbine speed controls the recycle rate. [144] The stirrer of the Carberry reactor is a basket filled with the catalyst. Each arm of the catalytic basket is acting as a differential reactor. Below and above the basket are impellers to direct the fluid flow, see Figure 3.19 c). The Carberry reactor achieves complete mixing in the gas phase and assumes gradient less operation. A drawback is that the temperature of the catalyst bed cannot be measured. [144]

3.3.2 Three-phase reactors

Three phase (gas-solid-liquid) reactor systems have been suggested for syngas from coal with low H/C ratio to avoid coking. Reactors such as slurry or trickle bed reactors ensure more efficient heat removal and less mass transfer limitations. In a trickle bed reactor, the packed bed of catalyst particles is stationary while a gas-liquid stream flows through the bed. Air Products investigated the LPMEOH™ technology, where the fine catalyst particles are suspended in mineral oil. Inside the reactor a heat exchanger transfers heat from the mineral oil to the outside (see Figure 3.20 a). This enables better temperature control, faster mass transfer and lower costs compared to fixed bed reactors. The LPMEOH™ pilot plant showed the ability to produce 300,000 L d⁻¹ of methanol in 1977 [66]. The reaction conditions were 215 °C and 30–50 bar [9].

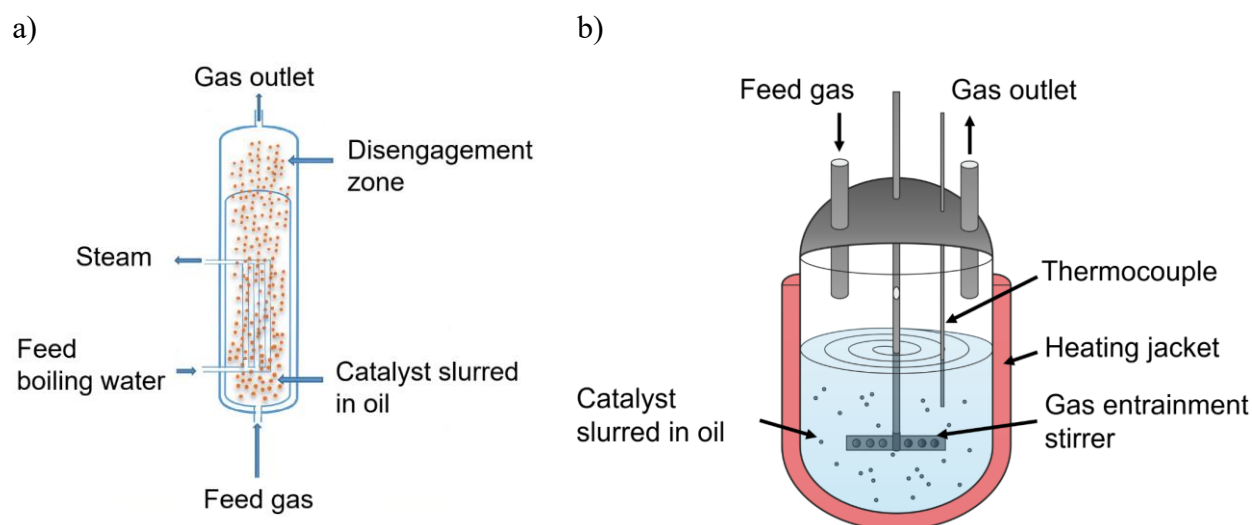


Figure 3.20. Three-phase reactor systems: a) LPMEOH™ slurry reactor technology by Air Products, adapted from [66], b) slurry reactor, adapted from [145].

While slurry phase CO hydrogenation to methanol has received less attention, there has been an increasing focus in research for the CO₂ hydrogenation to methanol [145,146]. The catalyst powder is suspended in a carrier liquid (see Figure 3.20 b)). The slurry system provides many advantages,

such as high mass and heat transfer rates, high productivity per unit reactor volume, simple construction, and low operating costs. Catalysts, whether as powder or nanoparticle, can be used without compensating a pressure drop. Properties of the slurry reaction system, such as gas permeability, heat capacity, viscosity, or solubility can be influenced by the choice of carrier oil. Higher gas permeability and solubility of methanol (and the by-product water via CO₂ hydrogenation) allow for higher conversions. Fluctuating feedstock composition for coal-derived syngas or for CO₂ hydrogenation using renewable hydrogen and waste CO₂ from industry can be buffered by the oil. The heat capacity of the oil can buffer the heat of reaction and stabilize the temperature as well, thus preventing the catalyst deactivation through thermal sintering caused by reaction temperature peaks. The limitations of the slurry reactors include backmixing, high attrition of catalysts and further downstream operations such as catalyst or product separation.[145,147]

3.3.3 Design of Experiments

For the methanol synthesis, which is based on equilibrium reactions (refer to Eqs. (3.6)-(3.8)), many reaction parameters, such as temperature, reaction pressure, partial pressures, reaction time, GHSV, catalyst to substrate ratio and more have an influence on the methanol productivity, selectivity, reaction kinetics and catalyst activity.

Before the introduction of statistical Design of Experiments (DoE), in the field of chemical engineering in the middle of the 20th century [148], the experimentation designs were simple and follow the trial-and-error or the one-factor-at-a-time (OFAT) experimentation method. OFAT varied one factor while the others are kept constant (see Figure 3.21). The interactions between factors k and the effect of one factor on the level of the other cannot be detected by OFAT. [149]

A systematic method to for identifying the cause-and-effect relationships for a given system, such as the methanol synthesis is the application of statistical DoE. This method is used to plan, conduct, analyze and interpret experiments resulting in objective and valid conclusions from data. The DoE technique was introduced by Sir R. A. Fisher in 1935, Edinburgh and London [148]. His primary objective was to determine the optimal combination of rainfall, sunlight, fertilizer, soil conditions and moisture for the best harvest, by using the DoE technique. [148,149]

A tool to vary many factors (e.g. reaction parameters) simultaneously is the factorial design. The simplest way involves two factors, each with two levels (2^2). With an increasing number of factors, the factorial design becomes an advantage (2^k). The factorial approach covers all combinations of

factors and their interactions. A full-factorial design can be time-consuming and involves many experiments (runs) (see Figure 3.21). However, within a given experimental budget or time the fractional factorial design is a more suitable approach. [150] This design approach reduces the number of experimental runs (2^{k-p}) by using a projection to interpolate the data in between. The subset of significant factors is equivalent to a factorial design. The trade-off through reducing the number of runs is the aliasing (confounding) of effects. The degree of the aliasing effect is measured by the resolution. As the alias effects increase, as the resolution decrease. [150,151] The OFAT, the factorial and the fractional factorial design are compared in Figure 3.21. It becomes apparent, that by switching from the OFAT to a factorial design, a lot more experimental space is covered, but still many experiments are required. With reductions, a fractional factorial design can cover up most of the experimental space with significantly less work.

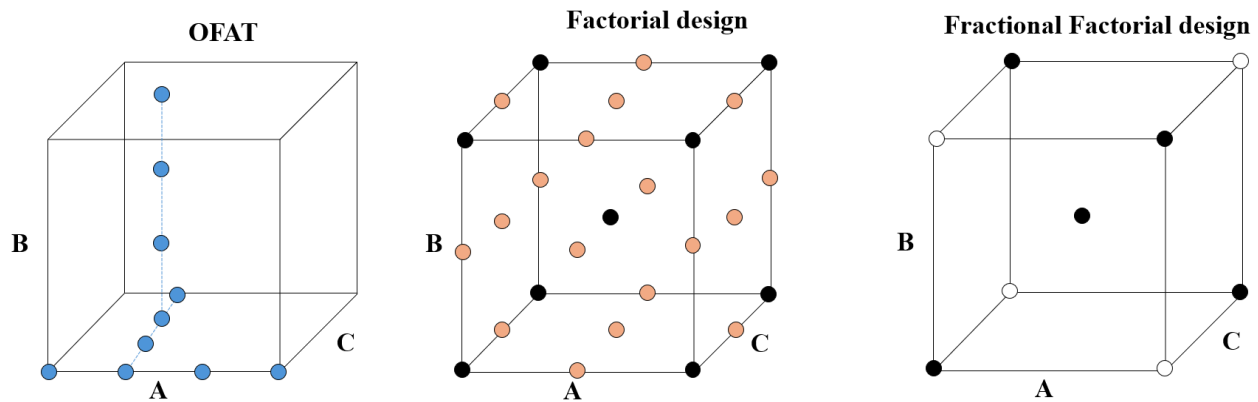


Figure 3.21. Comparison of OFAT with a 3^3 full-factorial design and a 2^3 fractional factorial design, adapted from [150,152].

Response Surface Methods (RSM) are advanced techniques for the optimization of fractional two-level and full-factorial designs. The center point, being the midpoint of all factors, is added to the design. For example, the center Point is 2 for factor A with 1 (low level) and 3 (high level). The added center point can reveal a curvature for a two-level fractional design, where a linear correlation is not enough to describe the system. That does not illustrate the complete system that would be received in a three-level factorial design, since it is more complex.

A central composition design (CCD), useful in RSM, is created by adding axis and center points to a two-level factorial design. Another experimental design for fitting response surfaces is the Box-Behnken design, in which not the edges (low and high level) of the cube design are experiments, but the midpoints of the cube edges and the center point are. [153] To assess the significance of experimental results, a statistical tool called analysis of variance (ANOVA) is applied. The total

variation of a data set is divided into individual components. The ANOVA computes the sum of squares, degrees of freedom, mean square, the F-test and p-test value. [151]

With the data from the ANOVA a Pareto chart can be rendered, showing the relative size of effects (see Figure 3.22). If one of the experimental runs is faulty, the fractional factorial design may become unbalanced, resulting in different standard errors for the effects. Not every effect has a significant impact on the system. The t-values of the effects stabilize the Pareto chart against faulty experimental runs. The dimensionless statistical scale is calculated by dividing the numerical effect by its related standard error (Eq. (3.26)) [150].

$$t\text{-value}_i = \frac{|Effect_i|}{\sqrt{MS_{Residual} \left(\frac{1}{N_+} + \frac{1}{N_-} \right)}} \quad (3.26)$$

In Eq. (3.26), N represents the number of responses from each level tested and MS is the mean square of the residuals. A special t-value, named after Carlo Emilio Bonferroni [154], the Bonferroni Limit considers the number of estimated effects by dividing it into the number of experiments performed, which reduced the probability of false-positive effects, refer to Eq. (3.27) [150,155]. The probability threshold, α , is used to control the false-positive effects and is also defined as type I error rate [150,156].

$$\text{Bonferroni Limit} = \frac{\alpha}{\text{number of experiments}} \quad (3.27)$$

The Bonferroni Limit is a correction for multiple comparison testing [157].

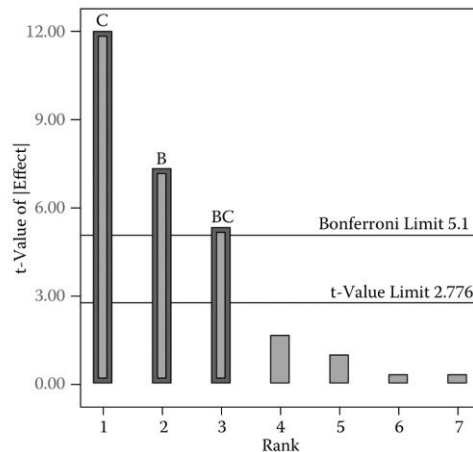


Figure 3.22. Example for a Pareto chart with t-Value and Bonferroni Limit [150].

4 Objective of the present work

Since the industrial revolution the CO₂ emissions rise and acts as a greenhouse gas causing global warming. To replace the fossil energy carriers and raw materials, alternative sources for hydrogen and carbon are required. H₂ generated by electrolysis of water using renewable energy and CO₂ emissions from industry exhaust gas to synthesize methanol represents an opportunity for the net zero emissions strategy and chemical energy storage. The commercially available Cu-based catalyst for methanol synthesis quickly deactivates by higher temperature (> 300 °C) and the water produced during the reaction of hydrogen and CO₂ [14,114].

The dissertation “CO₂ Hydrogenation to Methanol in Different Reactor Concepts using Metal-doped Indium-based Catalysts” focuses on various aspects of the application of promising In₂O₃-based catalysts for renewable methanol synthesis from CO₂ and H₂ in different reactor concepts.

The initial objective is to investigate the phase transition reversibility of a pure In₂O₃/In(OH)₃ system under typical methanol synthesis conditions using a fixed bed reactor. The hydration reaction of In₂O₃ to In(OH)₃ could diminish the catalytic activity such as for the Cu-based catalyst. For this, the catalytic data under various reaction conditions for both, In₂O₃ and In(OH)₃ are investigated. With the catalytic data, along with a computational study, predictions about operation strategies will be made to prevent catalyst degradation.

ZrO₂ supported In₂O₃ enhances the catalytic activity compared to pure In₂O₃ [16]. In the next stage, the impact of different ZrO₂-supports as well as preparation methods for indium impregnation are to be tested in the same fixed bed reactor setup. The aim here is to further increase the catalytic performance by adding In₂O₃/ZrO₂ with either H₂-spillover favoring metals like Cu and Ni or with CO₂-adsorbing metals like Ce and Mg. After the catalyst screening the stability is demonstrated.

A further objective is to study the reaction profiles of In₂O₃/ZrO₂ and metal promoted In₂O₃/ZrO₂ compared to the state-of-the-art Cu-based catalyst using an innovative CPR. This aims to investigate the simultaneous acquisition of temperature, reactants, products, and spatially resolved reaction profiles during methanol synthesis via CO₂ hydrogenation. The influence of reaction conditions such as pressure, temperature and volumetric flow rate is to be determined with the most active In₂O₃/ZrO₂-catalyst. Characteristic reaction parameters such as the Carberry Number to approximate extraparticle mass transfer [158] or the activation energies are to be calculated using the acquired results.

Objective of the present work

The final objective of this work is to optimize the application of In-based catalysts and the reaction parameters using a three-phase slurry batch reactor setup. For this purpose, the most active catalyst is determined by catalyst screening and selected for a parameter optimization study. A DoE and a statistical evaluation are applied aiming to maximize the yield of methanol. The best performing catalyst is compared to the copper-based catalyst for CO₂ hydrogenation as well as for CO hydrogenation. The stability of the slurry system is investigated for multiple consecutive batch experiments.

5 Materials and methods for experimental evaluation

5.1 Used chemicals and materials

The following chapter lists all chemicals and materials used for the catalysts synthesis and experimental procedure. Table 5.1 shows the used gases for the synthesis of methanol and online gas chromatography. The used supports, precursors and chemicals for catalyst preparation as well as the commercial reference materials are listed in Table 5.2. The carrier liquids used for the studies in the batch reactor for slurry experiments are shown in Table 5.3.

Table 5.1. List of used gases.

Gas	Composition	Manufacturer	Purity
Hydrogen	H ₂	Linde	99.999 %
Carbon dioxide in hydrogen mixture	CO ₂ /H ₂ (25 %/75 %)	Westfalen	99.995 % (CO ₂) 99.999 % (H ₂)
Carbon dioxide	CO ₂	Linde	99.995 %
Helium	He	Linde	99.996 %
Argon	Ar	Heide Gas	99.996 %
Nitrogen	N ₂	Air Liquide	99.999

Table 5.2. Used supports, precursors and chemicals for catalyst preparation and used reference catalysts.

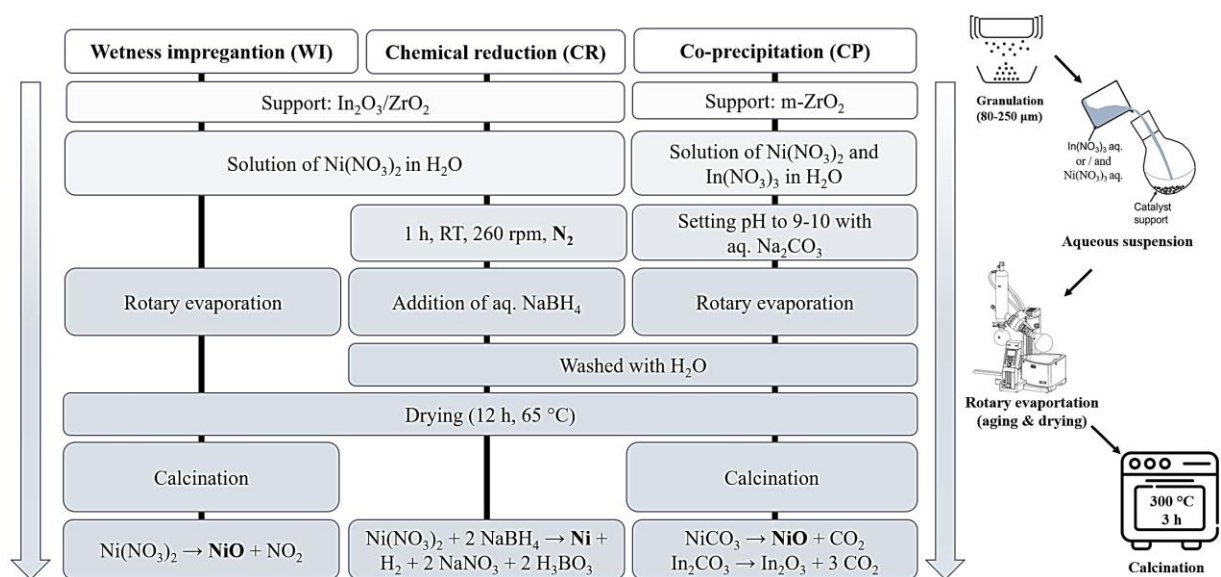
Chemicals	Composition	Manufacturer	LOT	Purity
Zirconium dioxide, pellets	ZrO ₂	Alfa Aesar	S08B075	n.a.
Zirconium dioxide, pellets	ZrO ₂	Saint-Gobain NorPro	SZ31164	n.a.
Indium(III) nitrate hydrate Puratronic®	In(NO ₃) ₃ • xH ₂ O	Alfa Aesar	62000138	≥ 99.999 %
Indium(III) oxide	In ₂ O ₃	Alfa Aesar	S23G014	99.9 %
Indium(III) hydroxide	In(OH) ₃	ThermoScientific	Y22F010	99.8 %
Cerium(III) nitrate hexahydrate	Ce(NO ₃) ₃ • 6 H ₂ O	ThermoScientific	A0442129	99.5
Magnesium nitrate hexahydrate	Mg(NO ₃) ₂ • 6 H ₂ O	ThermoScientific	61301307	≥ 99.8 %
Nickel(II) nitrate hexahydrate	Ni(NO ₃) ₂ • 6 H ₂ O	SuboLab	1068	n.a.
Copper(II) nitrate trihydrate	Cu(NO ₃) ₂ • 3 H ₂ O	Acros Organics	A0431206	99 %
Copper-based MeOH catalyst, pellets	CuO/ZnO/Al ₂ O ₃	Alfa Aesar	I06Z036	n.a.
Sodium carbonate	Na ₂ CO ₃	Grüssig	9190	99.5 %
Sodium borohydride	NaBH ₄	Acros Organics	A0397479	98 %
Ethanol	C ₂ H ₆ O	VWR Chemicals BHD	19E024003	99.98 %

Table 5.3. Carrier liquids used for the slurry reactor.

Carrier liquids	Composition	Manufacturer	LOT	Purity
Light mineral oil	Mixture of aliphatic hydrocarbons	Sigma Aldrich	330779	99.99 %
Downtherm A	Eutectic mixture of bisphenol (C ₁₀ H ₁₀) and diphenyl oxide (C ₁₀ H ₁₀ O)	Sigma Aldrich	44570	n.a.
H18-DBT	Perhydrodibenzyltoluol	Hydrogenious	C0021	Degree of hydrogenation 93-95 %
Helisol 10 A	Mixture of linear chain Polydimethylsiloxane	Wacker	OM48048	n.a.

5.2 Catalyst preparation

The In₂O₃/ZrO₂ catalysts were prepared using already published methods: wetness impregnation (WI) [16,106], chemical reduction (CR) [159] or co-precipitation method (CP) [119]. In general, the ZrO₂ pellets were granulated to 80-250 μm (two-phase studies) or 32-80 μm (three-phase studies). An aqueous solution of In(NO₃)₂·xH₂O or In(NO₃)₂·xH₂O, along with Ce(NO₃)₃·6 H₂O, Mg(NO₃)₂·6 H₂O, Cu(NO₃)₂·3 H₂O or Ni(NO₃)₂·6 H₂O was added. If necessary, the pH value was adjusted using aqueous Na₂CO₃ (CP), or NaBH₄ is added for reduction (CR). The aqueous suspension was then aged and dried using a rotary evaporator. Afterward, the powder was heated to 300 °C (heating rate 5 °C/K) and calcined for 3 h. The schematic procedure for different synthesis methods of metal promoted In₂O₃-based catalysts is shown in Figure 5.1, using the example of Nickel. Comprehensive details of the catalyst preparation are described in the publications and corresponding Supporting Information.


 Figure 5.1. Preparation of Ni-In₂O₃/ZrO₂ by different methods.

5.3 Different reactor setups

The following chapter describes the setup of the plants used, including a picture and a corresponding flow diagram.

5.3.1 Fixed bed reactor setup (two-phase)

The experimental studies for the publications [18,19] were carried out in an integral operated fixed bed reactor setup (see Figure 5.2). The fixed bed reactor as well as the periphery was made of stainless steel (1.4571). The reactor tube with an inner diameter of 20 mm was connected to the periphery with a silver plated VCR face seal fitting.

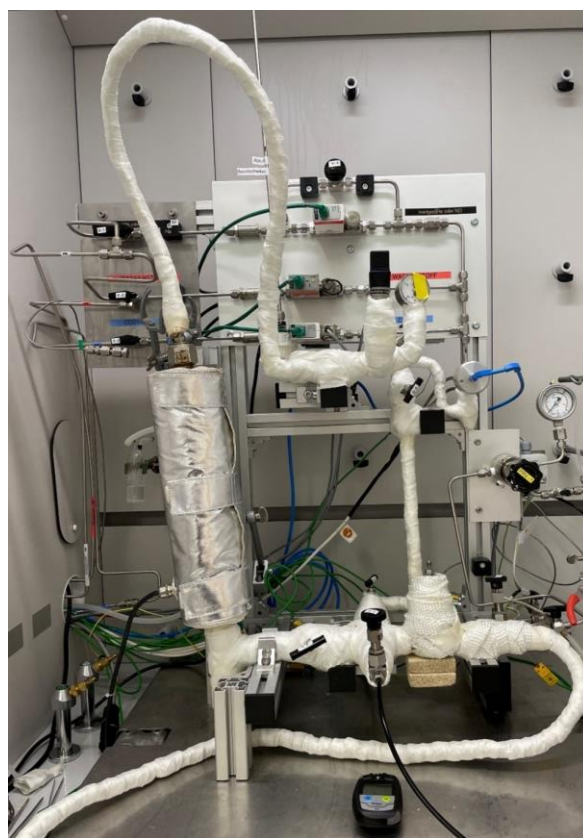
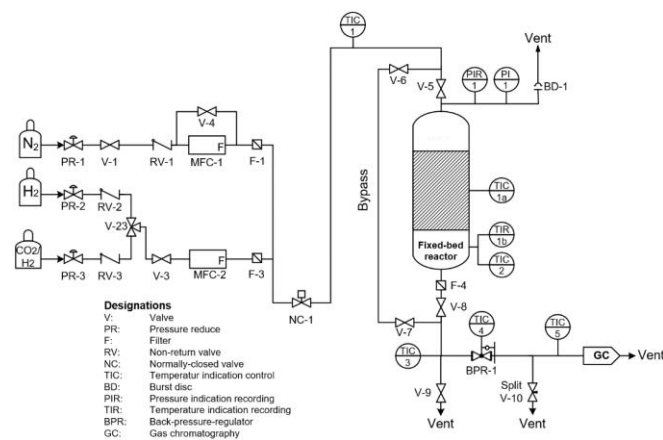


Figure 5.2. Piping and instrumentation diagram (left) and a picture (right) of the fixed bed reactor setup.

Two mass-flow controllers (MFC-1, MFC-2, Bronkhorst Prestige FG-201 CV) were used to introduce the gases N_2 , H_2 and the reactant gas mixture CO_2/H_2 (1/3). The calibration curves applied to set define volume flows can be found in the Appendix of this thesis (Chapter 9.1.2). The gases flowed through a heated pipe (TIC-1) downwards into the reactor tube. Non-return valves (RV-1, RV-2, RV-3) are installed to prevent backmixing of the gases. A back-pressure regulator (BPR-1,

Dutch Regulators) is used to adjust the desired reaction pressure. For safety reasons, a normally closed pneumatic valve (NC-1) stops the gas supply during an emergency shutdown. Additionally, a burst disc (BD-1, 100 bar \pm 10 %) protects the setup from too high pressures. The plug valves (V-1, V-2) are required as an additional safety feature for manually opening or closing the gas supply. The manually 3-way switching valve is used for changing gas feed to either H₂ or CO₂/H₂. The plug valves V-4 – V-9 are operated to manually purge the reactor or the bypass. The reactor is heated by a heating mantle and the catalyst bed temperature is controlled in tandem with a thermocouple located at the reactor wall (TIC-2), and inside the catalyst bed (TIC-1). The reactor outlet and the downstream pipes are heated (TIC-3, TIC-4, TIC-5) to avoid condensation of reaction products such as water and methanol. After the BPR-1, V-10 splits the gas output to prevent a buildup of pressure for the following GC analysis.

5.3.2 Compact Profile Reactor setup (two-phase)

The experimental studies for the publication [20], were carried out in a two-phase Compact Profile reactor setup (see Figure 5.3), which is operated both integrally and differentially. The following setup differs from the previous setup (Chapter 5.3.1) due to the reactor.

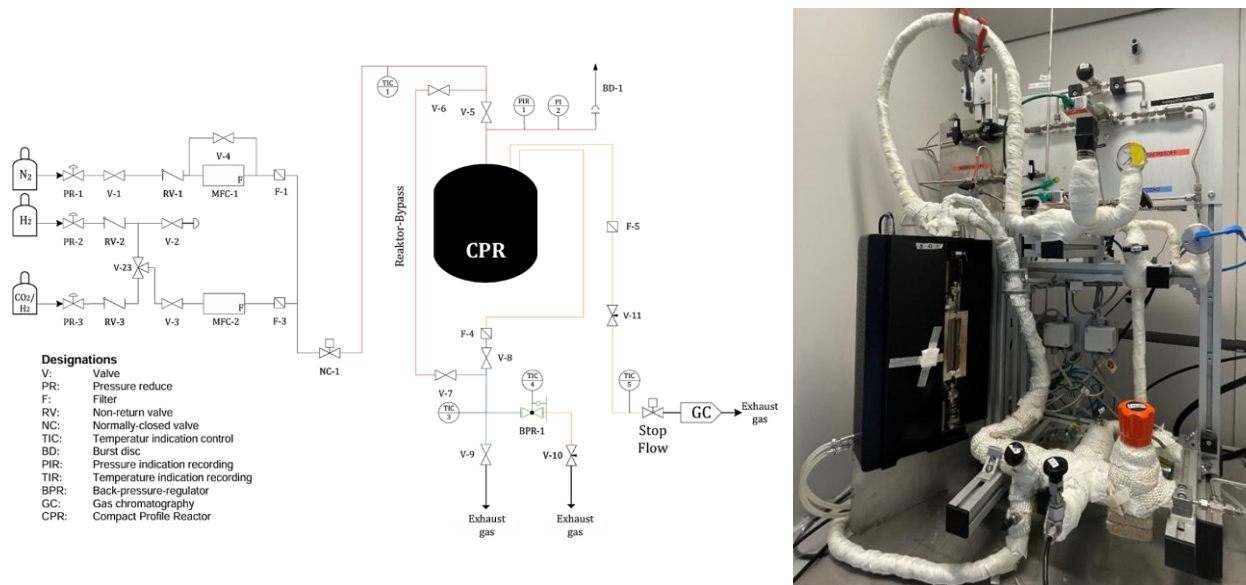


Figure 5.3. Piping and instrumentation diagram (left) and a picture (right) of the CPR.

The CPR (REACNOSTICS GmbH) consists of a stainless-steel tube that is 182 mm long with an inner diameter of 4 mm. The outlet of the tube is connected to the BPR-1 and exhaust gas system. Inside the tube is a stainless-steel capillary with four orifices (diameter: 75 μ m) in the wall. A

thermocouple at the location of the four orifices measures the temperature of the catalyst bed. The outlet of the capillary is connected to a needle valve (V-11), which regulates the pressure and flow to the GC. The reactor tube and all pathways are heated inside of an isolated chamber. The temperatures are controlled with the Software from REACNOSTICS. The outlets of the chamber are heated (TIC-5) to avoid condensation. The reactor tube is moved with a guide rail along the fixed capillary in the axial direction for both integral and differential measurements.

5.3.3 Three-phase Stirred-tank reactor setup in batch mode

The following three-phase (slurry) stirred-tank reactor setup in batch operation mode (see Figure 5.4) was used for the investigation described in the publication [21]. The reactor (R-1, Paar Instruments) and the peripheral gas pipes are made out of stainless steel (1.4571). The reactor R-1 (vessel number QW11817AD 911817 T316 4560 0911 13351) has a volume of 600 mL, an inner diameter of 6.35 cm, and is equipped with a controller (SIC-1, Paar 4843) to adjust the stirrer speed. The connection between the reactor vessel and the reactor head is sealed with a flat gasket made of PTFE.

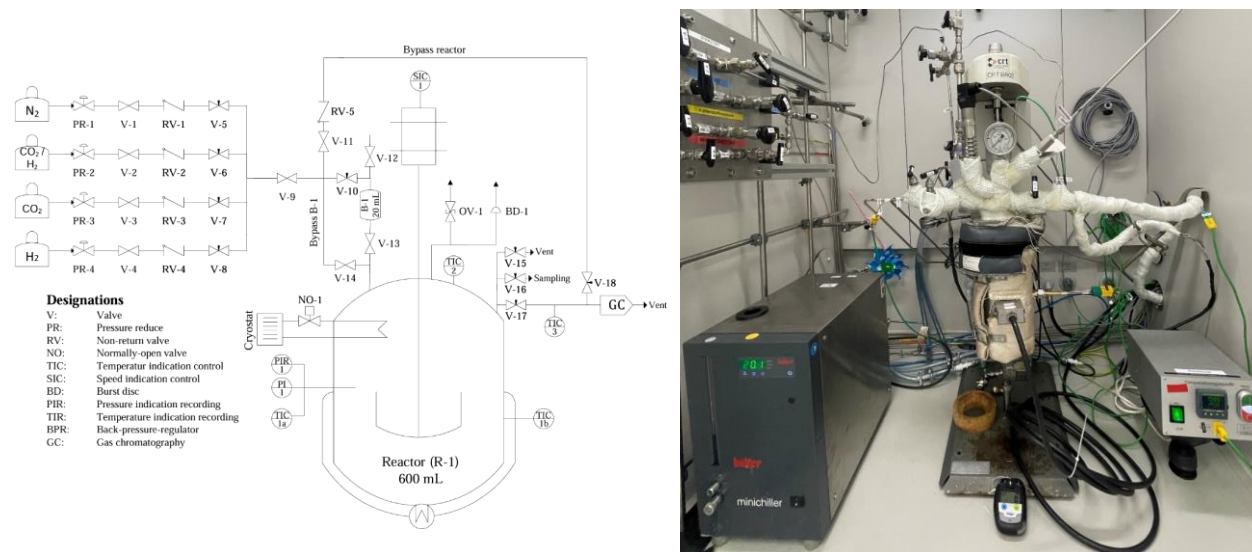


Figure 5.4. Piping and instrumentation diagram (left) and a picture (right) of the slurry batch reactor setup.

Inside the reactor, is a four-bladed gas entrainment stirrer with a diameter of 3 cm, along with a thermocouple (type J) and a cooling loop. The combination of internal (TIC-1a) and external (TIC-1b) thermometers enables cascade control of the heating power of the heating mantle. To

protect the reactor from overheating, a cooling loop is installed in the gas phase of the reactor. This loop is fed by a normally open pneumatic valve (NO-1) connected to a cryostat (Huber Minichiller) set to 20 °C. The reaction pressure is monitored and recorded using a digital pressure indicator (PIR-1) and an analog pressure gauge (PI-1). Protection against pressure peaks is provided by a pressure relief valve (OV-1) with an opening pressure of 85 bar and a bursting disk (BD-1) with a bursting pressure of 103 bar ($\pm 5\%$). With this setup, reactions can be carried out at temperatures up to 350 °C and pressures up to 80 bar.

Reactants and inert gases (N_2 , CO_2 , CO , H_2) are added manually via plug valves (V-1-V-4) and metering valves (V-5-V-8). No-return valves (RV-1-RV-5) regulate the gas flow direction and prevented gas backmixing. Reaction gas can be removed from the reactor through valves V-15 to V-17, either for sampling into a separate vessel, for gas phase analysis using the GC, or for exhaust release. The reactor head, including its periphery, was heated to 120 °C using a separate heating controller (TIC-2). The gas line from the reactor to the GC was also heated to 200 °C with a separate heating controller (TIC-3) to prevent the condensation of reaction products.

5.4 Experimental Details

The following chapters describe the experimental procedure for the methanol synthesis using different reactors, namely the fixed bed, compact profile and slurry batch reactor. Each setup was checked for pressure-tightness with a pressure drop of less than 20 mbar h^{-1} at 80 bar.

5.4.1 Two-phase Methanol Synthesis Using the Fixed Bed Reactor setup

Inside the reactor, a porous, cylindrical frit was placed on the thermocouple and subsequently covered with glass wool to allow for a packing of the catalyst around the thermocouple tip. The reactor tube was positioned tightly around the frit, and the lower VCR screw connection was tightened using a sealing washer. Usually, 5.0 g of indium-based catalyst (particle size: 80 -250 μm) was mixed with inert quartz beads (beads size: 200 -300 μm). The mixture was then filled into the reactor tube from above using a measuring rod, ensuring a catalyst bed height of 5 cm and a central position of the thermocouple in the fixed bed. Subsequently, more glass wool is used to cover the catalyst bed from the top to hold it tight. A VCR sealing was placed at the upper end of the reactor tube, and both screw connections were sealed to ensure a gas-tight system. The setup was inertized three times with approximately 10 bar of nitrogen. The reactor and its periphery were then preheated to 200 °C under a nitrogen flow of 300 mL_N min^{-1} for one hour to remove physisorbed surface

species. In the case of metal-promoted catalysts, as well as the CZA, *in situ* reduction and activation were carried out by 500 mL_N min⁻¹ of 10 % hydrogen in nitrogen for one hour. Afterwards the reaction pressure was adjusted by the BPR-1 and the reaction temperature was set. After reaching the desired temperature, the continuous supply of the feed gas mixture (CO₂/H₂ = 1/3) and the required volumetric flow rate was initiated. The settings of the gas flows, as well as the temperature and pressure signals, were recorded and controlled using the Labview software. It also enabled the automatic execution of various operating states.

The gas composition was automatically analyzed with the online-GC in 30-minute intervals by programming a measurement sequence in the GC software CompassCDS. An operating point was considered to be at steady state if the methanol concentration in the product gas changed by no more than 0.1% in volume over three consecutive measurements.

At the end of the experiment, the reactor was cooled to room temperature (3 K min⁻¹) under a nitrogen flow of 1000 mL_N min⁻¹. After cooling and inertizing the system, the setup was slowly depressurized by opening BPR-1. The reactor was opened, the catalyst was removed, sieved to remove the glass beads and stored under an argon atmosphere until further characterization.

5.4.2 Two-phase Methanol Synthesis Using the CPR setup

First the orifices position of the capillary was determined, marked closely with a pen. Another marking was made 5 cm away from the orifices position for orientation later on, when the capillary is covered by the fixed bed. The distance from the orifices to the upper end of the capillary is 18.1 cm, which is also the mounting depth for the thermocouple in the capillary.

The CPR tube with the capillary inside was filled from position 0.5 to 5.5 cm with pure catalyst material (particle size: 80-250 μm) and fixated by a bed of quartz wool plugs. The tube was then mounted on the guide rail, connected to the inlet and outlet pipes, and the thermocouple was inserted into the capillary up to the orifices position.

After fitting, the setup was pressurized to 5 bar with nitrogen to test the stability of the fixed bed inside the tube. Then the setup was preheated to $T = 180$ °C (periphery upstream), $T = 250$ °C (reactor including the fixed bed) and $T = 200$ °C (periphery downstream) for at least 9 h under a N₂ flow of 200 mL_N min⁻¹. For metal-promoted catalysts, as well as the CZA, *in situ* reduction and activation were carried out using 500 mL_N min⁻¹ of 10 % hydrogen in nitrogen for one hour. Then the reaction pressure was adjusted by the BPR-1, the reaction temperature was set and the reactor

was moved to the 6 cm position. This position is located behind the catalyst bed and represents the integral operation mode. After reaching the desired temperature, the continuous supply of the feed gas mixture ($\text{CO}_2/\text{H}_2 = 1/3$) under the required volumetric flow rate was initiated. The capillary was connected to the online GC. The gas composition was automatically analyzed by the online GC at 30-minute intervals using a programmed measurement sequence in the GC software CompassCDS. An operating point was considered to be at steady state if the methanol concentration in the product gas varied by no more than 0.1% in volume over three consecutive measurements. The catalyst bed was analyzed from end position 6.0 cm to the beginning position 0.0 cm in 0.5 cm increments over three consecutive measurements. The moving velocity between the measuring points was set to $30 \mu\text{m s}^{-1}$. The settings of the gas flows, as well as the temperature and pressure signals of the periphery, were recorded and controlled using the Labview software. The CPR was controlled and recorded by its dedicated control unit and software.

At the end of the experiment, the reactor was cooled to room temperature (3 K min^{-1}) under a nitrogen flow of $500 \text{ mL}_N \text{ min}^{-1}$. After cooling and inertizing, the setup was slowly depressurized by opening BPR-1. The reactor was opened, the catalyst was removed and stored under an argon atmosphere until further characterization.

5.4.3 Three-phase Methanol Synthesis Using the Batch Reactor setup

To carry out the catalytic performance for the three-phase methanol synthesis in a batch reactor, 100 mL of the carrier liquid was added to a glass liner. The desired mass of catalyst (usually 2 g particle size: 32-80 μm) was then added to the carrier liquid. The filled glass liner was inserted into the stainless steel reactor, which was then sealed to the reactor head using a teflon sealing ring. The heating mantle was fitted to the reactor. The inertization of the reactor was performed by stirring with the gas entrainment stirrer at 200 rpm and purging three times with 5 bar of nitrogen. The reactor was then purged three times with 5 bar CO_2 to remove the nitrogen, filled with 8.5 bar CO_2 at room temperature, and heated to the desired reaction temperature. After reaching the reaction temperature, the excess CO_2 was vented until the pressure was reduced to 15.0 bar. The reactor was then filled with H_2 to a total pressure of 75.0 bar, and a GC measurement confirmed the target H_2/CO_2 composition of 4:1. The stirrer speed was increased to 1200 rpm, defining the start of the reaction. After 3 hours, three gas samples were measured consecutively at 10-minute intervals using the online GC to determine the CO, CO_2 , and MeOH content. After successfully determining the gas phase composition, the reaction was stopped by reducing the stirrer speed to 200 rpm and

cooling overnight. After cooling, the gas phase was purged, and the reactor was inertized three times with 5 bar nitrogen before switching off the stirrer. The catalyst was then separated from the carrier liquid using a filter (pore size 4–12 μm), washed three times with 10 mL of isopropanol, followed by three washes with 10 mL of cyclohexane. The catalyst was then dried at room temperature and stored in an argon atmosphere.

5.5 Applied analytics

This chapter provides an overview of the analytical devices and methodology used in this work to characterize the indium-based catalysts and to evaluate the catalytic performance.

5.5.1 Online Gas Chromatography

The gas phase composition for all setups was quantified using an online gas chromatography (*Bruker 450-GC*), which was connected with a heated pipe to the reactor outlet. Inside the GC four gas chromatography columns (Restek Q-Bond, Restek U-Bond, Bruker Swax, Bruker Molsieve 5 Å) are used to separate the different gases and two flame ionization detectors (FID), one thermal conductivity detector (TCD) combined with a methanizer are used to analyze the gas composition. The calibration curves necessary for this are shown in the Appendix 9.1.1. More details are described in the Supporting Information of [21] in the Appendix 9.6.

5.5.2 Fourier-transform infrared spectroscopy

An online Fourier-transform infrared spectroscopy (FTIR) was used to determine the residence time distribution in the two-phase setups at different volume flows (refer to the Appendix Chapter 9.1.3 and 9.1.4), The measurements were performed using a X-STREAMXEGP-IR from Emerson Process Management in a pulse tracer experiment by switching the feed from nitrogen to CO_2 (tracer) for 12 s.

5.5.3 Thermogravimetric Analysis

Thermogravimetric analysis (TGA) was performed to determine the mass loss, relating to water via conversion of $\text{In}(\text{OH})_3$ to In_2O_3 . A *SETSYS Evolution TGA-DTA* from Setaram Instrumentation was used for this analysis. In the publication [18], Chapter 6.1 are further details described.

5.5.4 Powder X-ray Diffraction

The structural characterization of the indium-based catalyst was carried out by powder X-ray diffraction (XRD) using a *Panalytical MPD X'Pert Pro* with a Cu-K α radiation ($\lambda = 0.1541$ nm). The particle sizes of the catalysts were calculated using the Scherrer equation based on the characteristic diffraction reflex [160]. The measurements were conducted by the X-ray service facility at Hamburg University.

5.5.5 Inductively Coupled Plasma Optical Emission Spectroscopy

The elemental compositions of the indium-based catalyst were identified using inductively coupled plasma optical emission spectroscopy (ICP-OES). Usually the sample was digested in 5 mL of concentrated H $_2$ SO $_4$ and 1 mL of fuming HNO $_3$. The analysis was carried out on an *ASCOR-spectrometer* (Fa. Spectro) using an argon plasma and quantified with optical emission spectroscopy by the central element analysis service at the Department of Chemistry, University of Hamburg.

5.5.6 X-ray Photoelectron Spectroscopy

X-ray photoelectron spectroscopy (XPS) was applied to analyze the oxidation states of the surface metals present in indium-based catalysts. XPS measurements were performed using a Thermo Scientific system with AlK α radiation (1484.6 eV) and a spot size of 400 μ m. Data processing was done using the Advantage 4.87 software. Signals were corrected using a "Smart" background. The measurements were conducted by Dr. Leonhard Schill at the Technical University of Denmark.

5.5.7 Nitrogen Physisorption

The determination of the of the catalysts surface area was conducted by the Brunauer-Emmet-Teller (BET) method, and the pore volume of the catalysts was calculated by using the Barrett-Joyner-Halenda (BJH) method via nitrogen physisorption at 77 K. This was performed with an *Autosorb iQ-MP/XR analyzer* (Quantachrome Instruments).

5.5.8 CO $_2$ -Temperature-Programmed Desorption

Temperature-programmed desorption of CO $_2$ (CO $_2$ -TPD) measurements investigated the CO $_2$ binding capacity and strength of the catalyst surface. The characterizations have been carried out with the *ChemBET Pulsar* (Faradaic Quantachrome Instruments) at the University of Hamburg.

5.5.9 H₂-Temperature-Programmed Reduction

Hydrogen temperature-programmed reduction (H₂-TPR) measurements investigated the reducibility of the catalyst surface. The analyses were performed with the *ChemBET Pulsar* (Faradaic Quantachrome Instruments) at the University of Hamburg. A detailed procedure can be found in the Appendix 9.6, or the Supporting Information of [21], respectively.

5.5.10 Scanning Electron Microscopy and Energy-Dispersive X-ray Spectroscopy

Scanning electron microscopy (SEM) was used to receive images of the catalyst surface via a *Zeiss LEO Gemini 1550* equipped with a field emission gun and a beam energy of 20 kV. Elemental maps were obtained by energy-dispersive X-ray spectroscopy (EDX) using an *Ultim Max 100* silicon drift detector (Oxford Instruments). The measurements were carried out at the department of electron microscopy at Hamburg University. A detailed procedure can be found in the Appendix 9.6, or the Supporting Information of [21], respectively.

5.5.11 High-Resolution Transmission Electron Microscopy

Additionally, morphological and compositional analyses were conducted with high-resolution transmission electron microscopy (HRTEM) and scanning transmission electron microscopy (STEM) with double-corrected (*CESCOR* and *CETCOR CEOS*) *JEOL JEM 2299FS* microscope equipped with an in-column image filter Ω -type, a high-angle annular dark-field (HAADF) detector and a *Gatan 4k UltraScan 1000* camera. EDX elemental maps were obtained by using EDX *JEOL JED-2300* analysis station with a 100 mm² silicon drift detector.

5.5.12 Nuclear Magnetic Resonance Spectroscopy

¹H and ¹³C nuclear magnetic resonance spectroscopy (NMR, 400 MHz, resolution) was employed to analyze the carrier liquids used for three-phase methanol synthesis. A *Bruker Avance III HD 400* was applied by the division of NMR spectroscopy at the University of Hamburg. The spectra were evaluated with the software *MestReNova*.

5.6 Calculations

This section outlines the mathematical fundamentals for calculating reaction parameters for methanol synthesis in both the two-phase continuously operated reactor and the three-phase batch operated reactor.

5.6.1 Calculations for the Two-Phase Continuous Methanol Synthesis

The calibrated MFC's adjusted a standard volume flow (\dot{V}_N) and the known feed gas ($y_{i,in}$) composition allowed the calculation of the molar flow (\dot{n}) of component i (Eq. (5.1)) entering the reactor, under consideration of the ideal gas law. The variables, p_N and T_N , are the standard pressure and temperature and R is the molar gas constant.

$$\dot{n}_{i,in} = \frac{p_N \cdot y_{i,in} \cdot \dot{V}_N}{R \cdot T_N} \quad (5.1)$$

The molar fractions y of CO, CO₂ and methanol are obtained from the online GC. Regarding the carbon balance of the reaction system, the total molar flow (Eq. (5.2)) at the reactor outlet is determined using the sum of the molar fractions.

$$\dot{n}_{total,out} = \frac{\dot{n}_{CO_2,in}}{y_{CO_2,out} + y_{CO,out} + y_{MeOH,out}} \quad (5.2)$$

The molar flow of component i at the reactor outlet ($\dot{n}_{i,out}$) was calculated as follows (Eq.(5.3)):

$$\dot{n}_{i,out} = \dot{n}_{total,out} \cdot y_{i,out} \quad (5.3)$$

The yield Y_{MeOH} and selectivity S_{MeOH} of methanol, the CO₂ conversion X_{CO_2} and various productivities P with different benchmarks, which are catalyst mass $m_{cat}(cat)$, BET surface $S_{BET}(surface)$ or active metal content ω (active metal), respectively are shown below. These were calculated according to the following equations, Eqs.(5.4)-(5.9):

$$Y_{MeOH} = \frac{\dot{n}_{MeOH}}{\dot{n}_{CO_2,in}} \cdot 100 \% \quad (5.4)$$

$$S_{MeOH} = \frac{\dot{n}_{MeOH,out} - \dot{n}_{MeOH,in}}{\dot{n}_{CO_2,in} - \dot{n}_{CO_2,out}} \cdot 100 \% \quad (5.5)$$

$$X_{CO_2} = \frac{Y_{MeOH}}{S_{MeOH}} \quad (5.6)$$

$$P_{cat} = \frac{\dot{n}_{MeOH,out} \cdot M_{MeOH}}{m_{cat}} \quad (5.7)$$

$$P_{surface} = \frac{P_{cat} \cdot 1000 \frac{mg}{g}}{S_{BET}} \quad (5.8)$$

$$P_{\text{active metal}} = \frac{P_{\text{cat}}}{(\omega_{\text{Indium}} + \omega_{\text{metal promoter}})} \quad (5.9)$$

The reaction rate r was calculated according to Eq. (5.10).

$$r_i = \frac{\dot{n}_{i,\text{in}} - \dot{n}_{i,\text{out}}}{m_{\text{cat}}} \quad (5.10)$$

For the relation of the standard volume flow (\dot{V}_N) to the catalyst volume (V_{cat}) the gas hourly space velocity ($GHSV$) was used (Eq. (5.11)).

$$GHSV = \frac{\dot{V}_N}{V_{\text{cat}}} \quad (5.11)$$

The Carberry number (Ca), a dimensionless quantity, is used to assess the presence of external mass transfer limitations in heterogeneous catalytic reactions. The mass-transfer limitation criteria $Ca < 0.05$ specifies that the diffusion resistance due to external mass transfer can be neglected. The following equation, Eq. (5.12) defines the Ca number [158].

$$Ca = \frac{r_{\text{obs}}}{ak_f c_b} < \frac{0.05}{|n|} \quad (5.12)$$

The specific external surface a of the spherical catalyst particle is calculated with the particle diameter d_p (Eq.(5.13)).

$$a = \frac{6}{d_p} \quad (5.13)$$

The mass transfer coefficient (k_f) was calculated by the correlation of Dwivedi for packed beds (Eq. (5.14)) [161]. The Sherwood number Sh involves the bed porosity ε_{bed} , the Reynolds (Re) and Schmidt (Sc) number (Eqs. (5.15)-(5.17)):

$$k_f = Sh \frac{D}{d_p} \quad (5.14)$$

$$Sh = \frac{1}{\varepsilon_{\text{bed}}} \cdot 0.453 \cdot Re^{1.453} \cdot Sc^{0.333} \quad (5.15)$$

$$Re = \frac{\rho_{\text{CO}_2,\text{H}_2} u d_p}{\mu_{\text{CO}_2,\text{H}_2}} \quad (5.16)$$

$$Sc = \frac{\mu_{\text{CO}_2,\text{H}_2}}{\rho_{\text{CO}_2,\text{H}_2} D} \quad (5.17)$$

The Re number requires the superficial velocity u and the density of the gas mixture $\rho_{\text{CO}_2,\text{H}_2}$. The density was determined via Aspen Plus V12 using SRK equation of state [72]. Based on the Wilke method [162] the gas viscosity $\mu_{\text{CO}_2,\text{H}_2}$ was estimated (Eq.(5.18)) , which requires the parameter ϕ Eq.(5.19):

$$\mu_{\text{CO}_2,\text{H}_2} = \sum_{i=1}^N \left(\frac{\mu_i y_i}{\sum_{j=1}^N y_j \phi_{i,j}} \right) \quad (5.18)$$

$$\phi_{i,j} = \frac{\left[1 + \left(\mu_i / \mu_j \right)^{1/2} + \left(M_i / M_j \right)^{1/4} \right]^2}{\left[8 \left(1 + M_i / M_j \right) \right]^{1/2}} \quad (5.19)$$

$\mu_{i,j}$ and $M_{i,j}$ are the viscosity and molar mass of each species. The viscosity of a pure component is calculated as follows (Eq. (5.20)) using the parameters in Table 5.4 [163].

$$\mu_{i,j} = \frac{C_1 T^{C_2}}{1 + \frac{C_3}{T} + \frac{C_4}{T^2}} \quad (5.20)$$

Table 5.4. Parameters for the viscosity of pure species and their diffusion volume [164].

Species	M_i (g mol ⁻¹)	C_1	C_2	C_3	C_4	$v_{ci,j}$
CO ₂	44.01	$2.148 \cdot 10^{-6}$	0.46	290	0	26.9
H ₂	2.016	$1.797 \cdot 10^{-7}$	0.685	-0.59	0	7.07

The molecular diffusions coefficient D , where $v_{ci,j}$ diffusion volume of each species, is calculated in Eq. (5.21)) [165]:

$$D_{\text{CO}_2,\text{H}_2} = \frac{10^{-7} T^{3/2} \sqrt{1/M_i + 1/M_j}}{p(v_{ci}^{3/2} + v_{cj}^{3/2})} \quad (5.21)$$

5.6.2 Calculations for the Three-Phase Batch Methanol Synthesis

The initial gas phase composition (at reaction time $t_R=0$ h) in the three-phase reactor setup was analyzed using the same gas chromatography as for the two-phase studies. After a typical reaction time of 3 h, the product gas composition was subsequently analyzed. The following equations, Eqs. (5.22) and (5.23) shows the calculation of the amount of substance n for a component i at measured pressure p , temperature T at any reaction time.

$$n_{\text{total}}(t_R) = \frac{p(t_R) \cdot V_{R,\text{gas}}}{R \cdot T(t_R)} \quad (5.22)$$

$$n_i(t_R) = y_i \cdot n_{\text{total}}(t_R) \quad (5.23)$$

The gas volume of the reactor $V_{R,\text{gas}}$ was calculated by subtracting the liquid volume (100 mL) from the total reactor volume (600 mL), resulting in a gas volume of 500 mL.

Eqs. (5.22) and (5.23) can be used to calculate the selectivity S_{MeOH} of methanol, the space-time-yield (STY) and P_{cat} , refer to Eqs.(5.24)-(5.26).

$$S_{\text{MeOH}} = \frac{n_{\text{MeOH}}}{n_{\text{CO}_2,0} - n_{\text{CO}_2}} \cdot 100 \% \quad (5.24)$$

$$STY = \frac{n_{\text{MeOH}} \cdot M_{\text{MeOH}}}{m_{\text{cat}} \cdot t_R} \quad (5.25)$$

$$P_{\text{cat}} = \frac{n_{\text{MeOH}} \cdot M_{\text{MeOH}}}{m_{\text{active metal}} \cdot t_R} \quad (5.26)$$

6 Cumulative part of the dissertation

The following cumulative part of the dissertation is based on the publications P1 to P4 [18–21], see Figure 6.1. First (P1), the catalytic performance of pure In_2O_3 and the reversibility of the phase transitions in In_2O_3 , $\text{In}(\text{OH})_3$ model system were investigated using a two-phase fixed bed reactor. The results were used for validation of the computational study (see Chapter 6.1) [18].

In the second publication (P2) [19], different ZrO_2 supports were loaded with In_2O_3 by different synthesis methods. The most active $\text{In}_2\text{O}_3/\text{ZrO}_2$ is promoted with various metals to enhance its catalytic performance. Different $\text{Ni-In}_2\text{O}_3/\text{ZrO}_2$ catalysts were synthesized either by chemical reduction, co-precipitation or wetness impregnation and compared for their catalytic performance in CO_2 hydrogenation to methanol. Additionally, the stability and activity over 100 h TOS was shown for the most promising In-based catalyst. The catalytic performance tests were conducted in a high-pressure continuous-flow fixed bed reactor setup (see Chapter 6.2).

In Chapter 6.3 (P3), the $\text{In}_2\text{O}_3/\text{ZrO}_2$ and metal promoted $\text{In}_2\text{O}_3/\text{ZrO}_2$ catalysts prepared by wetness impregnation were spatially investigated, compared with the state-of-the-art $\text{Cu}/\text{ZnO}/\text{Al}_2\text{O}_3$ catalyst. An objective was to reveal the influence of reaction conditions such as total pressure, temperature, or GHSV to the reaction profiles. The spatially resolved reaction profiles were determined in a two-phase fixed bed CPR [20].

Chapter 6.4 (P4) demonstrates the application of a supported In_2O_3 -based catalyst in a three-phase stirred-tank reactor concept. This chapter focuses on catalyst and parameter optimization studies for slurry phase CO_2 hydrogenation to methanol.

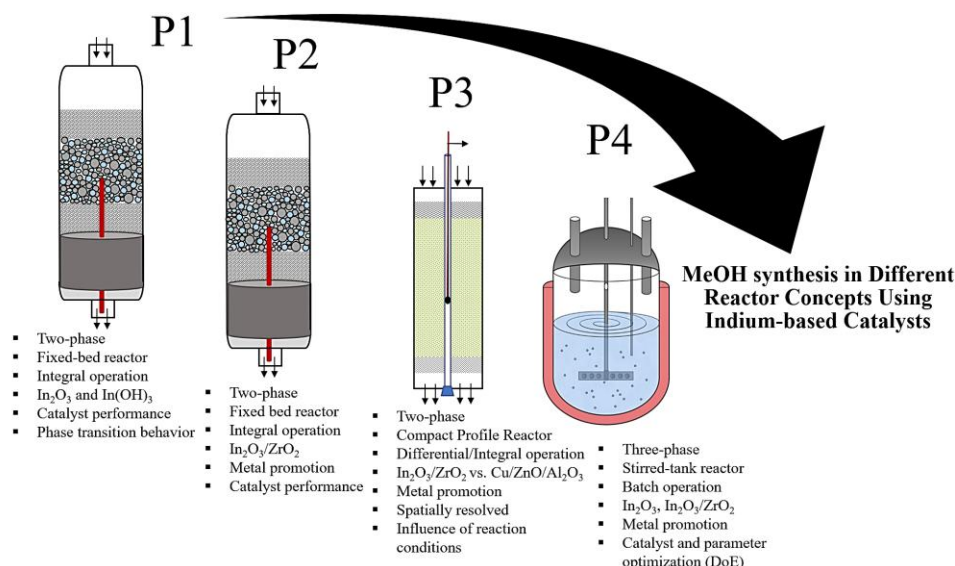


Figure 6.1. Schematic illustration of the cumulative part of the dissertation.

6.1 Influence of the phase transition of pure In_2O_3 in two-phase methanol synthesis

P1

Effect of Conversion, Temperature and Feed Ratio on $\text{In}_2\text{O}_3/\text{In}(\text{OH})_3$ Phase Transitions in Methanol Synthesis Catalysts: A Combined Experimental and Computational Study

Philipp Kampe, Anne Wesner, Patrick Schühle, Franziska Hess, and Jakob Albert

P. Kampe, A. Wesner, P. Schühle, F. Hess, J. Albert. “Effect of Conversion, Temperature and Feed Ratio on $\text{In}_2\text{O}_3/\text{In}(\text{OH})_3$ Phase Transitions in Methanol Synthesis Catalysts: A Combined Experimental and Computational Study”, *ChemPlusChem*, **2023**, 88, e202300425, DOI: doi.org/10.1002/cplu.202300425

Published under a Creative Commons license.

The following article [18] reports about the phase transition of neat In_2O_3 or $\text{In}(\text{OH})_3$ during CO_2 hydrogenation with and without rWGS. A computational study illustrates a dummy catalytic cycle and Gibbs free energy change curves for catalyst dehydration and rehydration with or without considering rWGS. The stability predictions were confirmed with experimental studies in a fixed bed reactor (integral operation) employing In_2O_3 and $\text{In}(\text{OH})_3$ under $p = 75$ bar and $\text{CO}_2/\text{H}_2=1/3$ (see Figure 6.2). Two different experimental setups were applied in combination with XRD and TGA analysis. The validated model is applied to predict the impact of hydrogen drop out on catalyst stability and to discuss practical reactor operation strategies to avoid catalyst degradation. The corresponding Supporting Information of the following article can be found in the Appendix Chapter 9.3 and details about the fixed bed reactor system in Chapter 9.1.3.

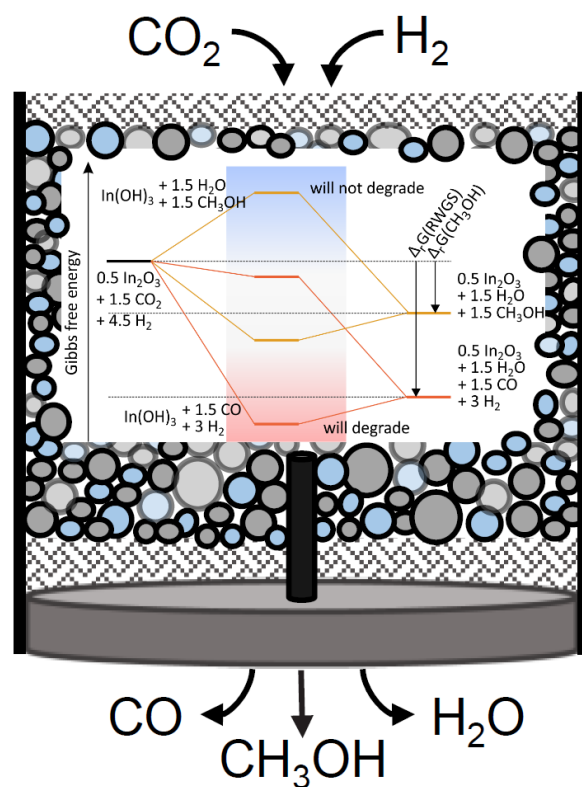


Figure 6.2. Stability calculations, predictions and experimental studies about $\text{In}_2\text{O}_3/\text{In}(\text{OH})_3$ phase transition behavior under CO_2 hydrogenation conditions to methanol [18].

Effect of Conversion, Temperature and Feed Ratio on $\text{In}_2\text{O}_3/\text{In}(\text{OH})_3$ Phase Transitions in Methanol Synthesis Catalysts: A Combined Experimental and Computational Study

Philipp Kampe,^[a] Anne Wesner,^[a] Patrick Schühle,^[b] Franziska Hess,^{*,[c]} and Jakob Albert^{*,[a]}

Catalytic hydrogenation of CO_2 to methanol has attracted lots of attention as it makes CO_2 useable as a sustainable carbon source. This study combines theoretical calculations based on the dummy catalytic cycle model with experimental studies on the performance and degradation of indium-based model catalysts for methanol synthesis. In detail, the reversibility of phase transitions in the $\text{In}_2\text{O}_3/\text{In}(\text{OH})_3$ system under industrial methanol synthesis conditions are investigated depending on conversion, temperature and feed ratio. The dummy catalytic cycle model predicts a peculiar degradation behavior of $\text{In}(\text{OH})_3$

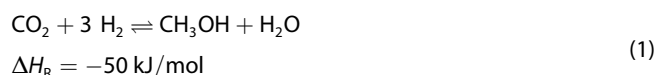
at 275 °C depending on the water formed either by methanol synthesis or the competing reverse water-gas-shift reaction. These results were validated by dedicated experimental studies confirming the predicted trends. Moreover, X-ray diffraction and thermogravimetric analysis proved the ensuing phase transition between the indium species. Finally, the validated model is used to predict how hydrogen drop out will affect the stability of the catalyst and derive practical strategies to prevent irreversible catalyst degradation.

Introduction

The economic and ecologic supply of the growing energy demand is a global challenge. In view of the climate change the future energy supply has to be based on renewable energies as well as alternative feedstocks.^[1] Electrolytically produced H_2 is of particular importance as a molecule to store energy and drive chemical catalytic processes. However, fluctuations in the H_2 flux due to the intermittent nature of renewable energy sources (hydrogen drop out) can impose severe strain on catalysts due to the change of reactant ratio in the feed and subsequent drop of conversion and catalyst bed temperature. Such a drop

out may cause irreversible degradation, from which the catalyst may not be able to recover without additional reactivation steps after hydrogen supply is restored. In order to stabilize catalysts operating under intermittent conditions against such degradation phenomena, a deep understanding of how temperature, conversion and reactant feed ratio affect catalyst stability is required. This enables the integrated design of new catalysts and of the linked processes to prevent irreversible degradation due to hydrogen drop out.

Besides hydrogen, a carbon source is required for methanol synthesis. Due to its significant contribution to the greenhouse effect, a special focus has to be drawn on the utilization of CO_2 from emissions. One possible strategy hereby is carbon capture and utilization.^[2] CO_2 is an abundant, non-toxic and renewable chemical. It is thermally stable and chemically inert with a standard formation enthalpy of -394 kJ/mol. Consequently, a large energy input for chemical conversion is necessary.^[3] Therefore, a promising way is the catalytic valorization of CO_2 with electrolytically produced H_2 from renewable energies to methanol, as shown in Eq. 1:^[4]



In the commercialized process, methanol is produced from syngas ($\text{CO}/\text{CO}_2/\text{H}_2$) via a $\text{Cu}/\text{ZnO}/\text{Al}_2\text{O}_3$ catalyst. Under typical reaction conditions ($T=200\text{--}300$ °C, $p=50\text{--}100$ bar and $\text{CO}/\text{CO}_2/\text{H}_2$ of 28/2/70) a selectivity of $S_{\text{MeOH}}=30\text{--}70\%$ can be achieved.^[5] Besides the exothermic hydrogenation of CO/CO_2 (Eq. 1–2) into methanol, also the endothermic reverse water-gas-shift (RWGS) reaction (Eq. 3) plays a role in the context of methanol synthesis and CO_2 hydrogenation:^[6]

[a] P. Kampe, A. Wesner, J. Albert
Institute of Technical and Macromolecular Chemistry
Universität Hamburg
Bundesstraße 45
20146 Hamburg (Germany)
E-mail: jakob.albert@uni-hamburg.de

[b] P. Schühle
Institute of Chemical Reaction Engineering
Friedrich-Alexander-Universität Erlangen-Nürnberg
Egerlandstraße 3
91058 Erlangen (Germany)

[c] F. Hess
Institut für Chemie
Technische Universität Berlin
Straße des 17. Juni 124
10623 Berlin (Germany)
E-mail: f.hess@tu-berlin.de

Supporting information for this article is available on the WWW under <https://doi.org/10.1002/cplu.202300425>

© 2023 The Authors. ChemPlusChem published by Wiley-VCH GmbH. This is an open access article under the terms of the Creative Commons Attribution Non-Commercial NoDerivs License, which permits use and distribution in any medium, provided the original work is properly cited, the use is non-commercial and no modifications or adaptations are made.



The RWGS reaction as undesired pathway is the thermodynamically preferred one under the applied reaction conditions and favored by high temperatures. For shifting the equilibrium to higher methanol selectivities, higher pressures and lower temperatures are necessary.^[7] However, not only thermodynamics but also kinetics and stability of the catalysts define the efficiency of a renewable methanol synthesis process. Kinetic modeling is widely used for the understanding of CO₂ hydrogenation and therefore, helps to develop efficient catalysts and reaction concepts.^[8]

Recently, various In₂O₃ based catalysts for CO₂ hydrogenation have been developed.^[9,10] Pure In₂O₃ shows only a low selectivity to methanol of $S_{\text{MeOH}} = 63\%$ ($T = 300^\circ\text{C}$, $p = 50 \text{ bar}$) due to the predominant competing RWGS reaction.^[11] The superior selectivity towards RWGS can be explained by the higher activation energy for the synthesis of methanol compared to RWGS.^[12] In further DFT and experimental studies, oxygen vacancies turned out to be the active sites for methanol formation, whereby one oxygen vacancy surrounded by three indium atoms leads to activation of CO₂ and the heterolytic splitting of H₂.^[12,13,14] Despite that, In₂O₃ has only a poor ability for H₂ activation.^[14,15] Previous experimental studies have further shown that the surface of bulk In₂O₃ is reduced at temperatures above 220°C, leading to metallic indium species in a H₂-rich atmosphere.^[12,16]

In₂O₃ based catalysts possess different chemical stability in CO₂ hydrogenation reactions depending on the reaction conditions. Tsoukalou et al. reported three distinct catalytic regimes (activation, stable performance, deactivation) during CO₂ hydrogenation by combining X-ray absorption spectroscopy (XAS), X-ray powder diffraction (XRD) and *in situ* transmission electron microscopy (TEM). Hereby, a reductive amorphization of the In₂O_{3-x} nanocrystallites progresses with time on stream, leading to an over-reduction to molten In⁰ being responsible for the deactivation.^[17]

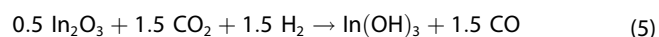
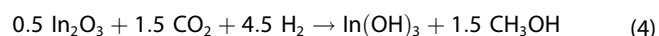
Aside from over-reduction to In⁰, In₂O₃-based catalysts also suffer from partial conversion to less active In(OH)₃, or from poisoning with feed gas impurities, such as sulfur and nitrogen-containing compounds.^[10] For the phase transition between In₂O₃ and In(OH)₃ species by hydration, the composition of the surrounding process gas plays a decisive role. Due to the thermodynamics of hydration reactions, we propose that the propensity of In₂O₃ to hydrate is intimately coupled to temperature and conversion in the catalyst bed. In this contribution, we investigate the influence of important reaction parameters on the stabilities of In₂O₃ and In(OH)₃ under typical methanol synthesis conditions by applying a computational model based on Gibbs free energies of reaction. We subsequently test the predictions by dedicated model experiments employing pure In₂O₃ and In(OH)₃ catalysts. We further discuss possible reactor

operation strategies to prevent catalyst degradation by phase transformation when hydrogen drop out occurs.

Results and Discussion

Theoretical modeling

Modeling the phase transitions of catalysts in fixed-bed reactors is challenging because the gas phase surrounding the catalyst is never at equilibrium. Likewise, the catalyst can never reach an equilibrium state and this is one of the core principles of catalytic processes. However, despite the lack of a clearly defined thermodynamically stable state of the catalyst, a steady state exists, which can be either static or dynamic, e.g., oscillating. In catalysts that undergo phase transitions, the steady state is determined by the kinetics of these phase transitions and the principle of minimum entropy production. If no information is available about how these phase transitions occur, something can still be learned about the stability of the phases based on the reaction conditions (like temperature, feed ratio, conversion, and selectivity): this can be achieved by studying the driving forces, specifically the changes in Gibbs free energy, and how they relate to the reaction conditions. However, when the gas feed is not at equilibrium, the degradation and reactivation proceed via different reactions due to the Gibbs free energy difference between the reaction products and reactants of the overall catalytic reaction. The reactions associated with degradation and reactivation then form a closed catalytic cycle, where the degraded catalyst represents an intermediate. In the case of In₂O₃/In(OH)₃, the hydration of In₂O₃, can occur via one of two pathways: methanol formation (Eq. 4) or CO formation (Eq. 5) through RWGS:



Reactivation of In(OH)₃ occurs via a simple dehydration reaction by releasing water:



Adding Eq. 4 and Eq. 6, or Eq. 5 and Eq. 6 results in two so-called dummy catalytic cycles as illustrated in Figure 1a). Note that for the application of this model, it is not a prerequisite that the dummy catalytic cycle describes the dominant reaction path, i.e., that the catalytic reaction proceeds via a solid-state reaction. However, the utility of this concept becomes immediately obvious if we recall the physical meaning of the Gibbs free energy as the maximal amount of work that a chemical reaction can exert. This insight can be used to evaluate the thermodynamic viability of proposed reaction mechanisms based on their intermediates with the highest and lowest Gibbs free energy. In the case of catalyst degradation, the Gibbs free energy of the intermediate in relation to the reactants indicates how rever-

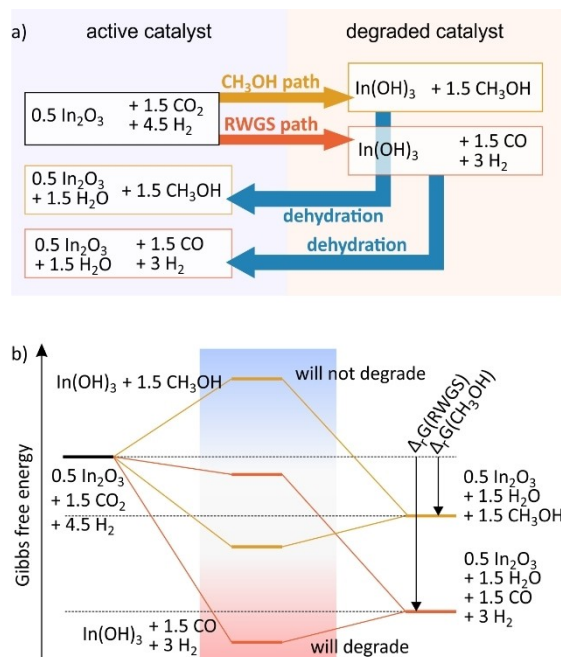


Figure 1. Illustration of the dummy catalytic cycle. a) Reactions converting CO_2 and H_2 via a two-step reaction into the products (H_2O , CH_3OH , and CO). b) Gibbs free energy profiles for dehydration and product formation in the CH_3OH and RWGS pathways.

sible a phase transition under nonequilibrium conditions is, as illustrated in Figure 1b).

Here, the level on the left represents the active catalyst, In_2O_3 , along with the two reactants. The two levels depicted to the far right represent again the active catalyst with the two possible products of the reaction, $\text{CH}_3\text{OH}/\text{H}_2\text{O}$ (orange), and $\text{CO}/\text{H}_2\text{O}$ (red). Methanol formation and RWGS have different $\Delta_r G$ as indicated by black arrows connecting the reactant and product Gibbs free energies, which places the final states at different levels. The $\Delta_r G$ for the two reactions are a function of conversion, selectivity, temperature, and reactant feed ratio. The intermediates for the two reactions are $\text{In}(\text{OH})_3$ and either CH_3OH or CO . Similarly, we can compute the hypothetical Gibbs free energy of this intermediate. If the intermediate is above the top dashed line, $\text{In}(\text{OH})_3$ will not be formed to a large extent, i.e., In_2O_3 is stable. If the intermediate is below the bottom dashed line, $\text{In}(\text{OH})_3$ is stable, i.e., the formation of $\text{In}(\text{OH})_3$ will be irreversible. If the CH_3OH or CO intermediate is in between the first and second line or between the first and third line, respectively, the formation of $\text{In}(\text{OH})_3$ is reversible. This means in practice that the catalyst enters a steady state, which can be either one or the other, and stabilization of either phase can be accomplished by tuning the kinetics of these phase transitions, for instance, by the appropriate selection of promoters or catalyst support.

We note that the application of this model, while not limited to any particular material or catalytic reaction,^[18] can also be applied to mixed oxides,^[19] and possibly also to supported catalysts. This requires, however, that the thermodynamic data are known, i.e., that the influence of a catalyst

support on the free enthalpy of reaction, can be estimated with sufficient reliability. Similarly, the kinetics of phase transitions can be taken into consideration quantitatively, for instance, to understand the influence of particle morphology on the life time of a catalyst.^[20] Kinetics can play a crucial role in determining the long-term stability of thermodynamically unstable materials in catalysis and they also determine the steady-state phase fractions if degradation is reversible.^[21] In the case of $\text{In}(\text{OH})_3/\text{In}_2\text{O}_3$, we observe no remarkable differences between our expectations from the purely thermodynamic treatment and our experimental observations. As a consequence, considering the kinetics in addition would add little additional insight at the present stage.

In the following, stability calculations regarding In_2O_3 under typical reaction conditions of $p = 75$ bar and a CO_2/H_2 ratio = 1/3 are undertaken. Therein, the influence of temperature in methanol synthesis without RWGS and with RWGS reaction on the hydration/dehydration behavior of In_2O_3 are investigated. These results were validated by experimental investigations in a fixed bed reactor due to different positions of the bed and a two-segment configuration. The model was applied to predict the influence of hydrogen drop out on the stability of the catalyst.

Stability of In_2O_3 under methanol synthesis without RWGS

Figure 2 shows the Gibbs free energy curves for three different reaction temperatures (200 °C, 250 °C, 300 °C) for a stoichiometric $p(\text{H}_2)/p(\text{CO}_2)$ mixture of 3:1 with a total pressure of 75 bar (i.e., $p_0(\text{CO}_2) = 18.75$ bar, $p_0(\text{H}_2) = 56.25$ bar) as a function of the CO_2 conversion, assuming that only CH_3OH and H_2O are formed as reaction products, i.e., the RWGS does not take place.

In each graph, the blue curve represents the free enthalpy of the dehydration reaction as given by Eq. 6. Negative values mean that dehydration of $\text{In}(\text{OH})_3$ is thermodynamically favorable and will occur to a large extent, while for positive values, dehydration is not thermodynamically favorable, but may still occur to a smaller extent. Rehydration of In_2O_3 due to the formation of CH_3OH via Eq. 4 will usually assume negative values, as long as the conversion remains below a certain threshold that depends on the reaction temperature. Naturally, the overall Gibbs free energy of the CO_2 reduction is given by the sum of dehydration and rehydration, as these reactions together form a full catalytic cycle (displayed by the green lines in Figure 2). The equilibrium conversion is indicated by a thick, black line, which is only visible in the diagram for 300 °C because equilibrium conversions at lower temperatures are over 30% and, therefore, outside the plot range.

Figure 2a shows the free enthalpy curves for 200 °C. Here, dehydration (blue curve) is exergonic at conversions below 2.3%. Dehydration becomes less favorable with increasing CO_2 conversion due to the presence of H_2O as a reaction product in the gas stream, which suppresses the release of H_2O from $\text{In}(\text{OH})_3$. The rehydration due to the formation of CH_3OH (orange curve) shows a similar trend, because the CO_2 content in the gas stream decreases and the CH_3OH content increases with

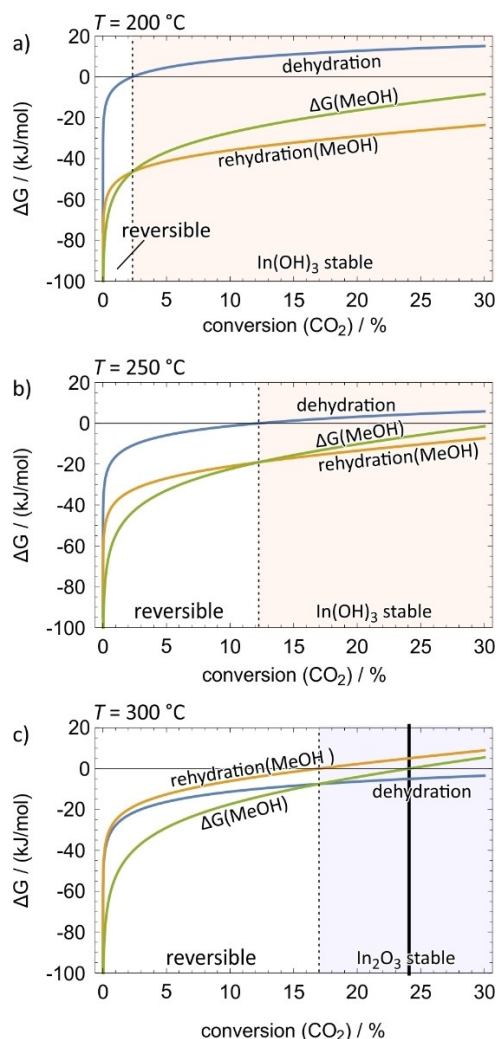


Figure 2. ΔG curves for catalyst dehydration and rehydration without considering RWGS. a) 200 °C, b) 250 °C, c) 300 °C for a CO_2/H_2 mixture of 1/3 at a total pressure of 75 bar. Black line: equilibrium conversion, blue curve: $\Delta_r G$ for dehydration reaction, orange curve: $\Delta_r G$ for rehydration through methanol formation, green curve: overall $\Delta_r G$ for methanol formation.

increasing CO_2 conversion. Therefore, we conclude that dehydration is not expected to occur at conversions over 2.3% at 200 °C (red shaded region), while at lower conversion, dehydration to form In_2O_3 is possible, but reversible, because both dehydration and rehydration are exergonic. This result indicates that at low temperatures, the phase transition will inevitably occur at conversions larger than 2.3% due to the formation of $\text{In}(\text{OH})_3$. Because $\text{In}(\text{OH})_3$ is favored at lower temperatures, this kind of phase transition may be self-accelerating due to lack of local heat production and resulting cold spot formation in partially degraded areas. Furthermore, the local heat production due to the exothermic CO_2 hydrogenation reaction depends on the local reaction rate, which tends to decrease with increasing reactant conversion. Note that, even at low conversion, the driving force for dehydration given by the blue curve is rather small, while the driving force for rehydration (orange curve) is much larger. This result alone, however, is insufficient to conclude whether $\text{In}(\text{OH})_3$ or In_2O_3 will dominate in the steady

state at low conversion. However, we can conclude that the fraction of $\text{In}(\text{OH})_3$ in the steady state will increase along the catalyst bed, i.e., the higher the local conversion, the more $\text{In}(\text{OH})_3$ will be present because the driving force for dehydration quickly approaches zero, while the driving force for rehydration remains at a large negative value within the whole range of $X \leq 2.3\%$.

Higher temperatures present a vastly different picture, as illustrated in Figure 2b, which shows the free enthalpy curves for 250 °C. At higher temperature, dehydration (blue curve) is possible over a larger range of conversions ($X < 12.2\%$), because higher temperature favors In_2O_3 over $\text{In}(\text{OH})_3$. Rehydration (orange curve) is still exergonic over the whole range of conversion. It is less favored with increasing conversion due to the accumulation of the reaction product CH_3OH , in the gas stream, and depletion of the reactants, CO_2 and H_2 . This means that dehydration and rehydration are thermodynamically reversible up to a conversion of 12.2%. At higher conversion (red shaded area), $\text{In}(\text{OH})_3$ is thermodynamically stable and will not be converted to In_2O_3 .

At 300 °C (Figure 2c), the situation is quite different because the dehydration curve now lies below zero over the whole conversion range, while the curve representing rehydration by methanol formation is endergonic at $X > 17\%$, indicating that $\text{In}(\text{OH})_3$ will dehydrate irreversibly, resulting in the formation of In_2O_3 . At conversions below 17%, rehydration is still possible, indicating reversible phase transition or coexistence of In_2O_3 and $\text{In}(\text{OH})_3$, with lower conversions favoring $\text{In}(\text{OH})_3$. Such reversible phase transitions may also contribute to faster sintering or particle reshaping.

The modeling results clearly show that the In_2O_3 catalyst will display enhanced stability against hydration at higher reaction temperatures. The influence of conversion on the stability of In_2O_3 is less straightforward; at low temperatures, the section of the catalyst bed that comes in contact with the feed at low conversion (i.e., close to the reactor inlet) will be less susceptible to phase transformation via $\text{In}(\text{OH})_3$ formation, while at high temperatures, the catalyst section in the high conversion zone, i.e., close to the reactor outlet, will be more stable.

Stability of In_2O_3 under methanol synthesis with RWGS

A realistic indium-based catalyst applied in CO_2 reduction does not have perfect selectivity towards methanol. In practice, the RWGS will dominate in the hot zone of the catalyst bed as it is thermodynamically favored over methanol formation at high temperatures. Therefore, the gas stream can be expected to contain additional H_2O formed by the RWGS; since the H_2O content in the gas stream is one of the main factors in the $\text{In}_2\text{O}_3/\text{In}(\text{OH})_3$ equilibrium, we assume that the occurrence of the RWGS can change the phase transition behavior. To determine the influence of RWGS on the phase transition, we assume that the catalyst operates at a certain selectivity towards RWGS that is extracted from the measured selectivities of our catalytic experiments presented below. For the following computations,

we thus employ averaged RWGS selectivities at $10^{-4}\%$ (CO conversion was below the detection limit), 10%, and 25% for 200 °C, 250 °C, and 300 °C, respectively. Figure 3 shows the resulting ΔG curves for these temperatures. Now there are two additional curves in each diagram, indicating the driving force for rehydration of the catalyst through CO formation (Eq. 5, red curves), and the total ΔG_{RWGS} (purple curve), which is typically more negative than ΔG_{MeOH} due to the lower selectivity of the indium-based catalyst towards RWGS (i.e., the actually produced amount of CO is less than expected from pure thermodynamics). The low CO content in the gas feed generally results in a high thermodynamic driving force toward CO formation.

With the RWGS, there is an additional reaction path for the catalyst to rehydrate (Eq. 5), while the dehydration reaction is the same as for methanol formation. Similar to the discussion

on Figure 2, we employ the driving forces of these reactions, particularly the intersections of the blue, red, and orange curves, with the abscissa, to assess whether the phase transition from $\text{In}(\text{OH})_3$ to In_2O_3 is reversible or irreversible, and now extend this approach by considering additional contributing reactions.

Figure 3a shows the ΔG curves for 200 °C, for which the dehydration and methanol curves look exactly the same as in Figure 2 a because the RWGS selectivity is close to zero. We observe two additional curves drawn in red (rehydration via RWGS) and purple (overall ΔG_{RWGS}), which appear in the negative range, indicating a high thermodynamic driving force for RWGS. In terms of phase transition, including the RWGS in our considerations does not alter the conclusions drawn from Figure 2 a, because the phase transition is still reversible at conversions lower than 2.3% due to dehydration, and both rehydration reactions having negative Gibbs free energies. Similarly, above a conversion of 2.3%, $\text{In}(\text{OH})_3$ is stable because the dehydration is now endergonic, indicating that $\text{In}(\text{OH})_3$ is unable to release water at high conversions.

At 250 °C, (Figure 3b) we observe that dehydration is exergonic at $X < 12.2\%$, and this curve is also unchanged compared to the case without considering the RWGS, as both reactions produce one molecule of H_2O per consumed molecule of CO_2 , i.e., the partial pressure of H_2O as a function of CO_2 conversion is independent of selectivity. Rehydration through methanol formation (orange curve) and RWGS (red curve) are both exergonic over the whole conversion range. Just like the case without RWGS, $\text{In}(\text{OH})_3$ is thermodynamically stable at conversions over 12.2%, while reversible conversion to In_2O_3 is possible at lower conversions.

Figure 3c displays the ΔG curves for 300 °C, where we observe that dehydration is exergonic over the whole range of conversion due to the high temperature. The formation of In_2O_3 is reversible through the methanol formation and RWGS reaction up to conversions of 21% and 31%, respectively. Due to the increased RWGS selectivity, we now observe that the orange curve indicating rehydration through methanol formation has shifted a little to higher CO_2 conversion, enlarging the reversible (white) region. Furthermore, without considering RWGS in the modeling, it was concluded that In_2O_3 is fully stable at higher conversions (Figure 2c). If RWGS is considered as well, it is revealed that rehydration via the RWGS is still possible at conversions over 21% (blue hatched region), i.e., In_2O_3 is favored at higher conversion, but not fully thermodynamically stable.

From the computational results, we derive two central hypotheses about the phase stability: (I) The $\text{In}(\text{OH})_3$ content post reaction will decrease with temperature, and (II) the $\text{In}(\text{OH})_3$ content in the catalyst bed at steady state will vary with conversion; more specifically: at low temperatures, more $\text{In}(\text{OH})_3$ will be present at low conversion, while at high temperatures, more $\text{In}(\text{OH})_3$ will be present at high conversion. To verify these hypotheses and demonstrate this unexpected behavior, we conducted a series of dedicated stability experiments.

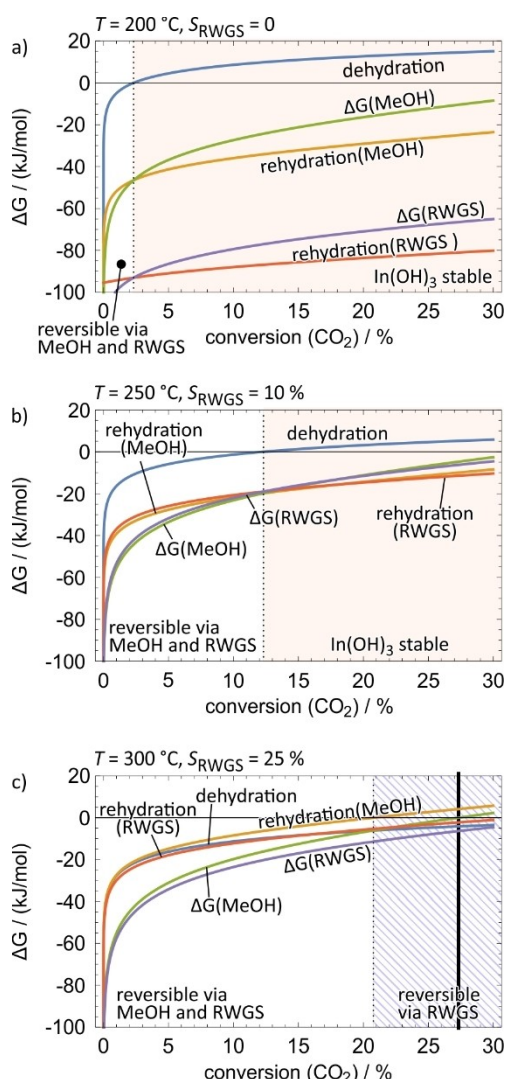


Figure 3. ΔG curves with RWGS based on experimental selectivities. a) 200 °C, b) 250 °C, c) 300 °C for a CO_2/H_2 mixture of 1/3 at a total pressure of 75 bar. Black line: equilibrium conversion, blue curve: ΔG for dehydration reaction, orange curve: ΔG for rehydration through methanol formation, green curve: overall ΔG for methanol formation, red curve: ΔG for rehydration through RWGS. purple curve: overall ΔG for RWGS.

Experimental investigations on catalyst stability in a fixed-bed reactor

For experimental evaluation of the thermodynamic predictions from the dummy catalytic cycle, different model catalysts as well as reactor configurations have been tested. All tests were performed under industrially relevant conditions, using a total pressure of $p = 75$ bar and a stoichiometric feed ratio of $\text{CO}_2/\text{H}_2 = 1/3$ in a fixed-bed reactor (for details see Figure S1 in the Supporting Information). The reaction studies were conducted at 200 °C, 250 °C, 275 °C and 300 °C, respectively.

Catalyst testing with experimental setup 1 (top, middle, and bottom configuration)

In the first experimental setup, commercial In_2O_3 or $\text{In}(\text{OH})_3$ was used as a catalyst material, representing the two sides of the dummy catalytic cycle, i.e. the two possible starting points of the rehydration/dehydration mechanism. The three different reaction temperatures, 200 °C, 250 °C, and 300 °C were adjusted one after another according to a defined heating ramp, without cooling down the reactor or changing the catalyst material in between. In_2O_3 and $\text{In}(\text{OH})_3$ were positioned either in top, middle or bottom position in relation to the thermocouple inside the reactor (Figure 4). The different positions modify the theoretical temperature profiles (Figure S2) in the reactor to evaluate the effects of temperature on the stability of In_2O_3 and

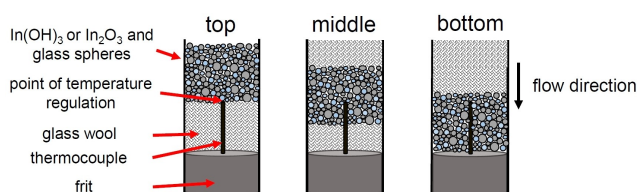


Figure 4. Schematic reactor configuration for the first experimental setup (top, middle or bottom position).

to compare the results with the predicted thermodynamic models. The ensuing phase transition between the indium species and crystal structure were determined via XRD and thermogravimetric analysis (TGA).

Moreover, real fixed-bed reactors have a temperature profile in the catalyst bed. At the entrance of the catalyst bed, the reaction rate is the highest, decreasing with increasing bulk height, leading to an integral temperature profile, due to reaction heat.

The integral temperature profile will increase over the height of the catalyst bed. The position of the thermocouple is either at the beginning and coldest spot of the catalyst bed (top position), in the middle (middle position) or at the end (bottom position) and therefore the hottest zone of the reactor (Figure S2).

For the first experimental setup, experimental data for In_2O_3 as a model catalyst are summarized in Table 1. It was observed that CO_2 conversion and methanol selectivity depend on the segment position for all investigated temperatures (middle = bottom > top). The middle and bottom position showed the highest CO_2 conversion and methanol selectivity for each temperature (Table 1) and a more homogenous temperature distribution (Figure S2). Table 2 shows the temperature dependence of CO_2 conversion and MeOH selectivity for In_2O_3 and $\text{In}(\text{OH})_3$ in the middle configuration of the experimental setup 1 (Figure 4).

Generally, conversion increased with a higher temperature while the selectivity of methanol decreased due to the competing endothermic RWGS reaction. Moreover, also the final partial pressure of water increased with increasing CO_2 conversion as both possible reactions contribute equally to water formation (Table S1).

For 200 °C, no CO formation by RWGS was observed and CO_2 conversions were similar for In_2O_3 (0.13%) and for $\text{In}(\text{OH})_3$ (0.15%). Here, only methanol is detectable, resulting in a selectivity $S(\text{MeOH})$ of 100%.

Table 1. Experimental data for In_2O_3 and standard deviation (see Eq. S4) determined in the first experimental setup, with $T = 200, 250$ and 300 °C hold for 3 h each, for a CO_2/H_2 mixture of 1/3 ($1200 \text{ Nml min}^{-1}$) and a total pressure of 75 bar.

T/°C	X (CO_2)/%			S (MeOH)/%		
	top	middle	bottom	top	middle	bottom
In_2O_3	200	0.08 ± 0.00	0.13 ± 0.00	0.14 ± 0.02	100 ± 0	100 ± 0
	250	0.66 ± 0.00	0.98 ± 0.02	0.94 ± 0.01	88 ± 0	87 ± 0
	300	2.40 ± 0.03	3.56 ± 0.04	3.26 ± 0.05	76 ± 0	73 ± 1

Table 2. Comparison of the experimental data of In_2O_3 and $\text{In}(\text{OH})_3$ with standard deviation (see Eq. S4) determined in the middle configuration, $T = 200, 250$ and 300 °C, for a CO_2/H_2 mixture of 1/3 at a total pressure of 75 bar.

T/°C	In_2O_3		$\text{In}(\text{OH})_3$	
	X_{CO_2} (%)	S_{MeOH} (%)	X_{CO_2} (%)	S_{MeOH} (%)
200	0.13 ± 0.00	100 ± 0	0.15 ± 0.02	100 ± 0
250	0.98 ± 0.02	87 ± 0	1.16 ± 0.00	86 ± 0
300	3.56 ± 0.04	73 ± 1	4.25 ± 0.13	71 ± 1

When temperature was increased to 250 °C, the RWGS selectivity rises to 13% for In_2O_3 and to 14% for $\text{In}(\text{OH})_3$. An average selectivity of 10% was determined for all positions /starting materials (see Table S2) and used for the simulations in Figure 3b). For $T=250\text{ }^\circ\text{C}$, In_2O_3 is mostly stable because the dehydration step is exergonic over the whole conversion range. The dehydration behavior is very sensitive to the temperature, both in terms of kinetics and thermodynamics. Therefore, the temperature distribution in the catalyst bed may be crucial, with regard to transformation to $\text{In}(\text{OH})_3$ at cold spots. For In_2O_3 , CO_2 conversion increases to 0.98% and for $\text{In}(\text{OH})_3$ to 1.16%, when going from 200 to 250 °C. Through the overall higher CO_2 conversion due to the higher temperature, an increased heat formation and water content in the system was registered.

For 300 °C, the RWGS selectivity reached 27% (In_2O_3) and 29% ($\text{In}(\text{OH})_3$), respectively. The average selectivity of 25% for all positions and starting materials was used for the modeling studies in Figure 3c). The CO_2 conversions for both starting materials are somewhat different with 3.56% (In_2O_3) and 4.25% ($\text{In}(\text{OH})_3$). This might be due to the different accessibility of

oxygen vacancies in both materials. The water partial pressure significantly increased due to the overall higher activity of the reaction system (Table S1).

The catalytic results suggest that $\text{In}(\text{OH})_3$ has been converted completely to In_2O_3 in the middle and bottom position at 300 °C. In comparison, In_2O_3 is not rehydrated to $\text{In}(\text{OH})_3$. In top position the catalytic performance was lower due to the overall lower catalyst bed temperature and the resulting higher $\text{In}(\text{OH})_3$ content. This can be explained with the observations carried out by XRD (Figure 5) and TGA-measurements (Figure 6) taken before and after reaction. XRD was used to identify the crystal structures of In_2O_3 and $\text{In}(\text{OH})_3$. Fresh and pure In_2O_3 in Figure 5a) (black line) was indexed to the cubic structure (blue square) whereas pure $\text{In}(\text{OH})_3$ in b) was indexed to the cubic structure (red oval) as well. After reaction, the XRD patterns with In_2O_3 as catalyst material displayed no reflections for $\text{In}(\text{OH})_3$. No reflection shift and no phase transition in any configuration were noticed. This was also verified by TGA, where no mass loss was measured with In_2O_3 as starting material (Figure 6a). For $\text{In}(\text{OH})_3$ as starting material (black line)

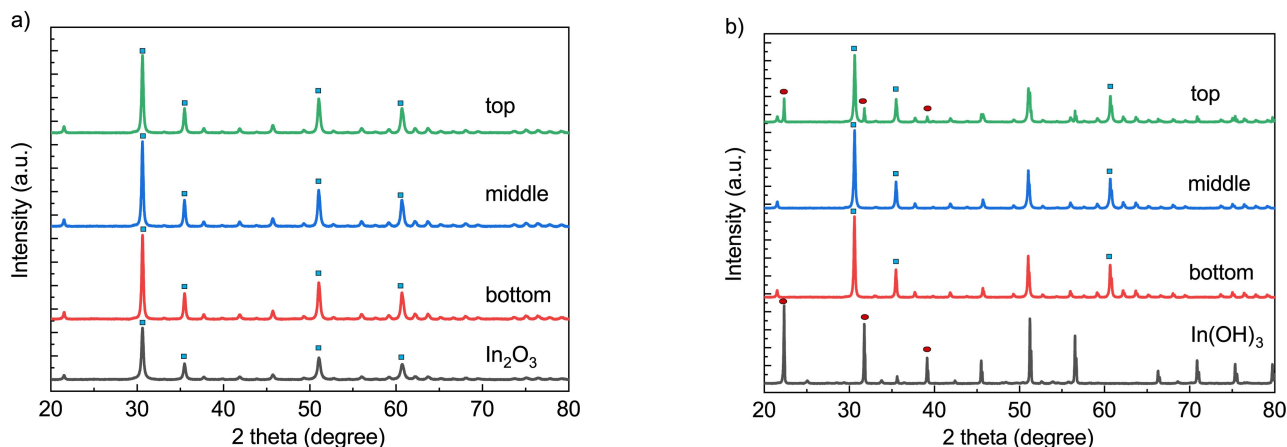


Figure 5. XRD for first experimental setup. In_2O_3 a) and $\text{In}(\text{OH})_3$ b) (before reaction, starting materials) for reactor configuration top, middle, bottom (after reaction) at 300 °C (after temperature ramp). Diffraction patterns for In_2O_3 (■), $\text{In}(\text{OH})_3$ (●) and InOOH (▲).

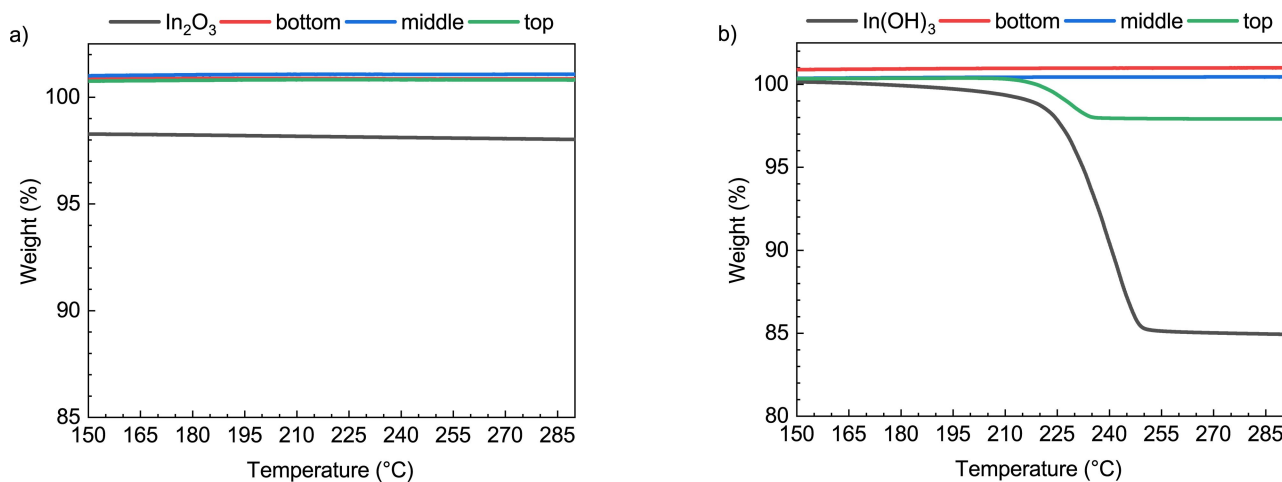


Figure 6. TGA data for the first experimental setup at 300 °C. In_2O_3 a) and $\text{In}(\text{OH})_3$ b) (before reaction, black) and after reaction in top (green), middle (blue) and bottom (red) configuration.

the XRD showed characteristic reflections in Figure 5b) indicating the existence of a cubic In_2O_3 phase (blue square) except for $\text{In}(\text{OH})_3$ (red oval), which is not fully converted into In_2O_3 in top position. No shift in the XRD reflections and no structure transition were observed, therefore only water was emitted. This was confirmed by TGA (Figure 6b), where a mass loss of 2.42% of $\text{In}(\text{OH})_3$ in top position was observed (see Table S3), suggesting a near-total conversion to In_2O_3 at 300 °C.

Regarding the integral temperature profile of the catalyst bed and the position of the thermocouple, there are new phenomena to consider. Therefore, we revealed the validity of the thermodynamic model about the stability of In_2O_3 .

Catalyst testing with experimental setup 2 (two-segment-configuration)

Computational results in the section **Theoretical modeling** predict strong dependence of the $\text{In}(\text{OH})_3$ dehydration behavior on the conversion due to the formed H_2O . At lower temperatures, we expect more $\text{In}(\text{OH})_3$ to be present at high conversions, while at higher temperatures, more $\text{In}(\text{OH})_3$ is expected at lower conversion. These hypotheses from the dummy catalytic cycle were studied in a dedicated experimental setup (Figure 7). In this second experimental setup (two-segment configuration), the catalyst bed was split into two identical segments, physically separated by a layer of glass wool to enable independent characterization of model catalysts from the low-conversion and high-conversion zone post reaction. As catalyst material, just $\text{In}(\text{OH})_3$ was used and the catalytic tests were performed under the same conditions as previously, adding an additional temperature step at 275 °C. For this experiment, the sample was extracted from the reactor after each temperature step and fresh $\text{In}(\text{OH})_3$ was used for the next

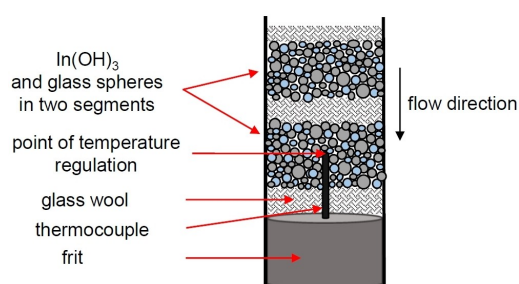


Figure 7. Schematic reactor configuration for the second experimental setup (two-segment-configuration).

experiment with a different temperature. In this reactor configuration, $\text{In}(\text{OH})_3$ was applied to examine the phase transition behaviour for different conversion ranges (and thereby, water contents) and temperatures. Depending on the CO_2 conversion in the first (top) segment, the second (bottom) segment operates with effluent gas in comparison to the first one, i.e., it is exposed to the reaction products, such as H_2O , methanol, and CO . Thereby, the influence of conversion on the rehydration/dehydration behaviour of the $\text{In}_2\text{O}_3/\text{In}(\text{OH})_3$ system could be examined for different temperatures. The separation of the catalyst bed prevents an overheating due to CO_2 hydrogenation and a lower integral temperature profile (see Figure S3). The phase transition that occurred and the crystal structure of the catalyst were determined via XRD and TGA for both layers separately.

For the second experimental setup, all experimental data of CO_2 hydrogenation and the calculated partial pressure of water are summarized in Table 3.

It was observed that the CO_2 conversion and methanol selectivity both depend on the temperature, as expected: The conversion of CO_2 increased with increasing temperature from 0.04% (200 °C) up to 3% (300 °C), while the selectivity of methanol decreased due to competing RWGS with higher temperature from 100% at 200 °C down to 76% at 300 °C.

For 200 °C in the second experimental setup, the CO_2 conversion ($X(\text{CO}_2) = 0.04\%$) as well as methanol-selectivity ($S(\text{MeOH}) = 100\%$), are consistent with the results obtained for the top position of the first experimental setup. XRD measurements (Figure 8) show only a slight phase transition to In_2O_3 (at about 30° and 35°), with the low-conversion section (top) containing more In_2O_3 than the high-conversion section (bottom). TGA shows an $\text{In}(\text{OH})_3$ amount of 82.11% of the low-conversion sample and 89.91% $\text{In}(\text{OH})_3$ in the high-conversion one (Table 4) after reaction, consistent with the XRD results. To explain this observation, one needs to consider that the upper section produces water through methanol synthesis, which influences the phase transition equilibrium during reaction in the lower segment. This reduces the thermodynamic driving force for dehydration as shown in Figure 3a) (blue) curve with increasing conversion. Dehydration is still exergonic at the experimentally determined 0.04% conversion, but rehydration is also possible and highly exergonic. We note that at 0.04% conversion, the influence of a temperature gradient due to the heat of reaction is negligible or the phase transition is too sluggish.

For 250 °C the CO_2 conversion reached 0.52%, which is in between the values reached in top and middle configuration of

Table 3. Experimental data and standard deviation (see Eq. S4) of setup 2 for temperatures of 200, 250, 275 and 300 °C for a CO_2/H_2 mixture of 1/3 at a total pressure of 75 bar. *simulated with ASPEN PLUS (for details see Table S1 in the Supporting Information).

T/°C	$X_{\text{CO}_2}/\%$	$S_{\text{MeOH}}/\%$	$p(\text{H}_2\text{O})/\text{bar}^*$
200	0.04 ± 0.00	100 ± 0	0.007
250	0.52 ± 0.00	100 ± 0	0.093
275	0.84 ± 0.06	82 ± 1	0.150
300	3.0 ± 0.02	76 ± 1	0.535

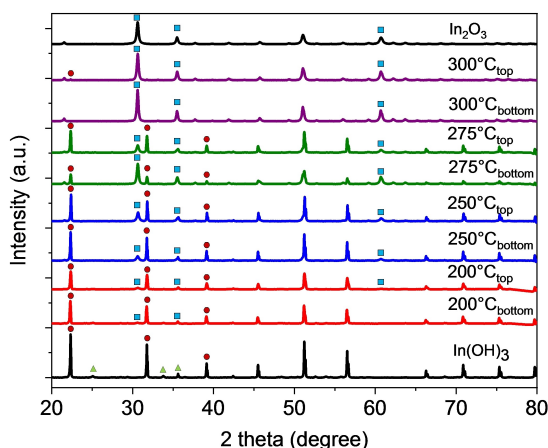


Figure 8. XRD data for the second experimental setup. $\text{In}(\text{OH})_3$ (before reaction) and for 200 °C (red), 250 °C (blue), 275 °C (green), 300 °C (purple) (after reaction) and In_2O_3 (reference), with diffraction patterns for In_2O_3 (■), $\text{In}(\text{OH})_3$ (●) and InOOH (▲).

	low-conversion zone, top/%	high-conversion zone, bottom/%
Pure	95.68	95.68
200 °C	82.11	89.91
250 °C	55.77	69.41
275 °C	62.06	22.65
300 °C	1.91	0.00

the first experimental setup (Table 3). The measured RWGS conversion was negligible, i.e., water was only formed by methanol synthesis ($p(\text{H}_2\text{O})=0.093$ bar). The XRD patterns in Figure 8 show more distinct peaks assigned to In_2O_3 in comparison to 200 °C. The peak intensity ratio between In_2O_3 and $\text{In}(\text{OH})_3$ is smaller in the high-conversion segment, consistent with the TGA results (Table 4, Figure 9). Herein, the bottom

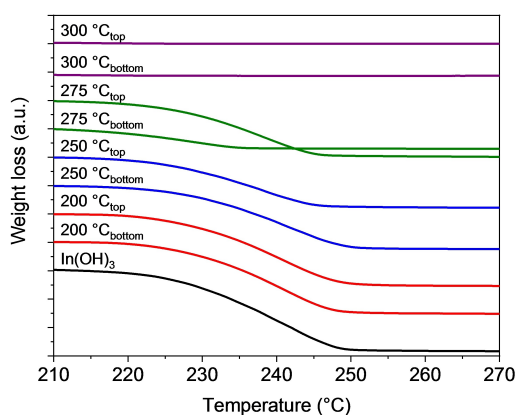


Figure 9. TGA data for second experimental setup. $\text{In}(\text{OH})_3$ (before reaction, black) and for 200 °C (red), 250 °C (blue), 275 °C (green), 300 °C (purple) (after reaction, top).

segment still shows a higher $\text{In}(\text{OH})_3$ amount (69.41 %) compared to the top segment (55.77 %), resulting from water release by phase transition of $\text{In}(\text{OH})_3$ to In_2O_3 . This is due to the formation of water in the segment above, which inhibits the release of water by phase transformation of $\text{In}(\text{OH})_3$. This is in good agreement with the prediction for this temperature and conversion from theoretical modeling.

For 275 °C the CO_2 conversion reached 0.84 % and the MeOH selectivity decreased to 82 % due to RWGS. Water formation increased ($p(\text{H}_2\text{O})=0.15$ bar) because of methanol synthesis and RWGS. In both segments the XRD patterns indicate a mixture of $\text{In}(\text{OH})_3$ and In_2O_3 . The peak intensity ratio between In_2O_3 and $\text{In}(\text{OH})_3$ is higher in the bottom segment (Figure 8), i.e., at high conversion. This is consistent with the TGA results, where the top and bottom segments show an $\text{In}(\text{OH})_3$ amount of 62.06 % and 22.65 %, respectively. For 275 °C, we detect substantially more $\text{In}(\text{OH})_3$ in the low-conversion segment, indicating that the trend has reversed compared to 200 °C and 250 °C (see Figure 9, green curve). This surprising finding can be explained on the basis of our computational model. The stability of In_2O_3 generally increases with increasing temperature due to the dehydration reaction, which is now exergonic over the whole accessible conversion range. Dehydration still shows the same dependence on the conversion as it did at lower temperature, i.e. the driving force decreases with increasing conversion. However, the phase transition from $\text{In}(\text{OH})_3$ to In_2O_3 is controlled not only by the dehydration, but also by the reverse reaction, i.e., hydration due to the formation of methanol and RWGS. The curves for the MeOH formation and RWGS indicate exergonic reaction at low conversion and endergonic reaction at high conversion, showing that the dehydration of $\text{In}(\text{OH})_3$ becomes irreversible at high conversion beyond a certain temperature threshold. We note that the experimentally measured conversion levels are below the intersection of the MeOH/RWGS curve at 275 °C. This is due to the significant uncertainty regarding the thermodynamic data of $\text{In}(\text{OH})_3$ and In_2O_3 , which gives rise to inaccurate temperature dependence of Gibbs free energies of reaction. However, the principal trends, i.e., that $\text{In}(\text{OH})_3$ is stable at low temperature and high conversion, while In_2O_3 is stable at high temperature and high conversion, and reversible phase transition is possible at both high and low temperature at low conversion, is unaffected by these inaccuracies.

For 300 °C, the CO_2 conversion further increased to 3 % (Table 3), which is in between the values of the top and middle configuration of the first experimental setup for $\text{In}(\text{OH})_3$ (Table S1). The separation in two segments inhibited the RWGS reaction due to less heating of the bed and shorter residence time in each bed. The observed RWGS selectivity reached 24 %, which matched with the studies in Figure 3 c). From the XRD data, we infer that $\text{In}(\text{OH})_3$ undergoes a complete phase transition to In_2O_3 in the high-conversion section (bottom), while some $\text{In}(\text{OH})_3$ remains in the low-conversion section (top).

The TGA data also showed no mass loss, indicating no $\text{In}(\text{OH})_3$ present in the bottom section, and only a small amount of $\text{In}(\text{OH})_3$ (1.91 %) in the top section, and therefore confirmed the trend for the stability of In_2O_3 (Table 4, Figure 9). From the

computational modeling, we expect that the conversion to In_2O_3 is irreversible at high conversions, while reversible transition is expected at low conversion, indicating a good agreement between theory and experiment.

Phase transition during hydrogen drop out

Finally, the model was employed to investigate how the catalyst will behave when the hydrogen content in the feed drops due to the instability of intermittent hydrogen sources. For a H_2 -deficient $p(\text{H}_2)/p(\text{CO}_2)$ ratio of 1/1, the free energy curves for different temperatures are shown in Figure 10.

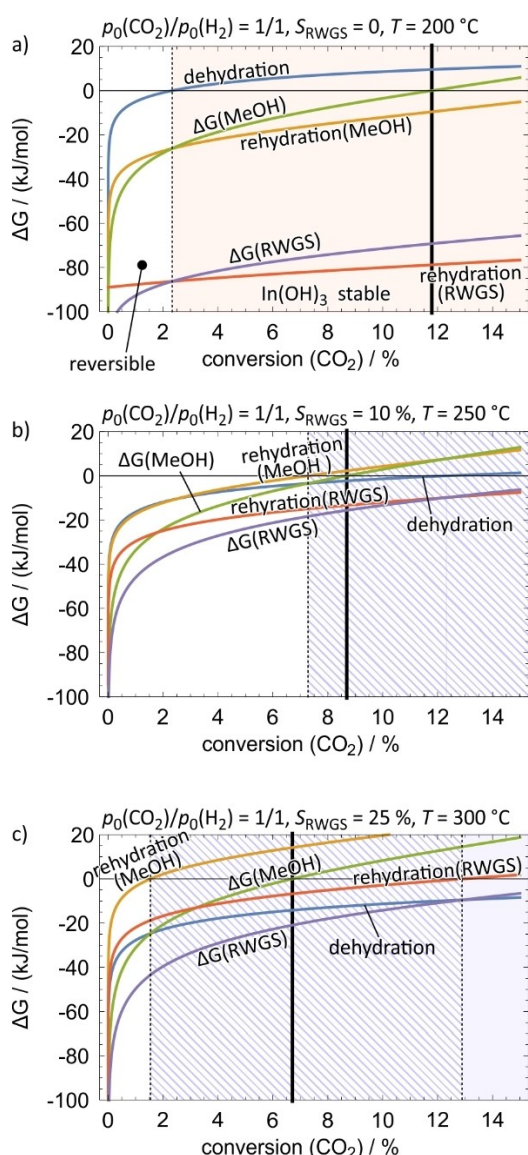


Figure 10. ΔG curves for variable $p(\text{H}_2)$ -deficient operation at $p(\text{H}_2)/p(\text{CO}_2) = 1/1$. a) 200°C , b) 250°C , c) 300°C at a total pressure of 37.5 bar. Black line: equilibrium conversion, blue curve: $\Delta_r G$ for dehydration reaction, orange curve: $\Delta_r G$ for rehydration through methanol formation, green curve: overall $\Delta_r G$ for methanol formation, red curve: $\Delta_r G$ for rehydration through RWGS. purple curve: overall $\Delta_r G$ for RWGS.

The first noticeable consequence of the reduced hydrogen content in the feed is a decrease of the equilibrium conversion to 11.7%, 8.5%, and 6.7% at 200°C , 250°C , and 300°C , respectively. This will result in a reduced reaction rate and may lead to a temperature drop in the reactor. At 200°C (Figure 10a), the reversible zone (white) still goes up to 2.3% conversion, indicating irreversible $\text{In}(\text{OH})_3$ formation at higher conversion. However, due to the reduced equilibrium conversion and reduced reaction rate under H_2 deficit, the white range now spans over a larger fraction of the catalyst bed, which would enhance the stability of In_2O_3 compared to a stoichiometric reactant ratio. At 250°C (Figure 10b), irreversible $\text{In}(\text{OH})_3$ formation does not occur because dehydration is exergonic below equilibrium conversion. Rehydration via methanol formation and RWGS is exergonic up to 7.3% conversion, leading to reversible $\text{In}(\text{OH})_3$ formation at low conversion. Above 7.3%, only the RWGS enables rehydration, indicating that In_2O_3 will be favored at higher conversion for H_2 deficit. The reversible formation of $\text{In}(\text{OH})_3$ through RWGS could be suppressed by co-feeding CO during hydrogen dropout. This would move the red curve representing $\text{In}(\text{OH})_3$ formation via RWGS up in Gibbs free energy, moving the region where In_2O_3 is fully stable to lower conversion. At 300°C (Figure 10c), the result looks quite similar, with the reversible zone stretching from 1.4% to beyond equilibrium conversion. In_2O_3 is fully stable only for conversions beyond the equilibrium line, what is irrelevant in practice. In summary, our model calculations for hydrogen-deficit operation suggest that stability is generally enhanced compared to a stoichiometric feed composition, both at high and low temperature.

The results give us practical guidance about reactor operation during hydrogen dropout. First of all, a drop of temperature below 250°C should be prevented, as lower temperature generally favors $\text{In}(\text{OH})_3$ formation. Due to the reduced heat of reaction at decreased reaction rates, stronger heating of the reactor may be required to retain the desired temperature and suppress $\text{In}(\text{OH})_3$ formation. At elevated temperature, $\text{In}(\text{OH})_3$ can be formed reversibly through RWGS, and this mode dominates over the largest fraction of the catalyst bed, possibly contributing to lower activity in the middle/high conversion zone of the reactor. If such degradation is observed in practice, co-feeding small amounts of CO (1%) could be considered to protect the catalyst from $\text{In}(\text{OH})_3$ formation. Naturally, reduction to In^0 must also be taken into account in these considerations, as this is another possible mode of degradation. Increased In^0 formation is, however, not expected, because the reactant feed at $p(\text{CO}_2)/p(\text{H}_2) = 1$ with e.g. 1% CO is still less reducing than the regular stoichiometric feed at $p(\text{CO}_2)/p(\text{H}_2) = 3$ (see Figure S4).

Conclusions

Employing a combination of thermodynamic considerations and dedicated stability experiments, we have shown that the phase transformation of In_2O_3 -based catalysts by conversion into $\text{In}(\text{OH})_3$ can be predicted by considering the reversibility of

dehydration and rehydration reactions. The thermodynamics of these reactions depend sensitively on the reaction conditions, most notably, on the temperature and conversion, due to the formation of H₂O, which suppresses the dehydration reaction at lower temperatures. The selectivities toward RWGS and methanol formation have only a minor influence on the phase transition because both reactions form equal amounts of H₂O per turnover. However, the relationship between In(OH)₃ formation and conversion is not straightforward; at lower temperature, In(OH)₃ formation is favored at higher conversion, while at higher temperature, lower conversion favors In(OH)₃ formation. This peculiar phase transition behavior was confirmed by dedicated model experiments, where the catalyst bed was split into a high-conversion and low-conversion section, and the two sections were characterized separately post-reaction. This approach allows to connect structural changes with the local gas atmosphere the catalyst is exposed to. These experiments confirm the aforementioned trend. Hereby, the inversion occurs between 250 °C and 275 °C, while the computational model predicts it at 285 °C. This small deviation can be explained by the uncertainty associated with the experiment-based thermodynamic data underlying our calculation. The basic trends, however, are not sensitive to these uncertainties. In addition to a change of the In(OH)₃ fraction along the catalyst bed, the catalyst is subject to reversible phase transitions at low conversion, which may contribute to fast catalyst particle sintering or reshaping.

We finally employed our model to examine how a change of p(CO₂)/p(H₂) ratio possibly influences catalyst degradation. Our results indicate that In(OH)₃ formation is not generally promoted by hydrogen dropout. Quite in contrast, at low temperature In₂O₃ is expected to be more stable due to lower water content in the gas feed. At higher temperatures, only RWGS is thermodynamically able to contribute to catalyst hydration, and even this could be suppressed by co-feeding CO during hydrogen drop out. The main risk for catalyst stability during hydrogen drop out stems from a temperature reduction due to reduced heat of reaction. This is important for the reactor design of methanol synthesis, because large scale fixed beds may have cold spots leading to locally increased In(OH)₃ formation.

Deactivation of heterogeneous catalysts in technical processes depends sensitively on the reaction conditions and local conversion levels. The methodology described here provides an intuitive access to understand the influence of reaction conditions on catalyst deactivation involving phase transitions or stoichiometry changes. This approach offers practical guidance on optimizing reactor operation to prevent catalyst degradation.

Experimental Section

Theoretical modeling

The Gibbs free energy change $\Delta_r G$ for each reaction is computed explicitly as a function of the reaction conditions:

$$\begin{aligned} \Delta_r G(T, p_{0,(\text{CO}_2, \text{H}_2, \dots)}, X, S_{\text{MeOH}}) \\ = \sum_i \nu_i \cdot \Delta_f G_i(T, p_{0,(\text{CO}_2, \text{H}_2, \dots)}, X, S_{\text{MeOH}}) \end{aligned} \quad (7)$$

Here, X and S_{MeOH} represent the CO₂ conversion and selectivity toward CH₃OH, respectively. T represents the temperature and p_{0, CO_2} and p_{0, H_2} represent the initial partial pressures of CO₂ and H₂. We assume that no product is present initially, with the exception of H₂O, which is present as an impurity with a concentration of 5 ppm, which is a typical impurity level for laboratory gas. Finally, ν_i and $\Delta_f G_i$ stand for the stoichiometric coefficient and Gibbs free energy of formation of species i .

The Gibbs free energy of formation is computed via:

$$\begin{aligned} \Delta_f G_i(T, p_{0,(\text{CO}_2, \text{H}_2, \dots)}, X, S_{\text{MeOH}}) \\ = \Delta_f H_i^0 - T \cdot \Delta_f S_i^0 + R \cdot T \cdot \log(a_i). \end{aligned} \quad (8)$$

The standard enthalpies and entropies of formation, $\Delta_f H_i^0$ and $\Delta_f S_i^0$ are taken from experimental data as given in Table 5. a_i represents the activity of species i , which is approximated as $a_i = p_i/p^0$ for the gas phase species. The activities of pure solid phases are defined as 1. R and p^0 are the general gas constant and standard pressure (10⁵ Pa). Inserting Eq. 7 into Eq. 8 results in Eq. 9:

$$\begin{aligned} \Delta_r G_i(T, p_{0,(\text{CO}_2, \text{H}_2, \dots)}, X, S_{\text{MeOH}}) \\ = \Delta_r G^0(T) + R \cdot T \sum_i \nu_i \ln(a_i). \end{aligned} \quad (9)$$

The thermodynamic data for the reactant molecules in the gas phase, In₂O₃ and In(OH)₃ are taken from the NIST database,^[22] the Springer Materials data collection,^[23] and primary literature,^[24] respectively (Table 5). We note that there is some uncertainty regarding the thermodynamic data of In(OH)₃ because it is not a well-studied material, and its thermodynamic data has to our knowledge not been assessed in the form of curated data collection. Because experimental measurements of the standard entropy of In(OH)₃ are not available in the literature to the best of our knowledge, we estimated it from the onset of the decomposition temperature of In(OH)₃ obtained from our TGA experiments on fresh In(OH)₃ (220 °C). Errors in the enthalpies of formation and standard entropies will mostly affect the temperature where transition from In(OH)₃ to In₂O₃ takes place, but not the trends, i.e., how a change of temperature, conversion or CO/H₂ ratio will affect the stability.

Table 5. Thermodynamic data employed in the model.

	$\Delta_f H^0 / (\text{kJ mol}^{-1})$	$S^0 / (\text{J K}^{-1} \text{mol}^{-1})$	Reference
CO ₂	−393.5	213.8	[22]
H ₂	0	130.7	[22]
CH ₃ OH(g)	−201.3	239.9	[22]
H ₂ O(g)	−241.8	188.8	[22]
CO	−110.5	197.7	[22]
In(OH) ₃	−927	127.1 ^a	[23]
In ₂ O ₃	−923	101.8	[24]

^a Estimate from the onset of In(OH)₃ decomposition in our TGA experiment (220 °C).

Catalytic experiments

Catalytic CO₂ hydrogenation was conducted in a high pressure continuous flow fixed-bed reactor (Figure S1). The reactor with an inner diameter of 20 mm was made of stainless steel (1.4571). A gas mixture of 25% CO₂ (4.5 grade) and 75% H₂ (5.0 grade) from *Westfalen*, as well as N₂ (5.0 grade) from *Air Liquide* were used. The reactant gas mixture with a CO₂/H₂ stoichiometric ratio of 1/3 was introduced by mass-flow controllers (*Bronkhorst Prestige FG-201 CV*) and flows downwards through the reactor tube. The reaction pressure was adjusted using a back-pressure regulator (*Dutch Regulators*). The temperature was controlled with a surrounding heating mantle and a thermocouple. Gas lines at the inlet and outlet of the reactor were heated to 180 °C in order to preheat the reaction gas and to prevent condensation of methanol and water in the outlet. Gas-flows and temperatures were automatically controlled by a LabVIEW (*National Instruments TM*) interface. The outlet gas composition was sampled every 30 min and analyzed using an online gas chromatograph (*Bruker 450-GC*), set up with four columns (Restek Q-Bond, Restek U-Bond, Bruker Swax, Bruker Molsieve 5 Å), a methanizer (for CO₂ and CO quantification), two flame ionization detectors (FIDs) and one thermal conductivity detector (TCD).

For the catalyst test experiments, Indium(III) oxide (99.9% metals basis) from *Alfa Aesar* and Indium(III) hydroxide (99.8% metals basis) from *Thermo Scientific* were used. For the first experimental setup, 5.0 g of In₂O₃ or In(OH)₃ was mixed homogeneously with quartz spheres and loaded into the reactor. The segment was positioned in top, middle or bottom position in relation to the thermocouple and held in place by a bed of quartz wool (see scheme in Figure 4). Prior to reaction, the dummy catalyst was pretreated at 200 °C under flowing N₂ (300 Nml min⁻¹) for 1 hour. Afterwards, the reactor was heated to the desired reaction temperature (200 °C, 250 °C, 300 °C) one after another in a ramp and each temperature was held for 3 hours. For the second experimental setup, 5.0 g of In(OH)₃ was mixed homogeneously with quartz spheres and split in two identical segments (see scheme in Figure 7). The segments were fixed and held in place by a bed of quartz wool. For each experimental setup, prior to reaction, the dummy catalyst was pretreated to 200 °C under flowing N₂ (300 Nml min⁻¹) for 1 hour. Then the reactor was heated to the reaction temperature (200 °C, 250 °C, 300 °C).

For every experimental setup, a CO₂/H₂ flow of 1200 Nml min⁻¹ was passed through the reactor to start CO₂-hydrogenation. The product gas analysis was performed by GC every 30 min under steady state reaction conditions. After the reaction, the reactor was cooled down (3 K min⁻¹) under a continuous flow of nitrogen (1000 Nml min⁻¹) and the catalyst was removed and stored under Argon (4.6 grade, *Heide Gas*). The detailed calculation of \dot{n} and the partial pressure of water ($p_{\text{H}_2\text{O}}$) are shown in the Supporting Information. CO₂ conversion $X(\text{CO}_2)$, yield $Y(\text{MeOH})$ and selectivity $S(\text{MeOH})$ of methanol were calculated applying Eqs. 10–12.

$$X_{\text{CO}_2} = \frac{\dot{n}_{\text{CO}_2, \text{in}} - \dot{n}_{\text{CO}_2, \text{out}}}{\dot{n}_{\text{CO}_2, \text{in}}} \cdot 100 \% \quad (10)$$

$$Y_{\text{MeOH}} = \frac{\dot{n}_{\text{MeOH}}}{\dot{n}_{\text{CO}_2, \text{in}}} \cdot 100 \% \quad (11)$$

$$S_{\text{MeOH}} = \frac{Y_{\text{MeOH}}}{X_{\text{CO}_2}} \quad (12)$$

Catalyst characterization

Thermogravimetric analysis was carried out using a *SETSYS Evolution TGA-DTA from Setaram Instrumentation*. The samples (~30 mg) were heated up from ambient temperature to 110 °C under nitrogen and the temperature was held for one hour in order to remove all water residues. Afterwards, the samples were heated up to 300 °C with 2 K/min and held for three hours to determine the mass loss, which was attributed to the formation of water by conversion of In(OH)₃ to In₂O₃. X-Ray diffraction was carried out using a *Panalytical MPD X'Pert Pro*, with a Cu-K_α-source. The measuring range was 10–80°, with a step size of 0.013° and a counting time of 73 seconds.

Acknowledgements

We thank the Central Analytics Department of the University of Hamburg (UHH) for carrying out the XRD measurements. Open Access funding enabled and organized by Projekt DEAL.

Conflict of Interests

The authors declare no conflict of interest.

Data Availability Statement

Research data are not shared.

Keywords: catalyst degradation · CO₂ hydrogenation · dummy catalytic cycle · indium · methanol synthesis

- [1] a) N. Armaroli, V. Balzani, *Angew. Chem. Int. Ed.* **2007**, *46*, 52–66; b) D. Gielen, F. Boshell, D. Saygin, *Nat. Mater.* **2016**, *15*, 117–120.
- [2] a) Z. Zhang, *Renewable and Sustainable Energy Reviews* **2020**, *109799*; b) K. M. K. Yu, I. Curcic, J. Gabriel, S. C. E. Tsang, *ChemSusChem* **2008**, *1*, 893–899; c) M. Aresta, A. Dibenedetto, A. Angelini, *Chem. Rev.* **2014**, *114*, 1709–1742.
- [3] a) P. Gao, *Nat. Chem.* **2017**, *9*, 1019–1024; b) A. Gulzar, A. Gulzar, M. B. Ansari, F. He, S. Gai, P. Yang, *Chemical Engineering Journal Advances* **2020**, *3*, 100013.
- [4] a) D. S. Marlin, E. Sarron, Ó. Sigurbjörnsson, *Front. Chem.* **2018**, *6*, 446; b) V. Dieterich, A. Buttler, A. Hanel, H. Spliethoff, S. Fendt, *Energy Environ. Sci.* **2020**, *13*, 3207–3252; c) P. Gao, L. Zhang, S. Li, Z. Zhou, Y. Sun, *ACS Cent. Sci.* **2020**, *6*, 1657–1670.
- [5] a) V. D. Dasireddy, B. Likozar, *Renewable Energy* **2019**, *140*, 452–460; b) R.-P. Ye, *Nat. Commun.* **2019**, *10*, 5698.
- [6] a) M. Bowker, *ChemCatChem* **2019**, *11*, 4238–4246; b) J. Zhong, X. Yang, Z. Wu, B. Liang, Y. Huang, T. Zhang, *Chem. Soc. Rev.* **2020**, *49*, 1385–1413.
- [7] a) W.-J. Shen, K.-W. Jun, H.-S. Choi, K.-W. Lee, *Korean J. Chem. Eng.* **2000**, *17*, 210–216; b) S. Kanuri, S. Roy, C. Chakraborty, S. P. Datta, S. A. Singh, S. Dinda, *Int'l J of Energy Research* **2022**, *46*, 5503–5522; c) K. Stangeland, H. Li, Z. Yu, *Ind. Eng. Chem. Res.* **2018**, *57*, 4081–4094.
- [8] S. Ghosh, J. Sebastian, L. Olsson, D. Creaser, *Chem. Eng. J.* **2021**, *416*, 129120.
- [9] a) O. Martin, A. J. Martín, C. Mondelli, S. Mitchell, T. F. Segawa, R. Hauert, C. Drouilly, D. Curulla-Ferré, J. Pérez-Ramírez, *Angew. Chem. Int. Ed.* **2016**, *55*, 6261–6265; b) P. Schühle, S. Reichenberger, G. Marzun, J. Albert, *Chem. Ing. Tech.* **2021**, *93*, 585–593; c) K. Lau, P. Schühle, S.-X. Liang, F. de Kock, J. Albert, S. Reichenberger, *ACS Appl. Eng. Mater.* **2021**, *4*, 9206–9215.
- [10] P. Schühle, M. Schmidt, L. Schill, A. Riisager, P. Wasserscheid, J. Albert, *Catal. Sci. Technol.* **2020**, *10*, 7309–7322.

- [11] Z. Lu, J. Wang, K. Sun, S. Xiong, Z. Zhang, C. Liu, *Green Chemical Engineering* **2022**, *3*, 165–170.
- [12] M. S. Frei, M. Capdevila-Cortada, R. García-Muelas, C. Mondelli, N. López, J. A. Stewart, D. Curulla Ferré, J. Pérez-Ramírez, *J. Catal.* **2018**, *361*, 313–321.
- [13] a) M. Dou, M. Zhang, Y. Chen, Y. Yu, *Catal. Lett.* **2018**, *148*, 3723–3731; b) A. Cao, Z. Wang, H. Li, J. K. Nørskov, *Catalysis Letters* **2021**, *11*, 1780–1786.
- [14] J. Ye, C. Liu, D. Mei, Q. Ge, *ACS Catal.* **2013**, *3*, 1296–1306.
- [15] S. Dang, B. Qin, Y. Yang, H. Wang, J. Cai, Y. Han, S. Li, P. Gao, Y. Sun, *Sci. Adv.* **2020**, *6*, eaaz2060.
- [16] T. Bielz, H. Lorenz, W. Jochum, R. Kaindl, F. Klauser, B. Klötzer, S. Penner, *J. Phys. Chem. C* **2010**, *114*, 9022–9029.
- [17] A. Tsoukalou, P. M. Abdala, D. Stoian, X. Huang, M.-G. Willinger, A. Fedorov, C. R. Müller, *J. Am. Chem. Soc.* **2019**, *141*, 13497–13505.
- [18] F. Hess, *ACS Catal.* **2022**, *12*, 1, 497–511.
- [19] C. Li, F. Hess, I. Djerdj, G. Chai, Y. Sun, Y. Guo, B. M. Smarsly, H. Over, *J. Catal.* **2018**, *357*, 257–262.
- [20] C. Li, Y. Sun, F. Hess, I. Djerdj, J. Sann, P. Voepel, P. Cop, Y. Guo, B. M. Smarsly, H. Over, *Appl. Catal. B* **2018**, *239*, 628–635.
- [21] Y. Sun, F. Hess, I. Djerdj, Z. Wang, T. Weber, Y. Guo, B. M. Smarsly, H. Over, *ChemCatChem* **2020**, *12* (21), 5511–5522.
- [22] P. J. Linstrom, W. G. Mallard, Eds., NIST Chemistry WebBook, NIST Standard Reference Database Number 69, National Institute of Standards and Technology, Gaithersburg MD, 20899, <https://doi.org/10.18434/T4D303>.
- [23] E. H. P. Cordfunke, R. J. M. Konings, W. Ouweltjes, *J. Chem. Thermodynamics* **1995** 431–433.
- [24] Landolt-Börnstein, Springer Materials, New Series IV/19 A4, **2001**, DOI: 10.1007/b71435.

Manuscript received: August 3, 2023
Revised manuscript received: August 25, 2023
Accepted manuscript online: August 25, 2023
Version of record online: ■■■

6.2 Investigations of supported In_2O_3 catalysts in a fixed bed reactor

P2

Indium-based Catalysts for CO_2 Hydrogenation to Methanol: Key Aspects for Catalytic Performance

Anne Wesner, **Philipp Kampe**, Nick Herrmann, Sebastian Eller, Charlotte Ruhmlieb, and Jakob Albert

A. Wesner, **P. Kampe**, N. Herrmann, S. Eller, C. Ruhmlieb, J. Albert. “Indium-based Catalysts for CO_2 Hydrogenation to Methanol: Key Aspects for Catalytic Performance”, *ChemCatChem*, **2023**, 15, e202301125, DOI: doi.org/10.1002/cctc.202301125

Published under a Creative Commons license.

The stability and catalytic activity of In_2O_3 is introduced in Chapter 6.1. To increase the catalytic activity of In_2O_3 , it is supported on ZrO_2 (refer to Chapter 3.2.2). The following study [19] combines different ZrO_2 -supports, as well as different preparation methods for $\text{In}_2\text{O}_3/\text{ZrO}_2$ catalysts using the fixed bed reactor system (integral operation) introduced before. The most active combination was doped with various metal oxides (CeO_2 , MgO , CuO or NiO) to increase the performance of CO_2 hydrogenation to methanol. $\text{NiO-In}_2\text{O}_3/\text{ZrO}_2$ enhanced the catalytic performance compared to pure $\text{In}_2\text{O}_3/\text{ZrO}_2$ from $4.25 \text{ g}_{\text{MeOH}} \text{ g}_{\text{active metal}}^{-1} \text{ h}^{-1}$ to $4.42 \text{ g}_{\text{MeOH}} \text{ g}_{\text{active metal}}^{-1} \text{ h}^{-1}$ at $300 \text{ }^\circ\text{C}$ and 75 bar . No methane formation or catalyst deactivation was observed during 100 h TOS. Intense catalyst characterization ICP-OES, XRD, XPS, N_2 -physisorption, CO_2 -TPD, H_2 -TPR and SEM-EDX provide key aspects for catalytic performance. These aspects include high surface area, preparation method and high CO_2 as well as H_2 adsorption capacities. Figure 6.3 illustrates the metal distribution of the most active $\text{NiO-In}_2\text{O}_3/\text{ZrO}_2$ catalyst. The corresponding Supporting Information of the following article can be found in the Appendix Chapter 9.4 and details about the fixed bed reactor system in Chapter 9.1.3.

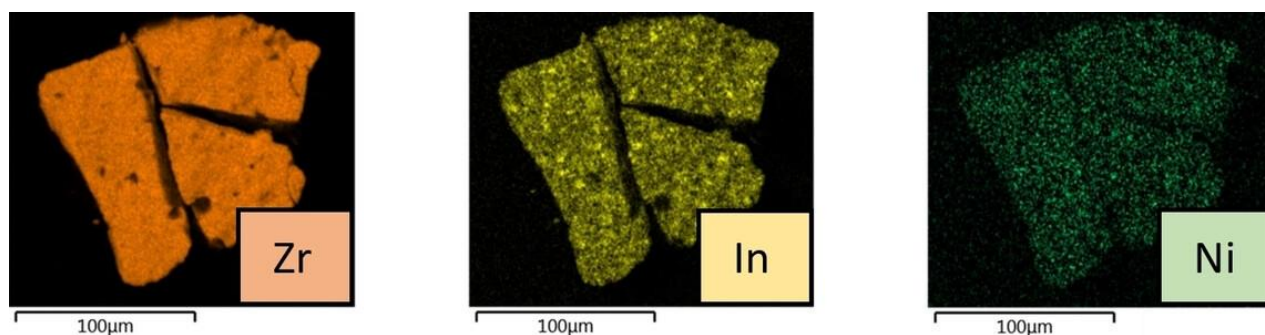


Figure 6.3. SEM-EDX elemental mapping of the most active $\text{NiO-In}_2\text{O}_3/\text{ZrO}_2$ catalyst for CO_2 hydrogenation to methanol [19].

Indium-based Catalysts for CO₂ Hydrogenation to Methanol: Key Aspects for Catalytic Performance

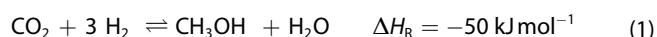
Anne Wesner^{+, [a]}, Philipp Kampe^{+, [a]}, Nick Herrmann,^[a] Sebastian Eller,^[a] Charlotte Ruhmlieb,^[b] and Jakob Albert^{*[a]}

CO₂ hydrogenation utilizing sustainably produced hydrogen and CO₂ derived from industrial exhaust gas represents a pivotal technology for chemical energy storage and climate change mitigation. This work aims to identify the best combination of catalyst support, synthesis method and promoter for In₂O₃/ZrO₂ catalysts in a typical fixed-bed configuration. Intense characterization using ICP-OES, XRD, XPS, N₂-physisorption, CO₂-TPD, H₂-TPR and SEM-EDX provide molecular insights into the different effects caused by various synthesis methods

and doping elements. Doping the most promising In₂O₃/ZrO₂ (M-SG) catalyst with 0.7 wt.% NiO by wetness impregnation using an ethanol/water mixture as a solvent, an increased methanol production rate of 0.497 g_{MeOH} · g_{cat}⁻¹ · h⁻¹ could already be achieved at 250 °C. Hereby, the low amount of highly dispersed NiO promotes H₂ activation via hydrogen spillover, leading to sustained catalytic activity for 100 hours of time-on-stream.

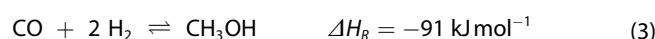
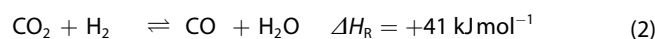
Introduction

The worldwide demand for energy is growing continuously, fossil resources are depleting, and atmospheric CO₂ levels are on the rise.^[1] As a result, there is a growing significance placed on the generation of energy from renewable sources such as solar, wind and biomass, as well as the capture, storage and use of CO₂ as a valuable raw material.^[2,3,4] In this context, methanol (MeOH) produced by electrolysis hydrogen and captured CO₂ has emerged as an efficient approach [Equation (1)].



Additionally, methanol forms the basis for various bulk chemicals, such as formaldehyde and olefins.^[4] However, the endothermic reverse water gas shift (RWGS) reaction [Equation (2)] considerably reduces the methanol selectivity under typical reaction conditions (200–300 °C, 50–100 bar).^[5] More-

over, CO as a by-product can also undergo hydrogenation to form methanol [Equation (3)].



For commercial applications, copper-based catalysts such as Cu/ZnO/Al₂O₃ are typically used for methanol synthesis from mixed syngas (CO/CO₂/H₂). Cu as an active metal facilitates hydrogen spillover, whereby active H atoms are generated on the metal surface through H₂-dissociation on the Cu-surface and subsequently migrate to the support material.^[6,7] In recent mechanistic studies involving CuZnO-containing catalysts, selectivity loss has been observed not only through the RWGS reaction but also through an additional pathway involving CO formation via methanol decomposition.^[8] However, this catalyst exhibits limited activity for CO₂ hydrogenation due to deactivation caused by the by-product H₂O.^[9] Moreover, temperatures exceeding 280 °C lead to thermal sintering of Cu, that impairs catalytic performance even further.^[10]

Recently, In₂O₃/ZrO₂ catalysts have demonstrated to be highly efficient catalysts for hydrogenation of CO₂ to methanol in several studies.^[11–14] Under typical reaction conditions of T=200–275 °C and p=35–75 bar, In₂O₃ generates oxygen vacancies that activate CO₂ for the formation of formate (HCOO⁻).^[15] The In₃O₅ ensemble adjacent to the vacancy stabilizes the heterolytic splitting of H₂. As a result, the formation of CO through RWGS is inhibited, leading to an increased methanol selectivity.^[14,16] The combination of In₂O₃ and ZrO₂ as a support achieved a synergistic effect at the interface between oxygen vacancy defects of the oxides.^[17] Adjusting the right particle size and morphology control are key factors for preparing Indium-based catalysts with high activity.^[18] The ZrO₂ carrier plays a crucial role in preventing the sintering of In₂O₃, thus ensuring long-time-stability of the

[a] A. Wesner,⁺ P. Kampe,⁺ N. Herrmann, S. Eller, Prof. Dr. J. Albert
 Institute of Technical and Macromolecular Chemistry
 Universität Hamburg
 Bundesstraße 45, 20146 Hamburg (Germany)
 E-mail: jakob.albert@uni-hamburg.de

[b] Dr. C. Ruhmlieb
 Institute of Physical Chemistry
 Universität Hamburg
 Grindelallee 117, 20146 Hamburg (Germany)

[†] These authors contributed equally to this work and therefore share first authorship.

Supporting information for this article is available on the WWW under <https://doi.org/10.1002/cctc.202301125>

© 2023 The Authors. ChemCatChem published by Wiley-VCH GmbH. This is an open access article under the terms of the Creative Commons Attribution Non-Commercial NoDerivs License, which permits use and distribution in any medium, provided the original work is properly cited, the use is non-commercial and no modifications or adaptations are made.

catalyst. According to proposed mechanisms, the oxygen vacancy filled after methanol desorption is regenerated through its hydrogenation by water formation.^[19] The composition of reducing and oxidizing components in the gas phase under common reaction conditions of CO₂ hydrogenation maintains the equilibrium between surface oxygen atoms and vacancies. This balanced configuration maintains the catalyst in an active state and hinders its deactivation.^[20] Moreover, phase-transitions caused by fluctuating conditions like hydrogen drop out caused by intermittent hydrogen sources like electrolysis may affect the catalytic performance of Indium-based catalysts.^[21]

The present study reveals the influence of different ZrO₂ carriers on In₂O₃/ZrO₂ catalysts, as well as the impact of different preparation methods in gas-phase CO₂ hydrogenation to methanol. Additionally, the impact of doping In₂O₃/ZrO₂ with various metal oxides (CeO₂, MgO, CuO, NiO) was investigated, as this has proven to increase the performance in slurry-phase CO₂ hydrogenation to methanol.^[22] Hereby, Ni and Cu might enhance H₂ dissociation and migration to the support surface, promoting oxygen vacancy formation pushing the system to higher methanol productivity.^[23,24] Another approach involved increasing the CO₂ adsorption capacity of In₂O₃/ZrO₂ by adding basic materials, such as Mg or Ce. On the one hand, Mg-based oxides are used as basic supports for Cu in CO₂ hydrogenation.^[25] CeO₂, on the other hand, serves as a catalyst for CO oxidation to CO₂ through generation of oxygen vacancies. These vacancies could also be active for CO₂ hydrogenation and enhance methanol selectivity.^[26]

Results and Discussion

Impact of different ZrO₂-supports on the catalytic performance of In₂O₃/ZrO₂-catalysts

ZrO₂ as a support material for In₂O₃ has shown to optimize oxygen vacancy formation being beneficial for CO₂ activation and effectively prevents sintering of In₂O₃, as proven by stability tests over 1000 h time-on-stream.^[12,14,27] The use of monoclinic ZrO₂ for supporting In₂O₃ allows epitaxial growth of In₂O₃, whereby the mismatching of the crystal lattices leads to formation of tensile forces. This, in turn, promotes the formation of an increased number of oxygen vacancies in In₂O₃, enhancing its catalytic properties. Additionally, vacancies in ZrO₂ being close to In₂O₃ may also interact and enforce methanol synthesis.^[12,14,25,28]

There are two established In₂O₃/ZrO₂ catalysts reported in literature, both utilizing monoclinic ZrO₂ as a support material.^[12,13] However, they exhibit distinct catalytic performance regarding methanol synthesis via CO₂ hydrogenation, despite containing the same amount of In. Therefore, in the following discussion, we will investigate the main characteristics of two different commercial monoclinic ZrO₂ supports for In₂O₃, referred to as Alfa Aesar (AA) and Saint Gobain (SG), and their influence on the resulting catalytic performance for CO₂ hydrogenation to methanol.

Synthesis procedures as described in the literature were utilized for the preparation of In₂O₃/ZrO₂-catalysts (see Supplementary methods). Throughout this study, In₂O₃/ZrO₂ catalysts used and prepared by Schühle et al.^[13] will be referred to as SAA, and In₂O₃/ZrO₂ catalysts used and prepared by Martin et al.^[12] as M-SG. Both catalysts were used for CO₂ hydrogenation to methanol at elevated reaction temperatures (250, 275 or 300 °C) and pressures (50 or 75 bar) in a high-pressure continuous-flow fixed-bed reactor setup (Figure S1). To put the In-based catalysts in perspective with the commercial Cu-based catalyst for methanol synthesis, we compared the methanol productivity at 250 °C for the same pressures (50 and 75 bar) at 250 °C. The commercial Cu/ZnO/Al₂O₃ catalyst shows a methanol productivity of $P_{\text{cat}} = 0.964 \text{ g}_{\text{MeOH}} \text{ g}_{\text{cat}}^{-1} \cdot \text{h}^{-1}$. (Figure S2).

Figure 1 summarizes the main catalytic results for In₂O₃/ZrO₂-catalysts at both pressure levels. In detail, In₂O₃/ZrO₂ (M-SG) shows both, higher P_{cat} and Y_{MeOH} independently of the applied reaction conditions (Table S1). A maximum methanol productivity of $0.470 \text{ g}_{\text{MeOH}} \cdot \text{g}_{\text{cat}}^{-1} \cdot \text{h}^{-1}$ for In₂O₃/ZrO₂ (M-SG) was achieved at 300 °C and 75 bar, whereby only $0.330 \text{ g}_{\text{MeOH}} \cdot \text{g}_{\text{cat}}^{-1} \cdot \text{h}^{-1}$ were achieved using In₂O₃/ZrO₂ (S-AA). Moreover, In₂O₃/ZrO₂ (M-SG) yielded a maximum Y_{MeOH} of 10.0% compared to In₂O₃/ZrO₂ (S-AA) with a Y_{MeOH} of only 6.8%. The equilibrium yield of methanol (12.9%, dotted line) was simulated for 300 °C and 75 bar using the property method Soave-Redlich-Kwong in ASPEN Plus. The experimental standard deviations of two different catalyst batches were determined by calculating the arithmetic means at the highest P_{cat} (Figure S3, Table S2).

Initial analysis of the ZrO₂ supports by ICP-OES (Table 1) confirmed high purity of both materials. XRD diffraction patterns confirmed a monoclinic crystal lattice for both ZrO₂ supports with characteristic-111 and 111 reflections at 28.18° and 31.47°, respectively, as well as smaller broad reflection for the 022 crystal lattices at 50.12° (Figure S6a). SEM analysis showed alike morphology for both supports (Figure S5a, b). Notably, ZrO₂ (SG) exhibited a significantly higher surface area than ZrO₂ (AA) with a BET-surface of 89 m²/g vs. 51 m²/g.

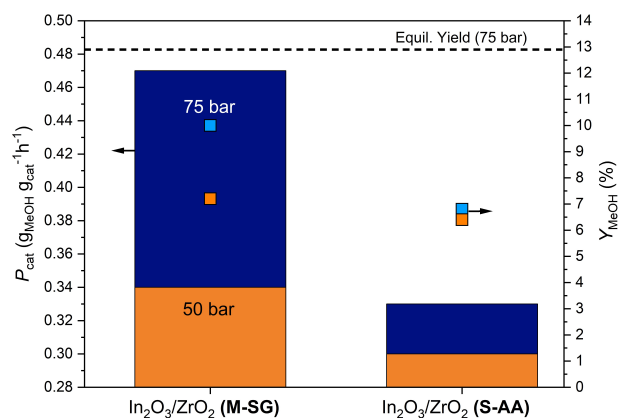


Figure 1. Evolution of productivity (left) and methanol yield (right) in dependency of total pressure $p = 50$ bar (orange) and $p = 75$ bar (blue) for different ZrO₂ supports (SG or AA). Simulated equilibrium yield at $T = 300$ °C and $p = 75$ bar. Reaction conditions: CO₂/H₂ = 1/3; GHSV = 8400 h⁻¹; TOS = 3 h; $T = 300$ °C; $h_{\text{bed}} = 5.1 \pm 0.1$ cm.

	In (wt. %) ^[a]	Zr (wt. %) ^[a]	S _{BET} (m ² /g) ^[b]	∅ pore radius (nm) ^[b]	pore volume (cm ³ /g) ^[b]	particle size (nm) ^[c]
ZrO ₂ (SG)	–	65.48	89.35	4.07	0.292	–
ZrO ₂ (AA)	–	66.49	51.27	5.69	0.238	–
In ₂ O ₃ /ZrO ₂ (M-SG)	11.08	56.28	75.96	3.39	0.214	11.84
In ₂ O ₃ /ZrO ₂ (S-AA)	11.11	56.28	44.97	5.67	0.174	16.91
In ₂ O ₃ /ZrO ₂ (S-SG)	9.82	56.52	75.36	3.70	0.222	11.77
In ₂ O ₃ /ZrO ₂ (M-AA)	10.91	60.33	49.14	5.71	0.203	16.91

[a] Determined by ICP-OES. [b] Measured by N₂-physorption. [c] Calculated using the Scherrer equation (Equation S1) based on the In₂O₃ (222) reflection in the XRD diffractograms (Figure S6a).

Furthermore, the average pore volume of ZrO₂ (SG) of 0.292 cm³/g was higher than for ZrO₂ (AA) with 0.238 cm³/g (Table 1). The average pore diameters for both ZrO₂ range in the mesoporous area between 4–6 nm.^[29,30] Both supports, however, showed only weak interactions with CO₂, as evident from the CO₂-TPD spectra (Figure 2a), that exhibit a desorption peak between 100–300 °C, that can be assigned to physisorbed CO₂.^[31,32] Desorption peaks assigned to chemisorbed CO₂ through thermally induced oxygen vacancies can be observed in a small amount.^[12,30] Nevertheless, ZrO₂ (AA) demonstrates slightly less interaction with CO₂ compared to ZrO₂ (SG) in the low temperature area (Figure 2a, Table S3). In H₂-TPR, negligible interactions with H₂ were observed for both support materials (Figure 2b, Table S4).

Elemental analysis confirmed the desired In loading of ~10 wt.% for both In₂O₃/ZrO₂ (M-SG) and In₂O₃/ZrO₂ (S-AA) catalysts (Table 1). Moreover, the incorporation of In₂O₃ in the monoclinic ZrO₂ structure was evident due to an additional pattern at 30.59° in XRD, assigned to 222 reflection of In₂O₃ (Figure S6a). SEM analysis revealed no significant change in morphology throughout the synthesis process (Figure S5)

SEM-EDX mapping further confirmed an overall homogeneous distribution of each element on the catalyst surface (Figure 3).

After impregnation, the surface area decreases equally by about 12% for both catalysts, along with a reduction of pore radius and volume (Table 1, Figure S6b). This observation indicates the agglomeration of In₂O₃ on the ZrO₂ surface as well as within the pores. Notably, the chemisorptive properties of the catalysts exhibited distinct changes compared to pure ZrO₂. As anticipated, the incorporation of In₂O₃ into the crystalline framework results in a shift of CO₂ desorption peaks to higher temperatures as well as an increased CO₂ desorption signal intensity, indicating an enhanced capacity to bind CO₂ (Figure 2a, Table S3). These results are in good agreement with literature.^[12,14,26,33] CO₂ adsorption of In₂O₃/ZrO₂ (M-SG) exhibited those of In₂O₃/ZrO₂ (S-AA) in both strength and capacity (Table S3). Between 250 °C and 350 °C the formation of an oxygen vacancy between two In atoms allows the bridging coordination of CO₂.^[12] The desorption peak in this range for In₂O₃/ZrO₂ (M-SG) shows a higher CO₂ uptake and therefore more surface In atoms are available leading to less bulk-In compared to In₂O₃/ZrO₂ (S-AA).

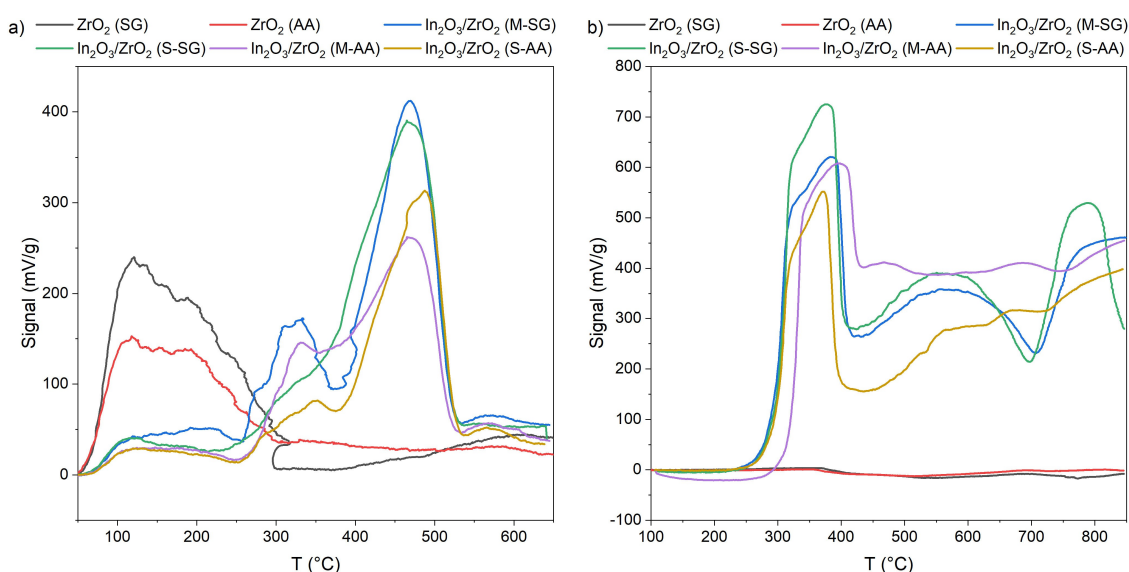


Figure 2. Chemisorptive analysis of different ZrO₂ supports (AA and SG) and In₂O₃/ZrO₂ catalysts (S-SG, S-AA and M-SG, M-AA): a) CO₂-TPD and b) H₂-TPR.

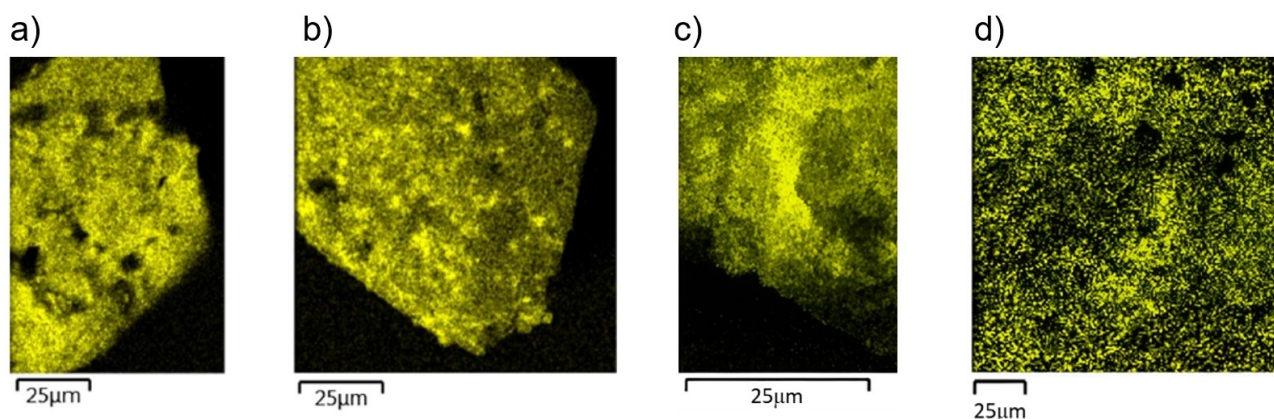


Figure 3. SEM-EDX mapping elemental analysis of In for a) $\text{In}_2\text{O}_3/\text{ZrO}_2$ (S-AA), b) $\text{In}_2\text{O}_3/\text{ZrO}_2$ (M-SG), c) $\text{In}_2\text{O}_3/\text{ZrO}_2$ (S-SG) and d) $\text{In}_2\text{O}_3/\text{ZrO}_2$ (M-AA).

Results of H_2 -TPR revealed a significant increase in the surface reducibility of $\text{In}_2\text{O}_3/\text{ZrO}_2$ catalysts compared to pure ZrO_2 . Furthermore, the reduction capacity of $\text{In}_2\text{O}_3/\text{ZrO}_2$ (M-SG) exhibits those of $\text{In}_2\text{O}_3/\text{ZrO}_2$ (S-AA) (Figure 2b). The TPR profile of $\text{In}_2\text{O}_3/\text{ZrO}_2$ (M-SG) showed two reduction peaks between around 100–420 °C and 420–470 °C, assigned to the reduction of surface species of In_2O_3 (100–420 °C)^[32] and reduction of bulk In_2O_3 (> 420 °C).^[34] Notably, $\text{In}_2\text{O}_3/\text{ZrO}_2$ (M-SG) exhibits higher H_2 adsorption capacity at lower temperatures, indicating and increased propensity for hydrogen dissociation during methanol synthesis (Table S4).^[35]

Impact of synthesis method on the catalytic performance of $\text{In}_2\text{O}_3/\text{ZrO}_2$ catalysts

Besides the different ZrO_2 supports (AA or SG), there is also a disparity in the synthesis method between $\text{In}_2\text{O}_3/\text{ZrO}_2$ (S-AA) and $\text{In}_2\text{O}_3/\text{ZrO}_2$ (M-SG). Martin (M) et al.^[12] utilize a solvent system containing ethanol and water (74/26 $\text{H}_2\text{O}/\text{EtOH}$ v/v), whereas Schühle et al.^[13] (S) employ pure water. Furthermore, (M) uses a substantially higher amount of solvent (47 $\text{mL}_{\text{solvent}}/\text{g}_{\text{ZrO}_2}$) in comparison to (S) with 20 $\text{mL}_{\text{solvent}}/\text{g}_{\text{ZrO}_2}$. Moreover, the synthesis procedure of (M) involves a significantly longer stirring time for synthesis of five hours comparing to (S) where the solvent is evaporated immediately after mixing the suspension without further stirring.

The aim of our study was to identify the determining key factors being responsible for the observed different catalytic activities of $\text{In}_2\text{O}_3/\text{ZrO}_2$ (S-AA) and $\text{In}_2\text{O}_3/\text{ZrO}_2$ (M-SG). Therefore, also hybrid catalysts were prepared by combining the original ZrO_2 -supports with the respective corresponding synthesis method. This resulted in $\text{In}_2\text{O}_3/\text{ZrO}_2$ (S-AA or S-SG) and $\text{In}_2\text{O}_3/\text{ZrO}_2$ (M-AA or M-SG). For $\text{In}_2\text{O}_3/\text{ZrO}_2$ (M-AA), the standard deviations of experimental procedure out of four experiments and two different batches were calculated (Figure S3 and Table S2).

A comparison of the CO_2 hydrogenation activity at 300 °C and 75 bar displays significant differences in the used ZrO_2 as well as synthesis method with regard both to productivity and

yield (Figure 4). Generally, catalysts prepared according to (M) showed higher P_{cat} (around 0.4402–0.470 $\text{g}_{\text{MeOH}} \cdot \text{g}_{\text{cat}}^{-1} \cdot \text{h}^{-1}$) than catalysts prepared according to (S) with only 0.320–0.399 $\text{g}_{\text{MeOH}} \cdot \text{g}_{\text{cat}}^{-1} \cdot \text{h}^{-1}$. Moreover, the ZrO_2 supports applied by (SG) gave better results than the one of (AA), related to the mass of catalyst.

Examining the productivity P_{surface} normalized to the surface area (Table 1) for all $\text{In}_2\text{O}_3/\text{ZrO}_2$ catalysts, the discernible impact of the synthesis method is evident (Figure S4). Whether considering ZrO_2 (SG) catalysts with $P_{\text{surface}} = 5.29$ and 6.19 $\text{mg}_{\text{MeOH}} \cdot \text{m}^{-2} \cdot \text{h}^{-1}$ (S-SG or M-SG) or ZrO_2 (AA) with $P_{\text{surface}} = 7.12$ and 8.18 $\text{mg}_{\text{MeOH}} \cdot \text{m}^{-2} \cdot \text{h}^{-1}$ (S-AA or M-AA), it can be seen, that catalysts prepared using the synthesis procedure of (M) exhibit higher normalized productivity. Nevertheless, the catalytic results show that the surface area of the employed ZrO_2 is the most significant influence on catalytic activity, while the synthesis method has a subordinated influence on the catalytic activity for CO_2 -hydrogenation.

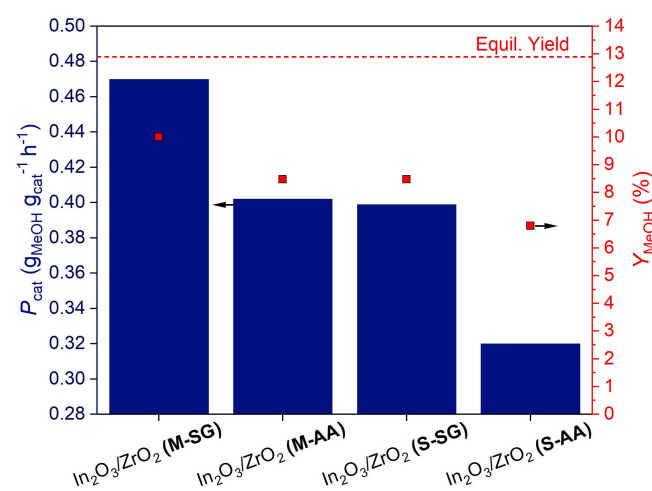


Figure 4. Influence of different ZrO_2 (SG or AA) supports and synthesis methods (M or S) on methanol yield and productivity in comparison to the calculated equilibrium yield. Reaction conditions: $\text{CO}_2/\text{H}_2 = 1/3$; $\text{GHSV} = 8400 \text{ h}^{-1}$; $T_{\text{OS}} = 3 \text{ h}$; $T = 300 \text{ °C}$; $p = 75 \text{ bar}$; $h_{\text{bed}} = 5.1 \pm 0.1 \text{ cm}$.

Elemental analysis of all catalysts confirmed the same amount of In loading of around 10 wt.% (Table 1). XRD diffraction patterns of all $\text{In}_2\text{O}_3/\text{ZrO}_2$ show characteristic patterns for monoclinic ZrO_2 as well as cubic In_2O_3 (Figure S6a). According to SEM analysis, no morphological changes can be observed due to the synthesis procedure (Figure S5, c–f). Furthermore, SEM-EDX mapping shows that In is dispersed homogeneously on ZrO_2 on a macroscopic level. Furthermore, no significant differences in the distribution of In_2O_3 on ZrO_2 for the different catalysts could be displayed (Figure 3). Additionally, the crystallite size of In_2O_3 on ZrO_2 was determined using the Scherrer-Debye equation (Equation S1, Table 1).^[36] Despite an overall homogeneous distribution, it is evident that the particle size is influenced by the type of ZrO_2 used rather than the synthesis method. Specifically, when ZrO_2 (SG) was employed, particle sizes were consistently smaller, with 11.84 nm for $\text{In}_2\text{O}_3/\text{ZrO}_2$ (M-SG) and 11.77 nm for $\text{In}_2\text{O}_3/\text{ZrO}_2$ (S-SG). In contrast, the use of ZrO_2 (AA) as a support resulted in a larger particle size of 16.91 nm for both $\text{In}_2\text{O}_3/\text{ZrO}_2$ (M-AA) and $\text{In}_2\text{O}_3/\text{ZrO}_2$ (S-AA). The smaller crystallite sizes observed with ZrO_2 (SG) as support correlate with higher catalytic performance.

Interestingly, chemisorptive data show that the catalysts differ significantly with respect to their adsorption as well as reduction behaviour. CO_2 -TPD results show that $\text{In}_2\text{O}_3/\text{ZrO}_2$ catalysts based on ZrO_2 (SG) have overall higher as well as stronger CO_2 binding capacities than those based on ZrO_2 (AA), which confirms stronger interactions between In_2O_3 and ZrO_2 (SG) (Figure 2a and Table S3). Regardless of the support used, the synthesis procedure of (M) leads to catalysts with overall higher CO_2 adsorption. Additionally, H_2 -TPR data show a strong dependency of the used ZrO_2 and the synthesis procedure. In detail, using ZrO_2 (AA) with the synthesis method of (M) enhanced the reduction capacity of 0.8 ($\text{In}_2\text{O}_3/\text{ZrO}_2$ (S-AA)) to the same amount as for the ZrO_2 -based SG catalysts with 1.06 ($\text{In}_2\text{O}_3/\text{ZrO}_2$ (M-AA)) (Figure 2b and Table S4).

Physisorptive analysis show, however, that the surface area as well as the pore volume of $\text{In}_2\text{O}_3/\text{ZrO}_2$ (M-AA) with 49.14 m^2/g and 0.203 cm^3/g is higher than for $\text{In}_2\text{O}_3/\text{ZrO}_2$ (S-AA) with 44.97 m^2/g and 0.174 cm^3/g (Table 1). Through the longer stirring time employed by (M) and the use of more solvent, it is possible that the metal particles have been able to gain access to enter the pores and thereby prevent their blocking.^[37,38] Additionally, there could be an effect of the solvent. Using ethanol instead of water as solvent for the impregnation lowers the polarity and could cause stronger interactions between In_2O_3 and ZrO_2 . This can be seen in the TPR results of ZrO_2 (AA)-based catalysts, where more species have been formed, which are reduced at higher temperatures, indicating formation of bulk In_2O_3 (Figure 2b and Table S4).^[38,39] This effect is not as strong for ZrO_2 (SG) based catalysts, which is due the overall higher surface area of ZrO_2 , decreasing the influence of the synthesis method.

Effect of Cu-, Ni-, Mg-, or Ce-as promoters on the catalytic performance of $\text{In}_2\text{O}_3/\text{ZrO}_2$ catalysts

To further enhance the catalytic performance of $\text{In}_2\text{O}_3/\text{ZrO}_2$ in CO_2 hydrogenation to methanol, various promoters (Cu, Ni, Mg, Ce) were added to the $\text{In}_2\text{O}_3/\text{ZrO}_2$ catalyst. These materials can enhance the formation of methanol in different ways. On the one hand side, basic materials like Ce as well as Mg can catalyze oxidation of in-situ formed CO by the competing RWGS reaction further to CO_2 , resulting in the formation of additional oxygen vacancies.^[2,19,23] Furthermore, it was shown that Ce and Mg as promoters can enhance the CO_2 adsorption capacity.^[40] Cu as well as Ni have the property of enhancing hydrogen spillover, whereby the atomic hydrogen takes part in the consecutive hydrogenation of carbon containing surface species to form methanol.^[7,41] In this study, the influence of different metal promoters for the $\text{In}_2\text{O}_3/\text{ZrO}_2$ (M-SG) catalyzed CO_2 hydrogenation to methanol was examined. Therefore, ZrO_2 (SG) as the most promising support was chosen and impregnated with In_2O_3 together with the respective promoters via co-precipitation (for detailed description see Supporting Information).

To evaluate the different catalytic activities of the various promoters, this study was carried out at 250 °C and 75 bar since lower reaction kinetics and theoretically higher equilibrium yield of MeOH $Y_{\text{Eq, MeOH}} = 28.9\%$ would be possible (calculated by the property method Soave-Redlich-Kwong in ASPEN Plus). Figure 5 shows a higher productivity of the Ce-promoted $\text{In}_2\text{O}_3/\text{ZrO}_2$ (0.083 $\text{g}_{\text{MeOH}} \cdot \text{g}_{\text{cat}}^{-1} \cdot \text{h}^{-1}$) compared to the Mg-promoted $\text{In}_2\text{O}_3/\text{ZrO}_2$ (0.049 $\text{g}_{\text{MeOH}} \cdot \text{g}_{\text{cat}}^{-1} \cdot \text{h}^{-1}$), but both metals decrease the catalytic activity of the pristine $\text{In}_2\text{O}_3/\text{ZrO}_2$ (M-SG) of 0.159 $\text{g}_{\text{MeOH}} \cdot \text{g}_{\text{cat}}^{-1} \cdot \text{h}^{-1}$ while keeping the selectivity S_{MeOH} of about 80%. Promoting the catalyst with Cu also downgrades the productivity ($P_{\text{cat}} = 0.088 \text{ g}_{\text{MeOH}} \cdot \text{g}_{\text{cat}}^{-1} \cdot \text{h}^{-1}$) while only slightly decreasing the selectivity ($S_{\text{MeOH}} = 75\%$). In contrast, the addition of Ni to $\text{In}_2\text{O}_3/\text{ZrO}_2$ catalysts increases the catalytic performance up to 0.221 $\text{g}_{\text{MeOH}} \cdot \text{g}_{\text{cat}}^{-1} \cdot \text{h}^{-1}$ compared to the unmodified $\text{In}_2\text{O}_3/\text{ZrO}_2$ (M-SG) with only a slight selectivity decrease to $S_{\text{MeOH}} = 66\%$.

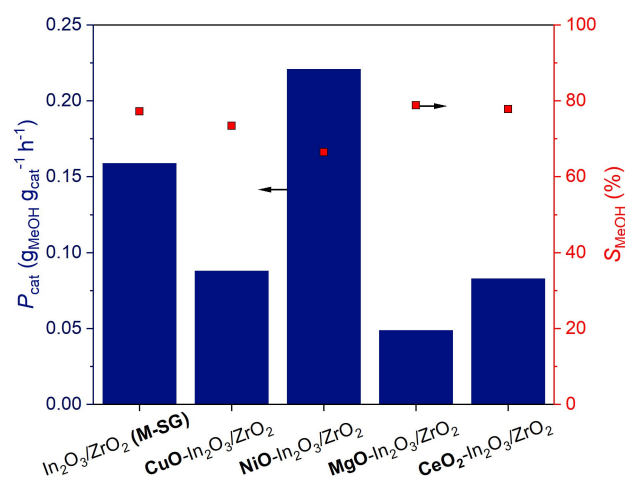


Figure 5. Catalytic performance of CuO-, NiO-, MgO- and CeO-promoted $\text{In}_2\text{O}_3/\text{ZrO}_2$ compared to $\text{In}_2\text{O}_3/\text{ZrO}_2$ (M-SG) Reaction conditions: $\text{CO}_2/\text{H}_2 = 1/3$; $\text{GHSV} = 8300 \text{ h}^{-1}$; $T_{\text{OS}} = 3 \text{ h}$; $T = 250 \text{ }^\circ\text{C}$; $p = 75 \text{ bar}$; $h_{\text{bed}} = 5.1 \pm 0.1 \text{ cm}$.

	Cu/Ni/Mg/Ce (wt. %) ^[a]	In (wt. %) ^[a]	Zr (wt. %) ^[a]	S_{BET} (m^2/g) ^[b]	\varnothing pore radius (nm) ^[b]	pore volume (cm^3/g) ^[b]
$\text{CuO-In}_2\text{O}_3/\text{ZrO}_2$	7.66	6.37	55.55	79.78	4.07	0.324
$\text{NiO-In}_2\text{O}_3/\text{ZrO}_2$	6.40	7.76	50.12	88.93	3.70	0.260
$\text{MgO-In}_2\text{O}_3/\text{ZrO}_2$	2.62	8.95	48.66	88.82	3.71	0.270
$\text{CeO}_2\text{-In}_2\text{O}_3/\text{ZrO}_2$	5.11	6.95	52.84	87.87	4.05	0.256

[a] Determined by ICP-OES. [b] Measured by N_2 -physisorption.

ICP-OES elemental analysis confirmed the successful impregnation of ZrO_2 with In_2O_3 and the respective promotor (Table 2), while SEM analysis revealed no change in morphology after impregnation (Figure S8). However, precipitation was not complete, as the desired loading of 10 wt.% for both, In and the respective promotor, could only be achieved up to 8 wt.%. XRD data show, that only patterns of ZrO_2 can be observed, but none of In_2O_3 or the respective promotors, indicating both exist in an amorphous state (Figure S9a). To assess the potential impact of slight variations in metal loadings on the catalytic performance, we examined also P_{metal} next to P_{cat} . P_{metal} involves normalizing productivity to the quantity of all active metals (Table 2), including Indium and the respective promotor. The enhanced catalytic activity of $\text{NiO-In}_2\text{O}_3/\text{ZrO}_2$ remains evident even when accounting all active surface species. P_{metal} of $\text{NiO-In}_2\text{O}_3/\text{ZrO}_2$ with $1.563 \text{ g}_{\text{MeOH}} \cdot \text{g}_{\text{metal}}^{-1} \cdot \text{h}^{-1}$ is higher than for pure $\text{In}_2\text{O}_3/\text{ZrO}_2$ with $1.437 \text{ g}_{\text{MeOH}} \cdot \text{g}_{\text{metal}}^{-1} \cdot \text{h}^{-1}$ (Figure S7). The conversion of CO_2 was 5.7% using the $\text{NiO-In}_2\text{O}_3/\text{ZrO}_2$ catalyst compared to 4.4% using the pure $\text{In}_2\text{O}_3/\text{ZrO}_2$ catalyst.

XPS analysis was performed to examine in which oxidation state the respective metals are present. XPS survey spectra of all catalysts exhibit the expected peaks for Zr3d, In3d, O1s as well

as a C1s peak, that can be attributed to surface impurities from the measurements (Figure 6). Each spectrum shows peaks corresponding to the presence of the promotor (Cu, Ni, Mg and Ce). The XPS deconvolution results reveal that In is only present as In_2O_3 in the catalyst and no metallic In^0 is present. The In3d signals in the XPS spectra are observed at binding energy values of approximately 445 eV (for In3d 5/2) and 453 eV (for In3d 3/2) (Figure S10a).^[42,43]

Interestingly, XPS analysis further confirm that Cu, Ni, Mg and Ce are all present in their oxidized form before and after reaction (Figure S10b–e). Cu2p spectra of $\text{CuO-In}_2\text{O}_3/\text{ZrO}_2$ reveal that Cu is present in its oxidized form as CuO with characteristic signals at 933 and 942 eV with a splitting of 19.8 eV.^[42–44] For NiO, the Ni2p spectra exhibit mainly signals corresponding to NiO at 855 and 873 eV.^[20,45] Mg is identified as magnesium oxide (MgO) based on the characteristic binding energy at 1305 eV.^[46] Ce3d spectra could be depicted into three regions with binding energy values of 882, 897 and 915 eV, that can be assigned to CeO_2 .^[47]

Physisorptive data show that synthesis via co-precipitation just led to a slight decrease of the BET-surface. All metal-promoted catalysts show BET-surfaces around $89 \text{ m}^2/\text{g}$ (Ni, Ce,

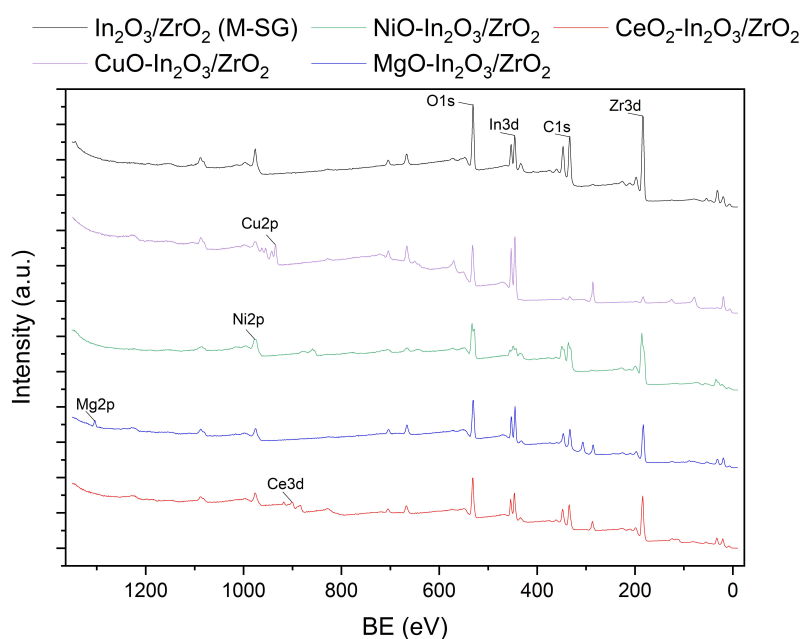


Figure 6. XPS survey spectra of $\text{In}_2\text{O}_3/\text{ZrO}_2$ (M-SG), as well as CuO-, NiO-, MgO-, and CeO_2 - promoted $\text{In}_2\text{O}_3/\text{ZrO}_2$.

Mg) or 80 m²/g (Cu). Therefore, incorporation of the metals via co-precipitation leads to higher surface areas compared to wetness impregnation as for In₂O₃/ZrO₂ (M-SG) with 76 m²/g. Range of pore sizes with overall pore radii of 3.7 to 4.1 nm as well as pore volumes with 0.26–0.32 cm³/g for the metal-incorporated In₂O₃/ZrO₂ catalysts are higher than for In₂O₃/ZrO₂ (M-SG) with 3.4 nm and 0.21 cm³/g, respectively (Table 2, Figure S9b). This suggests the presence of all metal oxides on the surface, but no penetration into the pores, as well as formation of agglomerates.

The incorporation of the promoters also leads to a change in CO₂ adsorption capacity (Figure 7a). In detail, adding MgO, CuO & NiO to In₂O₃ lead to a higher overall CO₂ adsorption capacity compared to the non-promoted catalyst (In₂O₃/ZrO₂ (M-SG)) by a factor of more than 1.5 (see Table S5). In the case of CeO₂, the adsorption capacity decreases by a factor of 0.8. The presence of NiO on the In₂O₃/ZrO₂-catalyst facilitates the reduction of the catalyst surface, as evidenced by the shift to lower temperatures required for H₂ adsorption in H₂-TPR experiments (Figure 7b). Overall, both higher CO₂ adsorption as well as easier reducibility contribute to a higher methanol productivity.

The decrease in activity for the CuO-In₂O₃/ZrO₂ catalyst compared to In₂O₃/ZrO₂ (M-SG) is significant in terms of both productivity and selectivity (Figure 5). This can be attributed to the differences in chemisorptive properties. When examining the CO₂-TPD data, it is observed that the overall CO₂ adsorption capacity of CuO-In₂O₃/ZrO₂ is higher. However, the temperature required for CO₂ desorption is also significantly elevated compared to In₂O₃/ZrO₂ (M-SG). Compared to In₂O₃/ZrO₂ (M-SG) with the highest CO₂ desorption temperature at 470 °C, the required temperature for CO₂ desorption increased about 100 °C up to 570 °C when CuO is incorporated (Figure 7a, Table S5). This indicates that the catalyst has a strong affinity for CO₂ adsorption, but the adsorption strength is excessive for efficient methanol production in subsequent steps. In H₂-TPR

data, a notable baseline shift is observed at higher temperatures (> 690 °C) for CuO-In₂O₃/ZrO₂ (Figure 7b, Table S6). This indicates that the bulk material is reduced and hydrogen evolves at higher temperatures.

Among all the catalysts studied, MgO-In₂O₃/ZrO₂ exhibited the lowest catalytic activity. This can be attributed to the unexpected decrease in CO₂ adsorption capacity strength, indicating weaker CO₂ adsorption at the catalyst's surface (Figure 7a, Table S5). Additionally, the incorporation of Mg results in a decrease in the reducibility of the catalyst, as evident from the H₂-TPR data (Figure 7b, Table S6).

In case of the CeO₂-In₂O₃/ZrO₂ catalyst compared to the non-promoted (In₂O₃/ZrO₂ (M-SG)), there is a decrease in overall adsorption capacity (Figure 7a, Table S5). This could be attributed to the formation of In₂O₃ and CeO₂ clusters, as observed in the EDX mapping analysis (Figure 8b). The inhomogeneous distribution of these clusters may hinder the adsorption of CO₂ and result in reduced adsorption capacity. This finding is also consistent with the TPR data (Figure 7b, Table S6) that shows a shift to higher reduction temperatures and lower reduction capacity for the CeO₂-In₂O₃/ZrO₂ catalyst, resulting from bulk formation. This, in turn, leads to a decrease in productivity.

In conclusion, particularly the incorporation of NiO significantly enhances the catalytic performance. The hydrogen spill-over effect facilitates H₂ adsorption, subsequently improving H₂ dissociation and migration to the support surface, resulting in higher methanol productivity and CO₂ conversion. This mechanism fosters the formation of oxygen vacancies, resulting in higher methanol productivity of the system. This enhancement is proven by chemisorptive analysis, showing significantly higher levels of both adsorbed CO₂ or H₂ compared to all other catalysts.

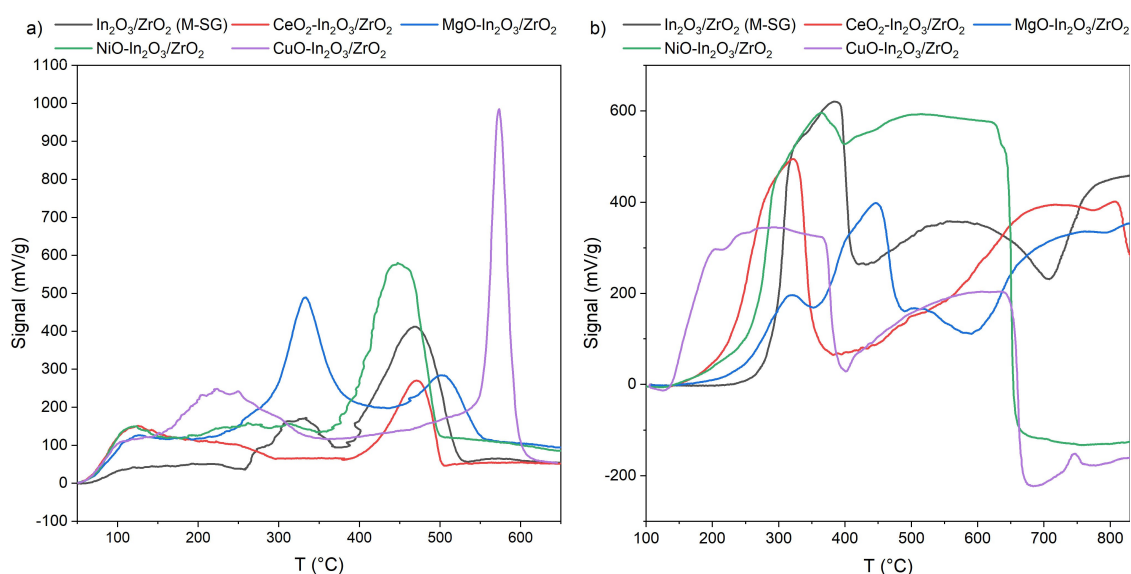


Figure 7. Chemisorptive analysis of CuO-, NiO-, MgO- and CeO₂-promoted In₂O₃/ZrO₂ compared to In₂O₃/ZrO₂ (M-SG): a) CO₂-TPD and b) H₂-TPR.

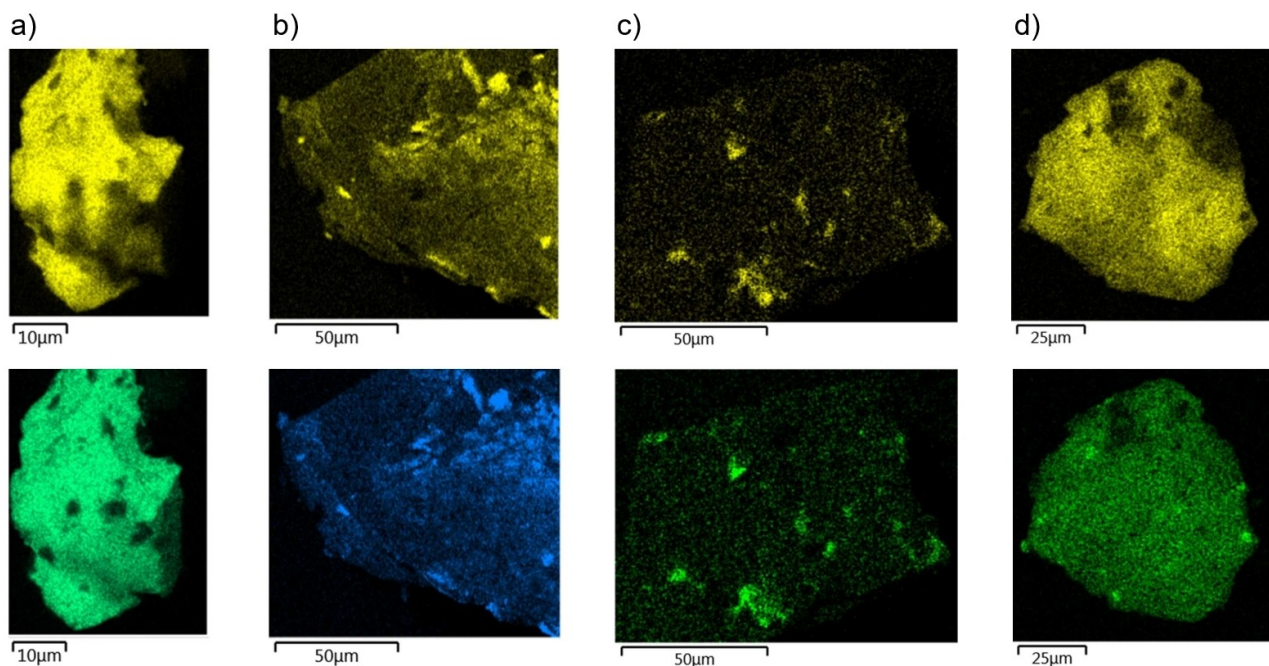


Figure 8. SEM-EDX elemental mapping images of a) NiO-In₂O₃/ZrO₂, b) CeO₂-In₂O₃/ZrO₂, c) MgO-In₂O₃/ZrO₂ and d) CuO-In₂O₃/ZrO₂. Top: In distribution (yellow); Bottom: metal promoter (green/blue).

Combination of NiO-promoting and optimized synthesis method on the catalytic performance of In₂O₃/ZrO₂ catalysts

Different synthesis methods were employed to incorporate the best performing NiO-promotor into In₂O₃/ZrO₂ catalysts, namely chemical reduction (CR), co-precipitation (CP), and wetness impregnation (WI). These NiO-incorporated In₂O₃/ZrO₂ catalysts were further evaluated for their catalytic performance in the CO₂ hydrogenation to methanol. Table 3 shows the textural composition of the synthesized catalysts.

ICP-OES elemental analysis confirmed the successful incorporation of Ni into the In₂O₃/ZrO₂ catalyst using all three preparation methods (Table 3). Interestingly, only 0.32 wt% of Ni could be incorporated via CR, while 0.69 resp. 0.76 wt% Ni could be incorporated by CP and WI at an overall constant In loading of around 10.5 wt%. Furthermore, XPS analysis indicate also the presence of NiO in all catalysts for the various synthesis methods. (Figure 9). The Ni2p core level spectrum of all catalysts shows again binding energies at 855 and 873 eV, which refer to Ni²⁺ species (Figure S13).^[20,45]

Physisorptive data show only small deviations in surface area (74–80 m²/g) as well as pore volume (0.216–0.258 cm³/g)

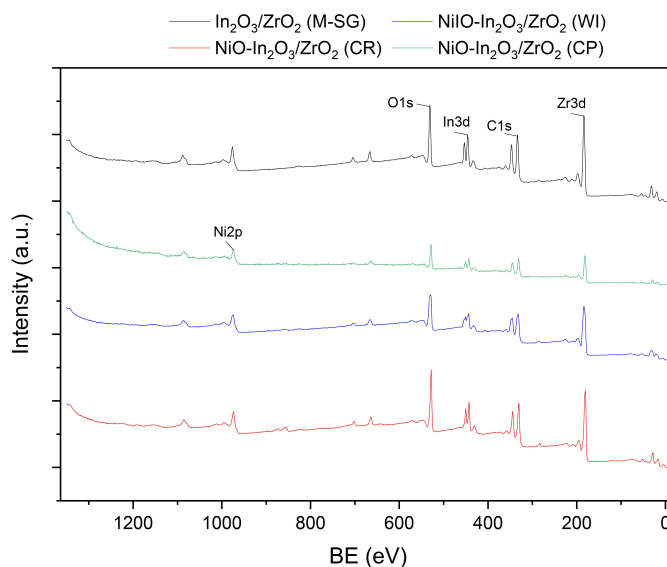


Figure 9. XPS survey spectra of NiO-In₂O₃/ZrO₂ prepared by WI, CR or CP compared with In₂O₃/ZrO₂ (M-SG).

Table 3. Textural composition of NiO-In₂O₃/ZrO₂ catalysts prepared by Wi, CR and CP.

	Ni (wt. %) ^[a]	In (wt. %) ^[a]	Zr (wt. %) ^[a]	S _{BET} (m ² /g) ^[b]	∅ pore radius (nm) ^[b]	pore volume (cm ³ /g) ^[b]
NiO-In ₂ O ₃ /ZrO ₂ (WI)	0.76	10.48	53.85	80.66	3.70	0.216
NiO-In ₂ O ₃ /ZrO ₂ (CR)	0.32	10.64	53.40	74.37	3.70	0.223
NiO-In ₂ O ₃ /ZrO ₂ (CP)	0.69	10.63	58.09	78.82	4.06	0.258

[a] Determined by ICP-OES. [b] Measured by N₂-physorption.

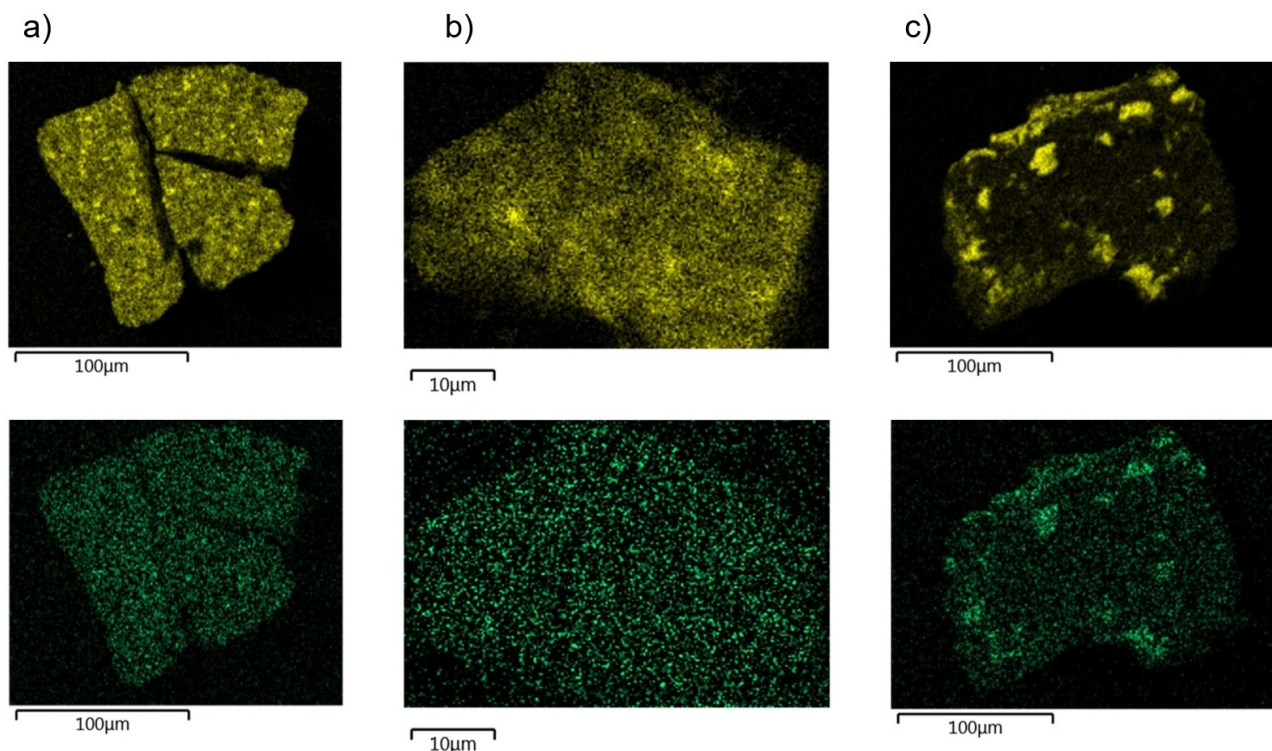


Figure 10. SEM-EDX elemental mapping images of Ni-In₂O₃/ZrO₂ prepared by a) WI, b) CR and c) CP. Top: In distribution (yellow); bottom: Ni distribution (green).

after impregnation for all preparation methods. However, the pore size distribution is nearly similar for the three synthesis methods with a medium pore size of 10 nm (Table 3, Figure S11b). Moreover, XRD data confirm patterns for crystalline In₂O₃ and ZrO₂, except for NiO-In₂O₃/ZrO₂ (CP), as already seen before, where just patterns for ZrO₂ are present, indicating an amorphous structure for In₂O₃. Furthermore, no distinct patterns can be seen for NiO in the diffractogram, indicating amorphous or nanocrystalline NiO species (Figure S11a).

SEM analysis was conducted to investigate the morphological changes after impregnation with Ni through the different synthesis techniques. No changes could be revealed in the morphology of the ZrO₂ supported catalysts after impregnation with In₂O₃ and NiO for all synthesis methods (Figure S12). Furthermore, SEM-EDX mapping demonstrates a macroscopic homogeneous distribution of both In and Ni for NiO-In₂O₃/ZrO₂ (WI) (Figure 10). The formation of agglomerates could be further supported by H₂-TPR analysis, where a baseline shift of NiO-In₂O₃/ZrO₂ (CR) could be deduced (see Figure 11b).

The overall H₂-reduction and CO₂ adsorption capacity of NiO-In₂O₃/ZrO₂ (CR) (0.72/0.87) as well as NiO-In₂O₃/ZrO₂ (CP) (0.96/0.91) are lower than for the pristine In₂O₃/ZrO₂ (M-SG) (Tables S7, S8). This indicates a poorer reducibility, explained by formation of agglomerates. NiO-In₂O₃/ZrO₂ (WI) exhibit improved H₂-reduction properties with 1.19 as well as increased CO₂ capacity values with 1.69. This can be explained by the formation of electronic defects by incorporation of NiO via WI as well as the already discussed H₂-spillover by Jiang et al.⁵⁵ (Figure 11a and b, Tables S7 and S8).

Figure 12 shows methanol productivities as well as selectivities for the four different synthesized catalysts. Compared to the non-promoted In₂O₃/ZrO₂ (M-SG) catalyst giving a productivity of $P_{\text{cat}} = 0.475 \text{ g}_{\text{MeOH}} \cdot \text{g}_{\text{cat}}^{-1} \cdot \text{h}^{-1}$, the productivity decreased if NiO is incorporated via CR, yielding a productivity of only $0.39 \text{ g}_{\text{MeOH}} \cdot \text{g}_{\text{cat}}^{-1} \cdot \text{h}^{-1}$. Moreover, NiO-In₂O₃/ZrO₂ (CP) and NiO-In₂O₃/ZrO₂ (WI) showed a higher methanol productivity of 0.482 and $0.497 \text{ g}_{\text{MeOH}} \cdot \text{g}_{\text{cat}}^{-1} \cdot \text{h}^{-1}$, respectively, when compared to In₂O₃/ZrO₂ (M-SG). Regarding selectivity, no significant decrease could be observed for any synthesis method.

Long-term stability of the NiO-In₂O₃/ZrO₂ (WI) catalyst

Finally, the MeOH productivity of the best performing NiO-In₂O₃/ZrO₂ (WI) catalyst was investigated for 100 h time-on-stream (Figure 13). After 12 h, the catalyst exhibited a maximum productivity of $0.162 \text{ g}_{\text{MeOH}} \cdot \text{g}_{\text{cat}}^{-1} \cdot \text{h}^{-1}$ at 250 °C and 75 bar. The MeOH productivity slightly decreased to $0.149 \text{ g}_{\text{MeOH}} \cdot \text{g}_{\text{cat}}^{-1} \cdot \text{h}^{-1}$ after 100 h. Moreover, no methane could be detected by GC analysis (Figure S14).

Post-mortem studies of the catalyst further revealed its stability. In detail, ICP-OES analysis indicate no leaching after 100 h TOS. Data of pre-reaction material (In-wt.% of 10.48, Zr-wt.% of 53.85 and Ni-wt.% of 0.76) are well in line with data of post-reaction material (In-wt.% of 10.36, Zr-wt.% of 53.39 and Ni-wt.% of 0.73), respectively. XRD patterns provide evidence of unchanged crystalline structure of In₂O₃ and ZrO₂ (Figure 14). Furthermore, no changes in morphology could be

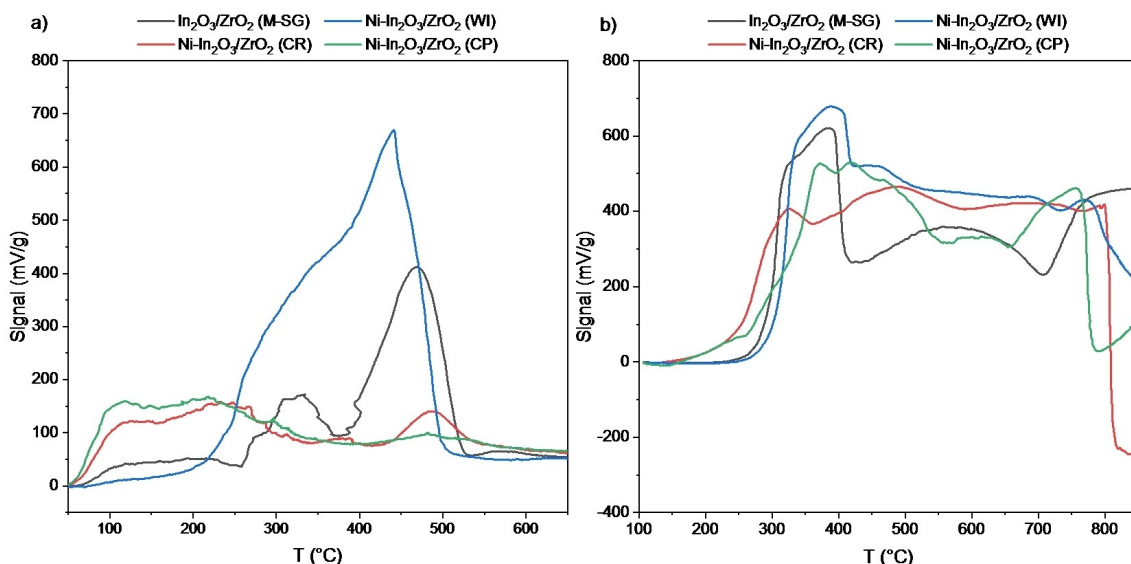


Figure 11. Chemisorptive analysis of NiO-In₂O₃/ZrO₂ prepared by WI, CR or CP compared to In₂O₃/ZrO₂ (M-SG): a) CO₂-TPD and b) H₂ TPR.

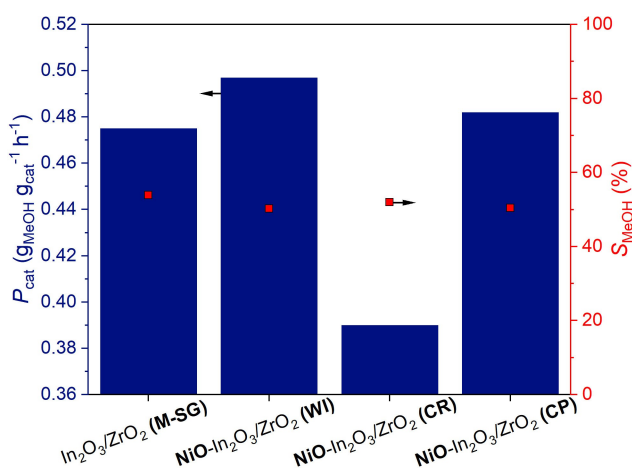


Figure 12. Impact of different synthesis methods for NiO-In₂O₃/ZrO₂ on the methanol productivity and selectivity. Reaction conditions: CO₂/H₂ = 1/3; GHSV = 8600 h⁻¹; TOS = 3 h; T = 300 °C; p = 75 bar; h_{bed} = 5.1 ± 0.1 cm.

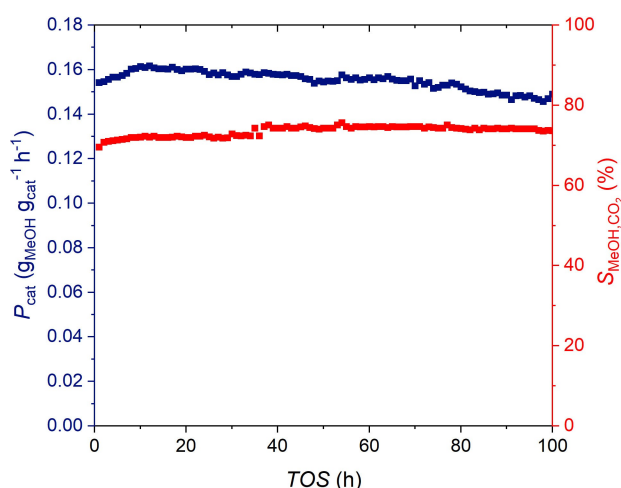


Figure 13. Stability of NiO-In₂O₃/ZrO₂ (WI) recorded over 100 h TOS. Reaction conditions: CO₂/H₂ = 1/3; GHSV = 4600 h⁻¹; T = 250 °C; p = 75 bar; h_{bed} = 5.0 cm.

observed in SEM (Figure 15). Finally, EDX-Mapping also shows no formation of agglomerates (Figure S15).

Conclusions

In this work, various In₂O₃/ZrO₂ catalysts have been investigated for their application in methanol synthesis. Hereby, different support materials, metal promoters as well as synthesis methods were applied to identify the best combination for gas-phase methanol synthesis. In detail, In₂O₃/ZrO₂ (M-SG) shows both higher P_{MeOH} and Y_{MeOH} independently of the applied reaction conditions with a maximum methanol productivity of 4.25 g_{MeOH} · g_{in}⁻¹ · h⁻¹ at 300 °C and 75 bar compared to In₂O₃/ZrO₂ (S-AA) mainly due to its higher surface area. Moreover, only a disparity in the synthesis method could be revealed. In the next step, several metals were used as promoters for the In₂O₃/ZrO₂

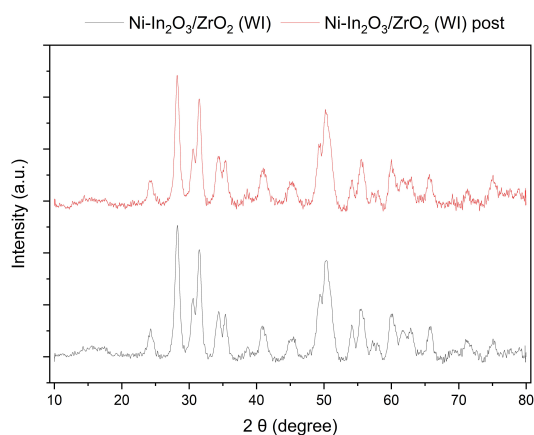


Figure 14. XRD patterns of NiO-In₂O₃/ZrO₂ (WI) before (black) and after (red) reaction.

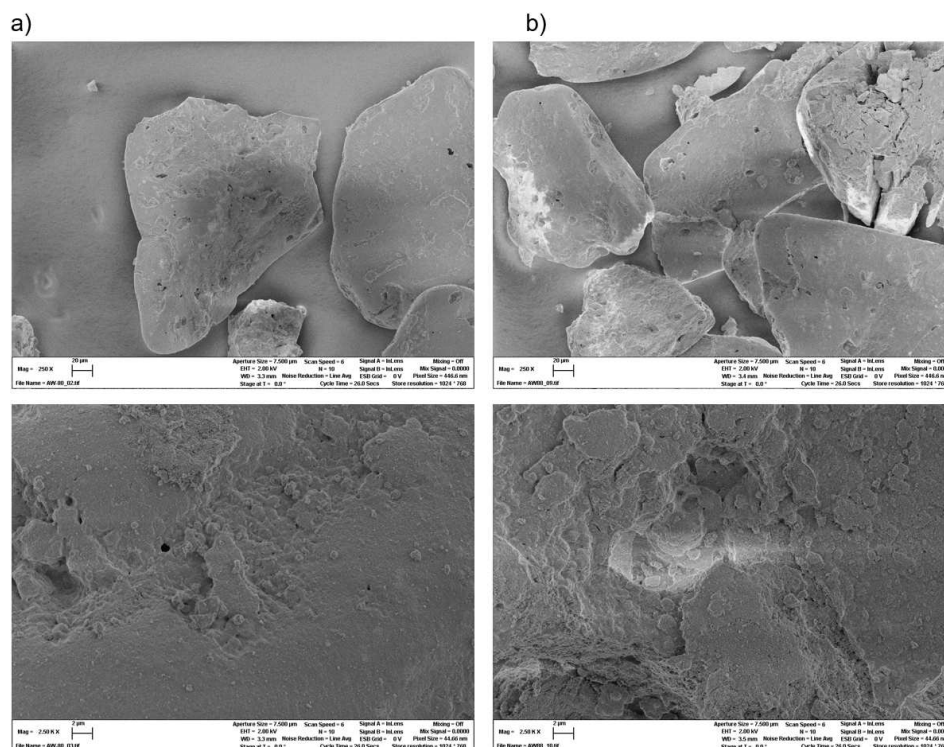


Figure 15. SEM images of Ni-In₂O₃/ZrO₂ (WI) before a) and after reaction b).

(M-SG) catalyst in order to further enhance its productivity. Hereby, the NiO-In₂O₃/ZrO₂ (M-SG) catalyst showed the best performance. Regarding the synthesis method, wetness impregnation using a water/ethanol solvent system has been found to be the most efficient preparation method for the incorporation of Ni into the In₂O₃/ZrO₂ (M-SG) catalyst. Overall, the NiO-promoted catalyst shows improved catalytic activity as well as stability because of a facilitated H₂-spillover and strong electronic interactions with the ZrO₂ support. The methanol productivity of In₂O₃/ZrO₂ (M-SG) could be increased from 0.475 g_{MeOH} · g_{cat}⁻¹ · h⁻¹ to 0.497 g_{MeOH} · g_{cat}⁻¹ · h⁻¹ by the addition of 0.8 wt% Ni without any methane formation. Finally, the NiO-In₂O₃/ZrO₂ catalyst remains stable and active over 100 h on stream paving the way for future applications in green methanol synthesis.

Experimental

Materials and catalyst preparation

All chemicals were obtained commercially and used as received without further purification. The In₂O₃/ZrO₂ catalysts were synthesized using wetness impregnation (WI) technique using different ZrO₂ supports. Furthermore, the dopants (Ni, Cu, Ce, Mg) have been incorporated either via wetness impregnation (WI), chemical reduction (CR) or co-precipitation (CP). Comprehensive description of the catalyst preparation can be found in the Supporting Information.

Catalyst characterization

The elemental compositions of all catalysts were determined using inductively coupled plasma optical emission spectroscopy (ICP-OES). The crystalline structure was analyzed via powder X-Ray diffraction (XRD), additional information about the oxidation states were obtained using X-ray photoelectron spectroscopy (XPS). The porosity, pore volume (BJH) as well as total surface area (BET) were determined by N₂-physisorption measurements. Scanning electron microscopy (SEM) and energy-dispersive X-ray spectroscopy (EDX) revealed catalyst morphology and metal dispersion. Chemisorption properties were evaluated by CO₂-temperature-programmed desorption (CO₂-TPD) and H₂-temperature-programmed reduction (H₂-TPR). Comprehensive descriptions of all characterization methods are given in the Supporting Information.

Catalyst testing / Catalytic evaluation

All experiments were performed in a high-pressure continuous-flow fixed-bed reactor setup (see Figure S1). Usually, 4.0 to 5.0 g of catalyst were loaded into the reactor and fixed by a bed of quartz wool. Prior to the reaction, the catalyst was pretreated at 200 °C under flowing N₂ (300 NmL · min⁻¹) for 1 hour. Subsequently, the temperature was set to 300 °C and a reaction gas mixture with a CO₂/H₂ stoichiometric ratio of 1/3 was fed using a flow rate of 1200 NmL · min⁻¹ into the reactor (*GHSV* = 8400–8600 h⁻¹, Equation S7), which was pressurized to 50 or 75 bar, respectively. Catalysts were tested for 3 h under steady-state conditions for performance comparison. Details of the experimental setup as well as equations for the calculation of the yield Y_{MeOH} , selectivity S_{MeOH} , CO₂ conversion X_{CO_2} and productivity P_{cat} , P_{surface} , P_{metal} are provided in the Supporting Information.

Acknowledgements

The authors acknowledge Dr. Michael Pabel from Saint-Gobain NorPro for supply of ZrO₂ and Dr. Leonhard Schill from DTU Lyngby for performing XPS measurements. The Central Analytics Department of UHH is gratefully acknowledged for Elemental analysis, X-ray diffraction and Electron microscopy. Open access provided by Project DEAL. Open Access funding enabled and organized by Projekt DEAL.

Conflict of Interests

There are no conflicts to declare.

Data Availability Statement

Research data are not shared.

Keywords: CO₂ hydrogenation · hydrogen spillover · indium-based catalysts · methanol synthesis

- [1] a) C. Panzone, R. Philippe, A. Chappaz, P. Fongarland, A. Bengaouer, *J. CO₂ Util.* **2020**, *38*, 314–347; b) M. Aresta, A. Dibenedetto, A. Angelini, *Chem. Rev.* **2014**, *114*, 1709–1742.
- [2] R.-P. Ye, et al., *Nat. Commun.* **2019**, *10*, 5698.
- [3] a) P. Gao, L. Zhang, S. Li, Z. Zhou, Y. Sun, *ACS Cent. Sci.* **2020**, *6*, 1657–1670; b) E. S. Rubin, H. Mantripragada, A. Marks, P. Versteeg, J. Kitchin, *Prog. Energy Combust. Sci.* **2012**, *38*, 630–671.
- [4] A. Álvarez, A. Bansode, A. Urakawa, A. V. Bavykina, T. A. Wezendonk, M. Makkee, J. Gascon, F. Kapteijn, *Chem. Rev.* **2017**, *117*, 9804–9838.
- [5] P. W. Andreas Jess, *Chemical Technology*, Wiley-VCH, Weinheim, **2013**, 685–686.
- [6] W.-J. Shen, K.-W. Jun, H.-S. Choi, K.-W. Lee, *Korean J. Chem. Eng.* **2000**, *17*, 210–216.
- [7] K.-D. Jung, A. T. Bell, *J. Catal.* **2000**, *193*, 207–223.
- [8] N. Ortner, D. Zhao, H. Mena, J. Weiß, H. Lund, S. Bartling, S. Wohlrab, U. Armbruster, E. V. Kondratenko, *ACS Catal.* **2023**, *13*, 60–71.
- [9] F. Studt, M. Behrens, E. L. Kunkes, N. Thomas, S. Zander, A. Tarasov, J. Schumann, E. Frei, J. B. Varley, F. Abild-Petersen, J. K. Nørskov, R. Schlögl, *ChemCatChem* **2015**, *7*, 1105–1111.
- [10] M. V. Twigg, M. S. Spencer, *Appl. Catal. A: General* **2001**, *212*, 161–174.
- [11] P. Schühle, M. Schmidt, L. Schill, A. Riisager, P. Wasserscheid, J. Albert, *Catal. Sci. Technol.* **2020**, *10*, 7309–7322.
- [12] O. Martin, A. J. Martín, C. Mondelli, S. Mitchell, T. F. Segawa, R. Hauert, C. Drouilly, D. Curulla-Ferré, J. Pérez-Ramírez, *Angew. Chem. Int. Ed.* **2016**, *55*, 6261–6265.
- [13] P. Schühle, S. Reichenberger, G. Marzun, J. Albert, *Chem. Ing. Tech.* **2021**, *93*, 585–593.
- [14] M. S. Frei, C. Mondelli, A. Cesarini, F. Krumeich, R. Hauert, J. A. Stewart, D. Curulla Ferré, J. Pérez-Ramírez, *ACS Catal.* **2020**, *10*, 1133–1145.
- [15] J. Ye, C. Liu, D. Mei, Q. Ge, *ACS Catal.* **2013**, *3*, 1296–1306.
- [16] K. Sun, Z. Fan, J. Ye, J. Yan, Q. Ge, Y. Li, W. He, W. Yang, C. Liu, *J. CO₂ Util.* **2015**, *12*, 1–6.
- [17] Y. Wei, F. Liu, J. Ma, C. Yang, X. Wang, J. Cao, *J. Mol. Catal.* **2022**, *525*, 112354.
- [18] K. Lau, P. Schühle, S.-X. Liang, F. de Kock, J. Albert, S. Reichenberger, *ACS Appl. Energ. Mater.* **2021**, *4*, 9206–9215.
- [19] S. Dang, B. Qin, Y. Yang, H. Wang, J. Cai, Y. Han, S. Li, P. Gao, Y. Sun, *Sci. Adv.* **2020**, *6*, eaaz2060.
- [20] M. Dou, M. Zhang, Y. Chen, Y. Yu, *Catal. Lett.* **2018**, *148*, 3723–3731.
- [21] P. Kampe, A. Wesner, P. Schühle, F. Hess, J. Albert, *ChemPlusChem* **2023**, *88*, e202300425.
- [22] P. Kampe, N. Herrmann, A. Wesner, C. Ruhmlied, J. Albert, *ACS Sustainable Chem. Eng.* **2023**, *11*, 14633–14644.
- [23] X. Jia, K. Sun, J. Wang, C. Shen, C. Liu, *J. Energy Chem.* **2020**, *50*, 409–415.
- [24] M. S. Frei, C. Mondelli, R. García-Muelas, J. Morales-Vidal, M. Philipp, O. V. Safonova, N. López, J. A. Stewart, D. C. Ferré, J. Pérez-Ramírez, *Nat. Commun.* **2021**, *12*, 1960.
- [25] N. Nomura, T. Tagawa, S. Goto, *React. Kinet. Catal. Lett.* **1997**, *63*, 21–25.
- [26] S. Dey, G. C. Dhal, *Materials Science for Energy Technologies* **2020**, *3*, 6–24.
- [27] K. Pokrovski, K. T. Jung, A. T. Bell, *Langmuir* **2001**, *17*, 4297–4303.
- [28] J. Wang, G. Zhang, J. Zhu, X. Zhang, F. Ding, A. Zhang, X. Guo, C. Song, *ACS Catal.* **2021**, 1406–1423.
- [29] K. S. W. Sing, *Pure Appl. Chem.* **1985**, *57*, 603–619.
- [30] M. Thommes, *Chem. Int.* **2016**, *38*, 25.
- [31] P. Sharma, P. Hoang Ho, J. Shao, D. Creaser, L. Olsson, *Fuel* **2023**, *331*, 125878.
- [32] T.-y. Chen, C. Cao, T.-b. Chen, X. Ding, H. Huang, L. Shen, X. Cao, M. Zhu, J. Xu, J. Gao, Y.-F. Han, *ACS Catal.* **2019**, 8785–8797.
- [33] P. Gao, et al., *ACS Catal.* **2018**, *8*, 571–578.
- [34] C.-Y. Chou, R. F. Lobo, *Appl. Catal. A: General* **2019**, *583*, 117144.
- [35] a) M. Bowker, *ChemCatChem* **2019**, *11*, 4238–4246; b) J. Zhong, X. Yang, Z. Wu, B. Liang, Y. Huang, T. Zhang, *Chem. Soc. Rev.* **2020**, *49*, 1385–1413.
- [36] A. Monshi, M. R. Foroughi, M. R. Monshi, *WJNSE* **2012**, *02*, 154–160.
- [37] A. V. Neimark, L. I. Kheifets, V. B. Fenelonov, *Ind. Eng. Chem. Prod. Res. Dev.* **1981**, *20*, 439–450.
- [38] P. Munnik, P. E. de Jongh, K. P. de Jong, *Chem. Rev.* **2015**, *115*, 6687–6718.
- [39] a) C. Li, W. Ying, F. Cao, H. Zhang, D. Fang, *Pet. Sci. Technol.* **2008**, *26*, 704–716; b) M. Tao, X. Meng, Y. Lv, Z. Bian, Z. Xin, *Fuel* **2016**, *165*, 289–297; c) F. T. Zangeneh, S. Mehrzama, S. Sahebdelfar, *Fuel Process. Technol.* **2013**, *109*, 118–123.
- [40] Maria C. Bacariza, Inês Graça, Suse S. Bebiano, José M. Lopes, Carlos Henriques, B. Zhao, Y. Pan, C. Liu, *Catal. Today* **2012**, *194*, 60–64.
- [41] a) Y. Yao, D. W. Goodman, *J. Mol. Catal. A: Chemical* **2014**, *383–384*, 239–242; b) Z. Zhang, C. Shen, K. Sun, C. Liu, *Catal. Commun.* **2022**, *162*, 106386.
- [42] I. N. Reddy, C. enkata Reddy, M. Cho, J. Shim, D. Kim, *Mater. Res. Express* **2017**, *4*, 86406.
- [43] J. Chastain, J. F. Moulder, *Handbook of X-ray photoelectron spectroscopy. A reference book of standard spectra for identification and interpretation of XPS data*, Physical Electronics, Eden Prairie, Minn., **1992**, 29–30.
- [44] M. C. Biesinger, L. W. Lau, A. R. Gerson, R. S. Smart, *Appl. Surf. Sci.* **2010**, *257*, 887–898.
- [45] M. C. Biesinger, *Surf. Interface Anal.* **2017**, *49*, 1325–1334.
- [46] a) N. C. Haider, J. Alonso, W. E. Swartz, *Z. Naturforsch. A* **1975**, *30*, 1485–1490; b) F. Khairallah, A. Glisenti, *Surf. Sci. Spectra* **2006**, *13*, 58–71.
- [47] a) E. Béche, P. Charvin, D. Perarnau, S. Abanades, G. Flamant, *Surf. Interface Anal.* **2008**, *40*, 264–267; b) X. Jiang, X. Li, J. Wang, D. Long, L. Ling, W. Qiao, *Catal. Sci. Technol.* **2018**, *8*, 2740–2749.

Manuscript received: September 7, 2023
Revised manuscript received: October 27, 2023
Accepted manuscript online: October 28, 2023
Version of record online: November 27, 2023

6.3 Spatially resolved study of supported In₂O₃ catalysts in a Compact Profile Reactor

P3

Spatially Resolved Reaction Profiles of CO₂ Hydrogenation to Methanol Using In-Based Catalysts in a Compact Profile Reactor

Philipp Kampe, Nick Herrmann, Charlotte Ruhmlieb, Maik Finsel, Oliver Korup, Raimund Horn and Jakob Albert

P. Kampe, N. Herrmann, C. Ruhmlieb, M. Finsel, O. Korup, R. Horn, J. Albert. “Spatially Resolved Reaction Profiles of CO₂ Hydrogenation to Methanol Using In-Based Catalysts in a Compact Profile Reactor”, *ACS Sustainable Chemistry & Engineering*, 2024, 12, 25, 9541-9549, DOI: doi.org/10.1021/acssuschemeng.4c03279

Published under a Creative Commons license.

In the previous Chapters 6.1 and 6.2, a continuous fixed bed reactor system with integral operation (sampling at the end of the catalyst bed) was used. This Chapter is based on publication [20]. The supported In_2O_3 -based catalysts were spatially examined using a two-phase fixed bed CPR (differential operation). This setup provides insights into simultaneous temperature and reaction profiles during CO_2 hydrogenation to methanol (see Figure 6.4). Nickel as a promoter significantly enhanced the catalytic activity of pure $\text{In}_2\text{O}_3/\text{ZrO}_2$, confirming the results in Chapter 6.2. The corresponding Supporting Information of the following article can be found in the Appendix Chapter 9.5 and details about the CPR in Chapter 9.1.4.

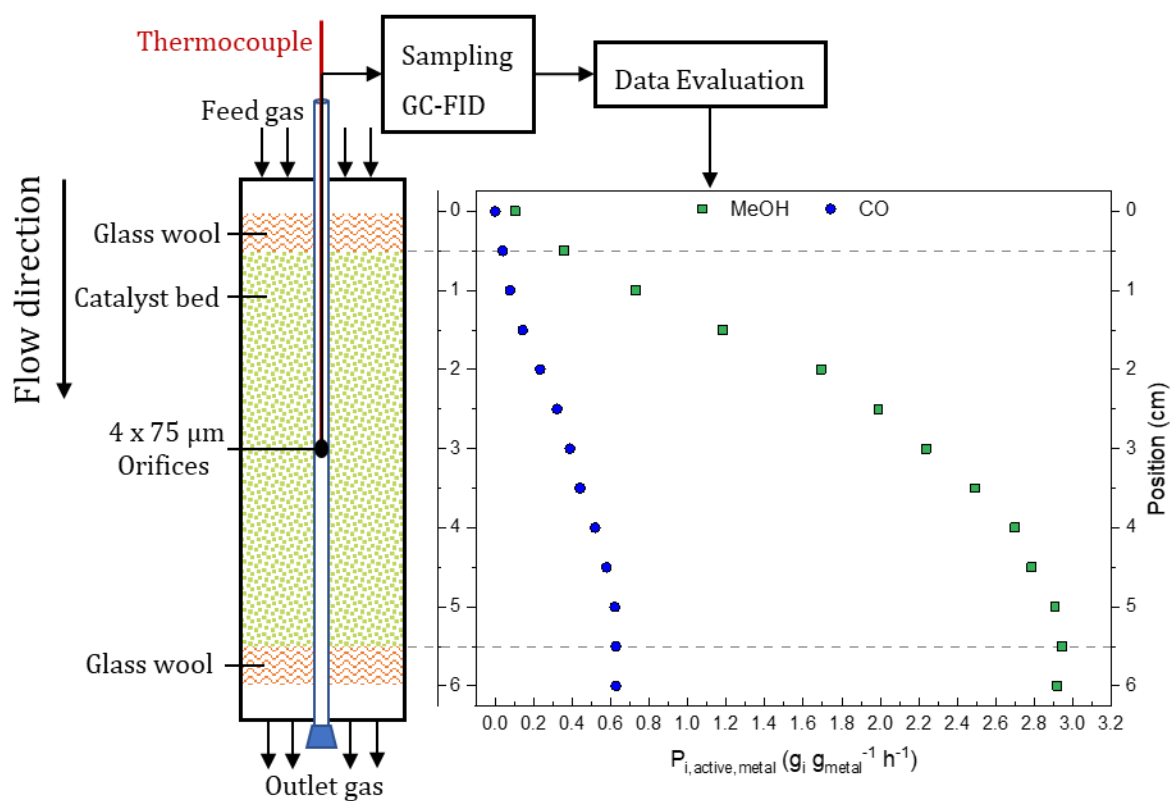


Figure 6.4. Schematic CPR design with corresponding productivity profiles for CO and MeOH at each position using Ni- $\text{In}_2\text{O}_3/\text{ZrO}_2$ catalyst [20].

Spatially Resolved Reaction Profiles of CO₂ Hydrogenation to Methanol Using In-Based Catalysts in a Compact Profile Reactor

Philipp Kampe,[†] Nick Herrmann,[†] Charlotte Ruhmlieb, Maik Finsel, Oliver Korup, Raimund Horn, and Jakob Albert*



Cite This: *ACS Sustainable Chem. Eng.* 2024, 12, 9541–9549



Read Online

ACCESS |



Metrics & More



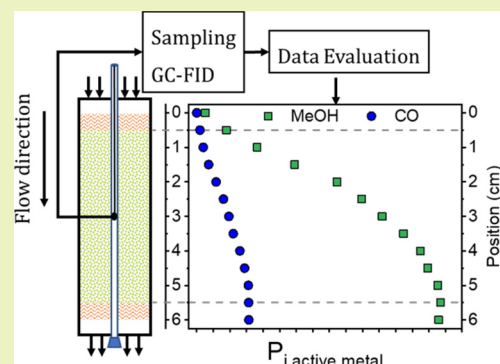
Article Recommendations



Supporting Information

ABSTRACT: The compact profile reactor (CPR) design allows for the simultaneous acquisition of species, temperature, and spatially resolved reaction profiles during high-pressure CO₂ hydrogenation to methanol. Indium-based catalysts for CO₂ hydrogenation have attracted significant scientific interest since they are more selective, efficient, and resistant to deactivation compared to the state-of-the-art copper-based catalyst. In this study, the reaction profile of In₂O₃/ZrO₂ catalysts is compared to that of the state-of-the-art Cu/ZnO/Al₂O₃ (CZA) catalyst in a high-pressure CPR. It is demonstrated that the addition of nickel as a promoter significantly enhanced the catalytic activity of pure In₂O₃/ZrO₂. The characterization by H₂ TPR and CO₂ TPD revealed an increased capacity for both hydrogen and CO₂. A detailed comparison and optimization of reaction conditions using Ni–In₂O₃/ZrO₂ as a catalyst are presented. In an optimized experiment, Ni–In₂O₃/ZrO₂ produces 4.90 g_{MeOH} g_{In+Ni}⁻¹ h⁻¹ at 275 °C, 50 bar, and 63,000 h⁻¹ with a methanol selectivity of 73%. Furthermore, no catalyst deactivation caused by metal leaching or sintering could be observed over 90 h time on stream.

KEYWORDS: methanol synthesis, compact profile reactor, CO₂ hydrogenation, indium oxide catalyst, Ni doping, hydrogen spillover



INTRODUCTION

The CO₂ emissions rise since the industrial revolution and have a significant effect as a greenhouse gas for global warming.¹ A promising approach for greenhouse gas reduction is the valorization of CO₂ from industrial off-gases with renewable hydrogen into valuable and sustainable products such as methanol.² Different reactor designs have already been employed for this task but were not thoroughly examined yet.

Industrial fixed-bed methanol reactors can be categorized into two types based on the approach used for heat removal within the catalyst bed: (A) adiabatic and (B) isothermal reactors.³ A typical adiabatic reactor consists of multiple catalyst beds (up to five) arranged in series within a single pressurized shell and with direct cooling (quench) or interstage heat exchange. For example, the ICI low-pressure quench converter operates at 50–100 bar and 270 °C by using the Cu/ZnO/Al₂O₃ (CZA) catalyst in a single bed. The quench gas is injected and distributed into the bed by lozenges. These traverse horizontally across the converter from one side to the other. A central pipe is used to feed the cold gas. The addition of cold, fresh, and recycled syngas helps to alleviate the reaction temperature. Caused by the variable void fraction along the catalyst bed, each catalyst pellet does not receive the same gas flow, resulting in irregular flux distribution. Thus, both hot and cold zones can be located in the bed.⁴ Thermal sintering of the CZA occurs at temperatures above 300 °C and

leads to deactivation.⁵ Lower temperatures, on the other hand, decelerate the reaction rate.

The Lurgi (now Air Liquide) converter, an isothermal reactor, is widely used in the industry for methanol synthesis. Typical operating conditions range from 50 to 100 bar and from 230 to 365 °C.⁴ An isothermal reactor integrates plates or tubes in the catalytic bed for heat removal and a more uniform distribution of the temperature. A shell-and-tube design supplies boiling water to the shell side, removing the reaction heat released by the catalyst on the tube side. Consequently, this approach ensures enhanced productivity, prolonged catalyst life, reduced byproduct formation, efficient recovery of reaction heat, and lower operating costs. The design with helically arranged tubes prevents catalytic stress caused by axial temperature variations, which is a classic problem in straight fixed-bed reactors.^{3,4}

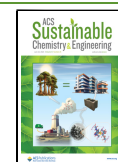
Although the temperature can be controlled in both reactors, they lack a fundamental understanding of gas-phase composition throughout the catalyst bed since there are only

Received: April 19, 2024

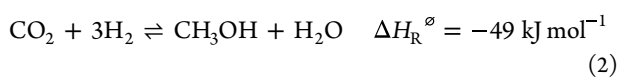
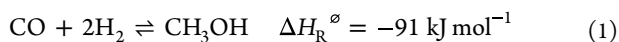
Revised: May 28, 2024

Accepted: May 29, 2024

Published: June 7, 2024



integral measurements for the reactors possible due to the reactor design. The main reactions in methanol synthesis are provided below.



The common industrial approach for methanol synthesis is using syngas (1) in combination with the state-of-the-art Cu/ZnO/Al₂O₃ catalyst.⁶ The major compounds of syngas are CO and H₂, while small amounts of CO₂ are added for an increase in catalyst activity.⁷ Compared to the CO hydrogenation, the CO₂ hydrogenation generates less reaction heat (2) and the endothermic rWGS (3) attenuates heat release in the process. The formation of water on the surface of the catalyst leads to deactivation by segregating Cu/ZnO and interrupting the strong metal–support interaction effect that is required for the catalyst activity.⁸ In the presence of CO₂, water and CO are formed via the competitive reverse water–gas shift reaction (rWGS, 3), which lowers the methanol selectivity. To enhance the stability of CZA and to shift the thermodynamic equilibrium toward methanol (according to Le Chatelier's principle), water can be removed in situ with novel membrane reactors (laboratory level).⁹ A slurry reactor concept using a carrier thermoliquid with the advantages of a simple construction, facile reactor control, and efficient heat storage has been already employed in more recent studies.^{10–12} Reducing particle sizes in slurry reactors allows for their use without the necessity to account for pressure drop along a catalyst bed. Additionally, this results in less attrition of the catalyst particles. Gaikwand et al. split the commercial CZA catalyst into three catalyst beds separated by empty sections.¹³ This study showed that methanol is produced through high-pressure direct CO₂ hydrogenation at low temperatures, while above 260 °C, methanol formation is facilitated by CO, which is generated through the rWGS reaction.

Indium-based catalysts have recently been studied extensively as alternative methanol synthesis catalysts by CO₂ hydrogenation.^{14–18} The ZrO₂ supported In₂O₃ catalyst also showed high stability, selectivity, and activity for CO₂ hydrogenation to methanol.^{10,16,19–29} In previous studies by Wesner and Kampe et al., the effects of the catalyst support, synthesis method, and metal promoter were identified to be key factors to increase the catalytic performance in the CO₂ hydrogenation to methanol.¹⁷

The objective of this paper is to provide first insights into spatially resolved measurements on indium-based methanol synthesis catalysts using a novel compact profile reactor (CPR) under high-pressure operating conditions. The CPR offers insights into reactant composition and temperature profiles in a scalable reactor tube and is already established at mild reaction conditions for various heterogeneously catalyzed reactions.^{30–33} In this work, we adapt a modified CPR to high-pressure methanol synthesis conditions and compare the reaction profiles of various indium-based catalysts to those of the commercial copper-based catalyst. In detail, the state-of-the-art Cu/ZnO/Al₂O₃ catalyst in relation to an In₂O₃/ZrO₂ catalyst will be spatially examined and discussed. Moreover, metal-promoted indium-based catalysts will be further investigated with a specific focus on the influence of certain

reaction parameters like pressure, GHSV, and temperature using the most promising catalyst.

EXPERIMENTAL DETAILS

Materials. The following reagents were used as precursors for catalyst synthesis: zirconium dioxide pellets (ZrO₂, Saint Gobain), indium nitrate (In(NO₃)₃, 99.999% Thermo Fisher Scientific), cerium nitrate hexahydrate (Ce(NO₃)₃·6H₂O, 99.5% Thermo Fisher Scientific), copper nitrate trihydrate (Cu(NO₃)₂·3H₂O, 99% Thermo Fisher Scientific), and nickel nitrate hexahydrate (Ni(NO₃)₂·6H₂O 99%, Sublab). A commercial copper-based catalyst (CuO/ZnO/Al₂O₃) was purchased from Alfa Aesar (product no. 45776). A gas mixture of hydrogen and carbon dioxide (25% CO₂, 4.5 grade and 75% H₂, 5.0 grade) from Westfalen was used for the catalytic experiments in the CPR reactor. Nitrogen (N₂, 5.0 grade, Linde) was used as a purging gas, and hydrogen (H₂, 5.0 grade, Linde) was used for the catalyst preforming. All chemicals were used as received without further purification.

Catalyst Synthesis. An In₂O₃/ZrO₂ catalyst with 10 wt % of indium loading was prepared by wet impregnation according to previously published methods.¹⁶ Zirconium dioxide pellets were first crushed and sieved to a particle size of 80–250 μm. In(NO₃)₃ (6.84 g) was dissolved in a solution of ethanol and deionized water (3:1, 850 mL), and ZrO₂ (18 g, 80–250 μm) was added. The suspension was stirred for 5 h (21 °C, 800 mbar), and the solvent was removed at elevated temperature and reduced pressure (70 °C, 200 mbar) afterwards. The residue was dried for 12 h (65 °C) and calcined for 3 h (300 °C, ramp of 5 °C min⁻¹) in a muffle furnace.

The synthesis of the metal-promoted M-In₂O₃/ZrO₂ catalysts with 1 wt % of promoter was done by wet impregnation. Metal nitrate was dissolved in deionized water (250 mL), and In₂O₃/ZrO₂ (15 g) was added. The suspension was stirred for 5 h (21 °C, 800 mbar), and the solvent was removed at elevated temperature and reduced pressure (70 °C, 200 mbar) afterwards. The residue was dried for 12 h (65 °C) and calcined for 3 h (300 °C, ramp of 5 °C min⁻¹).

Catalyst Characterization. Inductively coupled plasma optical emission spectroscopy (ICP-OES) was used for determining the elementary composition of the catalysts. Hereby, 100 mg of a catalyst sample was digested in 5 mL of conc. H₂SO₄ and 1 mL of fuming HNO₃. It was then atomized in an argon plasma, and the composition was quantified using optical emission spectroscopy. The characterization was carried out on an ASCOR-spectrometer (Fa. Spectro) by the central element analysis service (Department of Chemistry, University of Hamburg).

Nitrogen physisorption was carried out with an Autosorb iQ-MP/XR analyzer (Fa. Quantachrome Instruments) at 77 K. First, the sample was degassed at 473 K at reduced pressure for 10 h prior to analysis. Using the Brunauer–Emmett–Teller (BET) model, the specific surface area of the sample was determined, and the pore volume was calculated by using the Barrett–Joyner–Halenda (BJH) model.

Temperature-programmed desorption of CO₂ (CO₂ TPD) and temperature-programmed reduction by H₂ (H₂ TPR) were measured using a ChemBET Pulsar (Fa. Quantachrome Instruments). Prior to CO₂ TPD, samples (0.3 g) were exposed to a He gas flow (80 mL/min) and heated up to 200 °C (10 K/min) for 1 h to remove surface H₂O. The loading of the surface with CO₂ was also carried out at 200 °C, followed by cooling to 50 °C. The sample was thereafter heated under a He gas flow (80 mL/min, 10 °C/min) to 700 °C, and the desorbed CO₂ was measured via a thermal conductivity detector (TCD). Prior to H₂ TPR, samples (0.3 g) were exposed to a N₂ gas flow (80 mL/min) and heated up to 180 °C (10°/min) for 1 h to remove surface H₂O, followed by cooling to 100 °C. The sample was heated again under a H₂/N₂ (5/95 v/v) gas flow (80 mL/min, 10 °C/min) to 850 °C. The used H₂ was measured by a thermal conductivity detector (TCD).

Powder X-ray diffraction (p-XRD) was carried out using a Panalytical MDP X'Pert Pro diffractometer using Cu Kα (λ = 0.1541 nm) radiation. The measuring range of the diffraction angle

was 10–80° and sampled using a rate of 0.013° with a counting time of 0.3 s. In₂O₃ particle sizes were calculated using a modified Scherrer equation³⁴ based on the characteristic diffraction reflections as described in the Supporting Information, eq S5. The XRD patterns for indium-based catalysts can be found in Figure S2.

Scanning transmission electron microscopy (SEM) was used to obtain images of the sample surface. A Zeiss LEO Gemini 1550 equipped with a field emission gun and a beam energy of 20 kV was used. Energy-dispersive X-ray spectroscopy (EDX) elemental maps were obtained by using an Ultim Max 100 silicon drift detector from Oxford Instruments. The SEM-EDX elemental mappings for all synthesized indium-based catalysts can be found in Figure S3.

Implementation of the Compact Profile Reactor (CPR) for High-Pressure Methanol Synthesis. CO₂ hydrogenation to methanol was carried out using a CPR (see Figure 1, Reacnostics

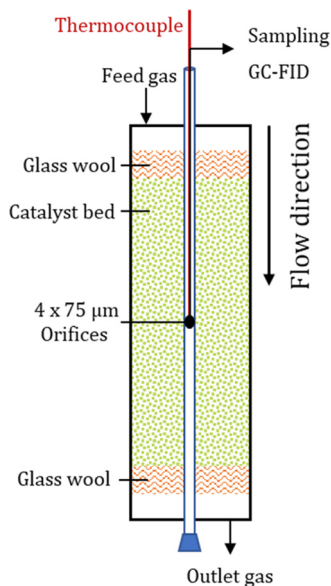


Figure 1. Graphical scheme of the compact profile reactor (CPR).

GmbH, Hamburg, Germany). The stainless-steel reactor tube (length: 182 mm; inner diameter: 4 mm; outer diameter: 6 mm) was filled with a 50 mm-long catalyst bed. The catalyst bed was fixated in between two 5 mm quartz wool plugs. Through the catalyst bed, a

stainless-steel capillary with four orifices in the wall (diameter: 75 μm) is placed at a defined position inside the reactor tube. Inside the capillary at the location of the four bores, the temperature of the catalyst bed is measured by a thermocouple. The reactor is installed on a guide rail, enabling movement along the capillary in the axial direction. This allows spatially resolved sampling of the gas phase through the orifices and measurement of the temperature in the catalyst bed using a thermocouple in the capillary (see Figure 1).

The capillary for sampling was connected to an online gas chromatograph (Bruker 450-GC), furnished with one thermal conductivity detector (TCD), two flame ionization detectors (FIDs), one methanizer, and four gas chromatography columns (Restek Q-Bond, Restek U-Bond, Bruker Swax, Bruker Molsieve 5 Å) to analyze the gas composition. For more details about the experimental setup, see Figure S1.

Calculations. The active metal productivities of methanol and CO $P_{i,\text{active metal}}$ are defined as the mass flow of the component $\dot{m}_{i,\text{out}}$ related to the active mass of the metal catalyst, which is the mass of the catalyst m_{cat} multiplied with the sum of the active metal $\sum \omega_{\text{active metal}}$

$$P_{i,\text{active metal}} = \frac{\dot{m}_{i,\text{out}}}{m_{\text{cat}} \times (\sum \omega_{\text{active metal}})} \quad (4)$$

The selectivity S_i for product i is calculated by determining the ratio of the desired product molar flow to the molar flow of consumed CO₂

$$S_i = \frac{\dot{n}_{i,\text{out}} - \dot{n}_{i,\text{in}}}{\dot{n}_{\text{CO}_2,\text{in}} - \dot{n}_{\text{CO}_2,\text{out}}} \times 100\% \quad (5)$$

The gas hourly space velocity (GHSV) was employed to establish a relationship between the standard volume flow (\dot{V}_N) and the catalyst volume (V_{cat})

$$\text{GHSV} = \frac{\dot{V}_N}{V_{\text{cat}}} \quad (6)$$

More details for the calculations are provided in the Supporting Information, eqs S1–S4.

RESULTS AND DISCUSSION

At first, the CPR was set up to run at the desired reaction temperature and pressure of up to 275 °C and 75 bar, respectively. A control experiment with glass beads was performed to investigate the volume-induced pressure drop and to exclude any blind activity. No catalytic activity was

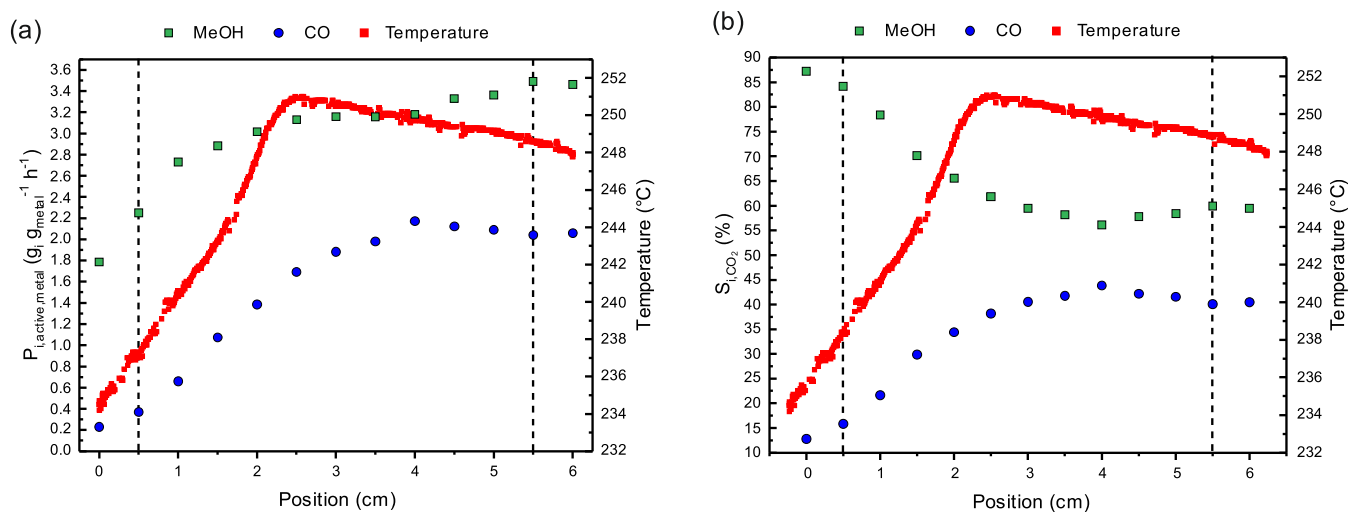


Figure 2. Spatially resolved temperature and product profile of CZA at $T = 250$ °C, $p = 50$ bar, $\text{GHSV} = 63,000$ h⁻¹, and a feed gas composition of CO₂/H₂ = 1/3. The measurements were taken between 5 and 35 h TOS. (a) Active metal productivity and (b) selectivity to MeOH (green) and CO (blue) and temperature profile (red).

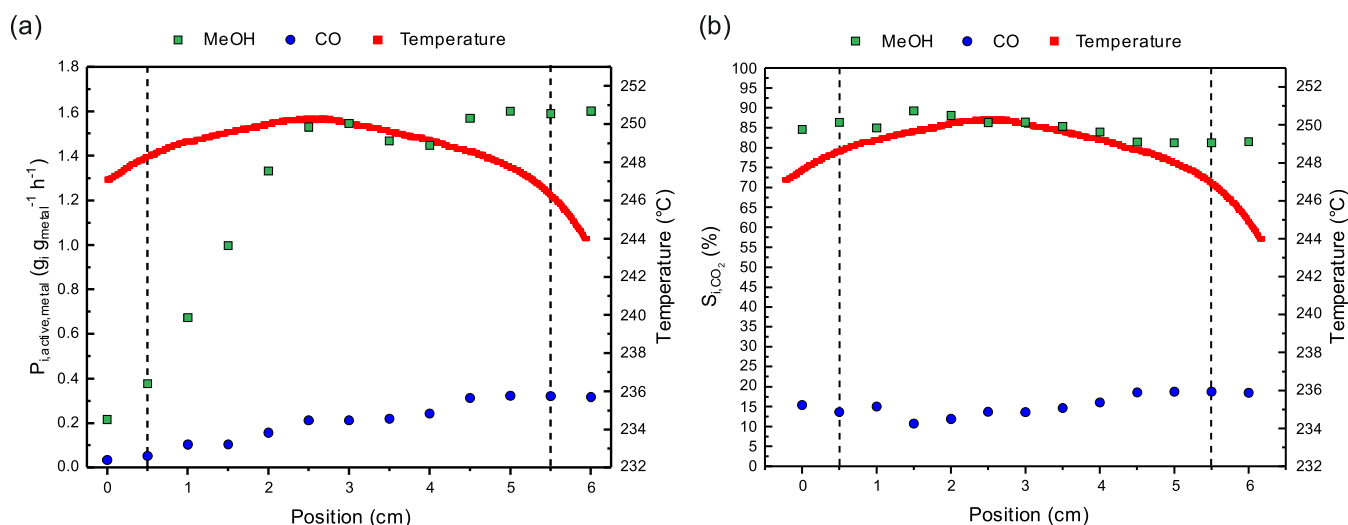


Figure 3. Spatially resolved temperature and product profile of In₂O₃/ZrO₂ at $T = 250$ °C, $p = 50$ bar, GHSV = 63,000 h⁻¹, and a feed gas composition of CO₂/H₂ = 1/3. The measurements were taken between 5 and 35 h TOS. (a) Active metal productivity and (b) selectivity of MeOH (green) and CO (blue) and temperature profile (red).

observed. At the maximum gas flow rate of 900 mL_N min⁻¹ (GHSV = 95,000 h⁻¹), CO₂/H₂ = 1/3 at 75 bar, a pressure drop below 0.2 bar was determined and can be neglected. For the In₂O₃-ZrO₂ catalyst, a range of 60–250 μm particle size showed the absence of internal mass transfer limitations according to the Weisz–Prater criterion of 0.015.³⁵ Therefore, a particle size range between 80 and 250 μm was applied for the CPR.

Applying the CPR Reactor for the Commercial Cu/ZnO/Al₂O₃ Catalyst. The catalyst of choice for industrial-scale fossil fuel-based methanol synthesis is the Cu/ZnO/Al₂O₃ catalyst (CZA). An alternative renewable approach is CO₂ hydrogenation using hydrogen from water electrolysis and CO₂ from industrial exhaust gases.²⁹ While the CZA catalyst is highly active and stable for CO hydrogenation, it deactivates under CO₂ hydrogenation reactions due to the formation of water.⁵ The characteristic properties of methanol catalysts strongly depend on both the applied CO amount and reaction conditions. The reaction profile of the CZA for methanol and the byproduct CO due to rWGS is shown in Figure 2 at 50 bar, 250 °C, GHSV = 63,000 h⁻¹, and a feed gas composition of CO₂/H₂ = 1/3. The measurements were taken after reaching steady-state conditions at 5 h time on stream (TOS) for each measurement point. The thermocouple inside the capillary measures the temperature of the gas flow at a certain position. An increase in temperature from the beginning of the catalyst bed was observed up to a maximum of 251 °C at 2.5 cm packing height. This can be attributed to the direct methanol formation by CO₂, which is exothermic. The competing endothermic rWGS reaction increases in the same reaction volume, buffering the temperature, leading to a slight decrease from the maximum. At about 4 cm of the catalyst bed, we observed the highest formation rate of CO (2.17 g_{CO}·g_{Cu}⁻¹·h⁻¹) and no significant change until the end of the catalyst bed (see Figure 2a). Presumably, the catalyst bed reached the highest temperature at this point, and from this point on, there is no significant change in the formation of MeOH or CO with a longer packing height. The selectivity of methanol stabilizes at around 58% (see Figure 2b). Over the entire catalytic bed, the active methanol productivity increases to 3.46 g_{MeOH}·g_{Cu}⁻¹·h⁻¹ at 6 cm.

For the CZA catalyst, Nielsen et al. concluded that at high conversions, the rate of methanol formation is optimal with a higher CO content. This can be traced back to the ability of CO to remove inhibiting surface-bound water via the WGS reaction.³⁶ Because of this effect, the methanol formation can be increased a little further at the end of the catalyst bed.

After 55 h time on steam, the active productivity at the reactor outlet decreased to 3.01 g_{MeOH}·g_{Cu}⁻¹·h⁻¹. The deactivation is a result of the accelerated crystallization of copper and zinc oxide induced by the byproduct water.^{37,38}

Applying the CPR Reactor for the In₂O₃/ZrO₂ Catalyst. A well-discussed and promising alternative catalyst for the direct CO₂ hydrogenation to methanol is the In₂O₃/ZrO₂ catalyst. While the CZA catalyst is sensitive to temperatures above 300 °C and in situ water formation (44% loss in activity over 100 h time on stream), the In₂O₃/ZrO₂ shows no loss in stability during 1000 h time on stream.¹⁶ For the first time, the spatial resolution of the product formation and temperature profile in the catalyst bed was performed using the CPR at 50 bar, 250 °C, GHSV = 63,000 h⁻¹, and a feed gas composition of CO₂/H₂ = 1/3. The measurements were taken under steady-state conditions after 5 h of TOS and 5 h for each measurement point (Figure 3). In comparison to the CZA, less methanol (1.60 g_{MeOH}·g_{In}⁻¹·h⁻¹ between 5.0 and 5.5 cm) and CO (0.32 g_{MeOH}·g_{In}⁻¹·h⁻¹) was produced (see Figure 3a). Therefore, less reaction heat is released and a lower temperature profile (between 244 and 250 °C) was observed. The lower catalytic activity of In₂O₃/ZrO₂ compared to that of CZA can be explained by the smaller surface area of 74 m²·g⁻¹ for In₂O₃/ZrO₂ compared to the 99 m²·g⁻¹ for CZA (Table S2). The high methanol selectivity varies slightly throughout the length of the catalyst bed between 81 and 89% (Figure 3b).

Applying the CPR Reactor for the Metal-Promoted In₂O₃/ZrO₂ Catalysts. Building on the work of Frei et al. and Kampe et al.,^{11,17,20} it was shown that nickel-promoted In₂O₃/ZrO₂ could enhance the catalytic performance compared to pure In₂O₃/ZrO₂. To determine the spatially resolved difference in catalytic performance, we tested the Ni–In₂O₃/ZrO₂ catalyst in the CPR at the same reaction conditions ($p = 50$ bar, $T = 250$ °C, see Figure 4).

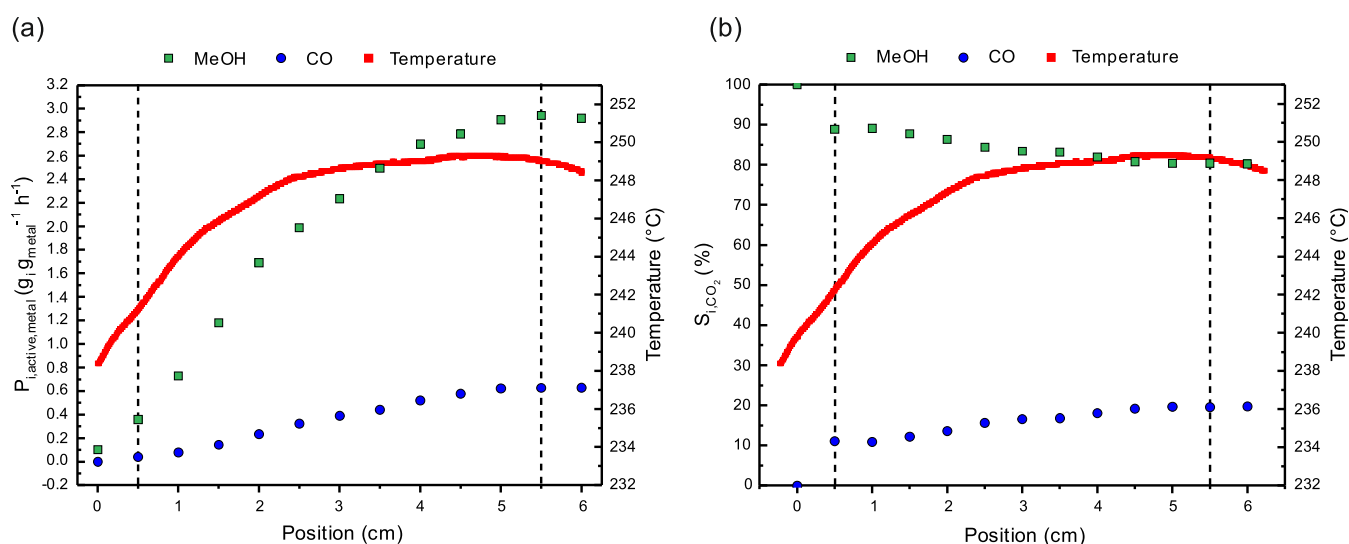


Figure 4. Spatially resolved temperature and product profile of Ni–In₂O₃/ZrO₂ at $T = 250$ °C, $p = 50$ bar, GHSV = 63,000 h⁻¹, and a feed gas composition of CO₂/H₂ = 1/3. The measurements were taken between 5 and 35 h TOS. (a) Active metal productivity and (b) selectivity of MeOH (green) and CO (blue) and temperature profile (red).

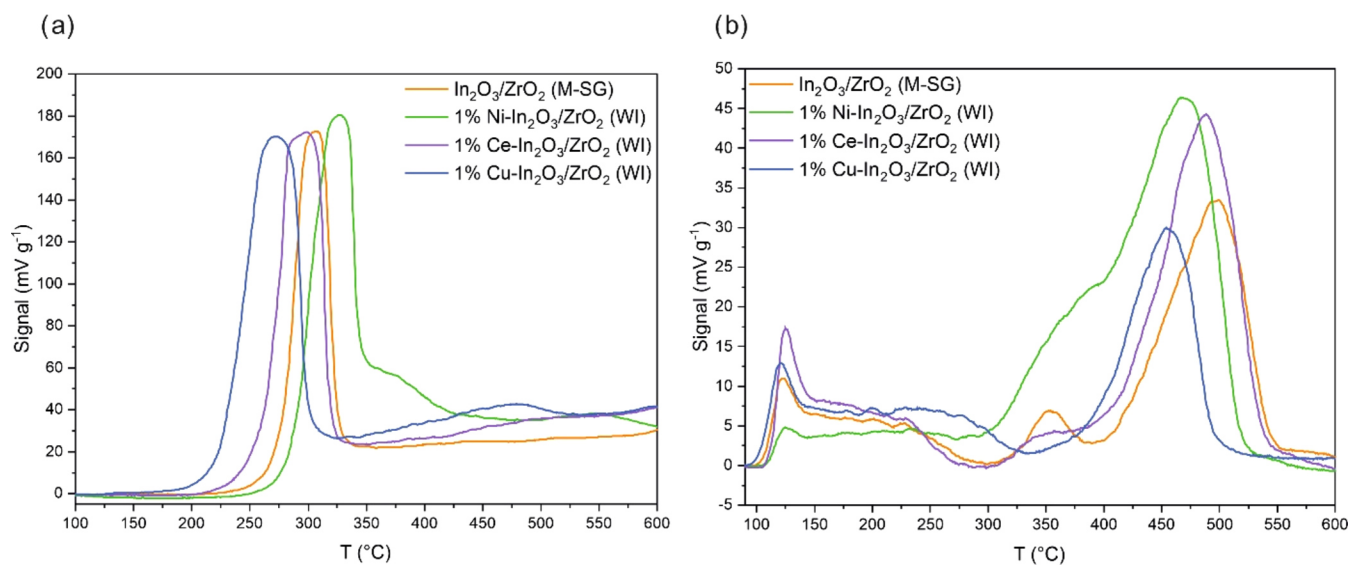


Figure 5. Reducibility and CO₂ adsorption capacity of the In₂O₃/ZrO₂ catalyst compared to the metal-promoted In₂O₃/ZrO₂ catalysts. H₂ TPR (a) and CO₂ TPD (b).

The addition of 0.76 wt % Ni to In₂O₃/ZrO₂ via wetness impregnation (Table S2) shows a tremendous increase in methanol productivity (2.94 g_{MeOH}·g_{In+Ni}⁻¹·h⁻¹ at 5.5 cm) compared to In₂O₃/ZrO₂ (1.59 g_{MeOH}·g_{In}⁻¹·h⁻¹ at 5.5 cm). This can be explained by a higher uptake of hydrogen and CO₂ compared to the other metal-promoted In-based catalysts (Figure 5). Notably, the reduction at temperatures above 350 °C exhibits a distinctive pattern for the nickel-promoted catalysts. The uptake of hydrogen can in part be attributed to the generation of oxygen vacancies, which in turn facilitate CO₂ adsorption and force methanol formation at the In₂O₃/ZrO₂ interface.³⁹ The vacancies are part of the active sites for CO₂ hydrogenation⁴⁰ through the substantially facilitated In₂O₃ reduction as reported by Frei et al.²⁰ The phenomenon of hydrogen spillover underscores the unique behavior of nickel in the reduction process,⁴¹ contributing to its highest total hydrogen uptake per gram of catalyst. In the context of CO₂ temperature-programmed desorption (CO₂ TPD), the

desorption of weakly adsorbed CO₂ occurs at 120 °C across all examined catalysts. Chemically bound CO₂ is subsequently desorbed, providing insights into potential binding sites and their strength. Remarkably, the nickel-promoted catalyst exhibits the highest capacity to adsorb CO₂ compared to that of the other catalysts. Coupled with weaker binding sites, this manifests as a broad shoulder in the temperature range of 300–400 °C and distinguishes the nickel-promoted catalyst from the others. The highest signal area for stronger binding sites could also be attributed to the nickel-promoted catalyst as well (around 475 °C).²⁰

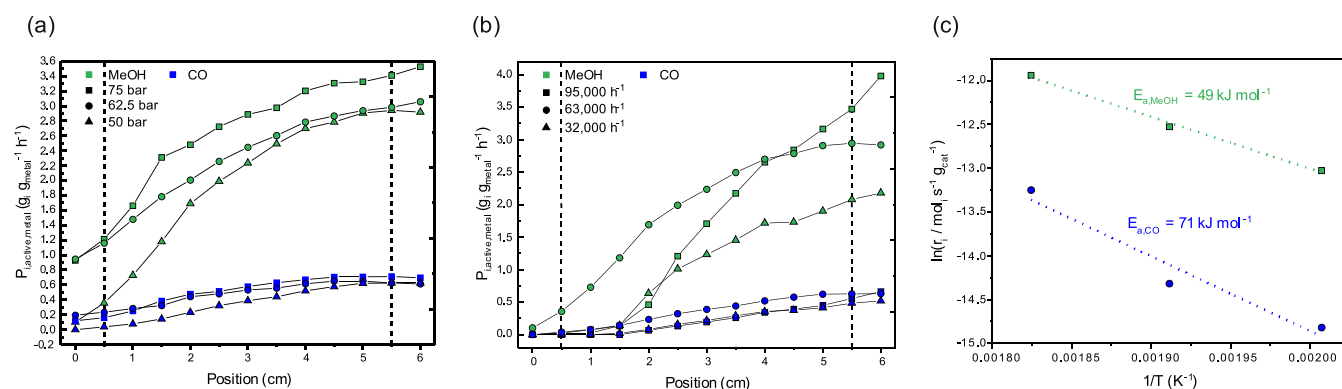
An increase of catalyst surface area (80.66 m²·g⁻¹) by Ni doping was observed as well, leading to a better accessibility of the reactants. No methanation was observed, which is well in line with the literature.^{11,17,20} After 90 h time on stream, the active productivity at the reactor outlet increased slightly from 2.96 g_{MeOH}·g_{In+Ni}⁻¹·h⁻¹ to 3.07 g_{MeOH}·g_{In+Ni}⁻¹·h⁻¹ with no apparent deactivation. Besides nickel, other promoter metals such as

Table 1. Integral Catalytic Performance (6.0 cm) of Pure and Metal-Promoted In₂O₃/ZrO₂ Catalysts at $p = 50$ bar ($H_2/CO_2 = 3:1$), $T = 250$ °C, and GHSV = 63,000 h⁻¹.^a

catalyst	$S_{MeOH}/\%$	$P_{MeOH,active,metal}/g_{MeOH} g_{metal}^{-1} h^{-1}$	$P_{CO,active,metal}/g_{CO} g_{metal}^{-1} h^{-1}$	nominal H ₂ reduction capacity	nominal CO ₂ adsorption capacity
In ₂ O ₃ /ZrO ₂	82 ± 0	1.60 ± 0.03	0.32 ± 0.00	1.00	1.00
Ce–In ₂ O ₃ /ZrO ₂	89 ± 1	1.52 ± 0.02	0.17 ± 0.03	1.28	1.26
Cu–In ₂ O ₃ /ZrO ₂	85 ± 2	1.90 ± 0.03	0.29 ± 0.05	1.52	0.70
Ni–In ₂ O ₃ /ZrO ₂	80 ± 0	2.96 ± 0.04	0.63 ± 0.02	1.40	1.56

^aNominal H₂ Reduction and CO₂ Adsorption Capacity.**Table 2. Effect of Reaction Conditions on the Integral Catalytic Performance of Ni–In₂O₃/ZrO₂ at the Outlet (6.0 cm) of the Compact Profile Reactor Using a Feed Gas Composition of CO₂/H₂ = 1/3**

parameter ^a	$S_{MeOH}/\%$	$P_{MeOH,active,In+Ni}/g_{MeOH} g_{In+Ni}^{-1} h^{-1}$	$P_{CO,active,metal}/g_{CO} g_{In+Ni}^{-1} h^{-1}$
50 bar	80 ± 0	2.96 ± 0.04	0.63 ± 0.02
62.5 bar	81 ± 0	3.06 ± 0.03	0.61 ± 0.01
75 bar	81 ± 0	3.54 ± 0.07	0.70 ± 0.03
32,000 h ⁻¹	79 ± 0	2.18 ± 0.01	0.52 ± 0.01
63,000 h ⁻¹	80 ± 0	2.96 ± 0.04	0.63 ± 0.02
95,000 h ⁻¹	84 ± 0	3.98 ± 0.03	0.67 ± 0.00
225 °C	83 ± 0	1.88 ± 0.02	0.33 ± 0.00
250 °C	80 ± 0	2.96 ± 0.04	0.63 ± 0.02
275 °C	73 ± 1	4.90 ± 0.01	1.57 ± 0.06

^aInfluence of total pressure at 250 °C and 63,000 h⁻¹, GHSV at 250 °C and 50 bar, and temperature at 50 bar and 63,000 h⁻¹.**Figure 6.** Influence of the reaction conditions on spatially resolved temperature and product profiles of Ni–In₂O₃/ZrO₂ using a feed gas composition of CO₂/H₂ = 1/3. The measurements were taken between 5 and 35 h TOS. (a) Pressure variation at $T = 250$ °C and GHSV = 63,000 h⁻¹. (b) GHSV variation at $T = 250$ °C and $p = 50$ bar and (c) apparent activation energies of MeOH (green) and CO (blue).

copper and cerium have been tested as well (Table 2). However, they showed a similar behavior in the CPR but were inferior in terms of methanol productivity compared to nickel doping, which underlines the outstanding performance of Ni as a promoter and correlates with the findings of H₂ TPR and CO₂ TPD. Moreover, all indium-based catalysts showed a significantly higher methanol selectivity ($S = 80$ – 90%) compared to the commercial CZA catalyst ($S = 40\%$) under the applied reaction conditions. A summary of the integral catalytic performance (6.0 cm) for the metal-promoted and pure In₂O₃/ZrO₂ is shown in Table 1. More details on the spatial reaction profiles for copper- and cerium-promoted catalysts can be found in the Supporting Information (Figure S5).

Influence of Reaction Conditions on the Catalytic Performance of the Ni–In₂O₃/ZrO₂ Catalyst in the CPR. Impact of Total Pressure. The impact of total pressure on the catalytic performance in the CPR is generally in accordance with the principle of Le Chatelier. With an increase in pressure, the overall productivity of methanol is higher throughout the

CPR (see Table 2 and Figure 6a). At 50 bar reaction pressure, the methanol productivity rises until a maximum productivity (2.92 g_{MeOH}·g_{In+Ni}⁻¹·h⁻¹) is achieved at the reactor outlet (6.0 cm). At 62.5 bar, an increase in methanol productivity (3.06 g_{MeOH}·g_{In+Ni}⁻¹·h⁻¹) past the catalyst bed could be observed. This could be increased to 3.53 g_{MeOH}·g_{In+Ni}⁻¹·h⁻¹ at 75 bar, indicating more headroom for the methanol generation due to the higher thermodynamic equilibrium conversion at higher pressure.⁴² The steep slope of methanol production from the beginning of the catalyst bed to about 4 cm could be attributed to the parallel hydrogenation of CO₂ and CO coming from the parallel rWGS reaction. The gradient of methanol production between 4 and 5.5 cm decreases, as CO formation no longer increases. Methanol selectivity remains constant at approximately 80%, regardless of pressure. The rWGS is not affected by pressure according to Le Chatelier's principle assuming an ideal gas. We observed a negligible impact of pressure on the CO production at the end of the catalyst bed. It is remarkable that the CO productivity reaches its highest point before the end of the catalyst bed (4.5 cm) and remains constant and

even decreases at the end of the catalyst bed. Therefore, a higher overall pressure with a longer reaction bed could be favorable for both an increase in methanol selectivity and productivity.

Effect of Contact Time/Influence of the Gas Hourly Space Velocity (GHSV). Similar to the effect of increasing pressure, a higher methanol productivity can be observed for higher GHSVs, shorter residence time, and a reduction of the thickness of the diffusion boundary layer (Figure 6b). This means that a shorter contact time is favorable for methanol generation using the Ni–In₂O₃/ZrO₂ catalyst. This agrees with the results of In₂O₃/ZrO₂ that were shown in the previous literature. Higher GHSVs shift the selectivity toward methanol, while low contact times increase the MeOH production rate, keeping the CO formation constant.¹⁶ According to the calculated Carberry number $Ca = 0.03$ (50 bar, 250 °C), the estimated extraparticle mass transfer does not limit the reaction rate ($Ca < 0.05$) at the boundary layer (detailed calculations are reported in the SI, Table S1 and eqs S6–S15).

As the GHSV increases, productivity seems to rapidly increase throughout the reaction profile. At 32,000 h⁻¹, the methanol productivity reaches 2.18 g_{MeOH}·g_{In+Ni}⁻¹·h⁻¹, increasing to 2.96 g_{MeOH}·g_{In+Ni}⁻¹·h⁻¹ at 63,000 h⁻¹ until the end of the catalyst bed. A further increase of the GHSV to 95,000 h⁻¹ resulted in a boost of methanol productivity up to 3.98 g_{MeOH}·g_{In+Ni}⁻¹·h⁻¹. The use of the CPR setup reveals a decrease in the temperature at the reactor inlet as the GHSV increases. The increase in heat dissipation is compensated by a higher reaction rate due to lower contact times, in turn leading to more reaction heat and an increase in the overall methanol productivity. If the gas feed is too high, cooling the catalyst bed below a threshold temperature of 238 °C, the reaction heat is not enough to keep the methanol reaction rate high, and the catalyst is almost completely inactive at first. If a temperature of 238 °C is reached, the catalyst is suddenly activated, showing a linear trend in methanol productivity to the end of the reactor (see Figure S6). With a better temperature control by preheating of the feed gas, the catalyst performance can be tweaked to reach even higher methanol productivities, while the commercial CZA catalyst has already reached the highest productivities at half the catalyst bed, producing more CO and reducing the methanol selectivity.

Effect of Temperature to Determine Apparent Activation Energies. Higher temperatures significantly favor the production of CO due to the endothermic rWGS reaction. At the reactor outlet (6.0 cm), an increase of CO productivity from 0.329 g_{CO}·g_{In+Ni}⁻¹·h⁻¹ at 225 °C to 1.58 g_{CO}·g_{In+Ni}⁻¹·h⁻¹ at 275 °C can be observed. This is in line with the selectivity of methanol, which decreases from 83% (225 °C) to 73% (275 °C). Due to higher reaction kinetics at higher temperature, the methanol productivity reaches its highest amount of 4.90 g_{MeOH}·g_{In+Ni}⁻¹·h⁻¹ in this study (see Table 2). The apparent activation energies ($E_{a,i}$) for methanol synthesis and the rWGS reaction (Figure 6c) were obtained from integral catalytic performance (6.0 cm) at different temperatures by using an Arrhenius plot. The methanol production requires less activation energy (49 kJ mol⁻¹) than CO production does (71 kJ mol⁻¹) using the Ni–In₂O₃/ZrO₂ catalyst in a CPR. This has also been revealed several times in the previous literature for fixed-bed reactors.^{6,20,43} The activation energies show no limitations due to mass transport, as confirmed by the Ca number.

Post-mortem Characterization of the Ni-Promoted In₂O₃/ZrO₂ Catalysts. In order to round up this study, the

properties of the best-performing Ni–In₂O₃/ZrO₂ catalyst after 90 h time on stream in the CPR were further investigated. The relative amount of indium (10.94%) and nickel (0.83%) determined by ICP-OES increased slightly, being in the range of its measurement accuracy. Therefore, no leaching due to the Mond process took place. The In₂O₃ particle size calculated using the (611) reflection patterns and the Scherrer equation (eq S5) was slightly reduced from 8.6 to 8.3 nm (see Figure S7) possibly due to surface attrition without sintering. The diffraction patterns before and after the reaction reveal no changes in morphology (see Figure S4). SEM-EDX mappings showed no agglomeration and well-dispersed indium and nickel distribution after the reaction (see Figure S8).

CONCLUSIONS

In this study, a compact profile reactor (CPR) was applied for the first time to study the differential reaction profiles along the reactor length for different methanol synthesis catalysts. Recording of the local temperature throughout the whole catalyst bed was also implemented at steady-state conditions. Reaction profiles of the state-of-the-art CZA catalyst showed a distinct hot spot of the catalyst bed at 2.5 cm, while the indium-based catalysts showed a more uniform temperature profile along the catalytic bed. This leads to better temperature control and reduces the risk of hot spots for In-based catalysts. The addition of nickel to In₂O₃/ZrO₂ increased the productivity of methanol from 1.60 g_{MeOH}·g_{Metal}⁻¹·h⁻¹ up to 2.96 g_{MeOH}·g_{Metal}⁻¹·h⁻¹ due to higher CO₂ adsorption capacity as well as promoted reducibility of the surface. The effect of different reaction conditions on the catalytic performance of Ni–In₂O₃/ZrO₂ using the CPR showed that higher pressure, GHSV, and temperature increased the methanol productivity. Since the Ni–In₂O₃/ZrO₂ catalyst is more selective and hinders the rWGS reaction, shorter contact times can therefore be beneficial for higher methanol yields. Contrarily, higher temperatures decrease methanol selectivity and shift the methanol yield to lower values. The CZA produced 3.46 g_{MeOH}·g_{Cu}⁻¹·h⁻¹ methanol but was overall less selective (58%) and prone to long-term deactivation. In addition, the Ni–In₂O₃/ZrO₂ catalysts exhibit a lower metal loading on the catalyst support compared to CZA. Our findings show that Ni–In₂O₃/ZrO₂ catalysts are highly promising for selective hydrogenation of CO₂ to methanol (80%) in a CPR.

ASSOCIATED CONTENT

Supporting Information

The Supporting Information is available free of charge at <https://pubs.acs.org/doi/10.1021/acssuschemeng.4c03279>.

Process flow diagram, supporting calculations, mass transfer limitation criteria, synthesis and characterization of metal-promoted In₂O₃/ZrO₂ catalysts, XRD patterns and SEM-EDX mappings, (611) reflection patterns of In₂O₃/ZrO₂-based catalysts, integration of H₂ TPR and CO₂ TPD curves, results and temperature gradient of other Ce- and Cu-promoted In₂O₃/ZrO₂ catalysts, supporting temperature profile at different GHSVs for the Ni–In₂O₃/ZrO₂ catalyst, and supporting postmortem characterization of the Ni-doped catalyst (PDF)

AUTHOR INFORMATION

Corresponding Author

Jakob Albert – Institute of Technical and Macromolecular Chemistry, Universität Hamburg, 20146 Hamburg, Germany; orcid.org/0000-0002-3923-2269; Email: jakob.albert@uni-hamburg.de

Authors

Philipp Kampe – Institute of Technical and Macromolecular Chemistry, Universität Hamburg, 20146 Hamburg, Germany; orcid.org/0000-0001-8843-1240

Nick Herrmann – Institute of Technical and Macromolecular Chemistry, Universität Hamburg, 20146 Hamburg, Germany; orcid.org/0009-0003-8227-8654

Charlotte Ruhmlied – Institute of Physical Chemistry, Universität Hamburg, 20146 Hamburg, Germany

Maik Finsel – Reacnostics GmbH, 20457 Hamburg, Germany

Oliver Korup – Institute for Chemical Reaction Engineering, Hamburg University of Technology, 21073 Hamburg, Germany

Raimund Horn – Reacnostics GmbH, 20457 Hamburg, Germany; Institute for Chemical Reaction Engineering, Hamburg University of Technology, 21073 Hamburg, Germany

Complete contact information is available at:

<https://pubs.acs.org/10.1021/acssuschemeng.4c03279>

Author Contributions

¹P.K. and N.H. contributed equally to this work and therefore share the first authorship.

Notes

The authors declare no competing financial interest.

ACKNOWLEDGMENTS

This project was funded by the Deutsche Forschungsgemeinschaft (DFG, German Research Foundation), SFB 1615-503850735. The authors thank the central analytics department and the X-ray Service Facility at Hamburg University for ICP-OES measurements and powder diffractograms. A special thanks to the department of electron microscopy for SEM-EDX measurements. We thank Dr. Michael Pabel from Saint-Gobain NorPro for the supply of ZrO₂. Open access funding was enabled and organized by Projekt DEAL.

REFERENCES

- (1) Arrhenius, S. On the Influence of Carbonic Acid in the Air upon the Temperature of the Ground. *Philosophical Magazine J. Sci.* **1896**, *5*, 237–276.
- (2) Schühle, P.; Schmidt, M.; Schill, L.; Riisager, A.; Wasserscheid, P.; Albert, J. Influence of gas impurities on the hydrogenation of CO₂ to methanol using indium-based catalysts. *Catal. Sci. Technol.* **2020**, *10*, 7309–7322.
- (3) Cui, X.; Kær, S. K. A comparative study on three reactor types for methanol synthesis from syngas and CO₂. *Chem. Eng. J.* **2020**, *393*, No. 124632.
- (4) Bozzano, G.; Manenti, F. Efficient methanol synthesis: Perspectives, technologies and optimization strategies. *Prog. Energy Combust. Sci.* **2016**, *56*, 71–105.
- (5) Twigg, M. V.; Spencer, M. S. Deactivation of supported copper metal catalysts for hydrogenation reactions. *Appl. Catal., A* **2001**, *212*, 161–174.
- (6) Klier, K.; Chatikavanij, V.; Herman, R. G.; Simmons, G. W. Catalytic Synthesis of Methanol from CO/H₂: The Effects of Carbon Dioxide. *J. Catal.* **1981**, *1982*, 343–360.
- (7) *Chemical Technology*; Andreas Jess, P. W., Ed.; Wiley-VCH: Weinheim, 2013.
- (8) Fichtl, M. B.; Schlereth, D.; Jacobsen, N.; Kasatkin, I.; Schumann, J.; Behrens, M.; Schlögl, R.; Hinrichsen, O. Kinetics of deactivation on Cu/ZnO/Al₂O₃ methanol synthesis catalysts. *Appl. Catal., A* **2015**, *502*, 262–270.
- (9) Cui, X.; Kær, S. K. Thermodynamic Analyses of a Moderate-Temperature Process of Carbon Dioxide Hydrogenation to Methanol via Reverse Water–Gas Shift with In Situ Water Removal. *Ind. Eng. Chem. Res.* **2019**, *58*, 10559–10569.
- (10) Schühle, P.; Reichenberger, S.; Marzun, G.; Albert, J. Slurry Phase Hydrogenation of CO₂ to Methanol Using Supported In₂O₃ Catalysts as Promising Approach for Chemical Energy Storage. *Chem. Ing. Tech.* **2021**, *93*, 585–593.
- (11) Kampe, P.; Herrmann, N.; Wesner, A.; Ruhmlied, C.; Albert, J. Catalyst and Parameter Optimization Study for Slurry-Phase Methanol Synthesis Using Ni-Doped Indium-Based Catalysts. *ACS Sustainable Chem. Eng.* **2023**, *11*, 14633–14644.
- (12) Jiang, Y.; Yang, H.; Gao, P.; Li, X.; Zhang, J.; Liu, H.; Wang, H.; Wei, W.; Sun, Y. Slurry methanol synthesis from CO₂ hydrogenation over micro-spherical SiO₂ support Cu/ZnO catalysts. *J. CO₂ Util.* **2018**, *26*, 642–651.
- (13) Gaikwad, R.; Reymond, H.; Phongprueksathat, N.; Rudolf von Rohr, P.; Urakawa, A. From CO or CO₂?: space-resolved insights into high-pressure CO₂ hydrogenation to methanol over Cu/ZnO/Al₂O₃. *Catal. Sci. Technol.* **2020**, *10*, 2763–2768.
- (14) Frei, M. S.; Mondelli, C.; Cesarini, A.; Krumeich, F.; Hauert, R.; Stewart, J. A.; Curulla Ferré, D.; Pérez-Ramírez, J. Role of Zirconia in Indium Oxide-Catalyzed CO₂ Hydrogenation to Methanol. *ACS Catal.* **2020**, *10*, 1133–1145.
- (15) Gao, P.; Zhang, L.; Li, S.; Zhou, Z.; Sun, Y. Novel Heterogeneous Catalysts for CO₂ Hydrogenation to Liquid Fuels. *ACS Cent. Sci.* **2020**, *6*, 1657–1670.
- (16) Martin, O.; Martín, A. J.; Mondelli, C.; Mitchell, S.; Segawa, T. F.; Hauert, R.; Drouilly, C.; Curulla-Ferré, D.; Pérez-Ramírez, J. Indium Oxide as a Superior Catalyst for Methanol Synthesis by CO₂ Hydrogenation. *Angew. Chem., Int. Ed.* **2016**, *55*, 6261–6265.
- (17) Wesner, A.; Kampe, P.; Herrmann, N.; Eller, S.; Ruhmlied, C.; Albert, J. Indium-based Catalysts for CO₂ Hydrogenation to Methanol: Key Aspects for Catalytic Performance. *ChemCatChem* **2023**, *15*, e202301125 DOI: [10.1002/cctc.202301125](https://doi.org/10.1002/cctc.202301125).
- (18) Wang, J.; Zhang, G.; Zhu, J.; Zhang, X.; Ding, F.; Zhang, A.; Guo, X.; Song, C. CO₂ Hydrogenation to Methanol over In₂O₃-Based Catalysts: From Mechanism to Catalyst Development. *ACS Catal.* **2021**, *11*, 1406–1423.
- (19) Jia, X.; Sun, K.; Wang, J.; Shen, C.; Liu, C. Selective hydrogenation of CO₂ to methanol over Ni/In₂O₃ catalyst. *J. Energy Chem.* **2020**, *50*, 409–415.
- (20) Frei, M. S.; Mondelli, C.; García-Muelas, R.; Morales-Vidal, J.; Philipp, M.; Safonova, O. V.; López, N.; Stewart, J. A.; Ferré, D. C.; Pérez-Ramírez, J. Nanostructure of nickel-promoted indium oxide catalysts drives selectivity in CO₂ hydrogenation. *Nat. Commun.* **2021**, *12*, No. 1960.
- (21) Zhang, Z.; Shen, C.; Sun, K.; Liu, C. Improvement in the activity of Ni/In₂O₃ with the addition of ZrO₂ for CO₂ hydrogenation to methanol. *Catal. Commun.* **2022**, *162*, No. 106386.
- (22) Frei, M. S.; Mondelli, C.; García-Muelas, R.; Kley, K. S.; Puértolas, B.; López, N.; Safonova, O. V.; Stewart, J. A.; Curulla Ferré, D.; Pérez-Ramírez, J. Atomic-scale engineering of indium oxide promotion by palladium for methanol production via CO₂ hydrogenation. *Nat. Commun.* **2019**, *10*, No. 3377.
- (23) Wei, Y.; Liu, F.; Ma, J.; Yang, C.; Wang, X.; Cao, J. Catalytic roles of In₂O₃ in ZrO₂-based binary oxides for CO₂ hydrogenation to methanol. *Molecular Catal.* **2022**, *525*, No. 112354.
- (24) Tsoukalou, A. *Development of In₂O₃-Based Catalysts for the Hydrogenation of CO₂ to Methanol: Elucidating the Structure-Performance Relationship, Active Sites and Reaction Mechanism*; ETH Zurich, 2022.

- (25) Sharma, P.; Hoang Ho, P.; Shao, J.; Creaser, D.; Olsson, L. Role of ZrO₂ and CeO₂ support on the In₂O₃ catalyst activity for CO₂ hydrogenation. *Fuel* **2023**, *331*, No. 125878.
- (26) Cannizzaro, F.; Hensen, E. J. M.; Filot, I. A. W. The Promoting Role of Ni on In₂O₃ for CO₂ Hydrogenation to Methanol. *ACS Catal.* **2023**, *13*, 1875–1892.
- (27) Tsoukalou, A.; Serykh, A. I.; Willinger, E.; Kierzkowska, A.; Abdala, P. M.; Fedorov, A.; Müller, C. R. Hydrogen dissociation sites on indium-based ZrO₂-supported catalysts for hydrogenation of CO₂ to methanol. *Catal. Today* **2022**, *387*, 38–46.
- (28) Kampe, P.; Wesner, A.; Schühle, P.; Hess, F.; Albert, J. Effect of Conversion, Temperature and Feed Ratio on In₂O₃ /In(OH)₃ Phase Transitions in Methanol Synthesis Catalysts: A Combined Experimental and Computational Study. *ChemPlusChem* **2023**, *88*, No. e202300425.
- (29) Lau, K.; Schühle, P.; Liang, S.-X.; Kock, F. de.; Albert, J.; Reichenberger, S. Laser-Generated InO_x/ZrO₂ Catalysts for CO₂ Hydrogenation: Role of In Situ Fragmentation and Ripening Control. *ACS Appl. Energy Mater.* **2021**, *4*, 9206–9215.
- (30) Aquino, A.; Korup, O.; Horn, R. Liquid Phase Epoxidation of Propylene to Propylene Oxide with Hydrogen Peroxide on Titanium Silicalite-1: Spatially Resolved Measurements and Numerical Simulations. *Ind. Eng. Chem. Res.* **2023**, *62*, 3098–3115.
- (31) Espinoza, D.; Wollak, B.; Sheppard, T. L.; Dippel, A.-C.; Sturm, M.; Gutowski, O.; Schmidt, M.; Korup, O.; Horn, R. Catalytic Profile Reactor for Multimodal Operando Measurements during Periodic Operation. *ChemCatChem.* **2022**, *14*, e202200337 DOI: 10.1002/cctc.202200337.
- (32) Pottbacker, J.; Jakobtorweihen, S.; Behnecke, A. S.; Abdullah, A.; Özdemir, M.; Warner, M.; Menon, M.; Bujalski, J. M.; Waller, D.; Korup, O.; Horn, R. Resolving gradients in an ammonia oxidation reactor under industrial conditions: A combined experimental and simulation study. *Chem. Eng. J.* **2022**, *439*, No. 135350.
- (33) Wollak, B.; Doronkin, D. E.; Espinoza, D.; Sheppard, T.; Korup, O.; Schmidt, M.; Alizadefanaloo, S.; Rosowski, F.; Schroer, C.; Grunwaldt, J.-D.; Horn, R. Exploring catalyst dynamics in a fixed bed reactor by correlative operando spatially-resolved structure-activity profiling. *J. Catal.* **2022**, *408*, 372–387.
- (34) Monshi, A.; Foroughi, M. R.; Monshi, M. R. Modified Scherrer Equation to Estimate More Accurately Nano-Crystallite Size Using XRD. *WJNSE* **2012**, *02*, 154–160.
- (35) Portillo, A.; Parra, O.; Aguayo, A. T.; Ereña, J.; Bilbao, J.; Ateka, A. Kinetic Model for the Direct Conversion of CO₂/CO into Light Olefins over an In₂O₃-ZrO₂/SAPO-34 Tandem Catalyst. *ACS Sustainable Chem. Eng.* **2024**, *12*, 1616–1624.
- (36) Nielsen, N. D.; Jensen, A. D.; Christensen, J. M. The roles of CO and CO₂ in high pressure methanol synthesis over Cu-based catalysts. *J. Catal.* **2021**, *393*, 324–334.
- (37) Studt, F.; Behrens, M.; Kunkes, E. L.; Thomas, N.; Zander, S.; Tarasov, A.; Schumann, J.; Frei, E.; Varley, J. B.; Abild-Pedersen, F.; et al. The Mechanism of CO and CO₂ Hydrogenation to Methanol over Cu-Based Catalysts. *ChemCatChem* **2015**, *7*, 1105–1111.
- (38) Wu, J.; Saito, M.; Takeuchi, M.; Watanabe, T. The stability of Cu/ZnO-based catalysts in methanol synthesis from a CO₂-rich feed and from a CO-rich feed. *Appl. Catal., A* **2001**, *218*, 235–240.
- (39) Tsoukalou, A.; Bushkov, N. S.; Docherty, S. R.; Mance, D.; Serykh, A. I.; Abdala, P. M.; C., Copéret, A.; Fedorov, C. R., Müller. *Surface Intermediates in In-Based ZrO₂-Supported Catalysts for Hydrogenation of CO₂ to Methanol.*
- (40) Ye, J.; Liu, C.; Mei, D.; Ge, Q. Active Oxygen Vacancy Site for Methanol Synthesis from CO₂ Hydrogenation on In₂O₃ (110): A DFT Study. *ACS Catal.* **2013**, *3*, 1296–1306.
- (41) Shen, H.; Li, H.; Yang, Z.; Li, C. Magic of hydrogen spillover: Understanding and application. *Green Energy & Environment* **2022**, *7*, 1161–1198.
- (42) Stangeland, K.; Li, H.; Yu, Z. Thermodynamic Analysis of Chemical and Phase Equilibria in CO₂ Hydrogenation to Methanol, Dimethyl Ether, and Higher Alcohols. *Ind. Eng. Chem. Res.* **2018**, *57*, 4081–4094.
- (43) Araújo; Mondelli; Pinheiro; Thaylan, C.; Agrachev, M.; Zou, T.; Willi, P. O.; Engel, K. M.; Grass, R. N.; Stark, W. J.; Safonova, O. V.; Jeschke, G.; et al. Flame-made ternary Pd-In₂O₃-ZrO₂ catalyst with enhanced oxygen vacancy generation for CO₂ hydrogenation to methanol. *Nat. Commun.* **2022**, *13*, No. 5610, DOI: 10.1038/s41467-022-33391-w.

6.4 Investigations of supported In_2O_3 in a slurry reactor

P4

Catalyst and Parameter Optimization Study for Slurry-Phase Methanol Synthesis Using Ni-Doped Indium-based Catalysts

Philipp Kampe, Nick Herrmann, Anne Wesner, Charlotte Ruhmlieb, and Jakob Albert

P. Kampe, N. Herrmann, A. Wesner, C. Ruhmlieb, J. Albert. “Catalyst and Parameter Optimization Study for Slurry-Phase Methanol Synthesis Using Ni-Doped Indium-Based Catalysts”, *ACS Sustainable Chemistry & Engineering*, 2023, 11, 14633-14644, DOI: doi.org/10.1021/acssuschemeng.3c05584

Reprinted (adapted) with permission from ACS Sustainable Chem. Eng. 2023, 11, 14633–14644. Copyright 2023 American Chemical Society.

The following Chapter is based on the article [21]. After investigating the catalytic performance of In_2O_3 -based catalysts in fixed bed reactors for two-phase methanol synthesis, this study focuses on their application and optimization in three-phase reactors (refer to Chapter 3.3.2). The slurry stirred-tank reactor setup poses the advantage of using catalysts with small particle sizes produced through co-precipitation, without causing high pressure losses such in two phase reactors.

The influence of nickel as a promoter on In_2O_3 obtained by different synthesis methods was determined in a slurry stirred-tank reactor setup in batch mode (see Figure 6.5). Also, a comparison of nickel doping with other metal promoters for $\text{In}_2\text{O}_3/\text{ZrO}_2$ catalysts on their catalytic performance was conducted. A statistical DoE and a stability test by recycling the slurry system were applied for the best performing $\text{Ni-In}_2\text{O}_3/\text{ZrO}_2$ catalyst. The hydrogenation of both CO and CO_2 was tested at $T = 300\text{ }^\circ\text{C}$ and $p = 75\text{ bar}$ [21]. Additional Supporting Information of the following article can be found in the Appendix 9.6.

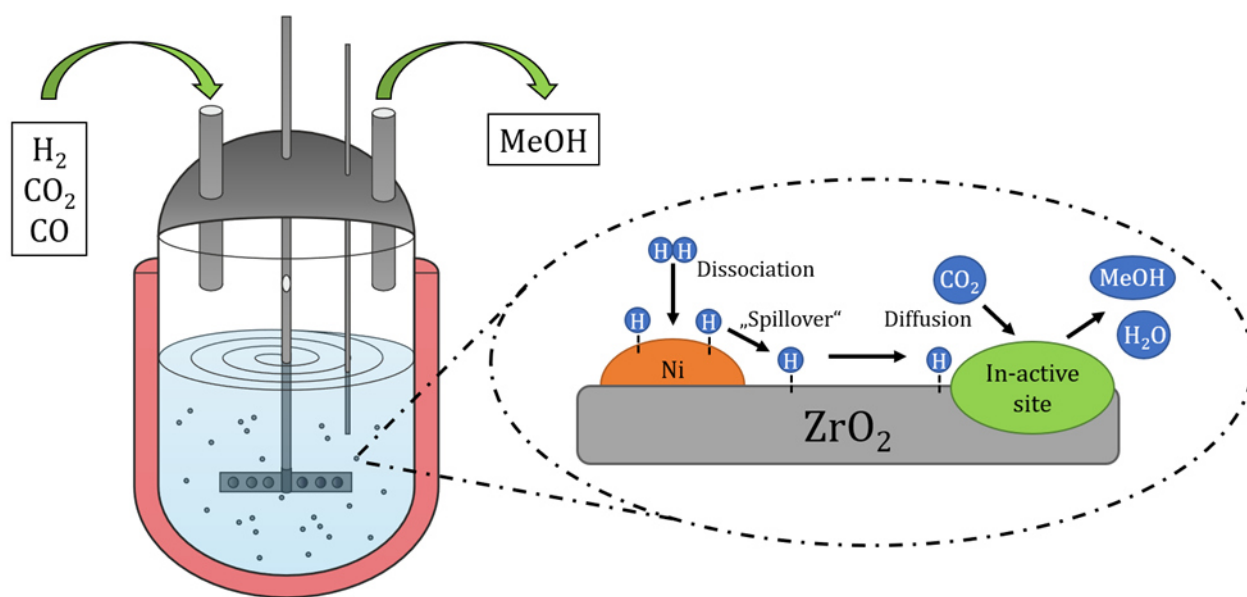


Figure 6.5. Illustration of the slurry batch reactor and the hydrogen spillover effect using $\text{Ni-In}_2\text{O}_3/\text{ZrO}_2$ catalyst [21].

Catalyst and Parameter Optimization Study for Slurry-Phase Methanol Synthesis Using Ni-Doped Indium-Based Catalysts

Philipp Kampe, Nick Herrmann, Anne Wesner, Charlotte Ruhmlieb, and Jakob Albert*

Cite This: *ACS Sustainable Chem. Eng.* 2023, 11, 14633–14644

Read Online

ACCESS |



Metrics & More



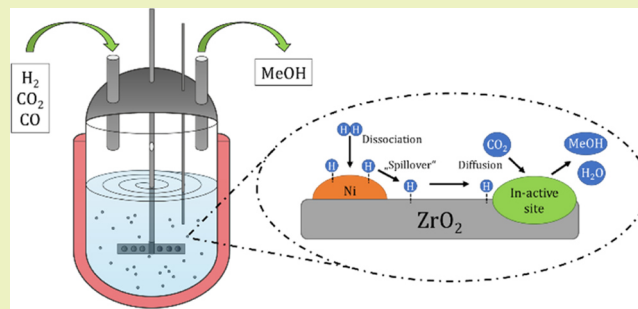
Article Recommendations



Supporting Information

ABSTRACT: Producing green methanol using renewable hydrogen and CO₂ in a slurry reactor is a promising approach for chemical energy storage and to mitigate global warming caused by industry emissions. A slurry reactor using mineral oil as a carrier liquid compensates for fluctuating conditions due to the high heat capacity and thermal stability. In the present study, metal-promoted In₂O₃/ZrO₂ catalysts have been synthesized by various preparation methods in combination with different support materials. Design of experiment studies aimed at finding optimum parameters for slurry-phase CO₂ hydrogenation. The Ni-doped In₂O₃/ZrO₂ catalyst prepared by coprecipitation achieved the highest activity and selectivity both for CO and CO₂ hydrogenation under industrially relevant conditions. Using industry syngas composition (H₂/CO/CO₂) with a molar ratio of 70/28/2 at 300 °C and 75 bar, a very high methanol productivity (6.84 g_{MeOH} g_{metal}⁻¹ h⁻¹) was achieved, being five times more efficient than the commercial Cu-based catalyst (1.25 g_{MeOH} g_{Cu}⁻¹ h⁻¹) related to the active metal content. Finally, the stability of the preferred slurry CO₂ hydrogenation system was proven over five reaction cycles, recycling both catalyst and carrier liquid in four successive runs, showing further potential for real industrial applications in the near future.

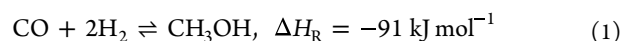
KEYWORDS: slurry reaction, methanol synthesis, CO₂ hydrogenation, indium oxide catalyst, metal doping, nickel, hydrogen spillover



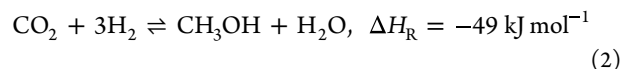
INTRODUCTION

The steady rise of global greenhouse gas emissions, especially CO₂ since the industrial revolution and the effort to reduce emissions, have led to new ways to mitigate global warming. The exhaust of energy-intensive industries such as iron and steel, refineries, and cement, releases significant amounts of CO₂ into the atmosphere.¹ Carbon capture and the use of exhaust gas are viable options for producing valuable bulk chemicals such as methanol. The advantages of methanol are broad with a relatively high energy density of 15.1 MJ L⁻¹ (comparable to natural gas or conventional fuels),² methanol has the capability of being used for chemical energy storage. Green hydrogen, produced by water electrolysis using renewable energy, can be chemically stored as methanol. This provides the possibility of using the existing fuel infrastructure for energy transportation. Energy recovery could be achieved by direct burning, steam reforming, or use in direct methanol fuel cells (DMFCs). Besides the aspect of energy storage, methanol can be used as a platform chemical, with increasing demand being one of the most important commodities. It is mainly used for formaldehyde, olefins, and higher hydrocarbon production.³

Traditionally, methanol has been synthesized by syngas (H₂/CO/CO₂) with a ratio of 70/28/2 according to eq 1 using the state-of-the-art Cu/ZnO/Al₂O₃ catalyst.⁴



With the development of a green methanol synthesis using renewable hydrogen and CO₂ as a carbon source, a stoichiometric amount of water as a by-product is produced (eq 2).



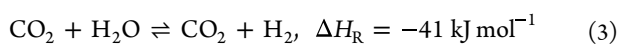
Reaction kinetics are significantly different using CO₂ compared to CO.⁵ The excess water formed on the surface of the catalyst can lead to deactivation. Temperatures higher than 300 °C lead to thermal sintering and deactivation of the Cu-based catalyst.⁶ Therefore, CO plays a major role in removing the surface-bound water via the water–gas-shift reaction (eq 3).⁵ This competitive reaction significantly lowers methanol selectivity at elevated temperatures.⁷

Received: September 1, 2023

Revised: September 7, 2023

Published: September 22, 2023





Besides that, the Cu-based catalyst is prone to deactivation by feed gas impurities such as H_2S , SO_2 , NO_2 , and NH_3 , commonly found in industrial CO_2 sources.⁸ There are a few Cu-based catalysts showing high methanol selectivity, but their long-term stability has not been demonstrated yet.⁹

For the hydrogenation of CO_2 to methanol, an alternative ZrO_2 supported In_2O_3 catalyst showed high activity and selectivity toward methanol synthesis in various studies.^{7,10–18} Hereby, catalysts prepared by different impregnation methods for an indium content of 10 wt % show the highest methanol productivity. $\text{In}_2\text{O}_3/\text{ZrO}_2$ prepared by wetness impregnation has shown the highest productivity of $0.11 \text{ g}_{\text{MeOH}} \text{ g}_{\text{cat}}^{-1} \text{ h}^{-1}$ in a fixed-bed reactor.⁷ This arises from the formation of oxygen vacancies in the lattice, which in turn can activate CO_2 . The vacancies are created by a reducing atmosphere with the formation of water as a by-product. The activation and heterolytic splitting of H_2 is facilitated by oxygen vacancies and surface hydroxides.¹⁹ With the possibility to tune the catalyst structure, the activity can be further increased and the competing CO formation via the reverse water–gas shift (RWGS) reaction can be suppressed in comparison to the current industrial Cu-based catalyst.²⁰ Earlier studies have shown that the productivity of the catalyst can be greatly improved if In_2O_3 is impregnated on the supporting metal oxide. The most beneficial ZrO_2 carrier prevents sintering of In_2O_3 and ensures long-time stability. Moreover, stability against nitrogen compounds (NH_3 , NO_2) in the feed gas, as well as hydrocarbons and pretreatment with hydrogen is ensured.⁸ The integration of noble metals such as Pd and Ru, as well as non-noble metals like Ni, proved to further improve the catalytic activity.^{12,14,21} The resulting hydrogen spillover effect leads to higher hydrogen availability on the catalyst surface wherein only a small amount of metal loading can boost the catalytic activity significantly.²² Nano-sized In_2O_3 particles can be generated via laser ablation and deployed on ZrO_2 surfaces to tune the microstructure of the catalyst and to adjust the catalyst activity as well.²³

In industrial methanol synthesis, fixed-bed reactors are used. For example, Lurgi's MegaMethanol process uses pressures between 50 and 100 bar and reaction temperatures between 200 and 300 °C.²⁴ Problems arise due to non-uniform formation of local hot spots resulting in a decrease in product selectivity and deactivation of the Cu-based catalyst in severe cases. This requires active cooling in strong exothermic reactions with a complex reactor design (multiple-shell reactor, by ICI). The reaction temperature in a multiple-shell reactor is maintained by the flow of cold gas introduced below each catalyst bed section.²⁵ Improvements are expected from new processes based on slurry and membrane reactors.^{26,27} With the advantages of simple construction, efficient heat storage, and easy reactor control, the slurry reactor concept has already been employed in more recent research. With the utilization of the carrier liquid, fluctuating heat flows can be buffered resulting in a more stable operation using variable gas flows.^{10,28} Smaller particle sizes may be used in slurry reactors without the need to compensate for a pressure drop along the catalyst bed. Furthermore, less attrition of catalyst particles occurs. Schühle et al. demonstrated that commercial light mineral oil is a suitable carrier liquid for slurry methanol synthesis (Figure S14). Also, H_2 excess ($\text{H}_2/\text{CO}_2 = 4/1$) resulted in the highest methanol productivity.¹⁰

In the present work, we aimed at further improving the $\text{In}_2\text{O}_3/\text{ZrO}_2$ catalyst¹⁰ for slurry-phase hydrogenation of CO_2 to methanol by rational design approaches. For this purpose, appropriate synthesis methods were compared, as well as the implementation of promoters for the facilitation of H_2 and CO_2 adsorption. After an initial promoter and support screening, the most promising catalyst was selected for a consecutive parameter optimization using a combination of design of experiment (DoE) and statistical evaluation using Design-Expert. Moreover, the feasibility of the improved catalyst system was evaluated both for CO_2 and CO hydrogenation and compared to the commercial Cu-based catalyst under industry feed gas composition. Finally, the recyclability of the most promising catalyst should be demonstrated.

EXPERIMENTAL DETAILS

Materials. All chemicals were obtained commercially and used as received without further purification. ZrO_2 support pellets (Alfa Aesar or Saint Gobain), indium(III) nitrate (99.999%, Thermo Scientific), indium(III) hydroxide (99.8%, Thermo Scientific), nickel(II) nitrate hexahydrate (99%, Sublab), cerium(III) nitrate hexahydrate (99.5%, Thermo Scientific), magnesium(II) nitrate hexahydrate (98–102%, Thermo Scientific), and zirconium(IV) oxynitrate hydrate (26.8%, Sigma Aldrich) were used for catalyst synthesis. A commercial copper-based catalyst $\text{CuO}/\text{ZnO}/\text{Al}_2\text{O}_3$ (Alfa Aesar) and an indium(III) oxide (99.9%, Alfa Aesar) were used as references. Light mineral oil (Sigma Aldrich) was used as a carrier liquid.²⁹ The gases H_2 (5.0 grade, Linde), CO_2 (4.5 grade, Linde), CO (3.7 grade, Linde), and N_2 (5.0 grade, Linde) were used for methanol synthesis in the slurry reaction system.

Catalyst Synthesis. A typical synthesis of the metal-promoted $\text{In}_2\text{O}_3/\text{ZrO}_2$ catalyst consisted of dissolving 13.4 g of $\text{In}(\text{NO}_3)_3 \cdot \text{H}_2\text{O}$ in 500 mL of distilled water. Additionally, a defined amount of $\text{Ni}(\text{NO}_3)_2 \cdot 6 \text{H}_2\text{O}$ (2.28 g), $\text{Ce}(\text{NO}_3)_3 \cdot 6 \text{H}_2\text{O}$ (1.42 g), or $\text{Mg}(\text{NO}_3)_2 \cdot 6 \text{H}_2\text{O}$ (6.54 g) corresponding to a theoretical loading of 1 wt % was dissolved as well. 40.0 g of ZrO_2 powder (32–80 μm) was suspended in the solution. The pH of the solution was raised to 9.2 by adding diluted NaOH. Subsequently, the solution was aged for 1 h under vigorous stirring. Afterward, 400 mL of distilled water was added to the suspension. The solvent was removed by vacuum filtration, and the residue was washed until a pH value of 7 was reached. The preliminary catalyst was dried at 65 °C for 12 h and calcined at 300 °C (2 K min^{-1} , 3 h). After crushing and its separation into fractions, around 36 g of catalyst in a size range of 32–80 μm was obtained.

All other catalysts used were synthesized according to known literature procedures. They are labeled with prefixes corresponding to the authors of the respective literature Martin (M-),⁷ Schühle (S-),¹⁰ Jia (J-),¹¹ Frei (F-),¹² and Zhang (Z-).¹³ The detailed synthesis procedures are described in the Supporting Information.

Catalyst Characterization. Inductively coupled plasma optical emission spectrometry (ICP-OES) was used to determine the elementary composition of each catalyst. 100 mg of the sample was digested in 5 mL of concentrated H_2SO_4 and 1 mL of fuming HNO_3 . It was then atomized in an argon plasma, and the composition was quantified using optical emission spectrometry. Characterization was performed on an ASCOR-spectrometer (Fa. Spectro) by the Central Element Analysis Services (Department of Chemistry, University of Hamburg).

Nitrogen physisorption was carried out at 77 K with an Autosorb iQ-MP/XR analyzer (Faraiaic Quantachrome Instruments). The sample was degassed at 473 K under vacuum for 10 h prior to analysis. The total surface area of the sample was determined using the Brunauer–Emmett–Teller (BET) model and the pore volume using the Barrett–Joyner–Halenda (BJH) model.

Powder X-ray diffraction (XRD) was carried out using a Panalytical MDP X'Pert Pro diffractometer using $\text{Cu K}\alpha$ ($\lambda = 0.1541 \text{ nm}$) radiation. The measuring range of the diffraction angle was 10–80°

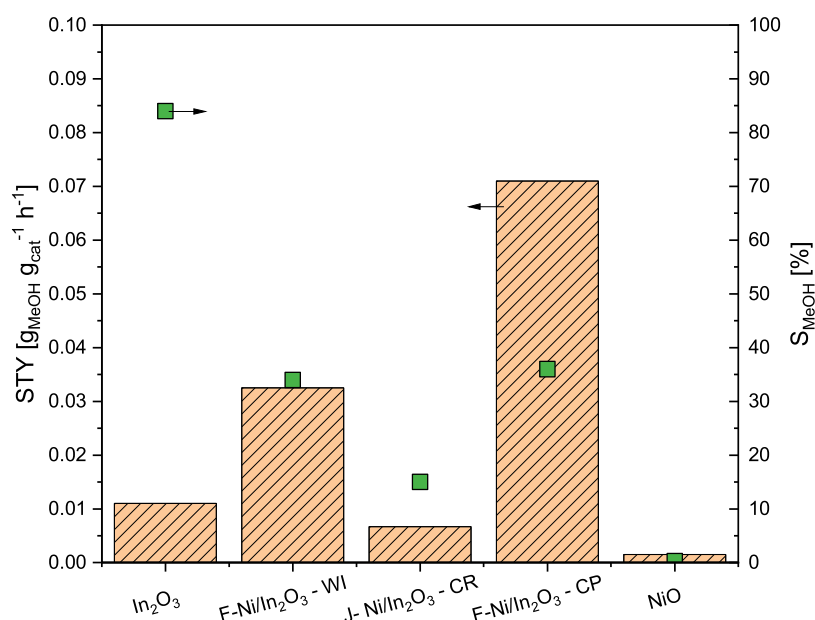


Figure 1. Influence of Ni as a promoter on In₂O₃ obtained by different synthesis methods on the methanol STY and selectivity. Reaction conditions: $T = 300\text{ }^{\circ}\text{C}$, $p = 75\text{ bar}$, $\text{H}_2/\text{CO}_2 = 4/1$, $m_{\text{cat}} = 2.0\text{ g}$, $N = 1200\text{ rpm}$, $V_{\text{oil}} = 100\text{ mL}$, $t_{\text{R}} = 3\text{ h}$.

and sampled at a rate of 0.013° with a counting time of 0.3 s. InOx particle sizes were calculated using the Scherrer equation based on the characteristic diffraction reflex and described in detail in the Supporting Information, eq S2.

High-resolution transmission electron microscopy (HRTEM) and scanning transmission electron microscopy (STEM) images were obtained by using a double-corrected (CESCOR and CETCOR, CEOS) JEOL JEM 2200FS microscope with an in-column image filter (Ω -type), a high-angle annular dark-field (HAADF) detector, and a Gatan 4K UltraScan 1000 camera at an accelerating voltage of 200 kV. Energy-dispersive X-ray spectroscopy (EDS) elemental maps were obtained by using a JEOL JED-2300 analysis station with a 100 mm² silicon drift detector.

Temperature-programmed desorption of CO₂ (CO₂-TPD) and temperature-programmed reduction by H₂ (H₂-TPR) were measured using a ChemBET Pulsar instrument (Fa. Quantachrome Instruments). Conditions for the measurements are outlined in Table S3 in the Supporting Information.

Catalytic Experiments in the Slurry Reactor. Batch Reactor Setup for Slurry Experiments. The reactions were carried out in a nonbaffled 600 mL stirred tank reactor (STR, Parr Instruments) with a diameter of 6.35 cm, using a glass liner inlet and a gas entrainment stirrer centered horizontally. The stirrer has four blades and a diameter of 3 cm and is located about 1 cm above the bottom of the reactor. The reactor, pipes, and valves were made of stainless steel (1.4571) and the gaskets were made out of poly(tetrafluoroethylene) (PTFE). For temperature adjustment, a thermocouple (Pt-100), a heating mantle (Horst), and a thermostat (Huber CS 33) were used. The reactor periphery was heated to 120–200 °C in order to prevent condensation of the reaction products. The addition of gases was performed manually via ball and needle valves. The pressure was controlled with an analogous and digital pressure gauge.

The reactor outlet was connected to an online gas chromatograph (Bruker 450-GC), equipped with two flame ionization detectors (FID), one thermal conductivity detector (TCD), one methanizer, and four gas chromatography columns (Restek Q-Bond, Restek U-Bond, Bruker Swax, Bruker Molsieve 5 Å) to analyze the gas composition. For more details of the setup and analysis conditions, refer to Figure S1 in the Supporting Information. For analysis of the carrier liquid, ¹H and ¹³C NMR (400 MHz, resolution) spectroscopy using a Bruker Avance III HD 400 spectrometer was applied.

Experimental Procedure. Before the reaction, the autoclave was filled with 100 mL of white mineral oil (carrier liquid). Between 1 and

2 g of catalyst (depending on the molar mass) was added to the carrier liquid, and the reactor bottom was installed. The stirred speed was set to 200 rpm and the reactor was initially purged with (at least 5 bar of) nitrogen three times and subsequently with CO₂ three times at room temperature. Enough CO₂ was filled in the reactor at room temperature to reach the desired partial pressure at the reaction temperature. The heating devices for the reactor and periphery were switched on. At the desired temperature, CO₂ excess was released and the autoclave was filled with H₂ to reach the desired gas composition of H₂/CO₂ = 4:1 at 75 bar total pressure. To start the gas entrainment, the stirrer speed was set to 1200 rpm, marking the starting point of the reaction (t_0). The initial and end gas composition was analyzed by online GC. All relevant process parameter calculations are described in the Supporting Information.

Calculations. The space-time yield of methanol STY in this work is defined as the mass of methanol m_{MeOH} formed during 3 h of reaction time t_{R} related to the mass of catalyst m_{cat} .

$$\text{STY} = \frac{m_{\text{MeOH}}}{m_{\text{cat}} \cdot t_{\text{R}}} \quad (4)$$

The productivity P_{cat} was calculated as the mass of methanol m_{MeOH} formed during 3 h of reaction time t_{R} related to the total mass of active metal $m_{\text{active metal}}$.

$$P_{\text{cat}} = \frac{m_{\text{MeOH}}}{m_{\text{active metal}} \cdot t_{\text{R}}} \quad (5)$$

With the initial (t_0) and end (t_{R}) amount of CO₂ the presented methanol selectivity S_{MeOH} is calculated as follows:

$$S_{\text{MeOH}} = \frac{n_{\text{MeOH}}}{n_{\text{CO}_2}^0 - n_{\text{CO}_2}} \times 100\% \quad (6)$$

RESULTS AND DISCUSSION

The aim of the following study was to improve the methanol STY using metal-promoted In₂O₃/ZrO₂ catalysts by keeping high selectivity in the favored slurry reaction system. In detail, the influence of Ni doping on the aforementioned In₂O₃/ZrO₂ catalyst,¹⁰ the choice of the right impregnation method, and a comparison of the preferred Ni impregnation strategy with other promoters (Ce and Mg) have been investigated. In a typical batch experiment, 2 g of the catalyst were tested under

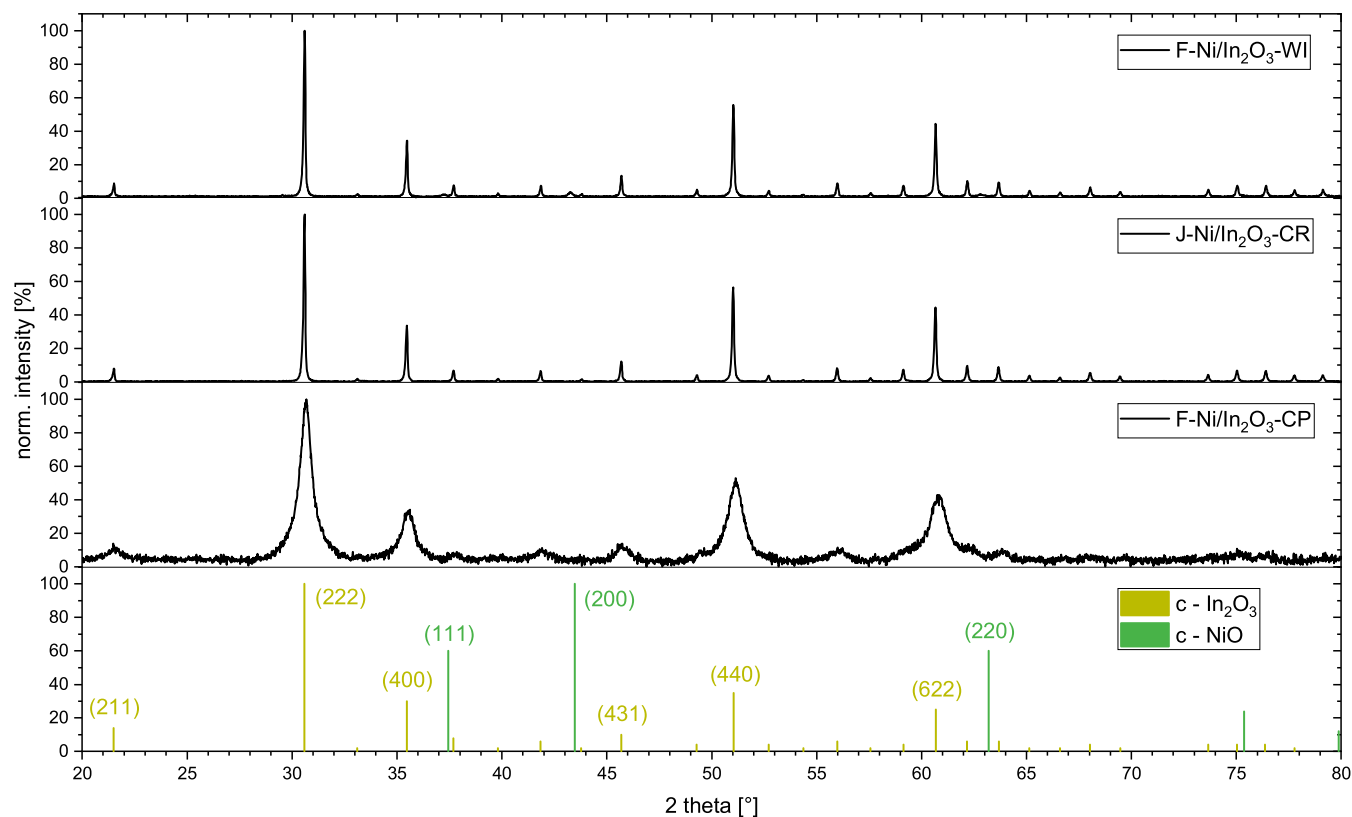


Figure 2. XRD patterns of Ni-promoted In_2O_3 catalysts prepared by different synthesis methods. Expected locations of cubic In_2O_3 (ICSD: 169420) and cubic NiO (ICSD: 9866) are shown at the bottom.

similar conditions $V_{\text{Oil}} = 100 \text{ mL}$, $T = 300 \text{ }^\circ\text{C}$, $p = 75 \text{ bar}$, $\text{H}_2/\text{CO}_2 = 4/1$, $t_{\text{R}} = 3 \text{ h}$, using light mineral oil as a carrier liquid and heat capacitor. After catalyst selection, a DoE study revealed the optimum combination of the reaction parameters for a maximized methanol STY. The performance of the newfound catalyst was compared to that of the commercial $\text{Cu}/\text{ZnO}/\text{Al}_2\text{O}_3$ catalyst for a current industry gas with a molar composition of $\text{H}_2/\text{CO}/\text{CO}_2 = 70/28/2$ and tested for its CO hydrogenation ability. Finally, the stability of the slurry CO_2 hydrogenation system was proven by recycling both the catalyst and carrier liquid in four successive runs.

Influence of Ni as a Promotor for Pristine In_2O_3 Without ZrO_2 Support. First of all, a blank test revealing the blind activity for the empty reactor setup and reference materials was performed (Figure S2). To investigate the influence of Ni as a potential promotor of In_2O_3 for CO_2 hydrogenation in the slurry reaction system, three different literature-known synthesis methods have been tested for catalyst preparation. In detail, wetness impregnation (WI), chemical reduction (CR), and coprecipitation (CP) have been used. For this purpose, the respective catalysts have been prepared according to the synthesis procedures described above (see the Experimental Section for details) to achieve around 10 wt % Ni loading. This could be confirmed by ICP-OES (Table S1). Figure 1 summarizes the results of various Ni doping approaches on In_2O_3 and different synthesis preparation methods on the methanol STY compared to pure In_2O_3 and NiO as references.

Pure In_2O_3 shows a very high methanol selectivity ($S = 84\%$) under the applied reaction conditions. Methanol STY is significantly higher ($0.011 \text{ g}_{\text{MeOH}} \text{ g}_{\text{cat}}^{-1} \text{ h}^{-1}$) compared to the experiment using pure NiO ($0.0015 \text{ g}_{\text{MeOH}} \text{ g}_{\text{cat}}^{-1} \text{ h}^{-1}$), showing

its catalytic potential. With the addition of Ni as a promotor, the methanol STY of the pristine In_2O_3 catalyst could be drastically increased in the cases of WI and CP synthesis (up to $0.075 \text{ g}_{\text{MeOH}} \text{ g}_{\text{cat}}^{-1} \text{ h}^{-1}$). The hydrogen spillover effect of Ni facilitates the dissociative adsorption of hydrogen and consecutive transport to the reaction sites on the metal surface.¹⁴ The average particle size of WI is 88.5 nm, and that for CP is 16.0 nm, as calculated by the Scherrer equation based on $\text{In}_2\text{O}_3(222)$ reflection (see Figure 2). Applying the CP synthesis method, smaller particles were formed and Ni could be well distributed on the catalyst surface (Figure S3) resulting in a higher activity compared to the WI method. Because less Ni is applied to the surface of In_2O_3 by using the WI method, it could possibly suppress the hydrogen spillover, resulting in a less active catalyst. Using the CR method, no increase in methanol STY could be observed. First, the average particle size for CR is 76.1 nm, larger than that for the CP particles (16.0 nm) (Figure 2). Second, Ni could not be well distributed on the In_2O_3 surface (Figure S3). The scanning transmission electron microscopy–energy-dispersive X-ray (STEM-EDX) mappings show no overlap of the In and Ni distribution. Instead, rather separate Ni domains have formed. Comparing particle analysis with catalytic performance, a synthesis method producing smaller particles with surface-available In_2O_3 and a highly dispersed Ni in the near vicinity is preferable for high methanol STY.

Influence of the Impregnation Method of In_2O_3 Supported on ZrO_2 . The next step was to study the influence of various impregnation methods of ZrO_2 -supported In_2O_3 catalysts on the slurry reaction system. Therefore, various $\text{InO}_x/\text{ZrO}_2$ catalysts have been compared for their STY under the same reaction conditions as those used before

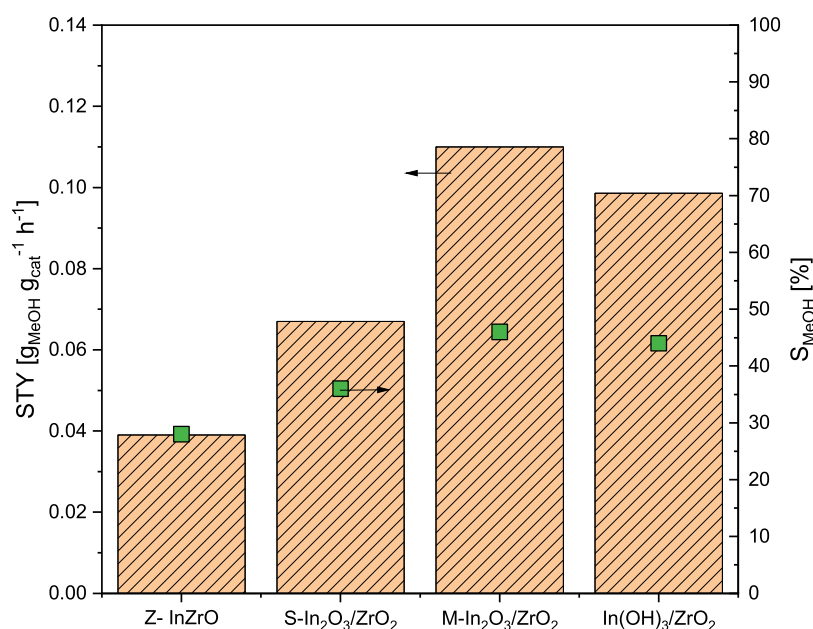


Figure 3. Influence of the impregnation method of In_2O_3 on ZrO_2 . Reaction conditions: $T = 300\text{ }^\circ\text{C}$, $p = 75\text{ bar}$, $\text{H}_2/\text{CO}_2 = 4/1$, $m_{\text{cat}} = 2.0\text{ g}$, $N = 1200\text{ rpm}$, $V_{\text{Oil}} = 100\text{ mL}$, $t_{\text{R}} = 3\text{ h}$.

(Figure 3). The prepared M- $\text{In}_2\text{O}_3/\text{ZrO}_2$ showed the highest methanol STY of $0.11\text{ g}_{\text{MeOH}} \text{g}_{\text{cat}}^{-1} \text{h}^{-1}$ and a moderate selectivity $S = 46\%$. S- $\text{In}_2\text{O}_3/\text{ZrO}_2$ with a similar indium content (11.09%) to M- $\text{In}_2\text{O}_3/\text{ZrO}_2$ (Table 1), showed a lower methanol STY of $0.067\text{ g}_{\text{MeOH}} \text{g}_{\text{cat}}^{-1} \text{h}^{-1}$ and a slightly lower selectivity ($S = 36\%$). This can be justified by the use of a different ZrO_2 support for the synthesis of S- $\text{In}_2\text{O}_3/\text{ZrO}_2$. The used ZrO_2 from Alfa Aesar (S- $\text{In}_2\text{O}_3/\text{ZrO}_2$) has a smaller BET surface area and a lower CO_2 adsorption capacity (see Table 1) than ZrO_2 from St. Gobain resulting in an overall lower performance of the S- $\text{In}_2\text{O}_3/\text{ZrO}_2$ catalyst. In comparison, Z-InZrO achieved the lowest methanol STY ($0.039\text{ g}_{\text{MeOH}} \text{g}_{\text{cat}}^{-1} \text{h}^{-1}$) and selectivity ($S = 28\%$). However, this was still higher compared with pristine In_2O_3 (Figure 1). In(OH)₃/ZrO₂ produced slightly less methanol ($0.099\text{ g}_{\text{MeOH}} \text{g}_{\text{cat}}^{-1} \text{h}^{-1}$) with a selectivity $S = 44\%$ compared to M- $\text{In}_2\text{O}_3/\text{ZrO}_2$. Under methanol synthesis conditions, In(OH)₃ dehydrates into In_2O_3 and therefore the activity was in the range of M- $\text{In}_2\text{O}_3/\text{ZrO}_2$.³⁰ However, a slightly lower STY was observed, which could be attributed to the surface reduction taking place before, subsequently initiating oxygen vacancies (Table 1). The experiment of the best-performing M- $\text{In}_2\text{O}_3/\text{ZrO}_2$ catalyst was repeated three times showing a very low standard deviation of $\pm 0.0025\text{ g}_{\text{MeOH}} \text{g}_{\text{cat}}^{-1} \text{h}^{-1}$ (Table S2 and Figure S4).

Table 1. Results Obtained from ICP-OES, N_2 Physisorption, and CO_2 -TPD for Selected Catalysts and ZrO_2 Carriers

	indium loading [wt %]	S_{BET} [$\text{m}^2 \text{g}^{-1}$]	pore radius [nm]	pore volume [$\text{cm}^3 \text{g}^{-1}$]	relative CO_2 adsorption capacity
ZrO_2 Alfa Aesar	0	51.27	5.69	0.24	1.00
ZrO_2 St.Gobain	0	89.35	4.07	0.29	1.26
S- $\text{In}_2\text{O}_3/\text{ZrO}_2$	11.1	44.97	5.67	0.17	1.27
M- $\text{In}_2\text{O}_3/\text{ZrO}_2$	11.1	72.30	3.39	0.20	1.91
Z-InZrO	69.2	49.39	5.02	0.18	0.26

Doping the Z-InZrO mixed oxide catalyst with Ni led to an increased STY of $0.10\text{ g}_{\text{MeOH}} \text{g}_{\text{cat}}^{-1} \text{h}^{-1}$ (see Figure S5). However, due to the very high amount of In needed, this catalyst was excluded from further studies. With regards to the relative CO_2 adsorption capacity (Table 1), the M- $\text{In}_2\text{O}_3/\text{ZrO}_2$ catalyst showed the highest CO_2 values, being twice as pure ZrO_2 . The relative CO_2 -adsorption capacity was measured by using the procedure described in Table S3. In order to compare the different materials, all peaks between 50 and $650\text{ }^\circ\text{C}$ in the TPD chromatogram (Figure S6) have been considered. The cumulated peak area of ZrO_2 from Alfa Aesar was set as 1 and the capacity for the other samples was calculated accordingly (Figure S6).

Comparison of Ni Doping with Other Promoters on Their Catalytic Performance. So far, doping of In_2O_3 -based catalysts has only been reported for CO_2 hydrogenation in fixed-bed reactors.^{11,14,21} However, the former experiments discussed in Figure 1 also indicate a possibly higher activity of pristine In_2O_3 prepared by CP using Ni as a promoter for slurry reactors. In addition, ZrO_2 as a support increases the catalytic activity of In_2O_3 as well (Figure 3). Consequently, a combination of both approaches using 1 wt % of promoter metal and 10 wt % In loading synthesized via the promising CP method has been chosen (Table S4 and Figure S9). Beyond the effect of Ni for an improved H_2 spillover effect, Ce and Mg having basic properties were also deemed suitable promoters for supported $\text{In}_2\text{O}_3/\text{ZrO}_2$. This attribute could lead to higher productivity for P_{cat} because of a higher CO_2 adsorption capability. In addition, CeO_2 can oxidize *in situ* formed CO to CO_2 due to the formation of more oxygen vacancies.³¹ Figure 4 shows the impact of the different promoters on the catalytic performance compared to M- $\text{In}_2\text{O}_3/\text{ZrO}_2$ (WI).

Ni- and Ce-promoted $\text{In}_2\text{O}_3/\text{ZrO}_2$ catalysts enhanced the metal-based productivity by up to 3.65 and $3.80\text{ g}_{\text{MeOH}} \text{g}_{\text{active metal}}^{-1} \text{h}^{-1}$, respectively, while being equally selective ($S = 48\%$) without forming methane (Figure S10). As stated previously, higher methanol yields can be attributed to the hydrogen spillover effect of Ni. Using Ce as a promoter, a

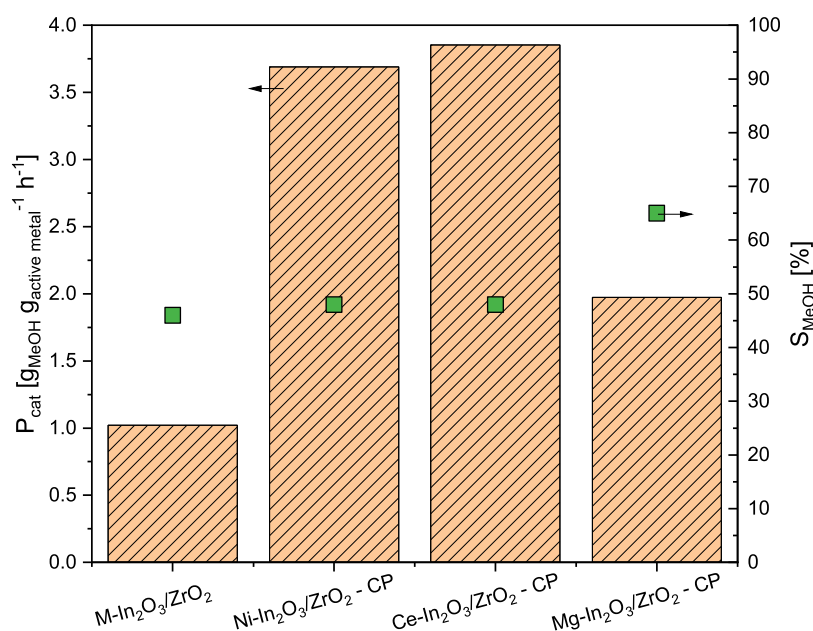


Figure 4. Comparison of the In₂O₃/ZrO₂ catalyst with various promoters on their catalytic performance. Reaction conditions: $T = 300$ °C, $p = 75$ bar, $\text{H}_2/\text{CO}_2 = 4/1$, $m_{\text{cat}} = 2.0$ g, $N = 1200$ rpm, $V_{\text{Oil}} = 100$ mL, $t_{\text{R}} = 3$ h.

higher CO₂ adsorption capacity could be observed by CO₂ TPD compared to the Ni-promoted catalyst while the peak temperatures were similar (Figure S7). Further explanation for the increased activity of the Ni-doped catalyst can be deduced from the characteristics of the H₂ TPR curves corresponding to a particular catalyst (Figure S8). The undoped M-In₂O₃/ZrO₂ catalyst features a narrow range where the reduction and consequently the uptake of hydrogen takes place between 280 and 420 °C. The Ni-promoted catalyst features the same range of reducibility while having a higher uptake of hydrogen, especially at the low-temperature peak at around 350 °C. The temperature range for reduction features a broadening from around 200 up to 550 °C compared to the unpromoted catalyst. This coincides with the preparation method by CP. It is assumed that many different-sized clusters of the promoter metal on the surface of In₂O₃/ZrO₂ are responsible for this behavior. Moreover, a broadening effect could be observed using the Ce-promoted catalyst as well. Using the Mg-doped In₂O₃/ZrO₂ catalyst also increased the metal-based productivity by up to 1.97 g_{MeOH} g_{active metal}⁻¹ h⁻¹ compared to the undoped catalyst. However, this effect was significantly less pronounced compared with the other two promoters. This goes in hand with a lower increase in the CO₂ adsorption capacity (Figure S7). Therefore, it was decided not to further pursue Mg as a promoter in the following studies.

Catalyst Selection for the DoE Study. In the course of finding the most promising catalyst for the parameter optimization study, both the Ni and Ce-doped catalysts showing promising performance and selectivity at 300 °C have to be considered further. For selecting one catalyst for the following DoE study and to estimate the influence of H₂ Spillover and CO₂ adsorption on the reaction kinetics, both catalysts containing a similar In (7.5 wt %) and promoter (1 wt %) loading (Table 2) were compared at a lower reaction temperature of 250 °C under otherwise identical reaction conditions (Figure 5).

For both systems, the methanol selectivity increased significantly up to $S = 70\%$ for the Ni and up to 82% for the

Table 2. Results Obtained from ICP-OES, N₂ Physisorption, and CO₂-TPD for Ni and Ce-Promoted In₂O₃/ZrO₂ Catalysts

	indium loading [wt %]	S_{BET} [$\text{m}^2 \text{g}^{-1}$]	pore radius [nm]	pore volume [$\text{cm}^3 \text{g}^{-1}$]	relative CO ₂ adsorption capacity
Ni-In ₂ O ₃ /ZrO ₂	7.44	87.12	3.70	0.256	1.00
Ce-In ₂ O ₃ /ZrO ₂	7.62	84.87	4.06	0.271	1.30

Ce-doped catalyst. This can be attributed to an increase in the equilibrium yield for methanol and a decrease in the endothermic RWGS reaction. Using Ce as a promoter suppressed the RWGS reaction, resulting in higher selectivity. Hereby, CeO₂ can oxidize CO to CO₂ resulting in an oxygen vacancy. The Ni-promoted catalyst shows a significantly higher metal-based productivity of up to 1.48 g_{MeOH} g_{active metal}⁻¹ h⁻¹ compared to the Ce-promoted catalyst (1.06 g_{MeOH} g_{active metal}⁻¹ h⁻¹) at 250 °C, due to a higher BET surface area (see Table 2) and improved reduction capacity (see Figure S8). Therefore, H₂ adsorption has a greater influence (rate-determining step) on the methanol formation than the higher CO₂ adsorption at lower reaction temperatures. The addition of Ni improved H₂ adsorption by the hydrogen spillover effect. This can be deduced from the H₂ TPR and CO₂ TPD measurements, with a higher hydrogen uptake at lower temperatures for the Ni-promoted catalyst. Ni-In₂O₃/ZrO₂ showed a maximum H₂ consumption peak located between 250 and 450 °C in the H₂ TPR attributed to Ni reduction (see Figure S8). The TPR, as well as HRTEM measurements, revealed highly dispersed Ni on the catalyst surface. Both catalysts showed no change in morphology after the reaction, derived from their respective XRD (Figures S11 and S12). From the perspective of selecting the most promising methanol synthesis catalyst, the Ni-promoted In₂O₃/ZrO₂ catalyst was chosen for the following DoE study.

DoE Study for Maximizing the Methanol Yield of the Ni-In₂O₃/ZrO₂ Catalyst. For the identification of significant

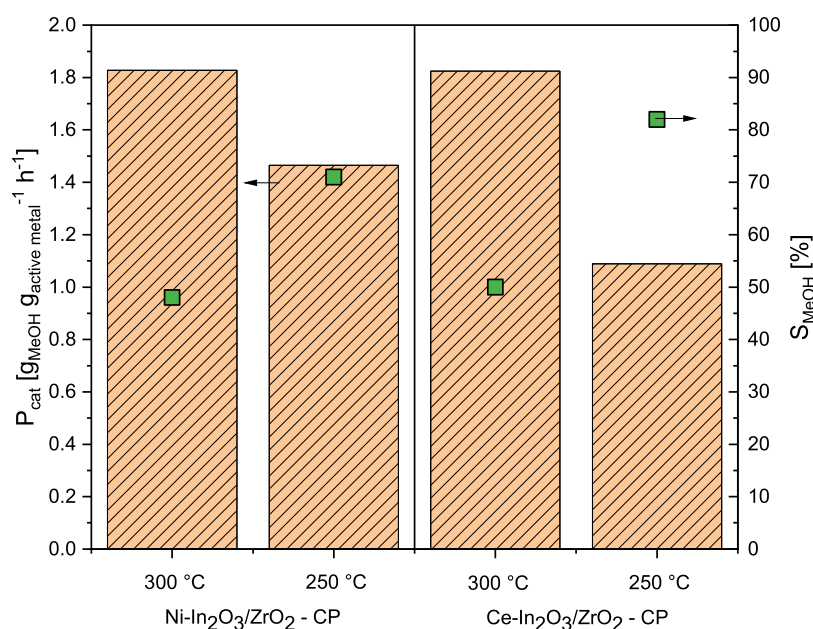


Figure 5. Dependency of the reaction temperature on the catalytic performance of the Ni and Ce-promoted $\text{In}_2\text{O}_3/\text{ZrO}_2$ catalyst. Reaction conditions: $T = 250\text{--}300\text{ }^\circ\text{C}$, $p = 75\text{ bar}$, $\text{H}_2/\text{CO}_2 = 4/1$, $m_{\text{cat}} = 2.0\text{ g}$, $N = 1200\text{ rpm}$, $V_{\text{OH}} = 100\text{ mL}$, $t_{\text{R}} = 3\text{ h}$.

factors for the methanol synthesis in the slurry reactor, a two-level fractional factorial test design with a resolution of IV was selected to study the effect of four typical and easy-to-change reaction variables. A resolution of IV was important for clarifying the two-way interaction of the selected variables. Additionally, four center points were added to take the possible curvature of the response surface into consideration. The high and low levels for the experimental design are listed in Table 3. All other factors were kept constant. The whole experimental plan for the DoE, comprising 12 experiments, can be found in the Supporting Information (Table S5). The model analysis is based on analysis of variance (ANOVA) techniques.³² The corresponding ANOVA table for the model is shown in Table 4.

With the help of a Pareto chart (Figure 6), the most significant factors were selected and included in the model. The model equation for the response “Yield Methanol [%]” and the coded and uncoded equations are shown in eqs 6 and 7.

$$Y_{\text{MeOH}} = 11.92 + 1.56A + 2.61B - 0.4388C + 0.1212D + 0.8513AC - 1.04D \quad (7)$$

$$Y_{\text{MeOH}} = 47.884 + 0.505A[\text{bar}] + 0.104B [^\circ\text{C}] - 9.39C[\text{g}] + 0.027D[\text{rpm}] + 0.136AD[\text{bar}^*\text{g}] - 0.00042AC[\text{bar}^*\text{rpm}] \quad (8)$$

Table 3. Variables and Their Ranges Employed in the DoE Study to Maximize the Methanol Yield

variable	low level	high level
A-pressure p	50 bar	75 bar
B-temperature T	250 $^\circ\text{C}$	300 $^\circ\text{C}$
C-catalyst mass m	1 g	2 g
D-stirrer speed N	1200 rpm	1600 rpm

The variable B-temperature has the highest significance and is above the calculated Bonferroni limit (4.38175). This is the significance level divided by the number of experiments performed, which reduced the probability of false-positive effects and is therefore certainly important for the model.³³ This correlates with the thermodynamic consideration of the equilibrium equation. The same can be assumed for the variable A-pressure that lies above the t -value (2.57058). This is calculated by the mean difference divided by the standard error. It represents the number of standard deviations separating the two means and is possibly important for the model. The effects of AD, AC, C-catalyst mass, and D-stirrer speed have been included in the model due to hierarchy reasons. Effects with lower values were neglected.

The results in Figure 7 show a strong influence of the reaction temperature and pressure on the methanol yield. As expected, the highest methanol yield (orange area) was achieved at a temperature of 300 $^\circ\text{C}$ and a pressure of 75 bar. The yield decreases with a lower temperature and pressure (from the orange over green to the blue area). The lowest yield of methanol (blue area) was found at 250 $^\circ\text{C}$ and 50 bar. The calculated methanol STY range from 0.042 $\text{g}_{\text{MeOH}} \text{g}_{\text{cat}}^{-1} \text{h}^{-1}$ at 250 $^\circ\text{C}$ and 50 bar, up to 0.268 $\text{g}_{\text{MeOH}} \text{g}_{\text{cat}}^{-1} \text{h}^{-1}$ at 300 $^\circ\text{C}$ and 75 bar. The four design points in the center of the plot (red circle at 275 $^\circ\text{C}$ and 62.5 bar) have an average STY of $0.145 \pm 0.013 \text{ g}_{\text{MeOH}} \text{g}_{\text{cat}}^{-1} \text{h}^{-1}$. However, no coherent curvature could be obtained with the available/present data. With the variables catalyst mass and stirrer speed having a negligible effect, methanol STY ($0.283 \text{ g}_{\text{MeOH}} \text{g}_{\text{cat}}^{-1} \text{h}^{-1}$) was predicted to reach a maximum at $T = 300\text{ }^\circ\text{C}$, $p = 75\text{ bar}$, $m_{\text{cat}} = 1.0\text{ g}$, $N = 1200\text{ rpm}$ (Figure S15). This was verified with an additional experiment resulting in a STY of $0.290 \text{ g}_{\text{MeOH}} \text{g}_{\text{cat}}^{-1} \text{h}^{-1}$ twice as high as that in the experiments using 2 g of the catalyst (Figure 5).

CO Hydrogenation Using the Ni-Doped $\text{In}_2\text{O}_3/\text{ZrO}_2$ Catalyst. Besides being a promising catalyst for green methanol synthesis using CO_2 as a carbon source, there is also the possibility of implementing the Ni- $\text{In}_2\text{O}_3/\text{ZrO}_2$ CP

Table 4. Analysis of the Variance (ANOVA) for the Developed DoE Model

source	SS	df	MS	F-value	p-value	R ²	R _{adj} ²	R _{pred} ²
model	90.09	6	15.02	9.22	0.0249	0.9326	0.8314	0.7737
A-pressure	19.38	1	19.38	11.90	0.0261			
B-temperature	54.55	1	54.55	33.50	0.0044			
C-catalyst mass	1.54	1	1.54	0.9457	0.3859			
D-stirrer speed	0.1176	1	0.1176	0.0722	0.8014			
AC	5.80	1	5.80	3.56	0.1322			
AD	8.72	1	8.72	5.35	0.0817			
curvature	32.36	1	32.36	19.88	0.0112			
residual	6.51	4	1.63					
lack of fit	0.1653	1	0.1653	0.0781	0.7980			
pure error	6.35	3	2.12					
cor total	128.97	11						

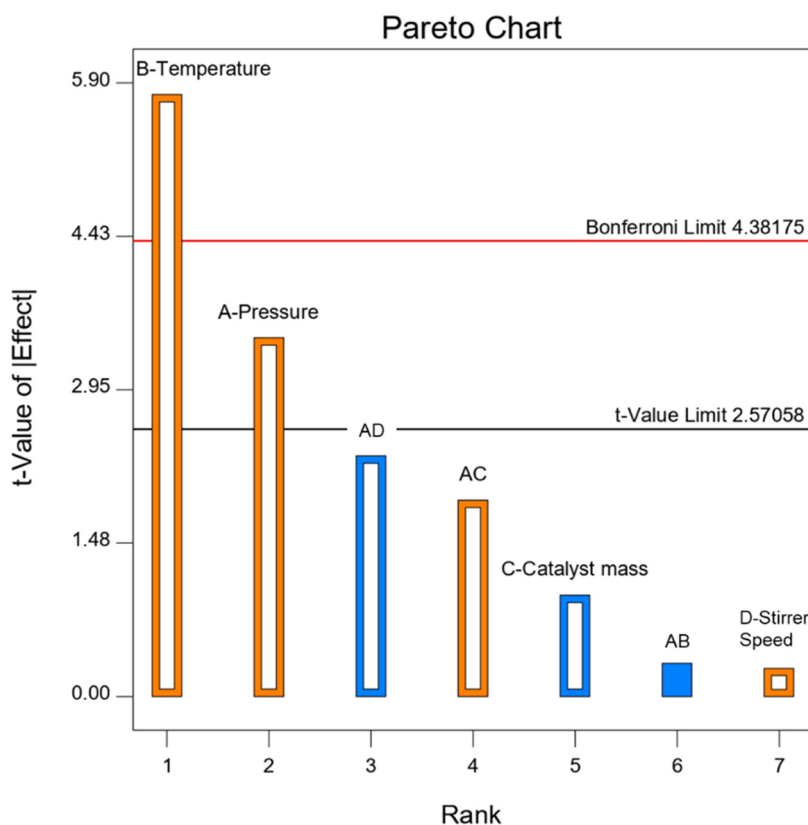


Figure 6. Pareto chart of the significant effects for the performed DoE.

catalyst in the current industrial process using CO as a carbon source. To investigate the ability of the catalyst to reduce CO (the main component in the classical methanol synthesis) as well, the reaction gas was adjusted to a stoichiometric composition of H₂/CO = 2/1 under the calculated optimal conditions derived from the DoE ($T = 300\text{ }^{\circ}\text{C}$, $p = 75\text{ bar}$, $m_{\text{cat}} = 1.0\text{ g}$, and $N = 1200\text{ rpm}$). One gram of the catalyst showed a STY of $0.49\text{ g}_{\text{MeOH}}\text{ g}_{\text{cat}}^{-1}\text{ h}^{-1}$ and a methanol selectivity of $S = 82\%$ for CO hydrogenation (Figure 8). This could be related to the possible higher equilibrium yield of methanol under the present reaction conditions.³⁴ It was demonstrated that the catalyst is also able to convert CO to methanol with a higher STY and selectivity than for green methanol synthesis using CO₂.

To contextualize these findings, the Ni–In₂O₃/ZrO₂ CP catalyst was compared to the industrial Cu-based catalyst using industry gas composition.

Catalyst Performance at Current Industry Gas Composition.

In the next set of experiments, the commercial Cu-based catalyst pellets were mortared and sieved to a particle size of 32–80 μm to match the size of the Ni–In₂O₃/ZrO₂ CP catalyst and to exclude additional diffusion limitations. The gas phase was adjusted to be composed of 70% H₂, 28% CO, and 2% CO₂ to reflect a typical industry gas composition. Very interestingly, the Ni–In₂O₃/ZrO₂ CP catalyst showed a slightly higher performance than using pure CO resulting in a metal-based productivity P_{cat} of $6.84\text{ g}_{\text{MeOH}}\text{ g}_{\text{Ni+In}}^{-1}\text{ h}^{-1}$ (Figure 9). Moreover, a very high selectivity of $S = 94\%$ was achieved. Compared to the Cu-based catalyst showing a selectivity of only $S = 83\%$, the Ni–In₂O₃/ZrO₂–CP catalyst was less selective to the (R)WGS reaction which could be explained by the reaction mechanism favoring the binding of the CO_x species in an oxygen vacancy instead of the metal surface.³⁵ The Cu-based catalyst also showed a

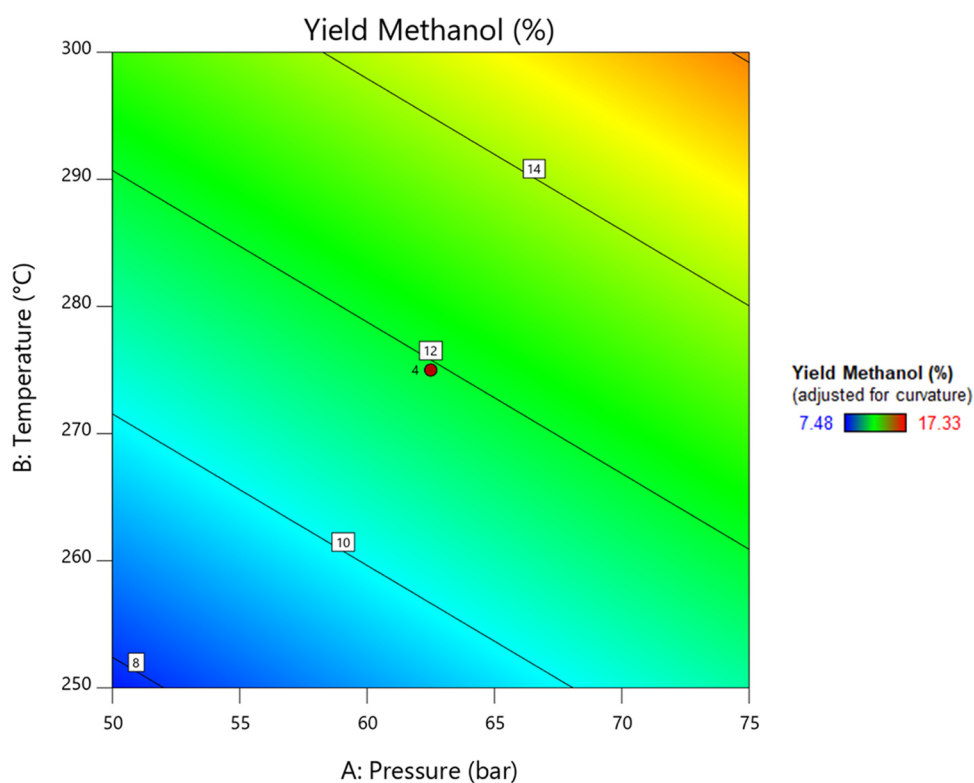


Figure 7. Contour-plot for the methanol yield depending on the main contributing variables, temperature, and pressure. The reaction time and gas phase composition were kept constant at $t_R = 3$ h and $H_2/CO_2 = 4/1$.

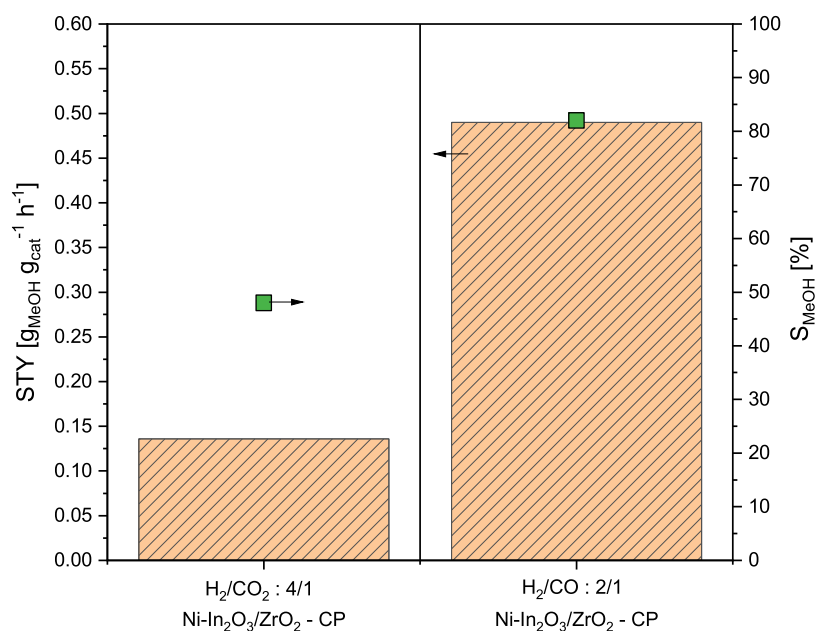


Figure 8. STY and selectivity of the Ni-doped In_2O_3/ZrO_2 catalyst using different carbon sources. Reaction conditions: $T = 300$ °C, $p = 75$ bar, $m_{cat} = 1.0$ g, $N = 1200$ rpm, $V_{Oil} = 100$ mL, $t_R = 3$ h.

drastically lower metal-based productivity P_{cat} of only 1.25 $g_{MeOH} g_{Cu}^{-1} h^{-1}$ which could be explained by the much higher loading of active metal of around 60% Cu compared to only 0.75 wt % Ni and 7.5 wt % In. Equilibrium was already reached after around 90 min of reaction time indicated by a constant reaction pressure and gas composition detected by GC.

Catalyst Stability. To investigate the stability of the preferred slurry CO_2 hydrogenation system, four reactions

have been carried out consecutively using the Ni- In_2O_3/ZrO_2 CP catalyst under optimized reaction conditions (300 °C, 75 bar, 1600 rpm). Figure 10 shows the STY for four consecutive runs in the slurry reactor. To ensure a clean gas phase with the same composition, the reactor was purged five times with nitrogen using a moderate stirring speed of 200 rpm between two consecutive runs.

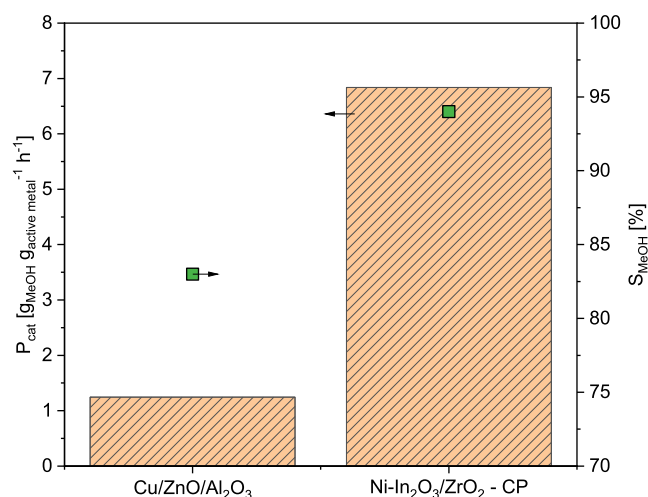


Figure 9. Comparison of the catalytic performance of commercial Cu/ZnO/Al₂O₃ and Ni–In₂O₃/ZrO₂–CP under industry gas composition. Reaction conditions: $T = 300\text{ }^{\circ}\text{C}$, $p = 75\text{ bar}$, $\text{H}_2/\text{CO}/\text{CO}_2 = 70/28/2$, $m_{\text{cat}} = 1.0\text{ g}$, $N = 1200\text{ rpm}$, $V_{\text{Oil}} = 100\text{ mL}$, $t_{\text{R}} = 3\text{ h}$.

In the first reaction using a fresh catalyst and mineral oil as a carrier liquid, a STY of $0.125 \pm 0.009\text{ g}_{\text{MeOH}}\text{ g}_{\text{cat}}^{-1}\text{ h}^{-1}$ was achieved. In the following recycling experiments, a similar STY between 0.114 and $0.134\text{ g}_{\text{MeOH}}\text{ g}_{\text{cat}}^{-1}\text{ h}^{-1}$ could be observed. There is no indication of significant deactivation observed besides recycling experiment 3. This dip in activity could contribute to an outlier in the measurement of the gas phase. The STY of the Ni–In₂O₃/ZrO₂–CP catalyst in the recycling experiments is in the same order of magnitude as the other experiments under similar conditions (Figure 4).

After methanol synthesis in the slurry reactor, the catalyst was separated from mineral oil by filtration and washed with iso-propanol. The composition of the catalyst before and after recycling was determined using ICP-OES (see Table 5).

Table 5. Elemental Composition Determined by ICP-OES of the Catalyst before (Pre) and after (Post) Recycling Experiments

	Ni (%)	indium (%)	zirconium (%)
Ni–In ₂ O ₃ /ZrO ₂ –CP—pre	0.75	7.44	57.71
Ni–In ₂ O ₃ /ZrO ₂ –CP—post	0.56	6.51	56.02

Due to the high abrasion of the catalyst at 1600 rpm, a lower loading of Ni and In could be detected. Leaching of the catalyst cannot be fully excluded, but it seems to have had no effect on the catalyst activity in the 4 recycling experiments with a total reaction time of 12 h.

The catalysts' morphological phase was analyzed further by powder XRD patterns before and after the stability test (Figures S11 and S12). There was no morphological phase change observed. ¹³C- and ¹H NMR characterization of the carrier liquid confirmed the stability for the total reaction time of 12 h (Figure S13).

CONCLUSIONS

In this work, a series of metal-doped In-based catalysts have been synthesized and tested for methanol synthesis in a slurry reactor. The addition of Ni to In₂O₃ drastically enhanced the STY of methanol. Ni/In₂O₃ prepared via CP produced $0.075\text{ g}_{\text{MeOH}}\text{ g}_{\text{cat}}^{-1}\text{ h}^{-1}$ compared to $0.011\text{ g}_{\text{MeOH}}\text{ g}_{\text{cat}}^{-1}\text{ h}^{-1}$ for pure In₂O₃. Supported In₂O₃/ZrO₂ catalysts also boosted the performance to $0.11\text{ g}_{\text{MeOH}}\text{ g}_{\text{cat}}^{-1}\text{ h}^{-1}$. These two increasing effects were combined in this study. In the best procedure, 0.75 wt % Ni and 7.5 wt % In were added to ZrO₂ as a support material by CP and acted as an effective catalyst for slurry-phase hydrogenation of both CO₂ and CO. A statistical and modeling tool (DoE) was applied and temperature and pressure were identified as the key performance parameters. The amount of catalyst used could be halved as well, having a negligible effect on the methanol yield in the examined conditions. The Ni–In₂O₃/ZrO₂ (CP) catalyst produced $0.109\text{ g}_{\text{MeOH}}\text{ g}_{\text{cat}}^{-1}\text{ h}^{-1}$ at a low temperature of 250 °C by

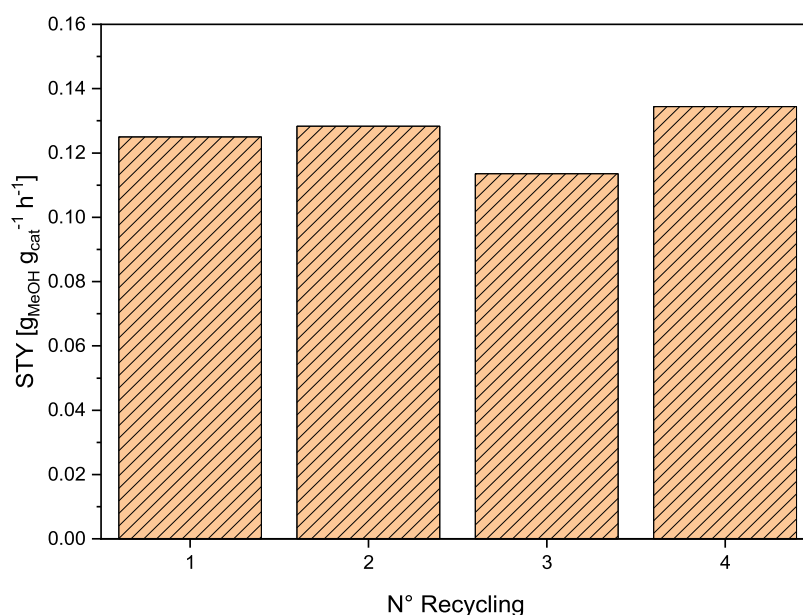


Figure 10. Examination of catalyst stability by recycling the catalyst and carrier liquid for four consecutive runs using similar reaction conditions: $T = 300\text{ }^{\circ}\text{C}$, $p = 75\text{ bar}$, $\text{H}_2/\text{CO}_2 = 4/1$, $m_{\text{cat}} = 2.0\text{ g}$, $N = 1600\text{ rpm}$, $V_{\text{Oil}} = 100\text{ mL}$, $t_{\text{R}} = 3\text{ h}$.

using pure CO₂ as a carbon source. At higher temperatures of 300 °C using CO as a carbon source under industry gas composition (H₂/CO/CO₂ = 70/28/2), the STY increased to 0.530 g_{MeOH} g_{cat}⁻¹ h⁻¹ with a very high selectivity *S* = 94%. In comparison, a commercial Cu-based catalyst produced more methanol (0.747 g_{MeOH} g_{cat}⁻¹ h⁻¹), but showed lower methanol productivity related to the active metal content and a lower selectivity *S* = 84%. To conclude, the study presented here could improve the slurry-phase hydrogenation of both CO and CO₂ using a very promising and recyclable Ni–In₂O₃/ZrO₂ (CP) catalyst.

■ ASSOCIATED CONTENT

SI Supporting Information

The Supporting Information is available free of charge at <https://pubs.acs.org/doi/10.1021/acssuschemeng.3c05584>.

Calculation of error bars; catalyst preparation; online GC analysis conditions; elementary composition; HRTEM images, HAADF and STEM-EDX elemental mapping of fresh catalysts; reproduction; blind activity of reactor setup and reference materials; CO₂ TPD and H₂ TPR conditions and results; batch comparison of Ni–In₂O₃/ZrO₂ catalysts; FID chromatograms for Ni–In₂O₃/ZrO₂ (CP); XRD patterns of fresh and used Ni–In₂O₃/ZrO₂; stability of used mineral oil determined by ¹H and ¹³C NMR and influence of different carrier liquids on the catalytic performance; and DoE implementation plan and influence factors (PDF)

■ AUTHOR INFORMATION

Corresponding Author

Jakob Albert – Institute of Technical and Macromolecular Chemistry, Universität Hamburg, 20146 Hamburg, Germany; orcid.org/0000-0002-3923-2269; Email: jakob.albert@uni-hamburg.de

Authors

Philipp Kampe – Institute of Technical and Macromolecular Chemistry, Universität Hamburg, 20146 Hamburg, Germany; orcid.org/0000-0001-8843-1240

Nick Herrmann – Institute of Technical and Macromolecular Chemistry, Universität Hamburg, 20146 Hamburg, Germany; orcid.org/0009-0003-8227-8654

Anne Wesner – Institute of Technical and Macromolecular Chemistry, Universität Hamburg, 20146 Hamburg, Germany

Charlotte Ruhmlied – Institute of Physical Chemistry, Universität Hamburg, 20146 Hamburg, Germany

Complete contact information is available at:

<https://pubs.acs.org/10.1021/acssuschemeng.3c05584>

Notes

The authors declare no competing financial interest.

■ ACKNOWLEDGMENTS

The authors acknowledge Dr. Michael Pabel from Saint-Gobain NorPro for material support. Moreover, the Central Analytics Department and the X-ray Service Facility at Hamburg University are acknowledged for ICP-OES measurements and powder diffractograms. A special thanks goes to the Department of Electron Microscopy for HRTEM and STEM-EDX measurements.

■ REFERENCES

- (1) Perathoner, S.; van Geem, K. M.; Marin, G. B.; Centi, G. Reuse of CO₂ in energy intensive process industries. *Chem. Commun.* **2021**, 57, 10967–10982.
- (2) Dieterich, V.; Buttler, A.; Hanel, A.; Spliethoff, H.; Fendt, S. Power-to-liquid via synthesis of methanol, DME or Fischer–Tropsch-fuels: a review. *Energy Environ. Sci.* **2020**, 13, 3207–3252.
- (3) Yarulina, I.; Chowdhury, A. D.; Meirer, F.; Weckhuysen, B. M.; Gascon, J. Recent trends and fundamental insights in the methanol-to-hydrocarbons process. *Nat. Catal.* **2018**, 1, 398–411.
- (4) Klier, K.; Chatikavanij, V.; Herman, R. G.; Simmons, G. W. Catalytic Synthesis of Methanol from CO/H₂: The Effects of Carbon Dioxide. *J. Catal.* **1981**, 1982, 343–360.
- (5) Nielsen, N. D.; Jensen, A. D.; Christensen, J. M. The roles of CO and CO₂ in high pressure methanol synthesis over Cu-based catalysts. *J. Catal.* **2021**, 393, 324–334.
- (6) Twigg, M. V.; Spencer, M. S. Deactivation of supported copper metal catalysts for hydrogenation reactions. *Appl. Catal., A* **2001**, 212, 161–174.
- (7) Martin, O.; Martín, A. J.; Mondelli, C.; Mitchell, S.; Segawa, T. F.; Hauert, R.; Drouilly, C.; Curulla-Ferré, D.; Pérez-Ramírez, J. Indium Oxide as a Superior Catalyst for Methanol Synthesis by CO₂ Hydrogenation. *Angew. Chem.* **2016**, 55, 6261–6265.
- (8) Schühle, P.; Schmidt, M.; Schill, L.; Riisager, A.; Wasserscheid, P.; Albert, J. Influence of gas impurities on the hydrogenation of CO₂ to methanol using indium-based catalysts. *Catal. Technol.* **2020**, 10, 7309–7322.
- (9) Zhong, J.; Yang, X.; Wu, Z.; Liang, B.; Huang, Y.; Zhang, T. State of the art and perspectives in heterogeneous catalysis of CO₂ hydrogenation to methanol. *Chem. Soc. Rev.* **2020**, 49, 1385–1413.
- (10) Schühle, P.; Reichenberger, S.; Marzun, G.; Albert, J. Slurry Phase Hydrogenation of CO₂ to Methanol Using Supported In₂O₃ Catalysts as Promising Approach for Chemical Energy Storage. *Chem. Ing. Tech.* **2021**, 93, 585–593.
- (11) Jia, X.; Sun, K.; Wang, J.; Shen, C.; Liu, C. Selective hydrogenation of CO₂ to methanol over Ni/In₂O₃ catalyst. *J. Energy Chem.* **2020**, 50, 409–415.
- (12) Frei, M. S.; Mondelli, C.; García-Muelas, R.; Morales-Vidal, J.; Philipp, M.; Safonova, O. V.; López, N.; Stewart, J. A.; Ferré, D. C.; Pérez-Ramírez, J. Nanostructure of nickel-promoted indium oxide catalysts drives selectivity in CO₂ hydrogenation. *Nat. Commun.* **2021**, 12, No. 1960.
- (13) Zhang, Z.; Shen, C.; Sun, K.; Liu, C. Improvement in the activity of Ni/In₂O₃ with the addition of ZrO₂ for CO₂ hydrogenation to methanol. *Catal. Commun.* **2022**, 162, No. 106386.
- (14) Frei, M. S.; Mondelli, C.; García-Muelas, R.; Kley, K. S.; Puértolas, B.; López, N.; Safonova, O. V.; Stewart, J. A.; Curulla Ferré, D.; Pérez-Ramírez, J. Atomic-scale engineering of indium oxide promotion by palladium for methanol production via CO₂ hydrogenation. *Nat. Commun.* **2019**, 10, No. 3377.
- (15) Wei, Y.; Liu, F.; Ma, J.; Yang, C.; Wang, X.; Cao, J. Catalytic roles of In₂O₃ in ZrO₂-based binary oxides for CO₂ hydrogenation to methanol. *Mol. Catal.* **2022**, 525, No. 112354.
- (16) Tsoukalou, A. *Development of In₂O₃-Based Catalysts for the Hydrogenation of CO₂ to Methanol: Elucidating the Structure-Performance Relationship, Active Sites and Reaction Mechanism*; ETH Zurich, 2022.
- (17) Sharma, P.; Hoang Ho, P.; Shao, J.; Creaser, D.; Olsson, L. Role of ZrO₂ and CeO₂ support on the In₂O₃ catalyst activity for CO₂ hydrogenation. *Fuel* **2023**, 331, No. 125878.
- (18) Cannizzaro, F.; Hensen, E. J. M.; Pilot, I. A. W. The Promoting Role of Ni on In₂O₃ for CO₂ Hydrogenation to Methanol. *ACS Catal.* **2023**, 13, 1875–1892.
- (19) Ghuman, K. K.; Wood, T. E.; Hoch, L. B.; Mims, C. A.; Ozin, G. A.; Singh, C. V. Illuminating CO₂ reduction on frustrated Lewis pair surfaces: investigating the role of surface hydroxides and oxygen vacancies on nanocrystalline In₂O(3-x)(OH)_y. *Phys. Chem. Chem. Phys.* **2015**, 17, 14623–14635.

- (20) Jiang, X.; Nie, X.; Guo, X.; Song, C.; Chen, J. G. Recent Advances in Carbon Dioxide Hydrogenation to Methanol via Heterogeneous Catalysis. *Chem. Rev.* **2020**, *120*, 7984–8034.
- (21) Dostagir, N. H. M.; Thompson, C.; Kobayashi, H.; Karim, A. M.; Fukuoka, A.; Shrotri, A. Rh promoted In_2O_3 as a highly active catalyst for CO_2 hydrogenation to methanol. *Catal. Sci. Technol.* **2020**, *10*, 8196–8202.
- (22) Shen, H.; Li, H.; Yang, Z.; Li, C. Magic of hydrogen spillover: Understanding and application. *Green Energy Environ.* **2022**, *7*, 1161–1198.
- (23) Lau, K.; Schühle, P.; Liang, S.-X.; de Kock, F.; Albert, J.; Reichenberger, S. Laser-Generated $\text{InO}_x/\text{ZrO}_2$ Catalysts for CO_2 Hydrogenation: Role of In Situ Fragmentation and Ripening Control. *ACS Appl. Energy Mater.* **2021**, *4*, 9206–9215.
- (24) Panzone, C.; Philippe, R.; Chappaz, A.; Fongarland, P.; Bengaouer, A. Power-to-Liquid catalytic CO_2 valorization into fuels and chemicals: focus on the Fischer–Tropsch route. *J. CO2 Util.* **2020**, *38*, 314–347.
- (25) Makhlin, V. A. Development and analysis of heterogeneous catalytic processes and reactors. *Theor. Found. Chem. Eng.* **2009**, *43*, 245–259.
- (26) Bozzano, G.; Manenti, F. Efficient methanol synthesis: Perspectives, technologies and optimization strategies. *Prog. Energy Combust. Sci.* **2016**, *56*, 71–105.
- (27) Li, Z.; Tsotsis, T. T. Methanol synthesis in a high-pressure membrane reactor with liquid sweep. *J. Membr. Sci.* **2019**, *570–571*, 103–111.
- (28) Wang, T.; Wang, J.; Jin, Y. Slurry Reactors for Gas-to-Liquid Processes: A Review. *Ind. Eng. Chem. Res.* **2007**, *46*, 5824–5847.
- (29) Sigma-Aldrich Safety Data Sheet, Mineral oil, Product Number 330779; Sigma-Aldrich, 2022.
- (30) Kampe, P.; Wesner, A.; Schühle, P.; Hess, F.; Albert, J. How do conversion, temperature and feed ratio control phase transitions of $\text{In}_2\text{O}_3/\text{In}(\text{OH})_3$ -based methanol synthesis catalysts? A combined experimental and computational study. *ChemPlusChem* **2023**, *88* (9), No. e202300425.
- (31) Dey, S.; Dhal, G. C. Cerium catalysts applications in carbon monoxide oxidations. *Mater. Sci. Energy Technol.* **2020**, *3*, 6–24.
- (32) Chatfield, C. *Statistics for Technology: A Course in Applied Statistics*; CRC Press, 1983.
- (33) Groenwold, R. H. H.; Goeman, J. J.; Le Cessie, S.; Dekkers, O. M. Multiple testing: when is many too much? *Eur. J. Endocrinol.* **2021**, *184*, E11–E14.
- (34) Behrendt, G.; Mockenhaupt, B.; Prinz, N.; Zobel, M.; Ras, E.-J.; Behrens, M. CO Hydrogenation to Methanol over Cu/MgO Catalysts and Their Synthesis from Amorphous Magnesian Goethite Precursors. *ChemCatChem* **2022**, *14* (17), No. e202200299.
- (35) Ye, J.; Liu, C.; Mei, D.; Ge, Q. Active Oxygen Vacancy Site for Methanol Synthesis from CO_2 Hydrogenation on In_2O_3 (110): A DFT Study. *ACS Catal.* **2013**, *3*, 1296–1306.

7 Comprehensive discussion

CO₂ hydrogenation to methanol is a promising approach for the utilization of captured CO₂ from industrial processes and for the defossilization of methanol synthesis. This work aims to increase the catalytic performance of In-based catalysts by metal-doping and by investigating this in different reactor concepts. Those are namely: a continuously operated fixed bed reactor (integral operation, two-phase reactor), a continuously operated compact profile reactor (integral or differential operation, two-phase reactor) and a stirred-tank reactor (batch operation, three-phase reactor) for the CO₂ hydrogenation to methanol.

Two-phase fixed bed reactor with an integral operation mode

First, the phase transition behaviors of pure In₂O₃ or In(OH)₃ and their catalytic activity in a fixed bed reactor was investigated at 75 bar and 200 °C, 250 °C, 275 °C and 300 °C, respectively, using a stoichiometric gas ratio of CO₂/H₂ = 3/1. Commercial In₂O₃ or In(OH)₃ was used representing the two possible sides of the predicted dummy catalytic cycle and two setups were applied as depicted in Figure 7.1.

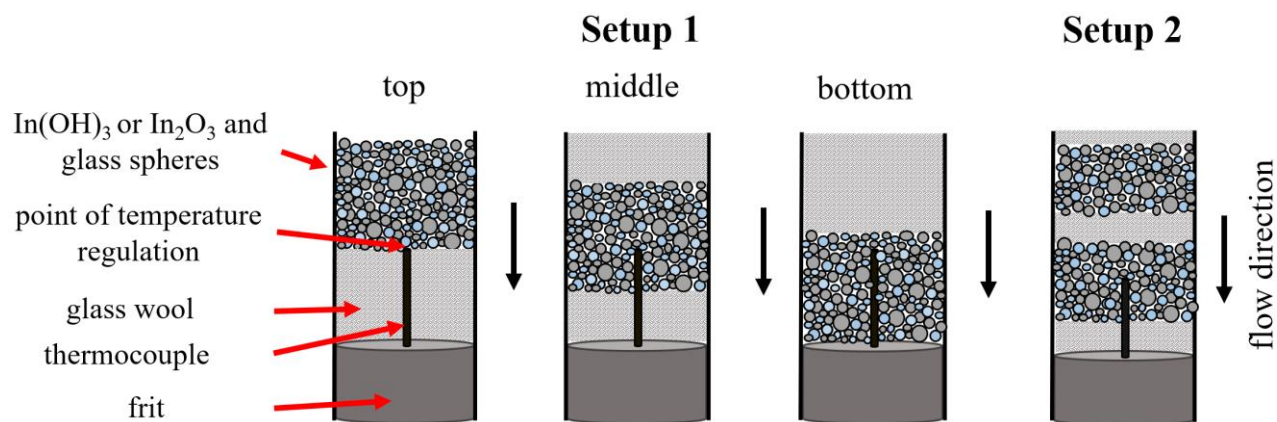


Figure 7.1. Illustration of experimental setup 1 and 2, adapted from [18].

In experimental setup 1 the influence of thermoelement position (top, middle or bottom position) in relation to the fixed bed was studied (see Figure 7.1). During the reaction, the temperature of the bed increases over the packing height due to the reaction heat of CO₂ hydrogenation. For the bottom position, the thermoelement is at the beginning and coldest spot of the catalyst bed. In the middle and top position, the temperature increases due to reaction heat. Therefore, the thermoelement at top position regulates the temperature at the hottest zone of the catalyst bed. The middle and bottom position reached the highest CO₂ conversion for each temperature with a higher temperature at the

end of the catalyst bed. The experimental data showed that the CO₂ conversion and the rWGS selectivity increased with higher temperatures for both, In₂O₃ and In(OH)₃. At 300 °C (middle configuration), the CO₂ conversion for In₂O₃ reached 3.56 % with 73 % selectivity and 4.25 % for In(OH)₃ with 71 % selectivity. After the reaction at 300 °C, TGA and XRD revealed no rehydration for In₂O₃. In contrast; a total conversion of In(OH)₃ to In₂O₃ in middle and bottom position, with a near-total conversion to In₂O₃ in top position was reached. The experimental setup 1 confirmed the validity of the thermodynamic model about In₂O₃ stability.

Theoretical modeling predicts a strong dependence of the In(OH)₃ dehydration behavior on the conversion due to H₂O formation. In(OH)₃ formation is favored at low temperatures and high conversion or at higher temperatures and lower conversion. Therefore In(OH)₃ is most stable at high H₂O partial pressure. This prediction was confirmed in experimental setup 2, in which the catalyst bed of In(OH)₃ was split into two identical segments, representing a low-conversion (top) and high-conversion (bottom) zone (see Figure 7.1). XRD and TGA showed that the bottom segment contained more In(OH)₃ than the upper segment after reaction. Water is released by phase transition of In(OH)₃ to In₂O₃ in the segment above, inhibiting the release in the bottom segment for temperatures between 200 °C and 250 °C. The trend is reversed between 250 °C and 275 °C, which was predicted by the model at 285 °C. The difference is due to the uncertainty associated with the experiment based thermodynamic data. The validated model was used to predict the effect of hydrogen drop out caused by fluctuating renewable energies and intermittent hydrogen sources on the stability of the catalyst. The main hazard for catalyst stability in this case is a temperature reduction caused by the reduced heat of reaction. This is crucial for the reactor design of methanol synthesis, since large-scale fixed beds usually have cold spots, resulting in an increased formation of In(OH)₃ locally.

The catalytic activity and stability of In₂O₃ catalysts can be enhanced by metal-support interactions using a catalyst support. In several studies [16,106,125,145,166,167] In₂O₃/ZrO₂ catalysts have shown to be highly active and selective for CO₂ hydrogenation to methanol. This dissertation was able to confirm that. Moreover, it further reveals key aspects for catalytic performance and increases the activity of In₂O₃/ZrO₂-based catalysts (see Figure 7.2).

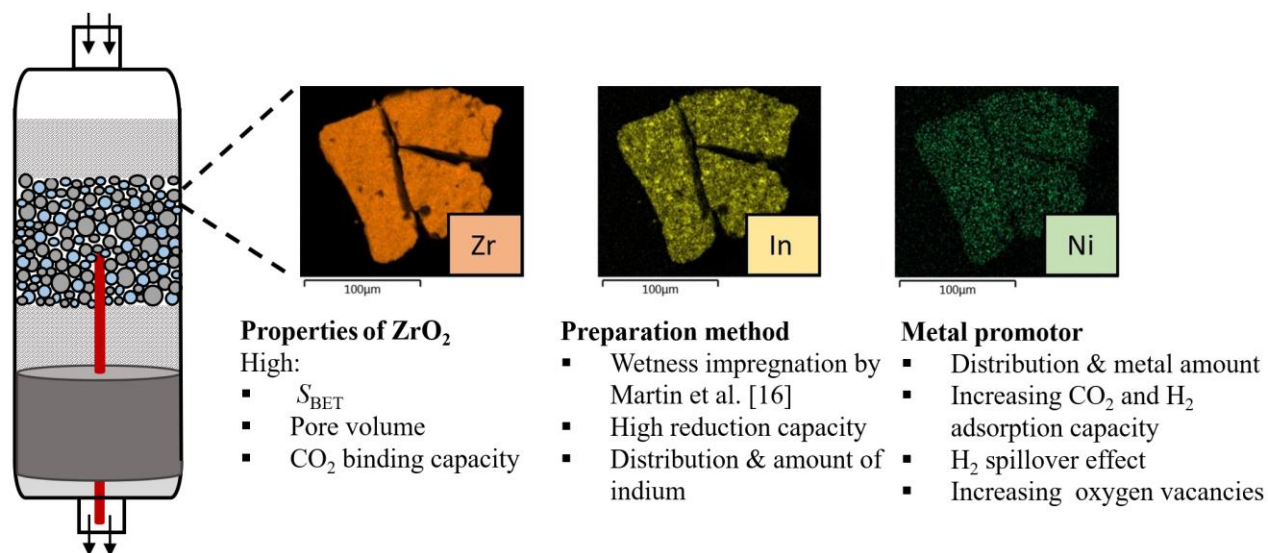


Figure 7.2. Illustration of key findings on catalyst activity of indium-based catalysts.

The most significant influence for In_2O_3/ZrO_2 catalysts is the surface area of the employed ZrO_2 . Higher surface areas and pore volumes increase the catalytic activity for CO_2 hydrogenation. To further increase the activity of the In_2O_3/ZrO_2 catalyst, CuO, NiO, MgO or CeO_2 , respectively were added by co-precipitation (CP) to enhance the CO_2 adsorption or hydrogen uptake capacity. The addition of NiO to In_2O_3/ZrO_2 raises the methanol productivity up to $0.221 \text{ g}_{MeOH} \text{ g}_{cat}^{-1} \text{ h}^{-1}$ and 66 % selectivity compared to pure In_2O_3/ZrO_2 with $0.159 \text{ g}_{MeOH} \text{ g}_{cat}^{-1} \text{ h}^{-1}$ and 77 % selectivity at 75 bar, 250 °C and 8300 h^{-1} of $CO_2/H_2 = 1/3$. This is in accordance with the enhance, activity of the Ni-promoted In_2O_3 in literature [119].

The hydrogen spillover effect induced by Ni promotes H_2 adsorption, improves H_2 dissociation and migration on the catalyst surface favoring the formation of oxygen vacancies. The H_2 TPR analysis confirms this showing higher adsorption of H_2 . Furthermore, the addition of Ni induced a higher CO_2 adsorption capacity confirmed by CO_2 TPD. With an optimization for the synthesis of NiO-promoted In_2O_3/ZrO_2 catalysts, the wetness impregnated (WI) catalysts showed to have a more homogeneous distribution of both In and Ni (SEM-EDX mapping), compare to Figure 7.2. Also, the H_2 reduction and CO_2 adsorption capacity are higher for NiO- In_2O_3/ZrO_2 (WI) than for chemically reduced (CR) or NiO- In_2O_3/ZrO_2 (CP) catalysts. NiO- In_2O_3/ZrO_2 (WI) produced $0.497 \text{ g}_{MeOH} \text{ g}_{cat}^{-1} \text{ h}^{-1}$ of methanol compared to $0.482 \text{ g}_{MeOH} \text{ g}_{cat}^{-1} \text{ h}^{-1}$ (CP) or $0.390 \text{ g}_{MeOH} \text{ g}_{cat}^{-1} \text{ h}^{-1}$ (CR) at 75 bar, 300 °C and 8300 h^{-1} of $CO_2/H_2 = 1/3$. This can be attributed to the formation of electronic defects, the H_2 spillover effect and fast electron transfer characteristics [168]. Martin et al.

[16] reported no deactivation of pure $\text{In}_2\text{O}_3/\text{ZrO}_2$ over 1000 h TOS. In our study, a long-term stability test over 100 h TOS using $\text{NiO-In}_2\text{O}_3/\text{ZrO}_2$ (WI) also confirmed stable performance with a productivity of $0.15 \text{ g}_{\text{MeOH}} \text{ g}_{\text{cat}}^{-1} \text{ h}^{-1}$ without methane formation. Post-mortem catalyst characterization showed no leaching of Ni (ICP-OES), no change in morphology (powder XRD and SEM) and no formation of agglomerates (SEM-EDX mapping).

Two-phase fixed bed reactor with an integral or differential operation mode

The metal-doped $\text{In}_2\text{O}_3/\text{ZrO}_2$ -based catalyst prepared by WI and the CZA catalyst were further studied in a CPR, which can be operated integrally or differentially. The spatially resolved reaction profile of the CZA catalyst revealed an increase in temperature from the beginning of the catalyst bed to a maximum of $251 \text{ }^\circ\text{C}$ at 2.5 cm packing height at 50 bar, and a $\text{GHSV} = 63,000 \text{ h}^{-1}$ (see Figure 7.3). This is in line with the strongly increasing exothermic formation of methanol and the less endothermic rWGS from the beginning of the catalyst bed to about 4 cm packing height. Until the end of the catalyst bed, no significant change was observed for the formation rate of CO ($2.17 \text{ g}_{\text{CO}} \text{ g}_{\text{Cu}}^{-1} \text{ h}^{-1}$) and a slightly rise of methanol productivity to $3.49 \text{ g}_{\text{MeOH}} \text{ g}_{\text{Cu}}^{-1} \text{ h}^{-1}$. The productivity decreased to $3.01 \text{ g}_{\text{MeOH}} \text{ g}_{\text{Cu}}^{-1} \text{ h}^{-1}$ after 55 h TOS due to accelerated crystallization of Cu and ZnO by the byproduct water [113,169]. This indicates that all involved reactions forming an equilibrium beyond the spot of the maximum temperature. For the pure and metal-doped $\text{In}_2\text{O}_3/\text{ZrO}_2$ -based catalyst, less methanol and CO was produced. Due to the less released reaction heat a lower temperature profile was observed. As demonstrated in the study before, NiO enhanced the catalytic activity from $1.60 \text{ g}_{\text{MeOH}} \text{ g}_{\text{In}}^{-1} \text{ h}^{-1}$ for pure $\text{In}_2\text{O}_3/\text{ZrO}_2$ to $2.96 \text{ g}_{\text{MeOH}} \text{ g}_{\text{In+Ni}}^{-1} \text{ h}^{-1}$ for $\text{NiO-In}_2\text{O}_3/\text{ZrO}_2$ at 50 bar, $250 \text{ }^\circ\text{C}$, $63,000 \text{ h}^{-1}$ of $\text{CO}_2/\text{H}_2 = 1/3$ and at the end of the reactor (6 cm), as depicted in Figure 7.3.

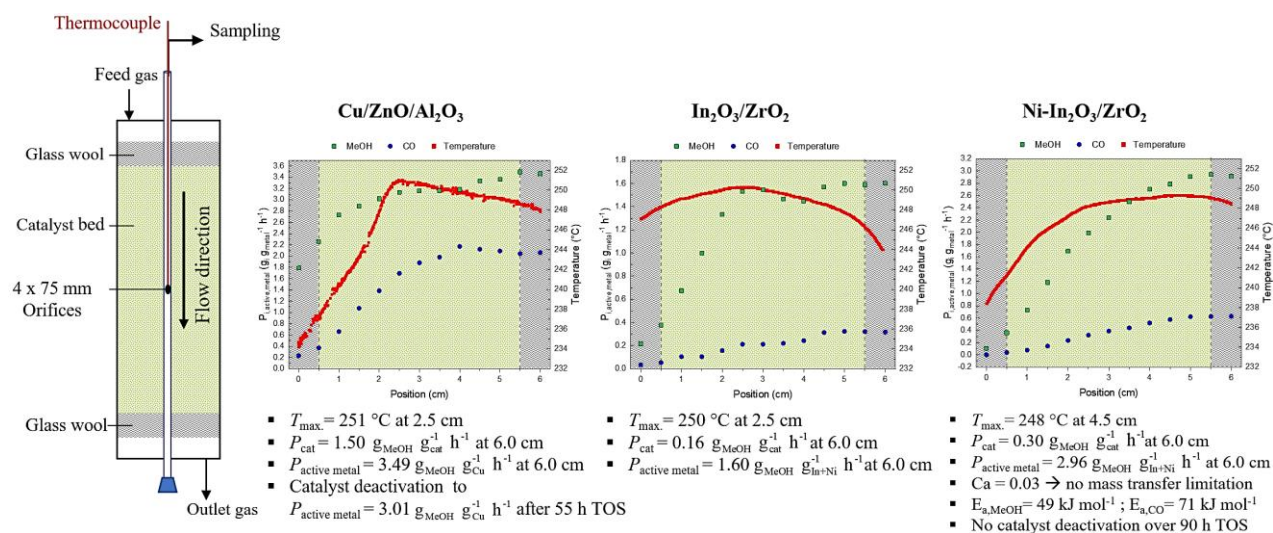


Figure 7.3. Illustration and comparison of the key results using the CPR setup at 50 bar, 250 °C, 63,000 h⁻¹ of CO₂/H₂= 1/3, [20].

The influence of reaction conditions showed a higher methanol productivity with increasing pressure which is in accordance with the principle of Le Chatelier. The spatially resolved reaction profiles are shifted in parallel to higher methanol productivities at higher pressures. The increase in pressure has a negligible impact on the rWGS as predicted by the principle of Le Chatelier. With higher GHSVs, respectively shorter contact and residence times, a higher methanol productivity can be observed, shifting the selectivity towards methanol as well. The CO formation rate remains constant. This is in agreement with the result in previous literature [16]. No mass transfer limitation according to the calculated Carberry Number $Ca = 0.03$ (50 bar, 250 °C) was estimated. Due to higher GHSVs, respectively higher volume flows the heat dissipation in the catalyst bed increased. This is compensated by a higher reaction rate due to lower contact times. A threshold temperature of 238 °C was identified between 1.5 and 2.0 cm packing height at 95,000 h⁻¹. Below the temperature the high gas flow cools the catalyst bed, keeping the methanol reaction rate low. Above 238 °C, the methanol reaction rate increases with a linear trend.

Higher reaction temperatures led to higher reaction kinetics which increased the methanol productivity up to $4.90 \text{ g}_{\text{MeOH}} \cdot \text{g}_{\text{In+Ni}}^{-1} \cdot \text{h}^{-1}$ at 275 °C, 50 bar and 63,000 h⁻¹ of CO₂/H₂= 1/3. The selectivity of methanol decreased from 83 % (225 °C) to 73 % (275 °C). The production of CO is favored due to the endothermic rWGS reaction. The apparent activation energy for the methanol synthesis requires 49 kJ mol⁻¹ and for the rWGS reaction 71 kJ mol⁻¹ indicating no limitations due to mass transport processes, as confirmed by the Carberry Number ($Ca = 0.03$). The study of

Portillo et al. [170] showed no internal mass transfer limitations conforming to the Weisz-Prater criterion of 0.015. Previous literature showed a similar trend for the activation energies [12,119,127]. As in the study before, the NiO-In₂O₃/ZrO₂ showed no catalyst deactivation caused by metal leaching or sintering over 90 h TOS in the CPR setup.

Batch operated three-phase stirred tank reactor

Metal-doped In-based catalysts were applied to slurry phase methanol synthesis. Various carrier liquids were tested, namely mineral oil, Helisol 10A, H18-DBT and Dowtherm™ A. Mineral oil showed the best performance and stability, which was also shown in the study by Schühle et al. [145]. Metal-doped catalysts prepared by the WI method dissolved in the carrier liquid after the reaction and were not considered further. Ni/In₂O₃ catalyst prepared by CP increased the methanol productivity to 0.075 g_{MeOH}·g_{cat}⁻¹·h⁻¹ compared to 0.011 g_{MeOH}·g_{cat}⁻¹·h⁻¹ for pure In₂O₃. The reaction conditions were: 75 bar, 300 °C and 1200 rpm using 2.0 g catalyst, 100 mL carrier oil, and a gas phase ratio of CO₂/H₂=1/4, because Schühle et al. [145] showed a slight H₂ excess of CO₂/H₂=1/4 caused in the highest methanol productivity.

The incorporation of In₂O₃ on ZrO₂ via CP boosted the performance up to 0.110 g_{MeOH}·g_{cat}⁻¹·h⁻¹, which is similar to the studies before. The addition of Mg, Ce or Ni to In₂O₃/ZrO₂ by CP showed that Ni or Ce boosted the catalytic activity up to 3.65 or 3.80 g_{MeOH}·g_{active metal}⁻¹·h⁻¹, respectively. Ni as a promoter is more active at lower temperature (250 °C) compared to Ce, due to an improved reduction capacity as well as a higher BET surface (see Figure 7.4). The addition of Ni improved the H₂ adsorption capacity via the hydrogen spillover effect as deduced from H₂ TPR measurements. A maximum H₂ uptake peak is located between 250 °C and 450 °C ascribed to Ni reduction and the creation of oxygen surface vacancies [119]. Ni also improved the CO₂ adsorption capacity. The addition of Ce increased the CO₂ adsorption capacity more than with the addition of Ni. Because magnesium increases the CO₂ adsorption capacity even further without a significant increase in reduction potential, H₂ adsorption has a higher impact on the methanol formation (RDS) than a higher CO₂ adsorption at 250 °C.

To maximize the methanol yield of Ni-promoted In₂O₃/ZrO₂, a statistical and modeling tool (DoE) was conducted. A two-level fractional factorial design with a resolution of IV was selected to study the effect of four easy to change reaction variables. The methanol yield is strongly influenced by reaction pressure (low level: 50 bar; high level: 75 bar) or temperature (low level: 250 °C; high level: 300 °C), see the Pareto Chart in Figure 7.4. The yield decreases with a lower pressure and

temperature. The variables stirrer speed (low level: 1200 rpm; high level: 1600 rpm) and catalyst mass (low level: 1 g; high level: 2 g) have no significant effect on the MeOH-yield. The model predicted $0.283 \text{ g}_{\text{MeOH}} \text{ g}_{\text{cat}}^{-1} \text{ h}^{-1}$ of methanol at 300 °C, 75 bar, 1200 rpm using 1.0 g catalyst, 100 mL carrier oil and a gas phase composition of $\text{CO}_2/\text{H}_2=1/4$. The model was verified with an additional experiment resulting in $0.290 \text{ g}_{\text{MeOH}} \text{ g}_{\text{cat}}^{-1} \text{ h}^{-1}$.

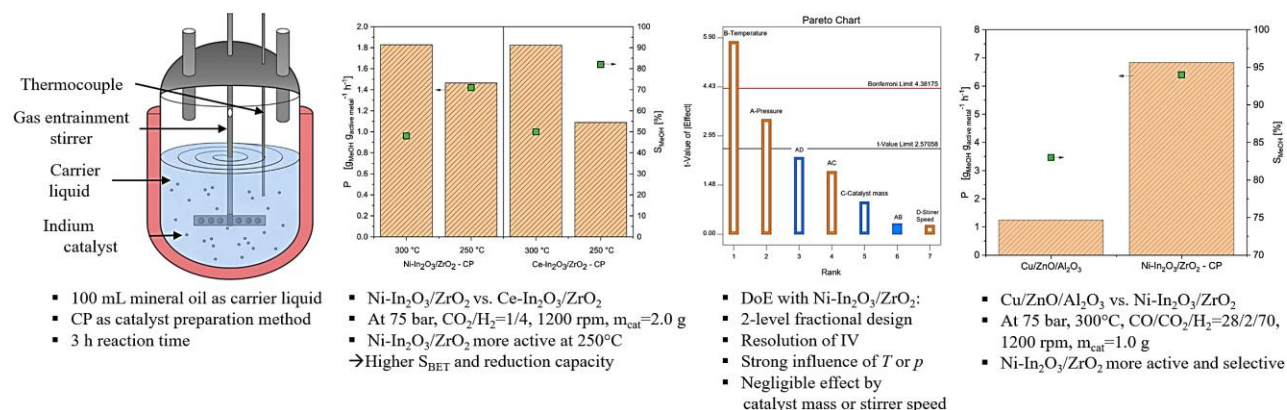


Figure 7.4. Key results of the three-phase system.

Under industry gas composition $\text{H}_2/\text{CO}/\text{CO}_2 = 70/28/2$ and the calculated optimal conditions, the Ni-In₂O₃/ZrO₂ (CP) catalyst reached $0.530 \text{ g}_{\text{MeOH}} \text{ g}_{\text{cat}}^{-1} \text{ h}^{-1}$, resp. $6.84 \text{ g}_{\text{MeOH}} \text{ g}_{\text{active metal}}^{-1} \text{ h}^{-1}$, with a methanol selectivity of 94 %. The commercial CZA catalyst produced more methanol related to catalyst mass $0.747 \text{ g}_{\text{MeOH}} \text{ g}_{\text{cat}}^{-1} \text{ h}^{-1}$, but less related to the active metal content ($1.25 \text{ g}_{\text{MeOH}} \text{ g}_{\text{active metal}}^{-1} \text{ h}^{-1}$) and likewise with a lower selectivity (84 %), Figure 7.4 right diagram.

To complete the study, the stability of the slurry reaction system was examined. Four reactions have been tested consecutively using the Ni-In₂O₃/ZrO₂ (CP) catalyst under optimized reaction conditions. No indication of significant deactivation was observed. The key results of the three-phase investigations are illustrated in Figure 7.4.

To conclude, the present thesis shows that the Ni-In₂O₃/ZrO₂ catalysts are highly promising for selective hydrogenation of CO₂ to methanol in different reactor concepts. Ni-In₂O₃/ZrO₂ catalysts exhibit a lower metal loading on catalyst support compared to the commercial CZA and a higher stability for CO₂ hydrogenation. High efficient catalysts for both two-phase and three-phase systems require a high surface area, as well as high CO₂ and H₂ adsorption capacity, and well distributed Ni and In. The preparation method of the catalysts also influences these properties. Catalysts prepared by WI are suitable for two-phase systems, whereas those prepared by CP are suited for three-phase

systems. The CO₂ hydrogenation to methanol is strongly influenced in both systems by temperature and pressure.

In further studies the Ni-In₂O₃/ZrO₂ catalysts should be tested on their performance with fluctuating feed gas compositions directly with CO/CO₂ from industry and H₂ from electrolysis. Also, the application for dimethyl ether production, methanol steam reforming or methanization should be investigated.

8 Bibliography

- [1] S. Arrhenius, *Philosophical Magazine and Journal of Science* **1896** (5), 237–276.
- [2] J. H. Wesseling, S. Lechtenböhmer, M. Åhman, L. J. Nilsson, E. Worrell, L. Coenen, *Renewable and Sustainable Energy Reviews* **2017**, 79, 1303–1313.
- [3] C. Panzone, R. Philippe, A. Chappaz, P. Fongarland, A. Bengaouer, *Journal of CO2 Utilization* **2020**, 38, 314–347.
- [4] *Handbook of energy storage: Demand, technologies, integration* (Eds: M. Sterner, I. Stadler), Springer, Berlin, Heidelberg **2019**.
- [5] R. Daiyan, I. MacGill, R. Amal, *ACS Energy Lett.* **2020**, 5 (12), 3843–3847.
- [6] A. Bloess, W.-P. Schill, A. Zerrahn, *Applied Energy* **2018**, 212, 1611–1626.
- [7] A. R. Dahiru, A. Vuokila, M. Huuhtanen, *Journal of Energy Storage* **2022**, 56, 105861.
- [8] Statista Research Department, Production capacity of methanol worldwide from 2018 to 2022, <https://www.statista.com/statistics/1065891/global-methanol-production-capacity/>, accessed 14 January 2024.
- [9] V. Dieterich, A. Buttler, A. Hanel, H. Spliethoff, S. Fendt, *Energy Environ. Sci.* **2020**, 13 (10), 3207–3252.
- [10] S. S. Araya, V. Liso, X. Cui, N. Li, J. Zhu, S. L. Sahlin, S. H. Jensen, M. P. Nielsen, S. K. Kær, *Energies* **2020**, 13 (3), 596.
- [11] A. Jess, P. Wasserscheid, *Chemical Technology*, Wiley-VCH, Weinheim **2013**.
- [12] K. Klier, V. Chatikavanij, R. G. Herman, G. W. Simmons, *Journal of Catalysis* **1981**, 1982 (74), 343–360.
- [13] X. Cui, S. K. Kær, *Chemical Engineering Journal* **2020**, 393, 124632.
- [14] M. V. Twigg, M. S. Spencer, *Applied Catalysis A: General* **2001**, 212 (1-2), 161–174.
- [15] M. B. Fichtl, D. Schlereth, N. Jacobsen, I. Kasatkin, J. Schumann, M. Behrens, R. Schlögl, O. Hinrichsen, *Applied Catalysis A: General* **2015**, 502, 262–270.
- [16] O. Martin, A. J. Martín, C. Mondelli, S. Mitchell, T. F. Segawa, R. Hauert, C. Drouilly, D. Curulla-Ferré, J. Pérez-Ramírez, *Angewandte Chemie (International ed. in English)* **2016**, 55 (21), 6261–6265.
- [17] Y. Wei, F. Liu, J. Ma, C. Yang, X. Wang, J. Cao, *Molecular Catalysis* **2022**, 525, 112354.

Bibliography

- [18] P. Kampe, A. Wesner, P. Schühle, F. Hess, J. Albert, *ChemPlusChem* **2023**, *88* (9), e202300425.
- [19] A. Wesner, P. Kampe, N. Herrmann, S. Eller, C. Ruhmlied, J. Albert, *ChemCatChem* **2023**, *15* (24).
- [20] P. Kampe, N. Herrmann, C. Ruhmlied, M. Finsel, O. Korup, R. Horn, J. Albert, *ACS Sustainable Chem. Eng.* **2024**, *12* (25), 9541–9549.
- [21] P. Kampe, N. Herrmann, A. Wesner, C. Ruhmlied, J. Albert, *ACS Sustainable Chem. Eng.* **2023**, *11* (39), 14633–14644.
- [22] United Nations Framework Convention on Climate, Paris Agreement, https://unfccc.int/files/meetings/paris_nov_2015/application/pdf/paris_agreement_english_.pdf, accessed 16 October 2023.
- [23] A. J. Schwab, *Elektroenergiesysteme: Erzeugung, Übertragung und Verteilung elektrischer Energie*, 5th ed., Springer Vieweg, Berlin **2017**.
- [24] S. Reker, J. Schneider, C. Gerhards, *Smart Energy* **2022**, *7*, 100083.
- [25] B. Cárdenas, L. Swinfen-Styles, J. Rouse, S. D. Garvey, *Energies* **2021**, *14* (24), 8524.
- [26] A. K. Rohit, K. P. Devi, S. Rangnekar, *Journal of Energy Storage* **2017**, *13*, 10–23.
- [27] W.-D. Steinmann, *Renewable and Sustainable Energy Reviews* **2017**, *75*, 205–219.
- [28] M. Hermesmann, T. E. Müller, *Progress in Energy and Combustion Science* **2022**, *90*, 100996.
- [29] O. Schmidt, A. Gambhir, I. Staffell, A. Hawkes, J. Nelson, S. Few, *International Journal of Hydrogen Energy* **2017**, *42* (52), 30470–30492.
- [30] M. Yu, E. Budiyo, H. Tüysüz, *Angewandte Chemie (International ed. in English)* **2022**, *61* (1), e202103824.
- [31] R. Bhandari, C. A. Trudewind, P. Zapp, *Journal of Cleaner Production* **2014**, *85*, 151–163.
- [32] A. Nechache, S. Hody, *Renewable and Sustainable Energy Reviews* **2021**, *149*, 111322.
- [33] S. E. Wolf, F. E. Winterhalder, V. Vibhu, L. G. J. de Haart, O. Guillon, R.-A. Eichel, N. H. Menzler, *J. Mater. Chem. A* **2023**, *11* (34), 17977–18028.
- [34] S. Sebbahi, A. Assila, A. Alaoui Belghiti, S. Laasri, S. Kaya, E. K. Hlil, S. Rachidi, A. Hajjaji, *International Journal of Hydrogen Energy* **2024**, *82*, 583–599.
- [35] M. Carmo, D. L. Fritz, J. Mergel, D. Stolten, *International Journal of Hydrogen Energy*

- 2013**, 38 (12), 4901–4934.
- [36] S. Shiva Kumar, H. Lim, *Energy Reports* **2022**, 8, 13793–13813.
- [37] GrInHy2.0, Green Industrial Hydrogen via steam electrolysis, <https://cordis.europa.eu/project/id/826350>, accessed 27 October 2023.
- [38] T. Smolinka, M. Günther, J. Garche, *Stand und Entwicklungspotenzial der Wasserelektrolyse zur Herstellung von Wasserstoff aus regenerativen Energien*, Berlin **2011**.
- [39] M. El-Shafie, *Results in Engineering* **2023**, 20, 101426.
- [40] X. Liu, R. Guo, K. Ni, F. Xia, C. Niu, B. Wen, J. Meng, P. Wu, J. Wu, X. Wu, L. Mai, *Advanced materials (Deerfield Beach, Fla.)* **2020**, 32 (40), e2001136.
- [41] A. S. Aricò, S. Siracusano, N. Briguglio, V. Baglio, A. Di Blasi, V. Antonucci, *J Appl Electrochem* **2013**, 43 (2), 107–118.
- [42] M. David, C. Ocampo-Martínez, R. Sánchez-Peña, *Journal of Energy Storage* **2019**, 23, 392–403.
- [43] M. Awad, A. Said, M. H. Saad, A. Farouk, M. M. Mahmoud, M. S. Alshammari, M. L. Alghaythi, S. H. Abdel Aleem, A. Y. Abdelaziz, A. I. Omar, *Alexandria Engineering Journal* **2024**, 87, 213–239.
- [44] M. Bonanno, K. Müller, B. Bensmann, R. Hanke-Rauschenbach, D. Aili, T. Franken, A. Chromik, R. Peach, A. T. S. Freiberg, S. Thiele, *Adv Materials Technologies* **2024**, 9 (2).
- [45] R. Hancke, P. Bujlo, T. Holm, Ø. Ulleberg, *Journal of Power Sources* **2024**, 601, 234271.
- [46] S. Shiva Kumar, V. Himabindu, *Materials Science for Energy Technologies* **2019**, 2 (3), 442–454.
- [47] W. Daud, R. E. Rosli, E. H. Majlan, S. Hamid, R. Mohamed, T. Husaini, *Renewable Energy* **2017**, 113, 620–638.
- [48] A. J. Shih, M. C. O. Monteiro, F. Dattila, D. Pavesi, M. Philips, A. H. M. Da Silva, R. E. Vos, K. Ojha, S. Park, O. van der Heijden, G. Marcandalli, A. Goyal, M. Villalba, X. Chen, G. T. K. K. Gunasooriya, I. McCrum, R. Mom, N. López, M. T. M. Koper, *Nat Rev Methods Primers* **2022**, 2 (1).
- [49] *Electrochemistry of Cleaner Environments* (Ed: J.O. Bockris), Springer US, Boston, MA **1972**.

Bibliography

- [50] M. Balat, *International Journal of Hydrogen Energy* **2008**, *33* (15), 4013–4029.
- [51] A. M. Oliveira, R. R. Beswick, Y. Yan, *Current Opinion in Chemical Engineering* **2021**, *33*, 100701.
- [52] S. Dürr, M. Müller, H. Jorschick, M. Helmin, A. Bösmann, R. Palkovits, P. Wasserscheid, *ChemSusChem* **2017**, *10* (1), 42–47.
- [53] B. C. Tashie-Lewis, S. G. Nnabuife, *Chemical Engineering Journal Advances* **2021**, *8*, 100172.
- [54] P. M. Modisha, C. N. M. Ouma, R. Garidzirai, P. Wasserscheid, D. Bessarabov, *Energy Fuels* **2019**, *33* (4), 2778–2796.
- [55] National Center for Biotechnology Information, Methanol, <https://pubchem.ncbi.nlm.nih.gov/compound/Methanol>, accessed 16 October 2023.
- [56] D. W. Stephan, *nature* **2013** (495), 54–55.
- [57] F. Schorn, J. L. Breuer, R. C. Samsun, T. Schnorbus, B. Heuser, R. Peters, D. Stolten, *Advances in Applied Energy* **2021**, *3*, 100050.
- [58] G. A. Olah, *Angewandte Chemie (International ed. in English)* **2005**, *44* (18), 2636–2639.
- [59] A. Galadima, O. Muraza, *Journal of Natural Gas Science and Engineering* **2015**, *25*, 303–316.
- [60] C. Palmer, D. C. Upham, S. Smart, M. J. Gordon, H. Metiu, E. W. McFarland, *Nat Catal* **2020**, *3* (1), 83–89.
- [61] C. Wang, N. Sun, N. Zhao, W. Wei, Y. Sun, C. Sun, H. Liu, C. E. Snape, *Fuel* **2015**, *143*, 527–535.
- [62] M. Yu, Y.-A. Zhu, Y. Lu, G. Tong, K. Zhu, X. Zhou, *Applied Catalysis B: Environmental* **2015**, *165*, 43–56.
- [63] A. Albarazi, M. E. Gálvez, P. Da Costa, *Catalysis Communications* **2015**, *59*, 108–112.
- [64] E. Meloni, M. Martino, V. Palma, *Catalysts* **2020**, *10* (3), 352.
- [65] A. Arman, F. Y. Hagos, A. A. Abdullah, R. Mamat, A. R. A. Aziz, C. K. Cheng, *IOP Conf. Ser.: Mater. Sci. Eng.* **2020**, *736* (4), 42032.
- [66] G. Bozzano, F. Manenti, *Progress in Energy and Combustion Science* **2016**, *56*, 71–105.
- [67] Y. Shen, J. Wang, X. Ge, M. Chen, *Renewable and Sustainable Energy Reviews* **2016**, *59*, 1246–1268.

Bibliography

- [68] M. Bukhtiyarova, T. Lunkenbein, K. Kähler, R. Schlögl, *Catal Lett* **2017**, *147* (2), 416–427.
- [69] H. Le Chatelier, *Comptes rendus hebd. Seanc. Acad. Sci. Paris*. **1884** (99), 786–789.
- [70] A. S. Aricò, S. Siracusano, N. Briguglio, V. Baglio, A. Di Blasi, V. Antonucci, *J Appl Electrochem* **2013**, *43* (2), 107–118.
- [71] A. Riaz, G. Zahedi, J. J. Klemeš, *Journal of Cleaner Production* **2013**, *57*, 19–37.
- [72] G. Soave, *Chemical Engineering Science* **1972** (27), 1197–1203.
- [73] P. Friedlingstein, M. O'Sullivan, M. W. Jones, R. M. Andrew, L. Gregor, J. Hauck, C. Le Quéré, I. T. Lujikx, A. Olsen, G. P. Peters, W. Peters, J. Pongratz, C. Schwingshackl, S. Sitch, J. G. Canadell, P. Ciais, R. B. Jackson, S. R. Alin, R. Alkama, A. Arneeth, V. K. Arora, N. R. Bates, M. Becker, N. Bellouin, H. C. Bittig, L. Bopp, F. Chevallier, L. P. Chini, M. Cronin, W. Evans, S. Falk, R. A. Feely, T. Gasser, M. Gehlen, T. Gkritzalis, L. Gloege, G. Grassi, N. Gruber, Ö. Gürses, I. Harris, M. Hefner, R. A. Houghton, G. C. Hurtt, Y. Iida, T. Ilyina, A. K. Jain, A. Jersild, K. Kadono, E. Kato, D. Kennedy, K. Klein Goldewijk, J. Knauer, J. I. Korsbakken, P. Landschützer, N. Lefèvre, K. Lindsay, J. Liu, Z. Liu, G. Marland, N. Mayot, M. J. McGrath, N. Metz, N. M. Monacci, D. R. Munro, S.-I. Nakaoka, Y. Niwa, K. O'Brien, T. Ono, P. I. Palmer, N. Pan, D. Pierrot, K. Pockock, B. Poulter, L. Resplandy, E. Robertson, C. Rödenbeck, C. Rodriguez, T. M. Rosan, J. Schwinger, R. Séférian, J. D. Shutler, I. Skjelvan, T. Steinhoff, Q. Sun, A. J. Sutton, C. Sweeney, S. Takao, T. Tanhua, P. P. Tans, X. Tian, H. Tian, B. Tilbrook, H. Tsujino, F. Tubiello, G. R. van der Werf, A. P. Walker, R. Wanninkhof, C. Whitehead, A. Willstrand Wranne, R. Wright, W. Yuan, C. Yue, X. Yue, S. Zaehle, J. Zeng, B. Zheng, *Earth Syst. Sci. Data* **2022**, *14* (11), 4811–4900.
- [74] National Oceanic and Atmospheric Administration, ESRL, Average carbon dioxide (CO₂) levels in the atmosphere worldwide from 1959 to 2022, <https://www.statista.com/statistics/1091926/atmospheric-concentration-of-co2-historic/>, accessed 30 November 2023.
- [75] J. Zhong, X. Yang, Z. Wu, B. Liang, Y. Huang, T. Zhang, *Chemical Society reviews* **2020**, *49* (5), 1385–1413.
- [76] N. von der Assen, P. Voll, M. Peters, A. Bardow, *Chemical Society reviews* **2014**, *43* (23), 7982–7994.
- [77] A. Bosoaga, O. Masek, J. E. Oakey, *Energy Procedia* **2009**, *1* (1), 133–140.

Bibliography

- [78] M. Voldsund, S. Gardarsdottir, E. de Lena, J.-F. Pérez-Calvo, A. Jamali, D. Berstad, C. Fu, M. Romano, S. Roussanaly, R. Anantharaman, H. Hoppe, D. Sutter, M. Mazzotti, M. Gazzani, G. Cinti, K. Jordal, *Energies* **2019**, *12* (3), 559.
- [79] R. T. Porter, M. Fairweather, M. Pourkashanian, R. M. Woolley, *International Journal of Greenhouse Gas Control* **2015**, *36*, 161–174.
- [80] J. Schittkowski, H. Ruland, D. Laudenschleger, K. Girod, K. Kähler, S. Kaluza, M. Muhler, R. Schlögl, *Chemie Ingenieur Technik* **2018**, *90* (10), 1419–1429.
- [81] P. Bains, P. Psarras, J. Wilcox, *Progress in Energy and Combustion Science* **2017**, *63*, 146–172.
- [82] G. H. Graaf, J. G. M. Winkelman, *Ind. Eng. Chem. Res.* **2016**, *55* (20), 5854–5864.
- [83] G. H. Graaf, P. J. J. M. Sijtsema, E. J. Stamhuis, G.E. H. Joosten, *Chemical Engineering Science* **1986** (41), 2883–2890.
- [84] G. H. Graaf, E. J. Stamhuis, A. A. C. M. Beenackers, *Chemical Engineering Science* **1988** (43), 3185–3195.
- [85] T. Henkel, *PhD thesis Technical University of Munich* **2011**.
- [86] *Ullmann's Encyclopedia of Industrial Chemistry: Heterogeneous Catalysis and Solid Catalysts* (Ed: O. Deutschmann, H. Knözinger, K. Kochloefl, T. Turek), Wiley-VCH Verlag GmbH & Co. KGaA, Weinheim, Germany **2009**.
- [87] F. Nestler, A. R. Schütze, M. Ouda, M. J. Hadrich, A. Schaadt, S. Bajohr, T. Kolb, *Chemical Engineering Journal* **2020**, *394*, 124881.
- [88] Methanol Market Services Asia, Metanol price and supply/demand, <https://www.methanol.org/methanol-price-supply-demand/>, accessed 14 January 2024.
- [89] M. R. Gogate, *Petroleum Science and Technology* **2019**, *37* (5), 559–565.
- [90] K. Shakeel, M. Javaid, Y. Muazzam, S. R. Naqvi, S. A. A. Taqvi, F. Uddin, M. T. Mehran, U. Sikander, M. B. K. Niazi, *Processes* **2020**, *8* (5), 571.
- [91] G. J. Millar, M. Collins, *Ind. Eng. Chem. Res.* **2017**, *56* (33), 9247–9265.
- [92] A. Pulyalina, V. Rostovtseva, I. Faykov, A. Toikka, *Polymers* **2020**, *12* (10).
- [93] S. Kang, F. Boshell, A. Goeppert, S. G. Prakash, I. Landälv, D. Saygin, *Innovation outlook: Renewable methanol*, International Renewable Energy Agency, Abu Dhabi **2021**.
- [94] *Methanol: The Basic Chemical and Energy Feedstock of the Future* (Eds: M. Bertau, H.

- Offermanns, L. Plass, F. Schmidt, H.-J. Wernicke), Springer Berlin Heidelberg, Berlin, Heidelberg **2014**.
- [95] G. Liu, H. Hagelin-Weaver, B. Welt, *Waste* **2023**, *1* (1), 228–248.
- [96] F. Studt, M. Behrens, E. L. Kunkes, N. Thomas, S. Zander, A. Tarasov, J. Schumann, E. Frei, J. B. Varley, F. Abild-Pedersen, J. K. Nørskov, R. Schlögl, *ChemCatChem* **2015**, *7* (7), 1105–1111.
- [97] D. Li, F. Xu, X. Tang, S. Dai, T. Pu, X. Liu, P. Tian, F. Xuan, Z. Xu, I. E. Wachs, M. Zhu, *Nat Catal* **2022**, *5* (2), 99–108.
- [98] I. Kasatkin, P. Kurr, B. Kniep, A. Trunschke, R. Schlögl, *Angewandte Chemie* **2007**, *119* (38), 7465–7468.
- [99] C. BALTES, S. VUKOJEVIC, F. SCHUTH, *Journal of Catalysis* **2008**, *258* (2), 334–344.
- [100] M.J.L. Ginés, N. Amadeo, M. Laborde, C.R. Apesteguía, *Applied Catalysis A: General* **1995** (131), 283–296.
- [101] A.A.G. Lima, M. Nele, E.L. Moreno, H.M.C. Andrade, *Applied Catalysis A: General* **1998** (117), 31–43.
- [102] F. Studt, M. Behrens, F. Abild-Pedersen, *Catal Lett* **2014**, *144* (11), 1973–1977.
- [103] Z. Li, N. Li, N. Wang, B. Zhou, P. Yin, B. Song, J. Yu, Y. Yang, *ACS omega* **2022**, *7* (4), 3514–3521.
- [104] D. R. Palo, R. A. Dagle, J. D. Holladay, *Chemical reviews* **2007**, *107* (10), 3992–4021.
- [105] Y. Yang, C. A. Mims, D. H. Mei, C. Peden, C. T. Campbell, *Journal of Catalysis* **2013**, *298*, 10–17.
- [106] P. Schühle, M. Schmidt, L. Schill, A. Riisager, P. Wasserscheid, J. Albert, *Catal. Sci. Technol.* **2020**, *10* (21), 7309–7322.
- [107] H. H. Kung, *Catalysis Today* **1992** (11), 443–453.
- [108] Bernard J. Wood, William E. Isakson, Henry Wise, *Ind. Eng. Chem. Prod. Res. Dev.* **1980** (19), 197–204.
- [109] E. Heracleous, V. Koidi, A. A. Lappas, A. Hauser, S. Haag, *Chemical Engineering Journal* **2022**, *444*, 136571.
- [110] R. Quinn, T. Dahl, B. Toseland, *Applied Catalysis A: General* **2004**, *272* (1-2), 61–68.
- [111] J. T. Sun, I. S. Metcalfe, M. Sahibzada, *Ind. Eng. Chem. Res.* **1999**, *38* (10), 3868–3872.

Bibliography

- [112] X. Zhai, J. Shamoto, H. Xie, Y. Tan, Y. Han, N. Tsubaki, *Fuel* **2008**, *87* (4-5), 430–434.
- [113] J. Wu, M. Saito, M. Takeuchi, T. Watanabe, *Applied Catalysis A: General* **2001** (218), 235–240.
- [114] K. Omata, M. Hashimoto, Y. Watanabe, T. Umegaki, S. Wagatsuma, G. Ishiguro, M. Yamada, *Applied Catalysis A: General* **2004**, *262* (2), 207–214.
- [115] B. Liang, J. Ma, X. Su, C. Yang, H. Duan, H. Zhou, S. Deng, L. Li, Y. Huang, *Ind. Eng. Chem. Res.* **2019**, *58* (21), 9030–9037.
- [116] J. Ye, C. Liu, D. Mei, Q. Ge, *ACS Catal.* **2013**, *3* (6), 1296–1306.
- [117] A. Tsoukalou, P. M. Abdala, D. Stoian, X. Huang, M.-G. Willinger, A. Fedorov, C. R. Müller, *Journal of the American Chemical Society* **2019**, *141* (34), 13497–13505.
- [118] K. Sun, Z. Fan, J. Ye, J. Yan, Q. Ge, Y. Li, W. He, W. Yang, C. Liu, *Journal of CO2 Utilization* **2015**, *12*, 1–6.
- [119] M. S. Frei, C. Mondelli, R. García-Muelas, J. Morales-Vidal, M. Philipp, O. V. Safonova, N. López, J. A. Stewart, D. C. Ferré, J. Pérez-Ramírez, *Nature communications* **2021**, *12* (1), 1960.
- [120] X. Jia, K. Sun, J. Wang, C. Shen, C. Liu, *Journal of Energy Chemistry* **2020**, *50*, 409–415.
- [121] M. S. Frei, C. Mondelli, R. García-Muelas, K. S. Kley, B. Puértolas, N. López, O. V. Safonova, J. A. Stewart, D. Curulla Ferré, J. Pérez-Ramírez, *Nature communications* **2019**, *10* (1), 3377.
- [122] Z. Han, C. Tang, J. Wang, L. Li, C. Li, *Journal of Catalysis* **2021**, *394*, 236–244.
- [123] D. Cai, Y. Cai, K. B. Tan, G. Zhan, *Materials (Basel, Switzerland)* **2023**, *16* (7).
- [124] M. Dou, M. Zhang, Y. Chen, Y. Yu, *Catal Lett* **2018**, *148* (12), 3723–3731.
- [125] M. S. Frei, C. Mondelli, A. Cesarini, F. Krumeich, R. Hauert, J. A. Stewart, D. Curulla Ferré, J. Pérez-Ramírez, *ACS Catal.* **2020**, *10* (2), 1133–1145.
- [126] K. Sun, C. Shen, R. Zou, C. Liu, *Applied Catalysis B: Environmental* **2023**, *320*, 122018.
- [127] Thaylan Pinheiro Araújo, Cecilia Mondelli, Mikhail Agrachev, Tangsheng Zou, Patrik O. Willi, Konstantin M. Engel, Robert N. Grass, Wendelin J. Stark, Olga V. Safonova, Gunnar Jeschke, Sharon Mitchell, Javier Pérez-Ramírez, *Nature communications* **2022** (13), 5610.
- [128] X. Cui, S. K. Kær, *Chemical Engineering Journal* **2020**, *393*, 124632.
- [129] K. Ountaksinkul, S. Sripinun, P. Bumphenkiattikul, A. Vongachariya, P. Praserttham, S.

- Assabumrungrat, *EJ* **2022**, *26* (12), 17–42.
- [130] A. Alarifi, S. Alsobhi, A. Elkamel, E. Croiset, *Energy Fuels* **2015**, *29* (2), 530–537.
- [131] G. Bozzano, F. Manenti, *Progress in Energy and Combustion Science* **2016**, *56*, 71–105.
- [132] F. Bisotti, M. Fedeli, K. Prifti, A. Galeazzi, A. Dell’Angelo, F. Manenti, *Ind. Eng. Chem. Res.* **2022**, *61* (5), 2206–2226.
- [133] U. Mondal, G. D. Yadav, *Green Chem.* **2021**, *23* (21), 8361–8405.
- [134] Air Liquide, Methanol, <https://engineering.airliquide.com/technologies/methanol>, accessed 19 February 2024.
- [135] Linde Engineering, Isothermal reactor, https://www.linde-engineering.com/en/process-plants/hydrogen_and_synthesis_gas_plants/gas_generation/isothermal_reactor/index.html, accessed 23 February 2024.
- [136] M. E. Sarvestani, O. Norouzi, F. Di Maria, A. Dutta, *Energy Conversion and Management* **2024**, *302*, 118070.
- [137] S. P. C. Perego, *Catalysis Today* **1999** (52), 133–145.
- [138] R. Gaikwad, H. Reymond, N. Phongprueksathat, P. Rudolf von Rohr, A. Urakawa, *Catal. Sci. Technol.* **2020**, *10* (9), 2763–2768.
- [139] A. Aquino, O. Korup, R. Horn, *Ind. Eng. Chem. Res.* **2023**, *62* (7), 3098–3115.
- [140] D. Espinoza, B. Wollak, T. L. Sheppard, A.-C. Dippel, M. Sturm, O. Gutowski, M. Schmidt, O. Korup, R. Horn, *ChemCatChem* **2022**, *14* (24).
- [141] J. Pottbacker, S. Jakobtorweihen, A. S. Behnecke, A. Abdullah, M. Özdemir, M. Warner, M. Menon, J. M. Bujalski, D. Waller, O. Korup, R. Horn, *Chemical Engineering Journal* **2022**, *439*, 135350.
- [142] F. Wolke, Y. Hu, M. Schmidt, O. Korup, R. Horn, E. Reichelt, M. Jahn, A. Michaelis, *Catalysis Communications* **2021**, *158*, 106335.
- [143] M. Wolf, N. Raman, N. Taccardi, R. Horn, M. Haumann, P. Wasserscheid, *Faraday discussions* **2021**, *229*, 359–377.
- [144] K. C. Pratt, in *Catalysis: Science and Technology* (Eds: J. R. Anderson, M. Boudart), Springer Berlin Heidelberg, Berlin, Heidelberg **1987**.
- [145] P. Schühle, S. Reichenberger, G. Marzun, J. Albert, *Chemie Ingenieur Technik* **2021**, *93* (4), 585–593.

Bibliography

- [146] Y. Jiang, H. Yang, P. Gao, X. Li, J. Zhang, H. Liu, H. Wang, W. Wei, Y. Sun, *Journal of CO2 Utilization* **2018**, *26*, 642–651.
- [147] *Multiple-Phase Reactors* (Ed: S. Li), Butterworth-Heinemann, Boston **2017**.
- [148] R. A. Fisher, *The Design of Experiments*, 1st ed., Oliver and Boyd, Edinburgh and London **1935**.
- [149] D. C. Montgomery, *Design and Analysis of Experiments*, 9th ed., John Wiley & Sons, Inc. **2017**.
- [150] M. J. Anderson, P. J. Whitcomb, *DOE simplified: Practical tools for effective experimentation*, CRC Press, Boca Raton, FL **2015**.
- [151] P. S. K. Krishnaiah, *Applied Design of Experiments and Taguchi Methods*, PHI Learning Private Limited, New Dehli **2012**.
- [152] C. J. Taylor, A. Pomberger, K. C. Felton, R. Grainger, M. Barecka, T. W. Chamberlain, R. A. Bourne, C. N. Johnson, A. A. Lapkin, *Chemical reviews* **2023**, *123* (6), 3089–3126.
- [153] K. Siebertz, D. van Bebber, T. Hochkirchen, *Statistische Versuchsplanung: Design of Experiments (DoE)*, 2nd ed., Springer Vieweg, Berlin **2017**.
- [154] C. E. Bonferroni, *Pubblicazioni del R Istituto Superiore di Scienze Economiche e Commerciali di Firenze* **1936**.
- [155] R. H. H. Groenwold, J. J. Goeman, S. Le Cessie, O. M. Dekkers, *European journal of endocrinology* **2021**, *184* (3), E11-E14.
- [156] *Encyclopedia of Systems Biology* (Eds: W. Dubitzky, O. Wolkenhauer, K.-H. Cho, H. Yokota), Springer, New York **2013**.
- [157] A. Dean, M. Morris, J. Stufken, D. Bingham, *Handbook of Design and Analysis of Experiments*, CRC Press, Boca Raton, FL **2015**.
- [158] Z. Peng, X. Liu, S. Li, Z. Li, B. Li, Z. Liu, S. Liu, *Scientific reports* **2017**, *7*, 39847.
- [159] Z. Zhang, C. Shen, K. Sun, C. Liu, *Catalysis Communications* **2022**, *162*, 106386.
- [160] A. Monshi, M. R. Foroughi, M. R. Monshi, *WJNSE* **2012**, *02* (03), 154–160.
- [161] P. N. Dwivedi, S. N. Upadhyay, *Ind. Eng. Chem. Process Des. Dev.*, *1977* (16, 2), 157–165.
- [162] *The Properties of Gases and Liquids* (Ed: B. E. Poling, J. M. Prausnitz, J. P. O'Connell), McGraw-Hill Education, New York **2001**.
- [163] *Perry's Chemical Engineers' Handbook: Physical and chemical data* (Ed: D. Friend B.

- Poling, G. Thomson, T. Daubert and E. Buck), McGraw-Hill, New York **2007**.
- [164] S. Poto, D. van Vico Berkel, F. Gallucci, M. Fernanda Neira d'Angelo, *Chemical Engineering Journal* **2022**, *435*, 134946.
- [165] M. de Falco, M. Capocelli, A. Basile, *International Journal of Hydrogen Energy* **2017**, *42* (10), 6771–6786.
- [166] K. Lau, P. Schühle, S.-X. Liang, F. de Kock, J. Albert, S. Reichenberger, *ACS Appl. Energy Mater.* **2021**, *4* (9), 9206–9215.
- [167] Y. Wei, F. Liu, J. Ma, C. Yang, X. Wang, J. Cao, *Molecular Catalysis* **2022**, *525*, 112354.
- [168] X. Jiang, X. Li, J. Wang, D. Long, L. Ling, W. Qiao, *Catal. Sci. Technol.* **2018**, *8* (10), 2740–2749.
- [169] F. Studt, M. Behrens, E. L. Kunkes, N. Thomas, S. Zander, A. Tarasov, J. Schumann, E. Frei, J. B. Varley, F. Abild-Pedersen, J. K. Nørskov, R. Schlögl, *ChemCatChem* **2015**, *7* (7), 1105–1111.
- [170] A. Portillo, O. Parra, A. T. Aguayo, J. Ereña, J. Bilbao, A. Ateka, *ACS sustainable chemistry & engineering* **2024**, *12* (4), 1616–1624.
- [171] Thermo Fisher Scientific, Copper based methanol synthesis catalyst. safety data sheet **2024**, <https://www.fishersci.de/store/msds?partNumber=15442437&countryCode=DE&language=de>, accessed 16 May 2024.
- [172] Sigma-Aldrich, Indium(III) nitrate hydrate. safety data sheet, <https://www.sigmaaldrich.com/DE/en/sds/aldrich/326135?userType=anonymous>, accessed 16 May 2024.
- [173] Sigma-Aldrich, Dowtherm®A. safety data sheet, <https://www.sigmaaldrich.com/DE/en/sds/aldrich/44570?userType=anonymous>, accessed 16 May 2024.
- [174] Sigma-Aldrich, Copper(II) nitrate trihydrate. safety data sheet, <https://www.sigmaaldrich.com/DE/en/sds/sigald/61194?userType=anonymous>, accessed 16 May 2024.
- [175] Sigma-Aldrich, Cerium(III) nitrate hexahydrate. safety data sheet, <https://www.sigmaaldrich.com/DE/en/sds/aldrich/238538?userType=anonymous>, accessed 16 May 2024.

Bibliography

- [176] IFA Institut für Arbeitsschutz der Deutschen Gesetzlichen Unfallversicherung, Sodium carbonate, <https://gestis.dguv.de/data?name=490211&lang=en>, accessed 16 May 2024.
- [177] IFA Institut für Arbeitsschutz der Deutschen Gesetzlichen Unfallversicherung, Nitrogen, <https://gestis.dguv.de/data?name=007070&lang=en>, accessed 16 May 2024.
- [178] IFA Institut für Arbeitsschutz der Deutschen Gesetzlichen Unfallversicherung, Methanol, <https://gestis.dguv.de/data?name=011240&lang=en>, accessed 16 May 2024.
- [179] IFA Institut für Arbeitsschutz der Deutschen Gesetzlichen Unfallversicherung, Indium(III) oxide, <https://gestis.dguv.de/data?name=109377&lang=en>, accessed 16 May 2024.
- [180] IFA Institut für Arbeitsschutz der Deutschen Gesetzlichen Unfallversicherung, Indium(III) hydroxide, <https://gestis.dguv.de/data?name=132616&lang=en>, accessed 16 June 2024.
- [181] IFA Institut für Arbeitsschutz der Deutschen Gesetzlichen Unfallversicherung, Ethanol, <https://gestis.dguv.de/data?name=010420&lang=en>, accessed 16 May 2024.
- [182] IFA Institut für Arbeitsschutz der Deutschen Gesetzlichen Unfallversicherung, Dibenzyltoluene, isomers, <https://gestis.dguv.de/data?name=492182&lang=en>, accessed 16 May 2024.
- [183] IFA Institut für Arbeitsschutz der Deutschen Gesetzlichen Unfallversicherung, Carbon monoxide, <https://gestis.dguv.de/data?name=001110&lang=en>, accessed 15 May 2024.
- [184] IFA Institut für Arbeitsschutz der Deutschen Gesetzlichen Unfallversicherung, Carbon dioxide, <https://gestis.dguv.de/data?name=001120&lang=en>, accessed 16 May 2024.
- [185] Sigma-Aldrich, Zirconium(IV) oxynitrate hydrate. safety data sheet **2024**, <https://www.sigmaaldrich.com/DE/en/sds/aldrich/346462?userType=anonymous>, accessed 16 May 2024.
- [186] Sigma-Aldrich, Nickel(II) nitrate hexahydrate. safety data sheet, <https://www.sigmaaldrich.com/DE/en/sds/sigald/244074?userType=anonymous>, accessed 16 May 2024.
- [187] IFA Institut für Arbeitsschutz der Deutschen Gesetzlichen Unfallversicherung, Nickel oxide, <https://gestis.dguv.de/data?name=001230&lang=en>, accessed 16 May 2024.

9 Appendix

9.1 Characterization of the setup

9.1.1 GC calibration curves for all setups

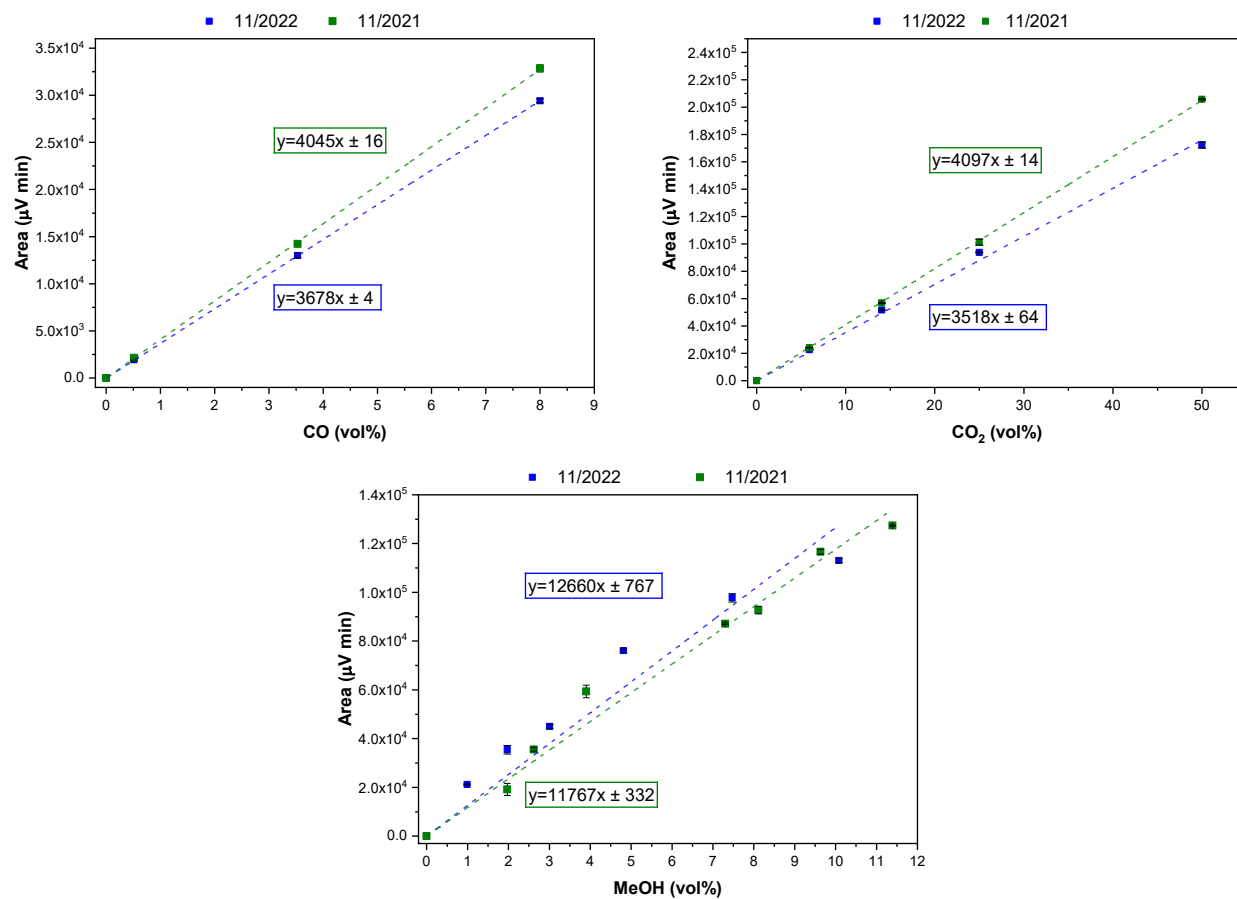


Figure 9.1. GC calibration curves for the quantification of CO, CO₂ and methanol. Calibration in November 2021 (green) and November 2022 (blue).

9.1.2 MFC calibration curves

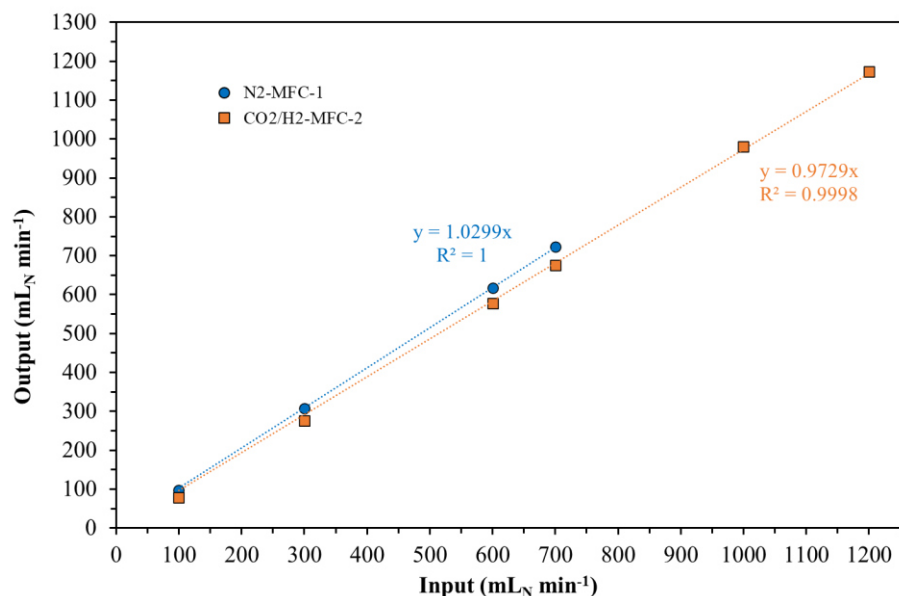


Figure 9.2. Calibration curves of MFC-1 and MFC-2, using a normalized gas meter (Hermann Pipersberg Jr. GmbH Reimscheid, number 1251754, year 1987).

9.1.3 Fixed bed reactor

A negative control experiment was performed at 300 °C, 75 bar, 600 mL_N min⁻¹ using CO₂/H₂ = 3/1 in a fixed-bed reactor filled with 5 cm quartz beads. While six hours TOS no catalytic activity was observed. The volume induced pressure drop was investigated under the same conditions using nitrogen. In this reactor setup the pressure drop in every configuration was below 0.1 bar. The residence time for the fixed bed reactor setup was evaluated in an empty, filled with Raschig rings or quartz beads reactor, respectively at 300 mL_N min⁻¹, 600 mL_N min⁻¹ and 1200 mL_N min⁻¹. The measurements were carried out in a pulse tracer experiment by switching the feed from nitrogen to CO₂ (tracer) for 12 s. The CO₂ pulse was analyzed using an online Fourier transform infrared spectrometer (FTIR), which continuously reproduced a time-resolved signal. The results are illustrated in Figure 9.3.

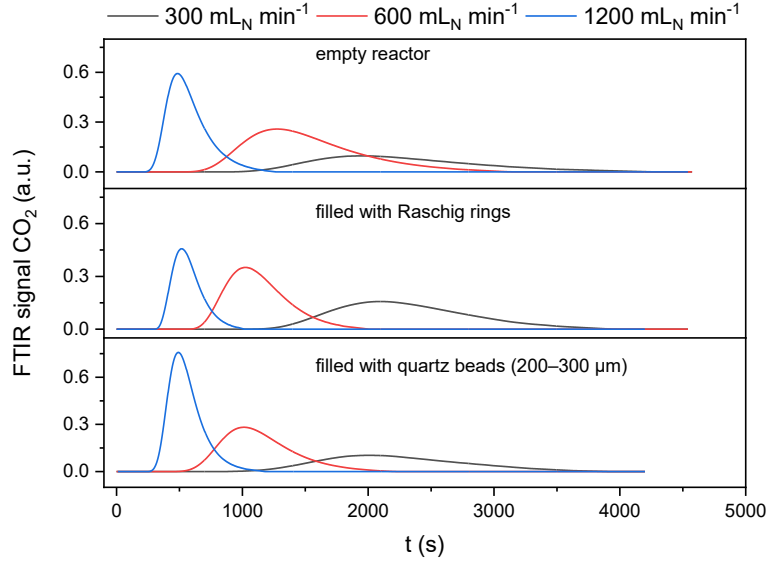


Figure 9.3. Illustration of the CO₂ pulse tracer test for different reactor fillings and volume flows measured by FTIR. At $t = 0$ s the nitrogen feed was switched to CO₂ for 12 s at 75 bar and 300 °C.

The residence time distribution $E(t)$ for discrete values n was calculated with the tracer concentration c of CO₂ as follows (Eq. (9.1)):

$$E(t) = \frac{c_{\text{CO}_2}(t)}{\int_0^{\infty} c_{\text{CO}_2}(t) dt} \approx \frac{c_{\text{CO}_2}(t)}{\sum_{i=1}^n c_{\text{CO}_2}(t) \cdot \Delta t} \quad (9.1)$$

The mean residence time t_m is defined by the Eq. (9.2):

$$t_m = \int_0^{\infty} t \cdot E(t) dt \approx \sum_{i=1}^n t_i \cdot E(t_i) \cdot \Delta t_i \quad (9.2)$$

The calculated mean residence times with different reactor fillings and volume flows for the fixed bed reactor are listed in Table 9.1.

Table 9.1. Mean residence times for an empty, filled with Raschig rings or filled with quartz beads reactor for different volume flows at 300 °C and 75 bar.

\dot{V} [mL _N min ⁻¹]	Empty [min]	Raschig rings [min]	Quartz beads [min]
300	37.2 ± 0.3	38.2 ± 0.4	37.0 ± 0.8
600	18.9 ± 0.1	18.8 ± 0.3	20.0 ± 1.3
1200	9.20 ± 0.1	9.50 ± 0.1	9.69 ± 0.2

9.1.4 Compact Profile Reactor

A negative control experiment for the CPR was performed analogously to Chapter 9.1.3 at $300 \text{ mL}_N \text{ min}^{-1}$ using $\text{CO}_2/\text{H}_2 = 3/1$ showing no catalytic activity. The volume induced pressure drop was investigated under the same conditions using nitrogen. In this reactor setup the pressure drop is listed in Table 9.2. The residence time was evaluated in a CPR filled with quartz beads at $300 \text{ mL}_N \text{ min}^{-1}$, $600 \text{ mL}_N \text{ min}^{-1}$ and $1000 \text{ mL}_N \text{ min}^{-1}$. The measurements and calculations were carried out analogously to Chapter 9.1.3 (see Figure 9.4, Table 9.2).

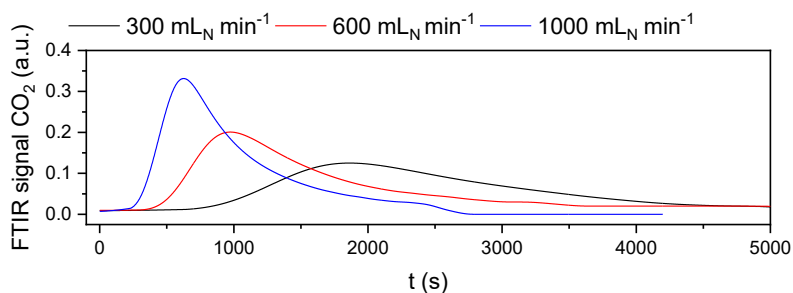


Figure 9.4. Illustration of the CO_2 pulse tracer test of the CPR filled with quartz beads ($200\text{--}300 \mu\text{m}$) at different volume flows measured by FTIR. At $t = 0 \text{ s}$ the nitrogen feed was switched to CO_2 for 12 s at 75 bar and $300 \text{ }^\circ\text{C}$.

Table 9.2. Mean residence times and pressure drops for the CPR filled with quartz beads for different volume flows at $300 \text{ }^\circ\text{C}$ and 75 bar.

\dot{V} [$\text{mL}_N \text{ min}^{-1}$]	Quartz beads [min]	Pressure drop [bar]
300	41.4 ± 3.2	0.01
600	29.5 ± 2.1	0.07
1000	14.6 ± 3.1	0.26

9.2 List of hazardous substances used according to GHS

Table 9.3. List of hazardous substances used according to globally harmonized system of classification and labelling of chemicals (GHS) part 1 [171–184]

Material	GHS-Symbol	Hazard statement	Precautionary statement
Ce(NO ₃) ₃ ·6 H ₂ O	GHS05, GHS09	H318-H410	P273-P280-P305+P351+P338-P391-P501
CO	GHS02, GHS04, GHS06, GHS08	H220-H280-H331-H360D-H372	P202-P210-P260-P304+P340+P315-P308+P313-P377-P381-P403-P405
CO ₂	GHS04	H280	P403
Cu(NO ₃) ₂ ·3 H ₂ O	GHS03 GHS05 GHS09	H272-H314-H410	P210-P260-P273-P280-P303+P361+P353-P305+P351+P338
CuO/ZnO/Al ₂ O ₃	GHS09	H410	P273-P391-P501
Downtherm® A	GHS07 GHS09	H315-H319-H335-H410	P261-P264-P271-P273-P302+P352-
Ethanol	GHS02 GHS07	H225-H319	P210-P233-P240-P241-P242-P305-P351+P338
H18-DBT	GHS08	H304-H413	P273-P301+P310-P331-P501
H ₂	GHS02 GHS04	H220-H280	P210-P377-P381-P403
He	GHS04	H280	P403
In(NO ₃) ₃ x H ₂ O	GHS03 GHS07	H272-H302+H312+H332	P210-P220-P280-P301+P312-P302+P352+P312 P304+P340+P312
In(OH) ₃	GHS08	H372-H412	P260-P264-P270-P273-P314-P501
In ₂ O ₃	GHS08	H372-H412	P260-P264-P270-P273-P314-P501
Methanol	GHS02 GHS06 GHS08	H225-H301+H311+H331-H370	P210-P233-P280 P301+P310-P303+P361+P353 P304+P340+P311
N ₂	GHS04	H280	P403
NaCO ₃	GHS07	H319	P264-P280-P305+P351+P338-P337+P313

Appendix

Table 9.4. List of hazardous substances used according to globally harmonized system of classification and labelling of chemicals (GHS) part 2 [185–187].

Material	GHS-Symbol	Hazard statement	Precautionary statement
Ni(NO ₃) ₂ ·6 H ₂ O	GHS03		
	GHS05		
	GHS07	H272-H302+H332-H315-H317- H318-H334-H341-H350-H360- H372-H410	P210-P273-P280-P301+P312- P305+P351+P338-P308+P313
	GHS08		
	GHS09		
NiO	GHS07	H317+H350i+H372+H413	P202-P260-P273-P280-P302+352- P308+P313
ZrO(NO ₃) ₂ · x H ₂ O	GHS03		
	GHS05	H272-H302-H314	P210-P260-P280-P301+P312- P303+P361+P353-P305+P351+P338
	GHS07		

9.3 Supporting Information of 1st publication (available online)

ChemPlusChem

Supporting Information

Effect of Conversion, Temperature and Feed Ratio on $\text{In}_2\text{O}_3/\text{In}(\text{OH})_3$ Phase Transitions in Methanol Synthesis Catalysts: A Combined Experimental and Computational Study

Philipp Kampe, Anne Wesner, Patrick Schühle, Franziska Hess,* and Jakob Albert*

Reactor setup

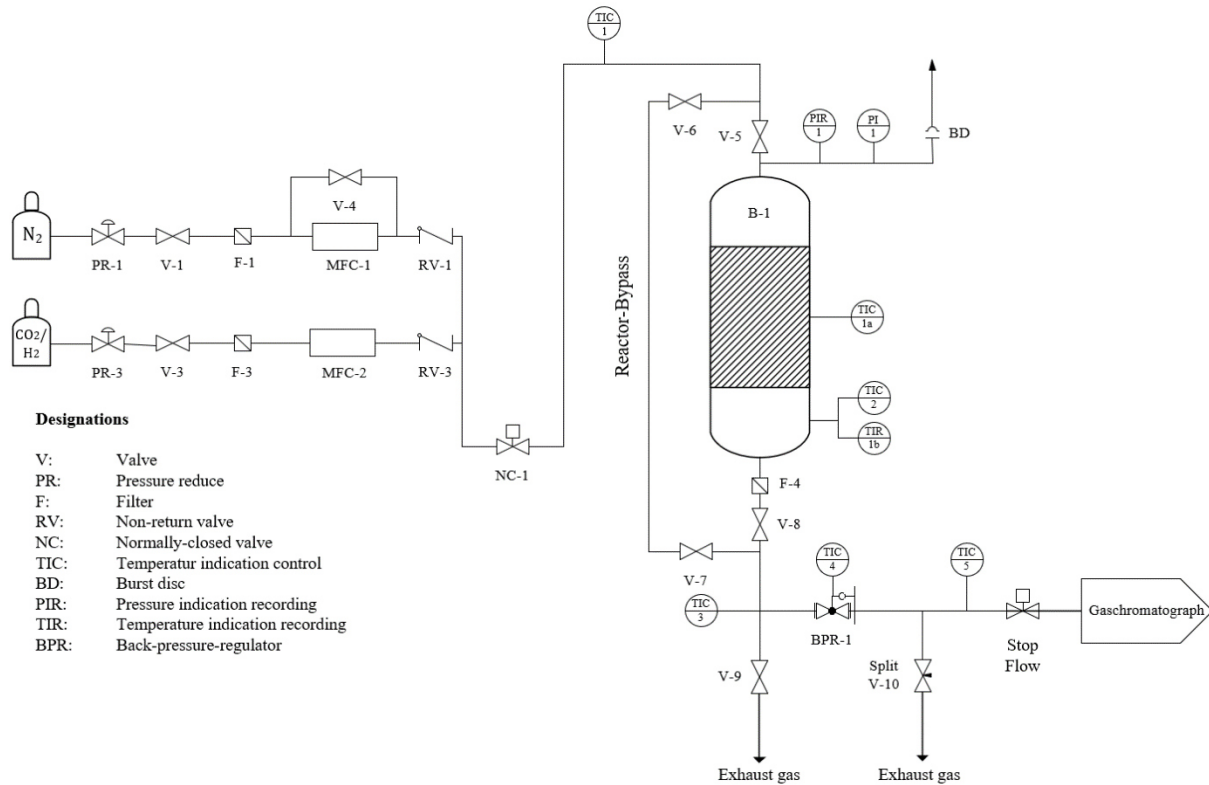


Figure S1. Piping and instrumentation diagram of the high-pressure continuous-flow fixed-bed reactor setup with periphery.

Temperature profiles

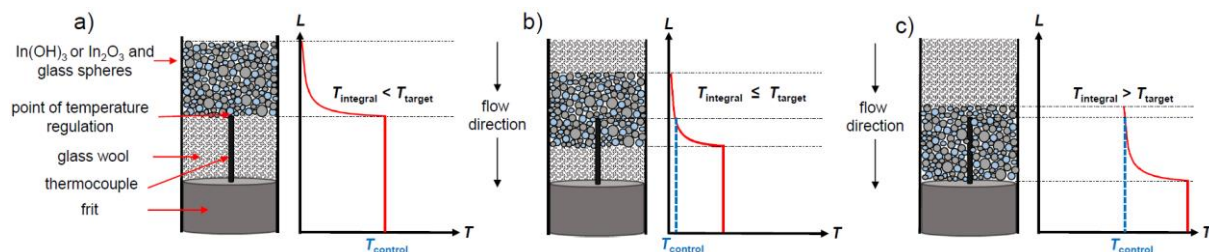


Figure S2. Theoretical temperature profile T_{integral} for CO_2 hydrogenation in experimental setup 1 for a) top, b) middle or c) bottom configuration.

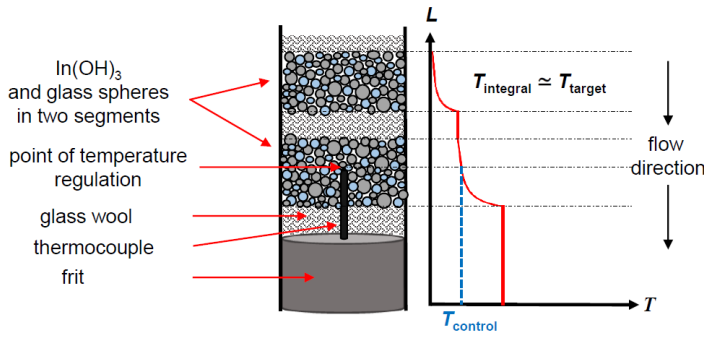


Figure S3. Theoretical temperature profile T_{integral} for CO_2 hydrogenation for two-segment-configuration.

Evaluation of process parameters

The calculation of process parameters to evaluate the catalytic performance was done as follows. Using the adjusted standard volume flow (V_N) and the known composition of the feed gas ($y_{i,in}$) enabled the calculation of the molar flow of component i entering the reactor, under consideration of the ideal gas law:

$$\dot{n}_{i,in} = \frac{p_N \cdot y_{i,in} \cdot V_N}{R \cdot T_N} \quad (\text{Eq. S1})$$

Thereby, p_N and T_N are standard pressure and temperature. Giving regard to the carbon balance of the reaction system, the total molar flow at the reactor outlet can be determined, using the molar fractions of CO_2 , CO and methanol, known from online gas chromatograph analysis:

$$\dot{n}_{ges,out} = \frac{\dot{n}_{\text{CO}_2,in}}{y_{\text{CO}_2,out} + y_{\text{CO},out} + y_{\text{MeOH},out}} \quad (\text{Eq. S2})$$

Thereafter, the molar flow of the component i , leaving the reactor was calculated as follows:

$$n_{i,out} = \dot{n}_{ges,out} \cdot y_{i,out} \quad (\text{Eq. S3})$$

The water partial pressures (see Table S1) were calculated by ASPEN modelling using the Peng-Robinson property method.

Table S1. Simulated partial water pressures using ASPEN PLUS modelling.

	T / °C	$n_{\text{H}_2\text{O}/\text{CO}_2} / \text{mol s}^{-1}$			$n_{\text{ges,aus}} / \text{mol s}^{-1}$			$x_{\text{H}_2\text{O}} / -$			$p_{\text{ges}} / \text{bar}$			ideal : $p_{\text{H}_2\text{O}} / \text{bar}$			Fugacity coefficient			real : $p_{\text{H}_2\text{O}} / \text{bar}$		
		200	250	300	200	250	300	200	250	300	200	250	300	200	250	300	200	250	300	200	250	300
$\text{In}(\text{OH})_3$	top	8.45E-08	5.60E-07	2.59E-06	8.17E-04	8.17E-04	8.15E-04	1.03E-04	6.86E-04	3.18E-03	75.31	75.39	75.10	0.01	0.05	0.24	0.942	0.942	0.939	0.0073	0.0487	0.2243
	middle	3.13E-07	2.36E-06	8.68E-06	8.17E-04	8.16E-04	8.11E-04	3.83E-04	2.90E-03	1.07E-02	75.21	75.37	75.36	0.03	0.22	0.81	0.942	0.939	0.933	0.0271	0.2050	0.7523
	bottom	3.36E-04	1.27E-06	6.64E-06	8.17E-04	8.16E-04	8.12E-04	4.11E-04	1.56E-03	8.17E-03	75.14	75.11	75.43	0.03	0.12	0.62	0.942	0.941	0.935	0.0291	0.1103	0.5762
In_2O_3	top	1.70E-07	1.24E-06	4.91E-06	8.17E-04	8.16E-04	8.14E-04	2.08E-04	1.52E-03	6.03E-03	75.62	75.26	75.18	0.02	0.11	0.45	0.942	0.941	0.937	0.0148	0.1074	0.4250
	middle	2.72E-07	2.00E-06	7.27E-06	8.17E-04	8.16E-04	8.12E-04	3.33E-04	2.45E-03	8.95E-03	75.56	75.27	75.27	0.03	0.18	0.67	0.942	0.94	0.934	0.0237	0.1737	0.6290
	bottom	2.80E-07	1.91E-06	6.66E-06	8.17E-04	8.16E-04	8.13E-04	3.42E-04	2.35E-03	8.19E-03	75.28	75.20	75.32	0.03	0.18	0.62	0.942	0.94	0.935	0.0243	0.1658	0.5768
$\text{In}(\text{OH})_3$	2 segments	7.77E-08	1.07E-06	6.18E-06	8.17E-04	8.16E-04	8.13E-04	9.50E-05	1.31E-03	7.60E-03	75.54	75.30	75.30	0.01	0.10	0.57	0.942	0.94	0.935	0.0068	0.0927	0.5353

The standard deviation is calculated using the “n-1” method out of three gas chromatography measurements per experiment:

$$\sigma = \sqrt{\frac{\sum(x-\bar{x})^2}{(i-1)}} \quad (\text{Eq. S4})$$

where i is the sample size and \bar{x} is the sample average value.

Table S2. Experimental data and standard deviation determined in the first experimental setup (top and middle), with $T = 200, 250$ and 300 °C, for a CO_2/H_2 mixture of 1/3 at a total pressure of 75 bar.

	T / °C	X_{CO_2} / %			S_{MeOH} / %		
		200	250	300	200	250	300
In_2O_3	top	0.08	0.61	2.40	100	88	76
		± 0.00	± 0.00	± 0.03	± 0	± 0	± 0
	middle	0.13	0.98	3.56	100	87	73
		± 0.00	± 0.02	± 0.04	± 0	± 0	± 1
bottom	0.14	0.94	3.26	100	87	68	
		± 0.02	± 0.01	± 0.05	± 0	± 0	± 1
$\text{In}(\text{OH})_3$	top	0.04	0.29	1.27	100	86	86
		± 0.00	± 0.02	± 0.07	± 0	± 0	± 1
	middle	0.15	1.16	4.25	100	86	71
		± 0.02	± 0.00	± 0.13	± 0	± 0	± 1
bottom	0.16	0.62	3.25	100	93	78	
		± 0.00	± 0.02	± 0.01	± 0	± 0	± 1

Table S3. Mass loss from TGA data for first experimental setup. In_2O_3 and $\text{In}(\text{OH})_3$ (before reaction, pure) and reactor configuration top, middle, bottom (after reaction).

Mass loss [%]							
In_2O_3				$\text{In}(\text{OH})_3$			
pure	top	middle	bottom	pure	top	middle	bottom
0	0	0	0	16.2	2.7	0	0

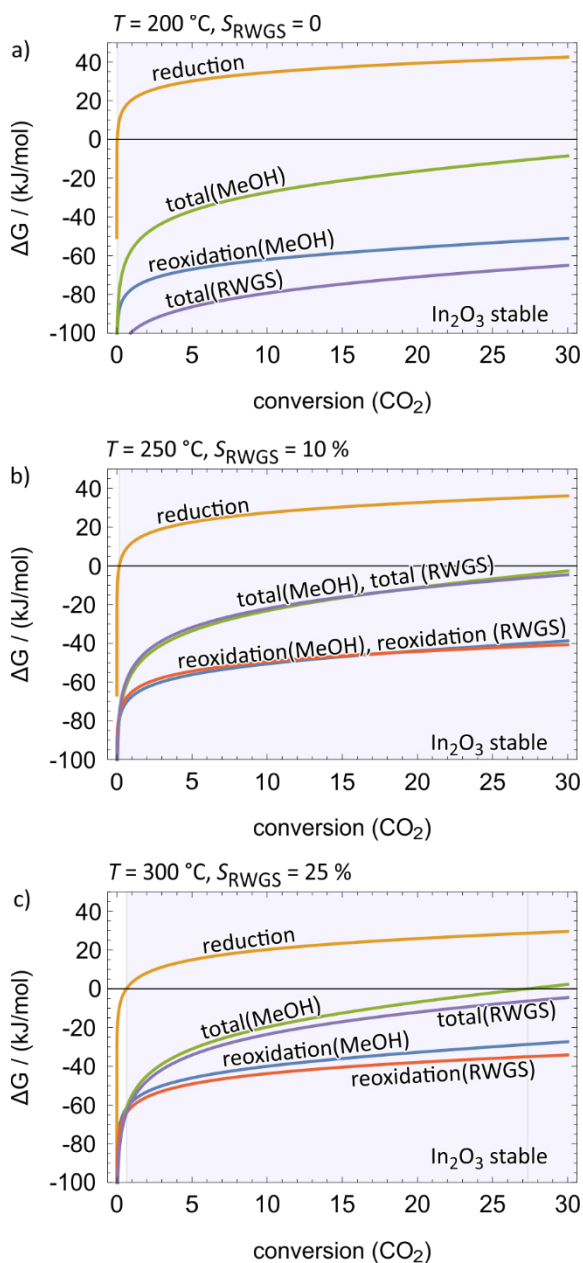
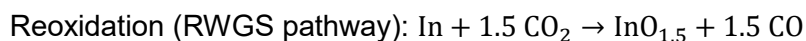
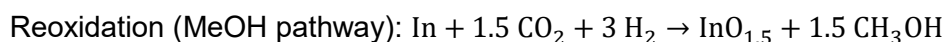
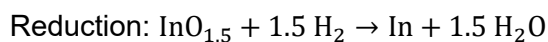


Figure S4. ΔG curves with RWGS for reduction to In^0 and reoxidation, based on experimental selectivities. a) 200 °C, b) 250 °C, c) 300 °C for a CO_2/H_2 mixture of 1/3 at a total pressure of 75 bar.

Additional simulations were carried out taking into consideration an alternative degradation pathway of In_2O_3 through the reduction to In^0 :



In Figure S4, the orange curve represents the reduction, which is identical for both MeOH and RWGS reaction pathways. The initial reduction is endergonic for all three temperatures with the exception of a small section at very low conversion under the assumption of a dry reaction feed. Reoxidation represented by the blue and red curves is exergonic over the whole conversion range for both reaction pathways, indicating that In_2O_3 is stable with respect to

reduction at the considered temperatures. At 300 °C, reduction to In^0 is reversible at conversion below 0.5 %. Reduction to In^0 is therefore not expected to occur in pure In_2O_3 -based catalysts, in agreement with our experimental results. We note that In^0 formation is frequently observed in ZrO_2 -supported In_2O_3 catalysts and is considered as the dominant degradation pathway. We consider this as a result of the altered redox behavior due to the catalyst-support interaction that facilitates the formation of oxygen vacancies in In_2O_3 , which we expect to be reflected in altered enthalpy of formation of the supported In_2O_3 . According to our estimates, this change can be rather small to have a noticeable effect; for instance, increasing the enthalpy of formation of In_2O_3 from -923 kJ/mol to -900 kJ/mol ($\Delta \approx 2.5 \%$) increases the width of the reversible window at low conversion from 0.5 % to 3 %, making the formation of In^0 far more likely. This is even more so the case if the reaction was operated at CO_2 deficit, at increased temperature, or with CO co-feed. While these influences can be qualitatively understood based on the present model, application to $\text{In}_2\text{O}_3@ZrO_2$ would require a somewhat accurate estimate of its enthalpy of formation; unfortunately, the influence of the support on the bulk thermodynamics of In_2O_3 are currently unknown.

9.4 Supporting Information of 2nd publication (available online)

ChemCatChem

Supporting Information

Indium-based Catalysts for CO₂ Hydrogenation to Methanol: Key Aspects for Catalytic Performance

Anne Wesner, Philipp Kampe, Nick Herrmann, Sebastian Eller, Charlotte Ruhmlieb, and Jakob Albert*

Table of Contents

Supplementary methods	2
Catalyst preparation	2
Catalyst characterization	4
Catalytic evaluation	6
Supplementary catalytic results and characterization of $\text{In}_2\text{O}_3/\text{ZrO}_2$	9
Supplementary characterization of $\text{CuO-}/\text{NiO-}/\text{MgO-}/\text{CeO}_2\text{-In}_2\text{O}_3/\text{ZrO}_2$	13
Supplementary characterization of $\text{NiO-In}_2\text{O}_3/\text{ZrO}_2$ (WI), (CR) and (CP)	18

This document contains 8 Tables and 15 Figures on 20 pages.

Supplementary methods

Catalyst preparation

All chemicals were obtained commercially and used as received without further purification.

CuO/ZnO/Al₂O₃

Copper based methanol synthesis catalyst were obtained commercially via Alfa Aesar, product no. 45776.

In₂O₃/ZrO₂

In₂O₃/ZrO₂ catalysts have been prepared through impregnation by already published synthesis methods according Martin et al. (In₂O₃/ZrO₂ M-AA, M-SG)^[12] or Schühle et al. (S-AA, S-SG)^[13]. In(NO₃)₃ · x H₂O Puratronic® (≥99.999 %, Alfa Aesar, VWR 10708.22) was used as a precursor. ZrO₂ oxide by Alfa Aesar (VWR 43814.36, referred as ZrO₂ (AA)), or St. Gobain (SZ 31164 NORPRO, referred as ZrO₂ (SG)) were used as a support. Prior synthesis ZrO₂ pellets were granulated to a particle size of 80-250 μm.

Synthesis of In₂O₃/ZrO₂ according to Martin ^[12]. In(NO₃)₃ · x H₂O (6.84 g) was dissolved in 630 mL of ethanol and 216 mL of dist. water. ZrO₂ (18 g) was added to the solution and the suspension was stirred for 5 h in a rotatory evaporator (111 rpm, room temperature, 800 mbar). After the solvent was removed, the impregnated powder was dried (65 °C, 12 h), heated with 5 °C/min to 300 °C and calcined for 3 h.

Synthesis of In₂O₃/ZrO₂ according to Schühle ^[13]: The stock solution was prepared by dissolving In(NO₃)₃ · x H₂O (10 g) in 25 mL of dist. water. The suspension was prepared by adding ZrO₂ (17.1 g) to the In(NO₃)₃ · x H₂O-stock solution (16.4 mL). An aqueous supernatant was removed in a rotary evaporator, followed by drying (65 °C, 12 h). Thereafter, the powder was heated with 5 °C /min to 300 °C and calcined for 3 h.

Promoted In₂O₃/ZrO₂ with different metals (Ce, Mg, Ni, Cu)

Bimetallic supported catalysts (CuO/NOi/CeO₂/MgO-In₂O₃/ZrO₂) have been prepared by co-precipitation. The used precursors were In(NO₃)₃ · x H₂O Puratronic® (≥ 99.999 %, Alfa Aesar, VWR 10708.22), Ce(NO₃)₃ · 6 H₂O (99.5 %, Thermo Scientific, VWR ACRO218691000), Mg(NO₃)₂ · 6 H₂O (≥ 98 %, Thermo Scientific,

VWR A10329.30), $\text{Ni}(\text{NO}_3)_2 \cdot 6 \text{H}_2\text{O}$ (n.s., SuboLab GmbH) and $\text{Cu}(\text{NO}_3)_2 \cdot 3 \text{H}_2\text{O}$ (99 %, Acros Organics). ZrO_2 (St. Gobain, SZ 31164 NORPRO, referred as ZrO_2 SG) and Na_2CO_3 (99,5 %, Grüssing) were used as a support material.

10 g Na_2CO_3 have been dissolved in 100 mL dist. H_2O . $\text{In}(\text{NO}_3)_3 \cdot x \text{H}_2\text{O}$ and the respective other metal-nitrate was dissolved in 250 mL dist. H_2O . The applied amounts of In_2O_3 and the metal-nitrates were calculated to be 10 wt.%. NaHCO_3 -solution was added to the nitrate solution until a pH-value of 9.2 was reached and 20 g ZrO_2 were added. The suspension was stirred in a rotary evaporator (111 rpm, room temperature, 800 mbar) for 1 h and another 500 mL dist. H_2O were added afterwards. The mixture was filtered and washed until the washing solution reached a pH value of 7. The impregnated powder was dried (65 °C, 12 h), heated with 5 °C/min to 300 °C and calcined for 3 h.

$\text{NiO-In}_2\text{O}_3/\text{ZrO}_2$ catalysts have been prepared by different synthesis methods. The used precursors were $\text{In}(\text{NO}_3)_3 \cdot x \text{H}_2\text{O}$ Puratronic® (≥ 99.999 %, Alfa Aesar, VWR 10708.22), $\text{Ni}(\text{NO}_3)_2 \cdot 6 \text{H}_2\text{O}$ (n.s. SuboLab GmbH) and Na_2CO_3 (99,5 %, Grüssing).

Wetness impregnation (WI)

$\text{Ni}(\text{NO}_3)_2 \cdot 6 \text{H}_2\text{O}$ (0.747 g) was dissolved in 250 mL of dist. H_2O and $\text{In}_2\text{O}_3/\text{ZrO}_2$ (M-SG, 15 g) was added to the solution. The suspension was stirred for 1 h in a rotatory evaporator (111 rpm, room temperature, 850 mbar). After the solvent was removed, the impregnated powder was dried (65 °C, 12 h), heated with 5 °C/min to 300 °C and calcined for 3 h.

Co-precipitation (CP)

10 g Na_2CO_3 have been dissolved in 100 mL of dist. H_2O . $\text{In}(\text{NO}_3)_3 \cdot x \text{H}_2\text{O}$ (6.75 g) and $\text{Ni}(\text{NO}_3)_2 \cdot 6 \text{H}_2\text{O}$ (1.24 g) were dissolved in 250 mL of dist. H_2O . NaHCO_3 -solution was added to the nitrate solution until a pH-value of 9.2 was reached and 20 g ZrO_2 were added thereafter. The suspension was stirred in a rotary evaporator (111 rpm, room temperature, 800 mbar) for 1 h and treated with another 500 mL of dist. H_2O , followed by filtration and washing until the solution reached a pH value of 7. The impregnated powder was dried (65 °C, 12 h), heated with 5 °C/min to 300 °C and calcined for 3 h.

Chemical reduction (CR)

The synthesis method was derived from Zhang et al.^[41] $\text{Ni}(\text{NO}_3)_2 \cdot 6 \text{H}_2\text{O}$ (0.747 g) was dissolved in 250 mL of dist. H_2O and $\text{In}_2\text{O}_3/\text{ZrO}_2$ (M-SG) (15 g) was added to the solution. The suspension was stirred for 1 h in a rotary evaporator (111 rpm, room temperature, 800 mbar) and subsequently heated up to 80 °C. An aqueous solution of NaOH was prepared ($n(\text{Ni}) : n(\text{NaOH}) = 1 : 3$) and treated with NaBH_4 ($n(\text{Ni}) : n(\text{NaBH}_4) = 1 : 4$). The NaOH-solution was added dropwise to the suspension and the mixture was stirred for 2 h in a rotatory evaporator (111 rpm, 80 °C, 800 mbar). Afterwards, the mixture was washed with dist. H_2O until a pH value of 7 and the impregnated powder was dried (65 °C, 12 h) thereafter.

Catalyst characterization

ICP-OES

Inductively coupled plasma optical emission spectrometry (ICP-OES) was employed for elemental composition analysis of each catalyst. 100 mg of each sample were dissolved in a mixture of 5 mL conc. H_2SO_4 and 1 mL conc. HNO_3 . Subsequently, the sample was atomized in an argon plasma and the resulting composition was quantified using optical emission spectrometry. The characterization was performed using an ASCOR-spectrometer (manufactured by Spectro) at the central element analysis service of the Department of Chemistry, University of Hamburg.

N₂-physisorption

Brunauer-Emmet-Teller (BET) surface area and Barrett-Joyner-Halenda (BJH) pore volume were determined by N_2 -physisorption at -196 °C by an Autosorb iQ-MP/XR instrument from Anton Paar. Prior to analysis, the sample was degassed under vacuum at 200 °C for 10 h.

XRD

Powder X-ray diffraction (p-XRD), was used to determine the crystal structure and was carried out using a Panalytical MDP X'Pert Pro diffractometer operated in the Bragg-Brentano geometry with $\text{Cu K}\alpha$ radiation ($\lambda = 0.1541 \text{ nm}$). The measuring range of the diffraction angle was 10-80 ° and sampled using a rate of 0.013 ° every 0.3 s.

The average particle size of In_2O_3 on ZrO_2 size was determined using Scherrer-Debye equation^[36]:

$$d = \frac{k\lambda}{\beta \cos\theta} \quad (\text{S1})$$

where k represents the shape factor (0.89), λ the wavelength used in X-ray diffraction, β is the Full Width at Half Maximum (FWHM) of the reflection and θ the Bragg angle. For the calculation the 2 2 2 reflection of In_2O_3 was used.

CO₂-TPD

CO₂-Temperature programmed desorption (CO₂-TPD) was used to determine CO₂ binding capacity and strength. Analysis have been carried out on a *ChemBET Pulsar* apparatus (Quantachrome Instruments). Prior to analysis, samples (0.3 g) were exposed to a He-gas flow (80 mL/min) and heated up to 200 °C (10 K/min) for 1 h to remove surface H₂O. The loading of the surface with CO₂ was also carried out at 200 °C, followed by cooling down to 50 °C. The sample was thereafter heated up under He gas flow (80 mL/min, 10 °C/min) to 700 °C and the desorbed CO₂ was measured via a *Thermal Conductivity Detector (TCD)*.

H₂-TPR

H₂-Temperature programmed reduction (H₂-TPR) was used to determine the reducibility of the surface. Analysis have been carried out on a *ChemBET Pulsar* apparatus (Quantachrome Instruments). Prior to analysis, samples (0.3 g) were exposed to N₂-gas flow (80 mL/min) and heated up to 180 °C (10 °/min) for 1 h to remove surface H₂O, followed by cooling down to 100 °C. The sample was heated up again under H₂/N₂ (5/95 v/v) gas flow (80 mL/min, 10 °C/min) to 850 °C. The used H₂ was measured by via Thermal Conductivity Detector (TCD).

XPS

X-ray photoelectron spectroscopy (XPS) was used to determine the oxidation states of the surface elements. Analysis have been carried out using a Thermo Scientific system at room temperature with Al K α -radiation (1484.6 eV) and a spot size of 400 μm . A flood gun was utilized to reduce charging effects of the samples. The resulting spectra were corrected by setting C1s binding energy at 284,8 eV. Data were processed by using Avantage 4.87 software.

Microscopy

High-resolution transmission electron microscopy (HRTEM) images were obtained using a double-corrected (CESCOR and CETCOR, CEOS) JEOL JEM 2200FS microscope with an in-column image filter (Ω -type), a high-angle annular dark-field (HAADF) detector, and a Gatan 4K UltraScan 1000 camera at an accelerating voltage of 200 kV. Energy-dispersive X-ray spectroscopy (EDX) elemental maps were obtained using a JEOL JED-2300 analysis station with a 100 mm² silicon drift detector.

Catalytic evaluation

All experiments were performed in a continuous-flow high-pressure fixed-bed reactor setup (inner diameter 20 mm) made of stainless steel (1.4571), surrounded by a heating jacket (see Figure S1). The reactant gas mixture consisting of 25 % CO₂ (4.5 grade) and 75 % H₂ (5.0 grade) from Westfalen as well as N₂ (5.0 grade) from Air Liquide was conveyed into the reactor by mass-flow controllers (Bronkhorst Prestige FG-201CV). The reaction pressure was adjusted with a back-pressure regulator (Dutch Regulators). The catalyst bed temperature was controlled with an inside located thermocouple. Reactor inlet and outlet gas lines were heated to 180 °C with regard to preheat the reaction gas and to avoid condensation of methanol and water. Every 30 min, the outlet steam was sampled and analyzed by online gas chromatography (Bruker 450-GC). The GC has four columns (Restek U-Bond, Restek Q-Bond, Bruker Swax, Bruker Molsieve 5 Å), a methanizer (for CO₂ and CO quantification), two flame ionization detectors (FIDs) and one thermal conductivity detector (TCD).

5.0 or 4.0 g of catalyst with a particle size of 80-250 μm (mixed homogeneously with quartz beads) were filled into the reactor and held in place by a bed of quartz wool. Prior to reaction, the catalyst was pre-treated at 200 °C under flowing N₂ (300 Nml min⁻¹) for 1 hour. The Ni and Cu containing catalysts were pre-reduced using 10 % H₂/N₂ (500 Nml min⁻¹) at 200 °C for 1 h. Thereafter, the catalyst bed was heated to 300 °C and the reaction gas mixture with a CO₂/H₂ stoichiometric ratio of 1/3 was fed with a flow of 1200 Nml min⁻¹ into the reactor, which was pressurized to 50 or 75 bar, respectively. Materials were tested 3 h under steady-state reaction conditions for performance comparison. Afterwards, the reactor was cooled to room temperature (3 K min⁻¹) under a continuous flow of nitrogen (1000 Nml min⁻¹) after reaction. The catalyst was removed and stored under Ar (4.6 grade. Heide Gas) for further analysis.

The yield Y_{MeOH} , selectivity S_{MeOH} and productivity P_{cat} were calculated according to the following equations.

$$Y_{\text{MeOH}} = \frac{\dot{n}_{\text{MeOH}}}{\dot{n}_{\text{CO}_2,\text{in}}} \cdot 100 \% \quad (\text{S2})$$

$$S_{\text{MeOH}} = \frac{\dot{n}_{\text{MeOH},\text{out}} - \dot{n}_{\text{MeOH},\text{in}}}{\dot{n}_{\text{CO}_2,\text{in}} - \dot{n}_{\text{CO}_2,\text{out}}} \cdot 100 \% \quad (\text{S3})$$

$$X_{\text{CO}_2} = \frac{Y_{\text{MeOH}}}{S_{\text{MeOH}}} \quad (\text{S4})$$

$$P_{\text{cat}} = \frac{\dot{m}_{\text{MeOH},\text{out}} \cdot M_{\text{MeOH}}}{m_{\text{cat}}} \quad (\text{S5})$$

$$P_{\text{surface}} = \frac{P_{\text{cat}} \cdot 1000 \frac{\text{mg}}{\text{g}}}{S_{\text{BET}}} \quad (\text{S6})$$

$$P_{\text{metal}} = \frac{P_{\text{cat}}}{(\omega_{\text{Indium}} + \omega_{\text{metal promoter}})} \quad (\text{S7})$$

The calculation of (2) to (4) was done as follows: the adjusted standard volume flow (\dot{V}_N) and the known feed gas ($y_{i,\text{in}}$) composition allowed the calculation of the molar flow of component i entering the reactor, under consideration of the ideal gas law.

$$\dot{n}_{i,\text{in}} = \frac{p_N \cdot y_{i,\text{in}} \cdot \dot{V}_N}{R \cdot T_N} \quad (\text{S8})$$

In (8), p_N and T_N are standard pressure and temperature. As for the carbon balance of the reaction system, the total molar flow at the reactor outlet can be determined from the molar fractions of CO_2 , CO and methanol known from online gas chromatograph analysis.

$$\dot{n}_{\text{ges},\text{out}} = \frac{\dot{n}_{\text{CO}_2,\text{in}}}{y_{\text{CO}_2,\text{out}} + y_{\text{CO},\text{out}} + y_{\text{MeOH},\text{out}}} \quad (\text{S9})$$

The molar flow of the component i , at the reactor outlet was calculated as follows.

$$n_{i,\text{out}} = \dot{n}_{\text{ges},\text{out}} \cdot y_{i,\text{out}} \quad (\text{S10})$$

The gas hourly space velocity ($GHSV$) was used to relate the standard volume flow (\dot{V}_N) to the catalyst volume (V_{cat}):

$$GHSV = \frac{\dot{V}_N}{V_{\text{cat}}} \quad (\text{S11})$$

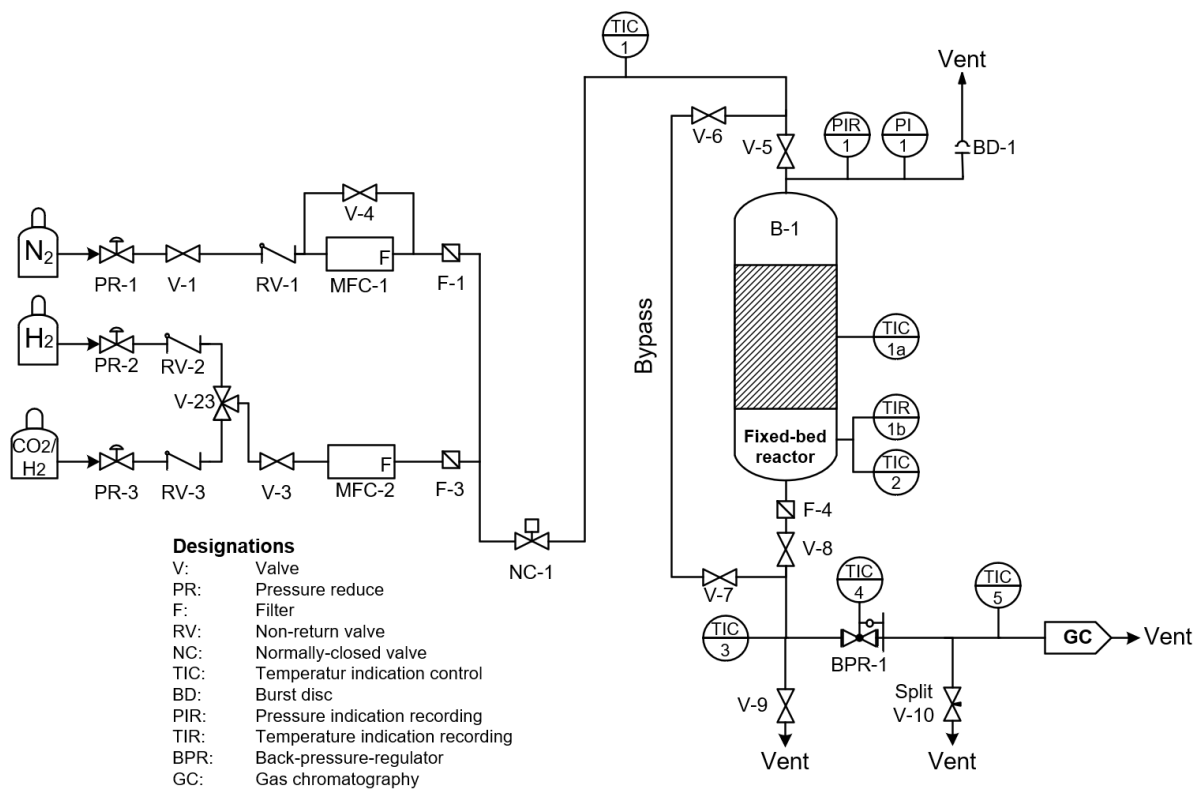


Figure S1. Instrumentation and piping diagram of the continuous-flow high-pressure fixed-bed reactor setup.

Supplementary catalytic results and characterization of In₂O₃/ZrO₂

Impact of different ZrO₂-supports and synthesis method on catalytic performance of In₂O₃/ZrO₂-catalysts.

Table S1. Catalytic performance of In₂O₃/ZrO₂ (M-SG) and (S-AA) during a temperature ramp from 250 to 275 to 300 °C and back to 250 °C with 1200 NmL·min⁻¹ at 50 and 75 bar.

In ₂ O ₃ /ZrO ₂	T / °C	X / %					$P_{cat} / g_{MeOH} g_{cat}^{-1} h^{-1}$					$Y_{MeOH,CO_2} / \%$					$S_{MeOH,CO_2} / \%$				
		250	275	300	275	250	250	275	300	275	250	250	275	300	275	250	250	275	300	275	250
M-SG	75 bar	4.4	9.3	18.7	8.6	3.6	0.16	0.30	0.47	0.29	0.14	3.4	6.4	10.0	6.1	3.0	77.2	69.3	53.5	70.9	83.0
	50 bar	3.3	7.5	15.2	7.0	3.0	0.12	0.23	0.34	0.22	0.12	2.6	5.0	7.2	4.7	2.5	79.7	66.5	47.6	67.3	81.3
S-AA	75 bar	2.3	5.6	12.5	5.4	2.3	0.10	0.19	0.33	0.19	0.10	1.9	3.9	6.8	3.8	1.9	80.7	69.1	54.4	71.1	82.8
	50 bar	2.5	5.5	11.5	5.3	2.3	0.10	0.18	0.30	0.18	0.10	2.0	3.9	6.4	3.9	2.0	81.9	71.6	56.1	73.6	85

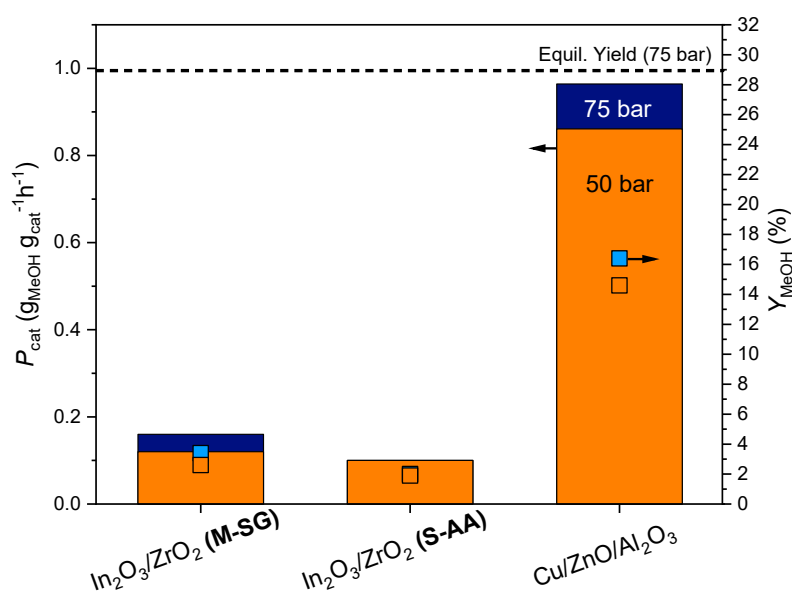


Figure S2. Methanol yield (squares) and productivity (bars) in dependency of total pressure $p = 50$ bar (orange) and $p = 75$ bar (blue) for different ZrO₂ supports (SG or AA) compared with the commercial Cu-based catalyst. Simulated equilibrium yield at $T = 250$ °C and $p = 75$ bar. Reaction conditions: CO₂/H₂ = 1/3; GHSV = 8400 h⁻¹; TOS = 3 h; $T = 250$ °C; $h_{bed} = 5.1 \pm 0.1$ cm.

Table S2. Evaluation of catalytic experiments using In₂O₃/ZrO₂ (M-AA), calculated arithmetic means and standard deviations at 75 bar and 300 °C.

	M-AA-1	M-AA-2	M-AA-2	M-AA-2	Arithmetic mean	Standard deviation
S_{CO_2} (%)	66.1	65.5	58.8	57.3	61.9	4.52
Y_{CO_2} (%)	8.47	8.54	8.47	8.62	8.53	0.071
P_{cat} (g _{MeOH} g _{cat} ⁻¹ h ⁻¹)	0.399	0.403	0.399	0.406	0.402	0.003

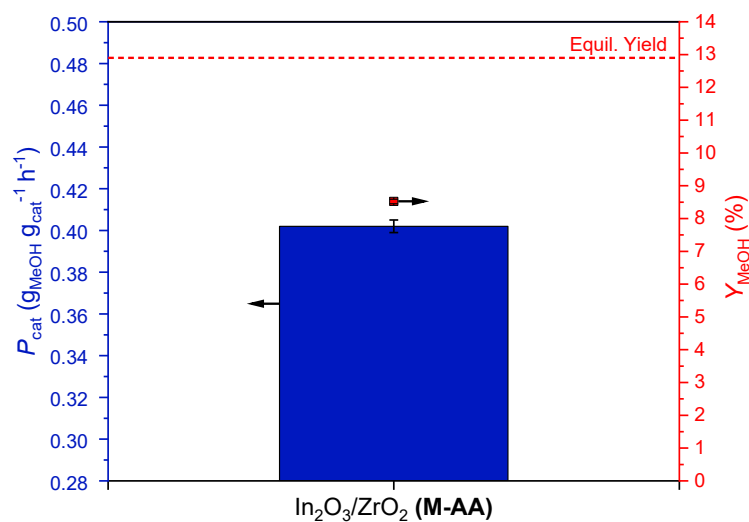


Figure S3. Methanol yield and active productivity of $\text{In}_2\text{O}_3/\text{ZrO}_2$ (M-AA) with calculated error bars out of two different batches and four experiments at 75 bar and 300 °C.

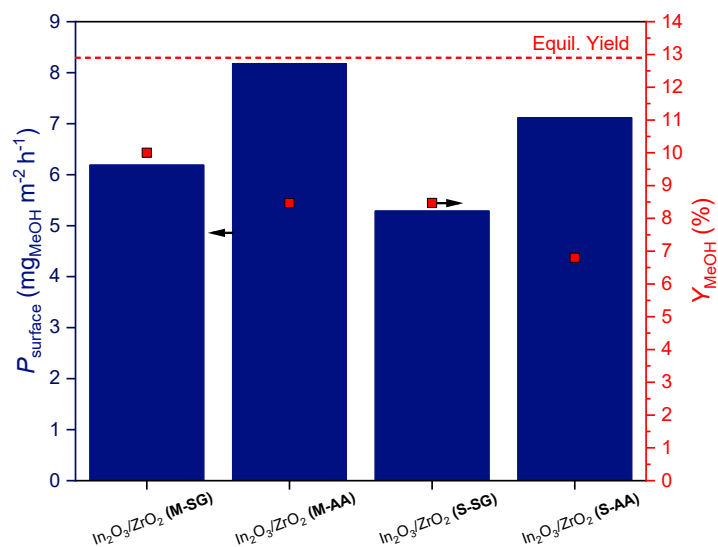
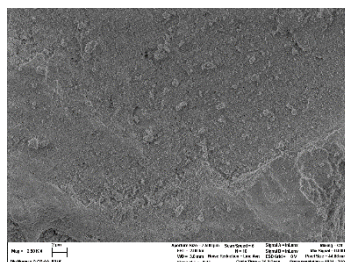
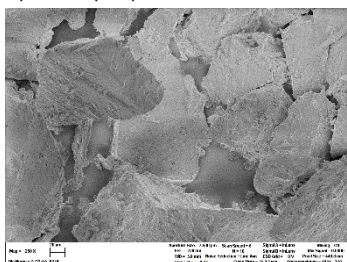
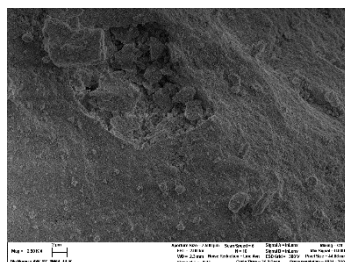
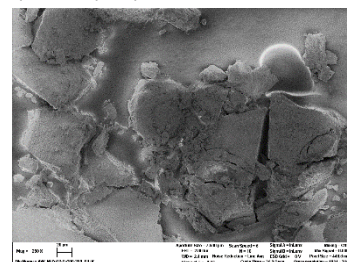


Figure S4. Influence of different ZrO_2 (SG or AA) supports and synthesis methods (M or S) on surface productivity P_{surface} , normalized to amount to the specific surfaces, and methanol yield in comparison to the calculated equilibrium yield. Reaction conditions: $\text{CO}_2/\text{H}_2 = 1/3$; $\text{GHSV} = 8400 \text{ h}^{-1}$; $\text{TOS} = 3 \text{ h}$; $T = 300 \text{ °C}$; $p = 75 \text{ bar}$; $h_{\text{bed}} = 5.1 \pm 0.1 \text{ cm}$.

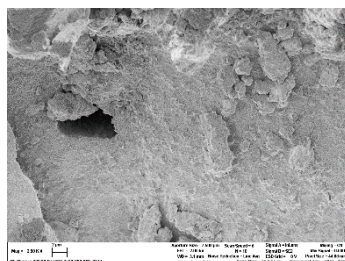
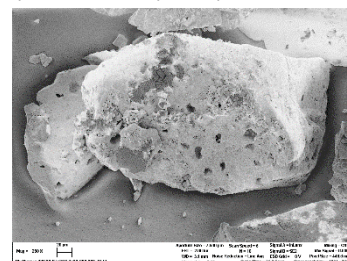
a) ZrO_2 (AA)



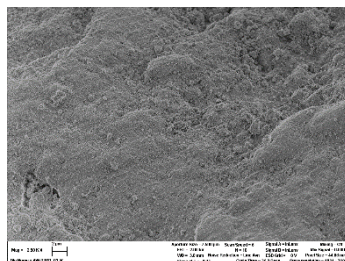
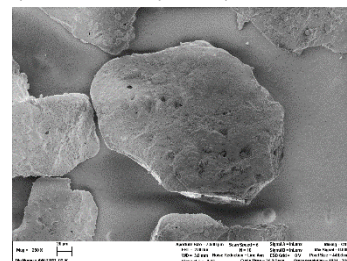
b) ZrO_2 (SG)



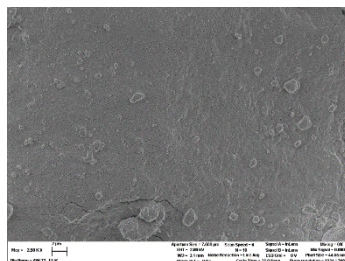
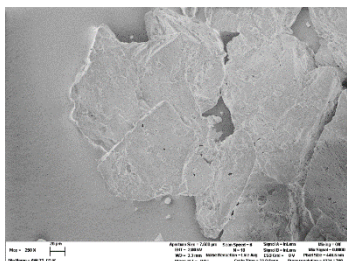
c) In_2O_3/ZrO_2 (S-AA)



d) In_2O_3/ZrO_2 (M-SG)



e) In_2O_3/ZrO_2 (S-SG)



f) In_2O_3/ZrO_2 (M-AA)

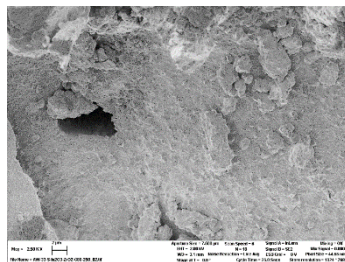
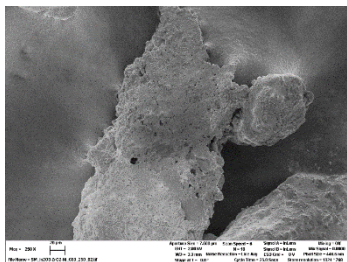


Figure S5. SEM images of a) ZrO_2 (AA) b) ZrO_2 (SG) c) In_2O_3/ZrO_2 (S-AA), d) In_2O_3/ZrO_2 (M-SG), e) In_2O_3/ZrO_2 (S-SG) and f) In_2O_3/ZrO_2 (M-AA).

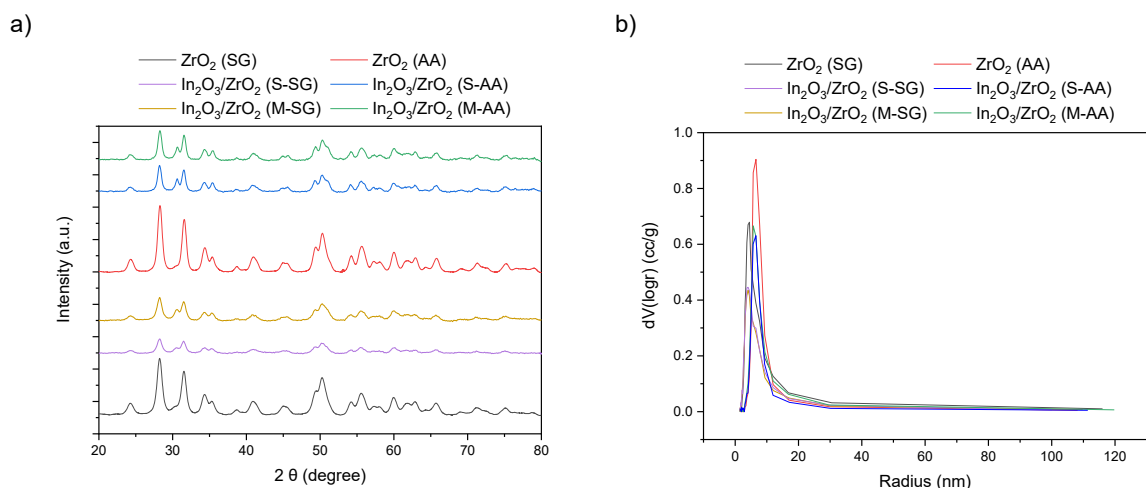


Figure S6. XRD patterns a) and pore size distribution determined by BJH method, b) for different ZrO₂ (AA and SG) and incorporated with In₂O₃ (S-AA, S-SG, M-AA and M-SG)

Table S3. Integral data of CO₂-TPD. Low (50 °C - 350 °C), high 350 °C - 650 °C and overall H₂ reduction capacity of ZrO₂ and In₂O₃/ZrO₂ material with In₂O₃/ZrO₂ (M-SG) as normed reference (1.00).

	nominal area of adsorption capacity		overall
	low	high	
ZrO ₂ (SG)	1.67	0.17	0.66
ZrO ₂ (AA)	1.21	0.19	0.52
In ₂ O ₃ /ZrO ₂ (M-SG)	1.00	1.00	1.00
In ₂ O ₃ /ZrO ₂ (S-SG)	0.59	1.12	0.95
In ₂ O ₃ /ZrO ₂ (M-AA)	0.58	0.82	0.74
In ₂ O ₃ /ZrO ₂ (S-AA)	0.50	0.75	0.67

Table S4 H₂-TPR integral data for low (110 °C - 420 °C), high 420 °C - 840 °C and overall area of ZrO₂ and In₂O₃/ZrO₂ material with In₂O₃/ZrO₂ (M-SG) as normed reference (1.00).

	nominal area of adsorption capacity		overall
	low	high	
ZrO ₂ (SG)	0.02	0.00	0.01
ZrO ₂ (AA)	0.03	0.00	0.01
In ₂ O ₃ /ZrO ₂ (M-SG)	1.00	1.00	1.00
In ₂ O ₃ /ZrO ₂ (S-SG)	1.08	1.05	1.06
In ₂ O ₃ /ZrO ₂ (M-AA)	0.78	1.18	1.06
In ₂ O ₃ /ZrO ₂ (S-AA)	0.74	0.82	0.80

Supplementary characterization of CuO-/NiO-/MgO-/CeO₂-In₂O₃/ZrO₂

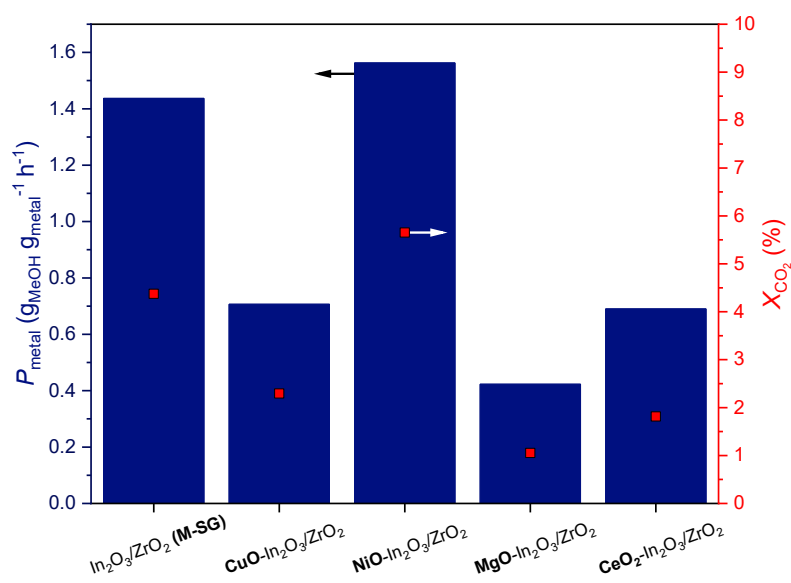
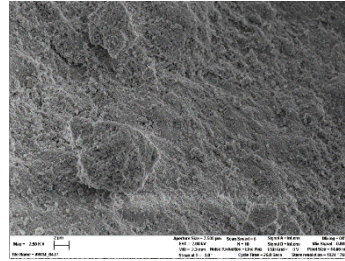
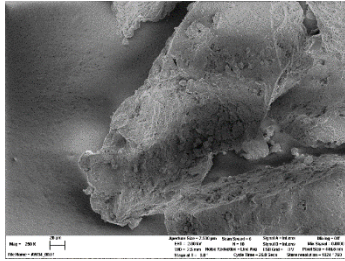
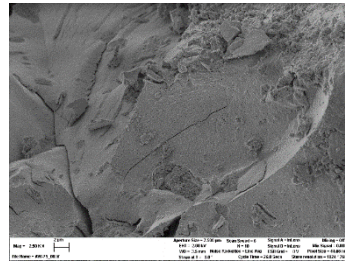
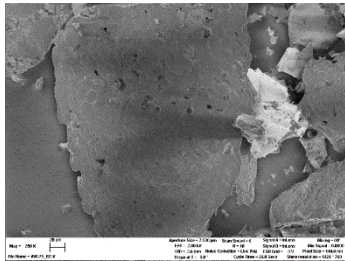


Figure S7. Catalytic performance of CuO-, NiO-, MgO- and CeO-promoted In₂O₃/ZrO₂ compared to In₂O₃/ZrO₂ (M-SG), productivity P_{metal} normalized to amount of active metals, CO₂ conversion. Reaction conditions: CO₂/H₂ = 1/3; GHSV = 8300 h⁻¹; TOS = 3 h; T = 250 °C; p = 75 bar; $h_{\text{bed}} = 5.1 \pm 0.1$ cm.

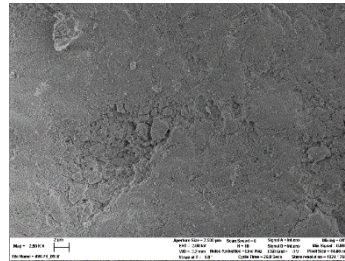
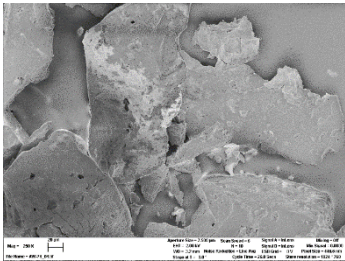
a) CuO-In₂O₃/ZrO₂



b) NiO-In₂O₃/ZrO₂



c) MgO-In₂O₃/ZrO₂



d) CeO₂-In₂O₃/ZrO₂

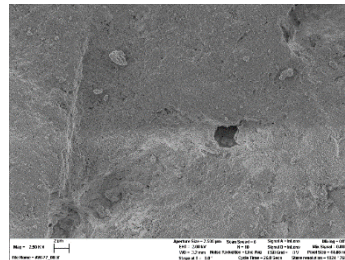
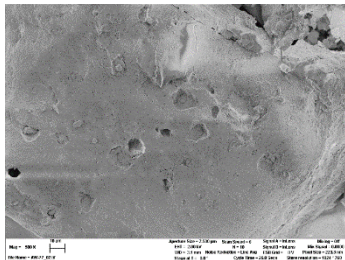


Figure S8. SEM images of a) CuO-In₂O₃/ZrO₂, b) NiO-In₂O₃/ZrO₂, c) MgO-In₂O₃/ZrO₂, d) CeO₂-In₂O₃/ZrO₂.

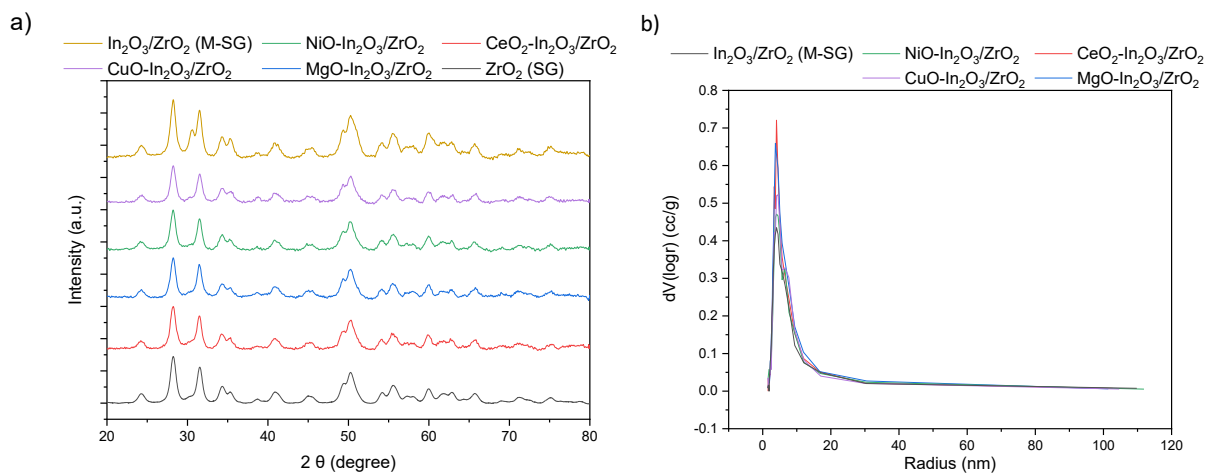
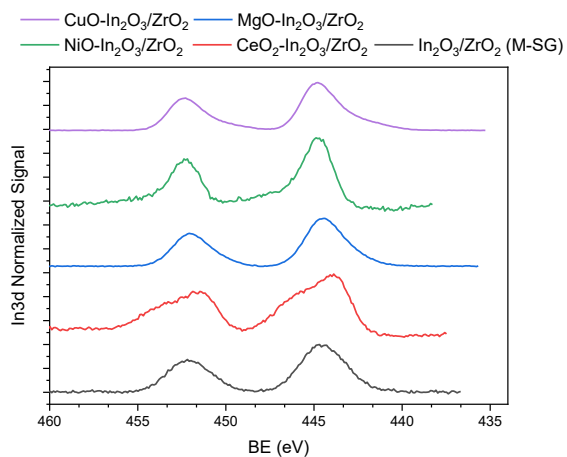
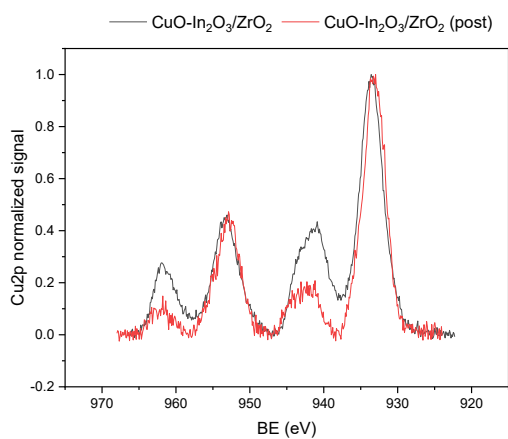


Figure S9. Analysis of CuO-, NiO-, MgO- and CeO₂-promoted In₂O₃/ZrO₂ compared to In₂O₃/ZrO₂ (M-SG): a) XRD pattern, b) pore size distribution (determined with BJH method).

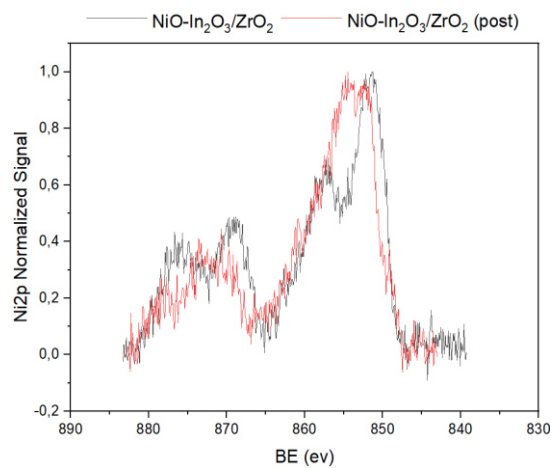
a)



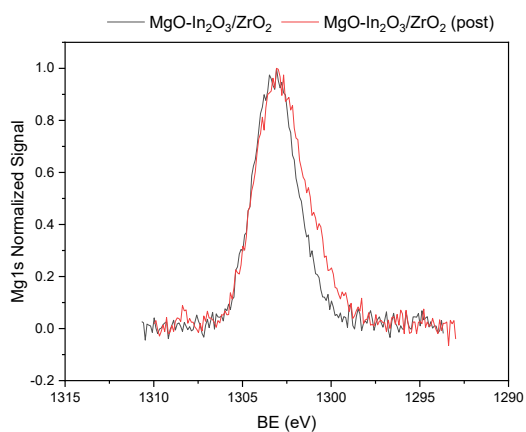
b)



c)



d)



e)

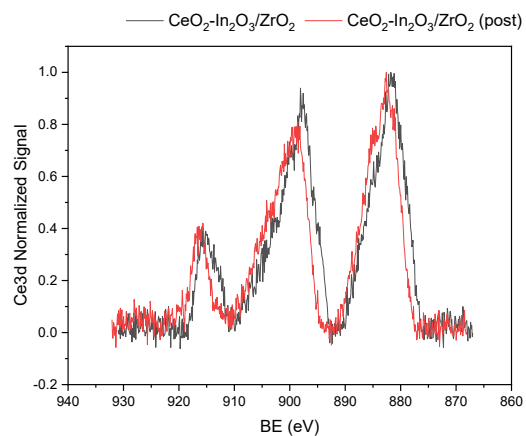


Figure S10. XPS spectra before (black) and after (red) reaction of a) In 3d for CuO-, NiO-, MgO- and CeO₂-promoted In₂O₃/ZrO₂ compared to In₂O₃/ZrO₂ (M-SG), b) Cu 2p for CuO-In₂O₃/ZrO₂, c) Ni 2p for NiO-In₂O₃/ZrO₂, d) Mg 1s for MgO-In₂O₃/ZrO₂ and e) Ce 3d for CeO₂-In₂O₃/ZrO₂.

Table S5 Integral data of CO₂-TPD. Low (50 °C - 350 °C), high (350 °C - 650 °C) and overall area of CuO-/ NiO-/ MgO-/CeO₂-In₂O₃/ZrO₂ with In₂O₃/ZrO₂ (M-SG) as normed reference (1.00).

	nominal area of adsorption capacity		overall
	low	high	
CuO-In ₂ O ₃ /ZrO ₂	2.30	1.15	1.53
NiO-In ₂ O ₃ /ZrO ₂	1.73	1.48	1.56
MgO-In ₂ O ₃ /ZrO ₂	2.89	0.85	1.52
CeO ₂ -In ₂ O ₃ /ZrO ₂	1.26	0.63	0.83
In ₂ O ₃ /ZrO ₂ (M-SG)	1.00	1.00	1.00

Table S6. H₂-TPR integral data for low (110 °C - 420 °C), high (420 °C - 840 °C) and overall area of CuO-/ NiO-/ MgO-/CeO₂-In₂O₃/ZrO₂ with In₂O₃/ZrO₂ (M-SG) as normed reference (1.00).

	nominal area of adsorption capacity		overall
	low	high	
CuO-In ₂ O ₃ /ZrO ₂	1.78	0.69	1.01
NiO-In ₂ O ₃ /ZrO ₂	1.31	0.90	1.02
MgO-In ₂ O ₃ /ZrO ₂	0.53	0.75	0.68
CeO ₂ -In ₂ O ₃ /ZrO ₂	0.81	0.79	0.80
In ₂ O ₃ /ZrO ₂ (M-SG)	1.00	1.00	1.00

Supplementary characterization of NiO-In₂O₃/ZrO₂ (WI), (CR) and (CP)

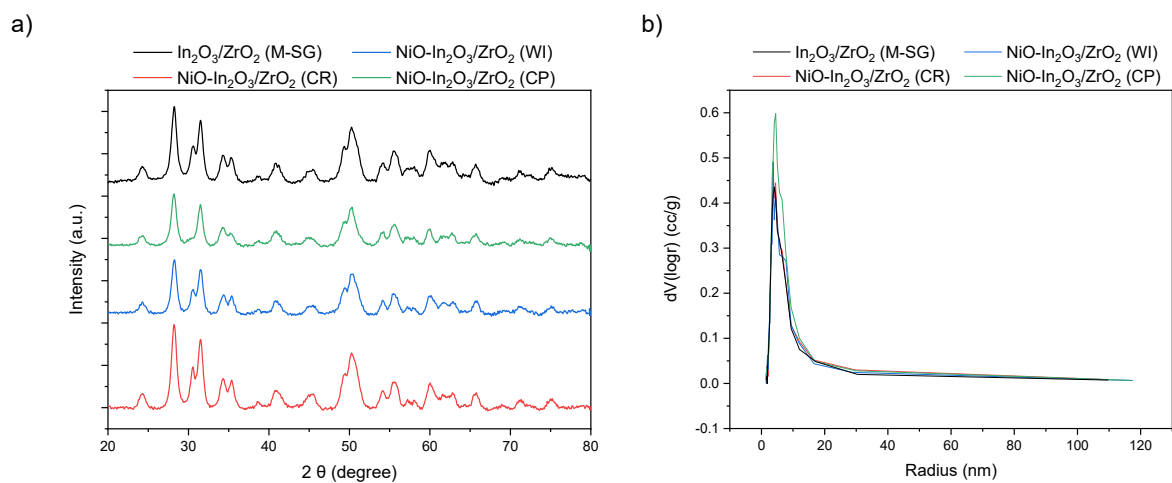


Figure S11. Analysis of NiO-In₂O₃/ZrO₂ prepared by WI, CR or CP compared with In₂O₃/ZrO₂ (M-SG): a) XRD pattern, b) pore size distribution (determined with BJH method).

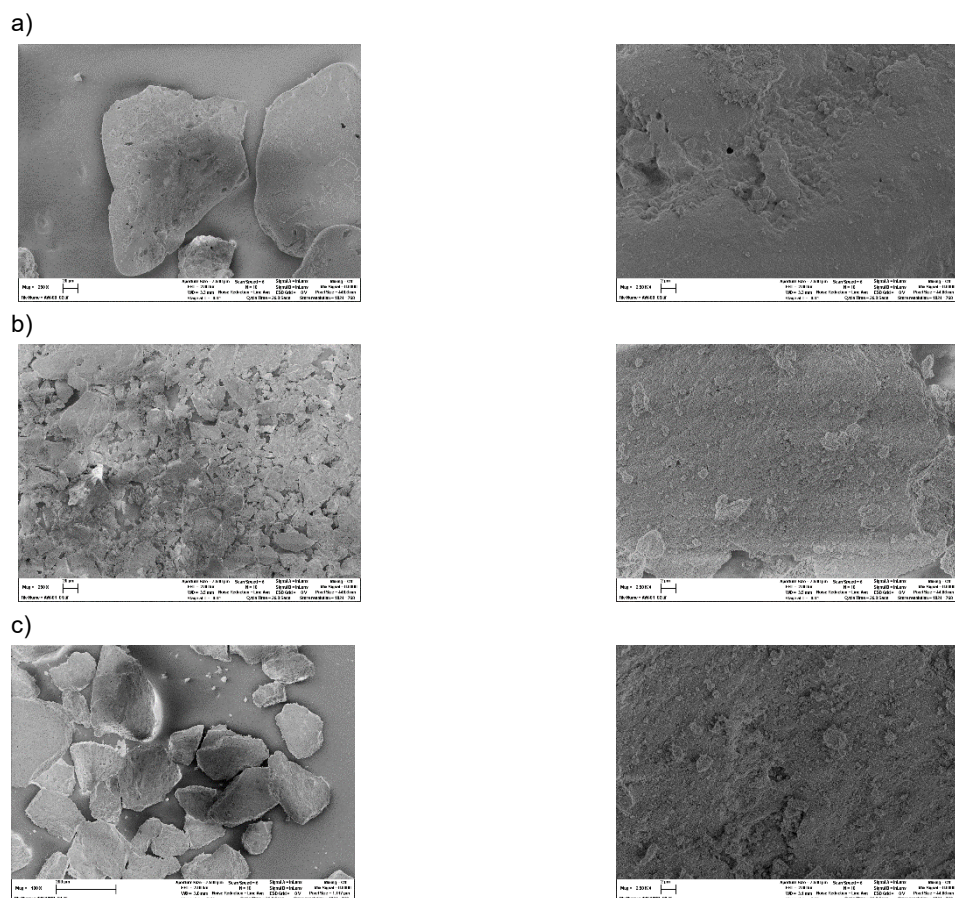


Figure S12. Backscattered electron analysis (left) and secondary electron analysis (right). SEM images of a) Ni-In₂O₃/ZrO₂ (WI), b) Ni-In₂O₃/ZrO₂ (CR) and c) Ni-In₂O₃/ZrO₂ (CP).

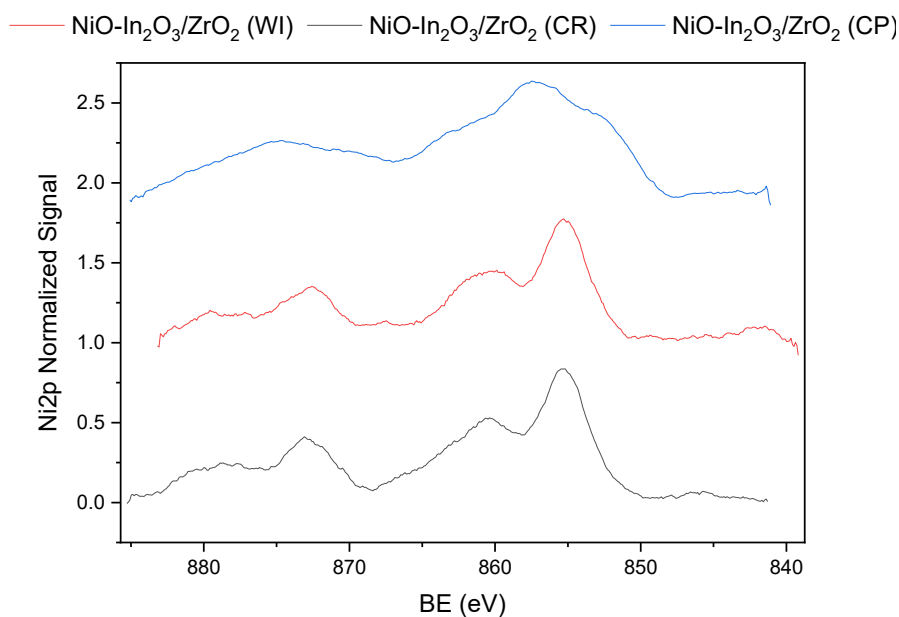


Figure S13. XPS spectra of Ni2p for Ni-In₂O₃/ZrO₂ prepared by WI, CP and CR.

Table S7. Integral data of CO₂-TPD. Low (50 °C - 350 °C), high (350 °C - 650 °C) and overall area of NiO-In₂O₃/ZrO₂ prepared by Wi, CR and CP with In₂O₃/ZrO₂ (M-SG) as normed reference (1.00).

	nominal area of adsorption capacity		overall
	low	high	
NiO-In ₂ O ₃ /ZrO ₂ (WI)	1.64	1.71	1.69
NiO-In ₂ O ₃ /ZrO ₂ (CR)	1.47	0.58	0.87
NiO-In ₂ O ₃ /ZrO ₂ (CP)	1.70	0.53	0.91
In ₂ O ₃ /ZrO ₂ (M-SG)	1.00	1.00	1.00

Table S8. H₂ TPR integral data for low (110 °C - 420 °C), high (420 °C - 840 °C) and overall area of NiO-In₂O₃/ZrO₂ prepared by Wi, CR and CP with In₂O₃/ZrO₂ (M-SG) as normed reference (1.00).

	nominal area of adsorption capacity		overall
	low	high	
NiO-In ₂ O ₃ /ZrO ₂ (WI)	1.05	1.25	1.19
NiO-In ₂ O ₃ /ZrO ₂ (CR)	0.75	0.70	0.72
NiO-In ₂ O ₃ /ZrO ₂ (CP)	1.05	1.25	1.19
In ₂ O ₃ /ZrO ₂ (M-SG)	1.00	1.00	1.00

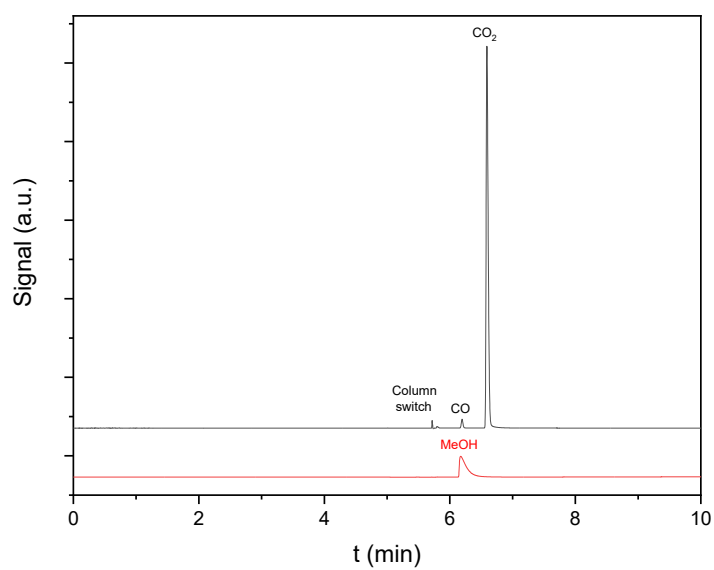


Figure S14. FID chromatogram for NiO-In₂O₃/ZrO₂ (WI): Valve switch-, CO-, CO₂- and MeOH peak. Reaction conditions: CO₂/H₂ = 1/3; GHSV = 4600 h⁻¹; T = 300 °C; p = 7.5 MPa; h_{bed} = 5.1 ± 0.1 cm.

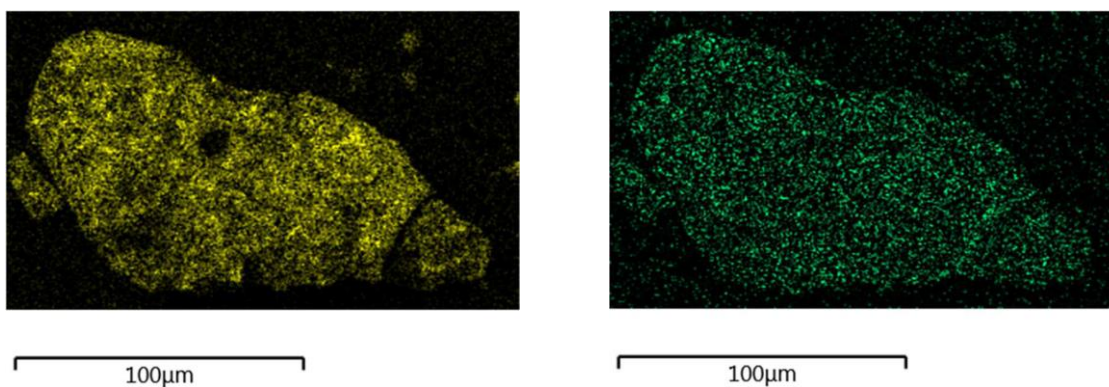


Figure S15. SEM-EDX elemental mapping images of Ni-In₂O₃/ZrO₂(WI) after 100 h TOS. In distribution left (yellow); Ni distribution right (green).

9.5 Supporting Information of 3rd publication (available online)

Supporting Information for

Spatially resolved reaction profiles of CO₂ hydrogenation to methanol using In-based catalysts in a compact profile reactor

Philipp Kampe^{a,1}, Nick Herrmann^{a,1}, Charlotte Ruhmlieb^b, Maik Finsel^c, Oliver Korup^c Raimund Horn^d and Jakob Albert^{a*}

^a Institute of Technical and Macromolecular Chemistry, Universität Hamburg, Bundesstraße 45, 20146 Hamburg, Germany

^b Institute of Physical Chemistry, Universität Hamburg, Grindelallee 117, 20146 Hamburg, Germany

^cReacnostics GmbH, Am Kaiserkai 30, 20457 Hamburg, Germany

^dInstitute for Chemical Reaction Engineering, Hamburg University of Technology, Am Schwarzenberg-Campus 1, 21073 Hamburg

¹These authors contributed equally to this work and therefore share first authorship.

* E-Mail: jakob.albert@uni-hamburg.de

This document contains 3 Tables and 8 Figures on 9 pages.

Process flow diagram

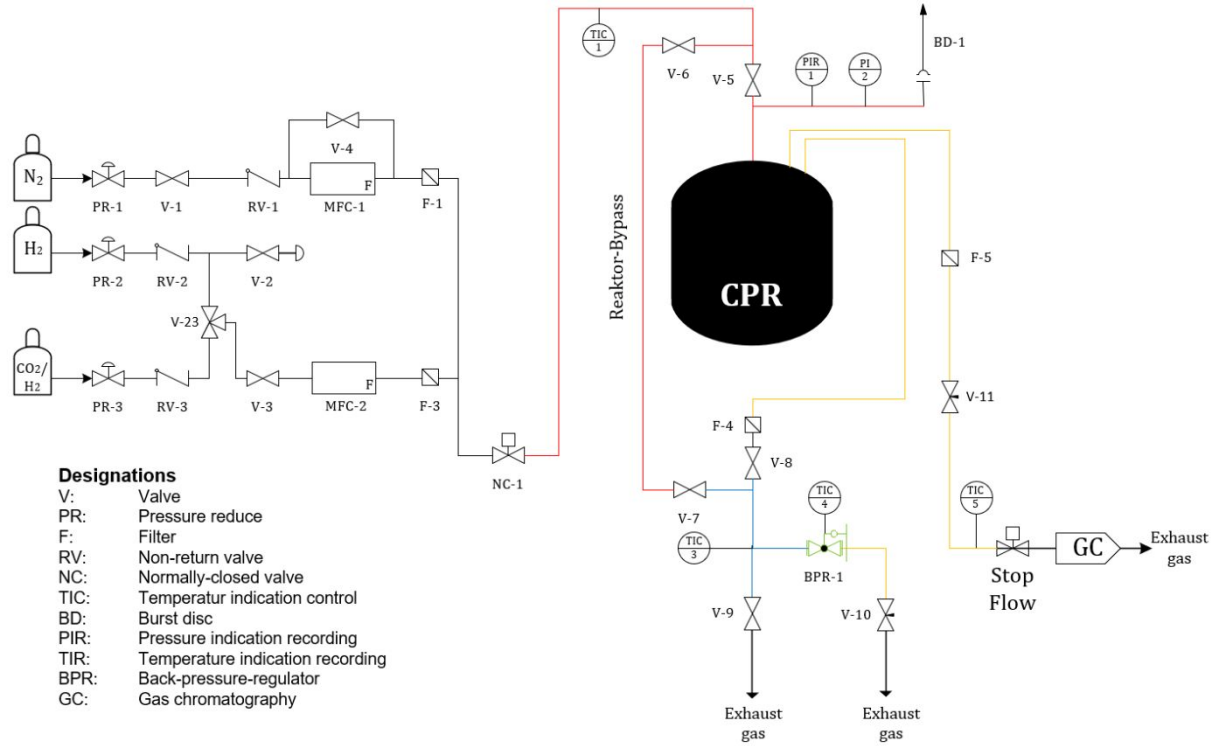


Figure S 1. Instrumentation and piping diagram of the high-pressure compact profile reactor setup.

Supporting Calculations

The molar flow of component i was calculated (S1) using the adjusted standard volume flow (\dot{V}_N), standard pressure p_N , standard Temperature T_N and known feed gas ($x_{i,in}$) composition assuming the ideal gas law.

$$\dot{n}_{i,in} = \frac{p_N \cdot x_{i,in} \cdot \dot{V}_N}{R \cdot T_N} \quad (S1)$$

Regarding the carbon balance of the reaction system, the total molar flow at the reactor outlet $\dot{n}_{ges,out}$ can be ascertained by utilizing the molar fractions of CO_2 , CO , and MeOH (S2), which are determined through online gas chromatograph analysis.

$$\dot{n}_{ges,out} = \frac{\dot{n}_{\text{CO}_2,in}}{x_{\text{CO}_2,out} + x_{\text{CO},out} + x_{\text{MeOH},out}} \quad (S2)$$

The component molar flow $\dot{n}_{i,out}$ at the reactor outlet was calculated as follows.

$$\dot{n}_{i,out} = \dot{n}_{ges,out} \cdot x_{i,out} \quad (S3)$$

With the molar flow of component i and the catalyst mass the reaction rate r was calculated according (S4):

$$r_i = \frac{\dot{n}_{i,in} - \dot{n}_{i,out}}{m_{cat}} \quad (S4)$$

The average particle size of the pure and metal doped In₂O₃ catalysts are estimated by the Scherrer equation from the (611) reflex:

$$d = \frac{\lambda k}{\beta \cos \theta} \quad (\text{S5})$$

where λ is the wavelength of the X-ray, k is the shape factor (0.89), β is the full width at half maximum (FWHM) of the reflection and θ is the Bragg angle.¹

Mass-transfer limitation criteria

The Carberry number, Ca, is used to estimate the external mass transfer limitation. Ca < 0.05 indicates that the diffusion resistance by external mass transfer may be neglected. The Ca number is defined with the following equation²:

$$\text{Ca} = \frac{r_{\text{obs}}}{a k_r c_b} < \frac{0.05}{|\ln|} \quad (\text{S6})$$

The specific external surface of the spherical catalyst particle is calculated with the particle diameter d_p :

$$a = \frac{6}{d_p} \quad (\text{S7})$$

The mass transfer coefficient (k_f) was calculated using the correlation by Dwivedi for packed beds³, where the Sherwood number Sh requires the bed porosity ε_{bed} , the Reynolds (Re) and Schmidt (Sc) number:

$$k_f = Sh \frac{D}{d_p} \quad (\text{S8})$$

$$Sh = \frac{1}{\varepsilon_{\text{bed}}} \cdot 0.453 \cdot Re^{1.453} \cdot Sc^{0.333} \quad (\text{S9})$$

$$Re = \frac{\rho_{CO_2,H_2} u d_p}{\mu_{CO_2,H_2}} \quad (\text{S10})$$

$$Sc = \frac{\mu_{CO_2,H_2}}{\rho_{CO_2,H_2} D} \quad (\text{S11})$$

The density of the gas mixture ρ_{CO_2,H_2} was determined via Aspen Plus V12 using Soave-Redlich-Kwong (SRK) equation of state.⁴ According to the Wilke method⁵ (Eq. S12) the gas viscosity μ_{CO_2,H_2} was estimated:

$$\mu_{CO_2,H_2} = \sum_{i=1}^N \left(\frac{\mu_i y_i}{\sum_{j=1}^N y_j \phi_{ij}} \right) \quad (\text{S12})$$

$$\phi_{ij} = \frac{\left[1 + \left(\mu_i / \mu_j \right)^{1/2} + \left(M_i / M_j \right)^{1/4} \right]^2}{\left[8 \left(1 + M_i / M_j \right) \right]^{1/2}} \quad (\text{S13})$$

$M_{i,j}$ and $\mu_{i,j}$ are the molar mass and viscosity of each species. The pure component viscosity is calculated as follows using the parameters.⁶

$$\mu_{i,j} = \frac{C_1 T^{C_2}}{1 + \frac{C_3}{T} + \frac{C_4}{T^2}} \quad (\text{S14})$$

Table S 1. Parameters for the viscosity of pure species and their diffusion volume ⁷.

Species	M _i (g mol ⁻¹)	C ₁	C ₂	C ₃	C ₄	v _{ci}
CO ₂	44.01	2.148·10 ⁻⁶	0.46	290	0	26.9
H ₂	2.016	1.797·10 ⁻⁷	0.685	-0.59	0	7.07

The molecular diffusions coefficient D, where v_{ci} is the viscosity of pure species, is calculated as follows ⁸:

$$D_{CO2,H2} = \frac{10^{-7}T^{3/2}\sqrt{1/M_i+1/M_j}}{P(v_{ci}^{3/2}+v_{cj}^{3/2})} \quad (S15)$$

Synthesis and Characterization of metal- promoted In₂O₃/ZrO₂ catalysts

Wetness impregnated In₂O₃/ZrO₂ based catalysts with the desired elemental composition of 10 wt% indium and eventually 1 wt% promotor were successfully prepared according to the protocol described in the catalyst synthesis section. The specific surface areas (BET) of the synthesized catalysts are comparable to previous literature and experiments ⁹⁻¹¹. The state-of-the-art Cu/ZnO/Al₂O₃ catalyst has a slightly higher BET surface area, but a significant smaller pore radius. The combined results can be seen in Table S2. For all experiments sieve fractions between 80-250 μm were used.

Table S 2. Textural properties of In₂O₃/ZrO₂ based catalysts and the commercial Cu/ZnO/Al₂O₃ catalyst.

	In (wt.%) ^a	Zr (wt.%) ^a	Cu/Ni/Ce (wt.%) ^a	S _{BET} (m ² /g) ^b	∅ pore radius (nm) ^b	pore volume (cm ³ /g) ^b	∅ In ₂ O ₃ crystallite size (nm) ^c
Cu/ZnO/Al ₂ O ₃	-	-	43.1	99	2.53	0.206	-
In ₂ O ₃ /ZrO ₂	10.05	60.90	-	74	3.40	0.224	8.56
Ni-In ₂ O ₃ /ZrO ₂	10.48	63.85	0.76	81	3.70	0.216	8.56
Cu-In ₂ O ₃ /ZrO ₂	10.45	62.25	0.95	72	4.07	0.218	8.56
Ce-In ₂ O ₃ /ZrO ₂	10.40	61.83	0.91	77	3.40	0.207	8.56

^a Determined by ICP-OES, deviation ± 10 %. ^b Measured by N₂-physisorption at 77 K, deviation ± 5 %. ^c Determined using the Scherrer equation and the corresponding (611) reflections of In₂O₃ in the XRD.

Powder X-ray diffraction (XRD) revealed a similar structure for the synthesized catalysts. The In₂O₃/ZrO₂ catalyst employed as a precursor for the metal promoted catalyst showed reflections for c-In₂O₃ and m-ZrO₂. For c-In₂O₃, the (h00) reflections (200), (400), (600), and (800) are present, as well as (222), (521), and (611). The FWHM of the (611) reflection was used to determine the average size of the single-crystalline domains since most of the other reflections partly overlapped with the signals of m-ZnO₂ (e.g. with (020) or (022)). Using Scherrer's equation, we calculated a mean single-crystal size of 8.6 nm for all In-based catalysts.¹ The most intense reflections in the XRD patterns are the (111) and (-111) reflections of m-ZnO₂ (Figure S2). From the (111) reflection a mean size of 11.3 nm can be calculated for the single-crystalline domains of ZrO₂. The In₂O₃/ZrO₂ catalyst precursor such as the method of synthesis does not affect their structure. The XRD for the catalysts with a metal promotor (Ni, Cu, Ce) were not much different from the original indium catalyst. No reflections of the corresponding promotor could be observed whereby a similar overall structure can be concluded (Figure S2). The SEM-EDX images show a uniform dispersion of indium and all promotors (Figure S3).

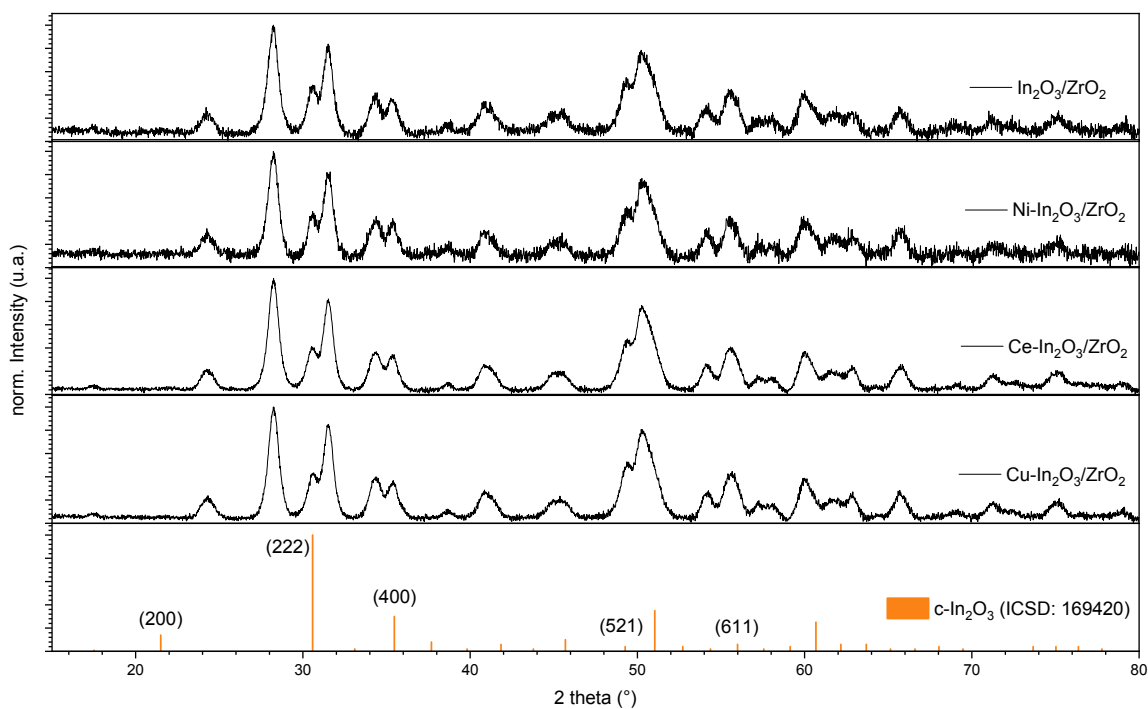


Figure S 2. XRD patterns for the $\text{In}_2\text{O}_3/\text{ZrO}_2$ and metal promoted catalysts. Expected locations of the $\text{c-In}_2\text{O}_3$ (ICSD: 169420) are shown at the bottom.

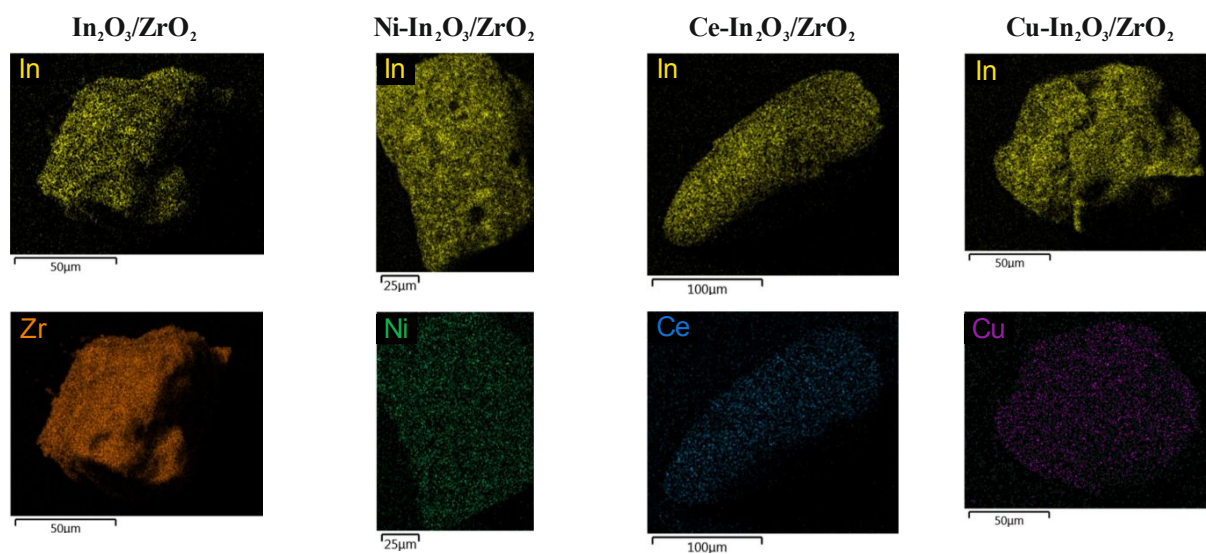


Figure S 3. SEM-EDX elemental mapping of $\text{In}_2\text{O}_3/\text{ZrO}_2$ based catalysts. Top: In distribution (yellow). Bottom: exemplary Zr distribution (orange) and metal promoter distribution (green (Ni) / blue (Ce) / purple (Cu)).

(611) reflection patterns of $\text{In}_2\text{O}_3/\text{ZrO}_2$ based catalysts

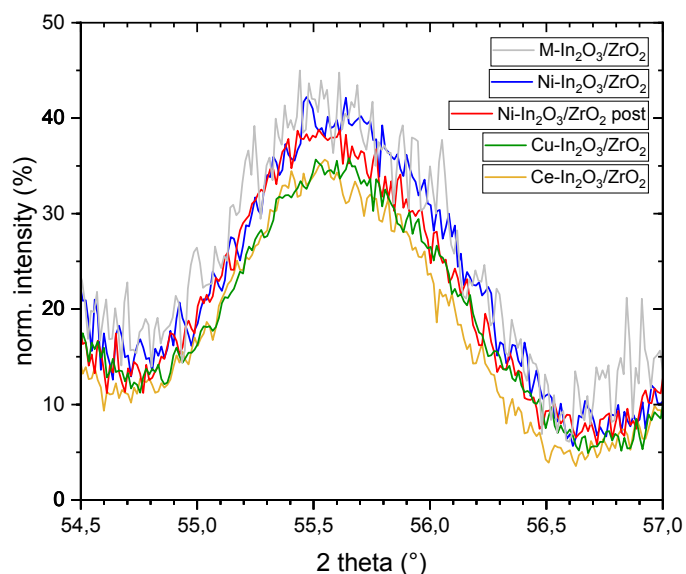


Figure S 4. Width of the (611) reflection used for the Scherrer evaluation of the $\text{In}_2\text{O}_3/\text{ZrO}_2$ based catalysts and for Ni- $\text{In}_2\text{O}_3/\text{ZrO}_2$ after 90 h time-on-stream.

Integration of H_2 TPR and CO_2 TPD curves

To better compare the metal promoted catalyst with the $\text{In}_2\text{O}_3/\text{ZrO}_2$ catalysts, the integral of the H_2 reduction curve and CO_2 desorption curve were calculated between 100 and 600 °C. The areas below the curves are proportional to the H_2 and CO_2 uptake. To obtain the nominal value, the areas for the $\text{In}_2\text{O}_3/\text{ZrO}_2$ catalysts were set to 1.00 and the areas of the metal promoted catalyst calculated accordingly. Table S3 provides the area for the integration of all measurements.

Table S 3: Calculated area for the H_2 TPR and CO_2 TPD and the calculated nominal reduction and adsorption capacity.

Catalyst	Area H_2 reduction (100-600 °C)	Area CO_2 reduction (100-600 °C)	Nominal H_2 reduction capacity	Nominal CO_2 adsorption capacity
$\text{In}_2\text{O}_3/\text{ZrO}_2$	13231.35	3963.26	1.00	1.00
Ce- $\text{In}_2\text{O}_3/\text{ZrO}_2$	16977.65	5008.24	1.28	1.26
Cu- $\text{In}_2\text{O}_3/\text{ZrO}_2$	20118.01	2775.01	1.52	0.70
Ni- $\text{In}_2\text{O}_3/\text{ZrO}_2$	18527.23	6169.30	1.40	1.56

Results and temperature gradient of other Ce- and Cu-promoted $\text{In}_2\text{O}_3/\text{ZrO}_2$ catalysts

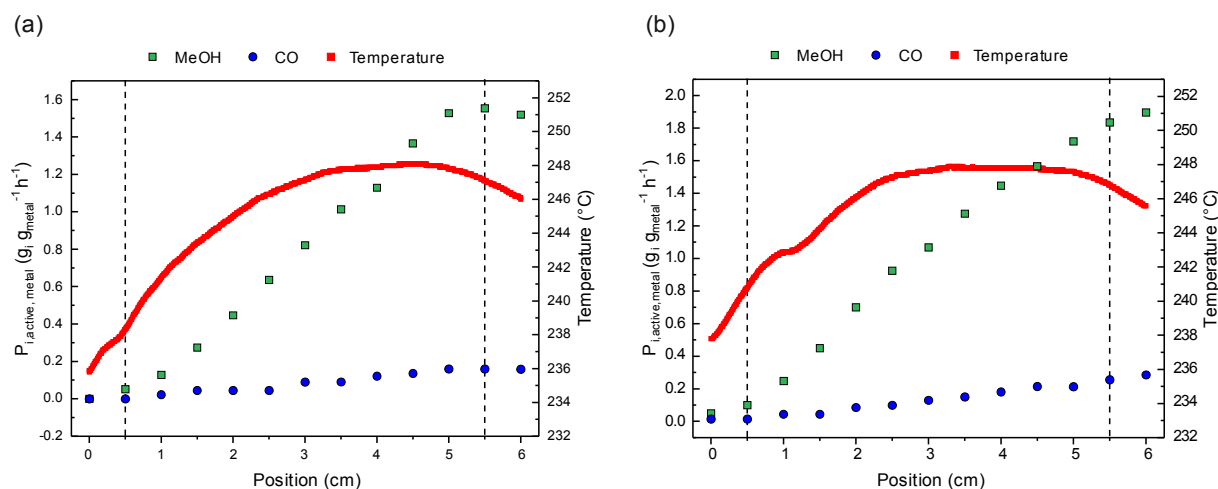


Figure S 5. Spatially resolved temperature and active productivity profile at $T = 250^\circ\text{C}$, $p = 50$ bar, GHSV = 63,000 h⁻¹ and feed gas composition of $\text{CO}_2/\text{H}_2 = 1/3$. The measurements were taken between 5 h and 35 h TOS. a) Ce-In₂O₃/ZrO₂ and b) Cu-In₂O₃/ZrO₂ of MeOH (green) and CO (blue), temperature profile (red).

Supporting temperature profile at different GHSVs

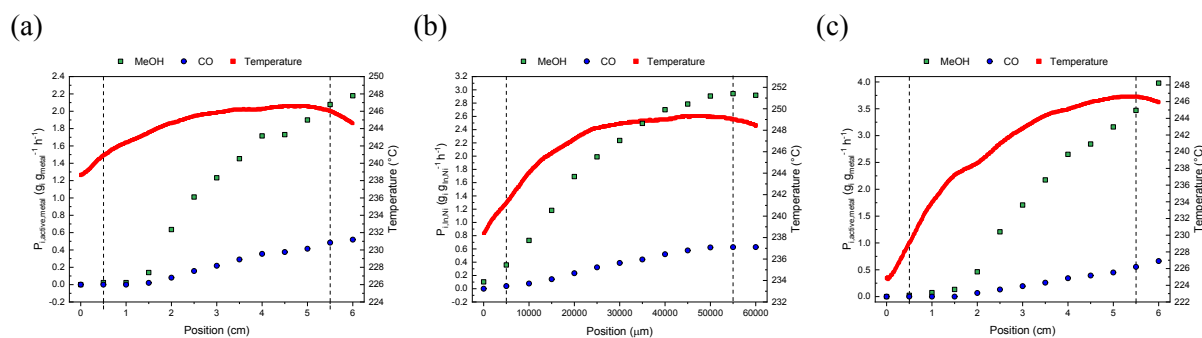


Figure S 6. Spatially resolved temperature and active productivity profile for Ni-In₂O₃/ZrO₂ at $T = 250^\circ\text{C}$, $p = 50$ bar at different GHSV (a) 32,000 h⁻¹ (b) 63,000 h⁻¹ (c) 95,000 h⁻¹. The measurements were taken between 5 h and 35 h TOS.

Supporting Post-mortem characterization of the Ni-doped catalyst

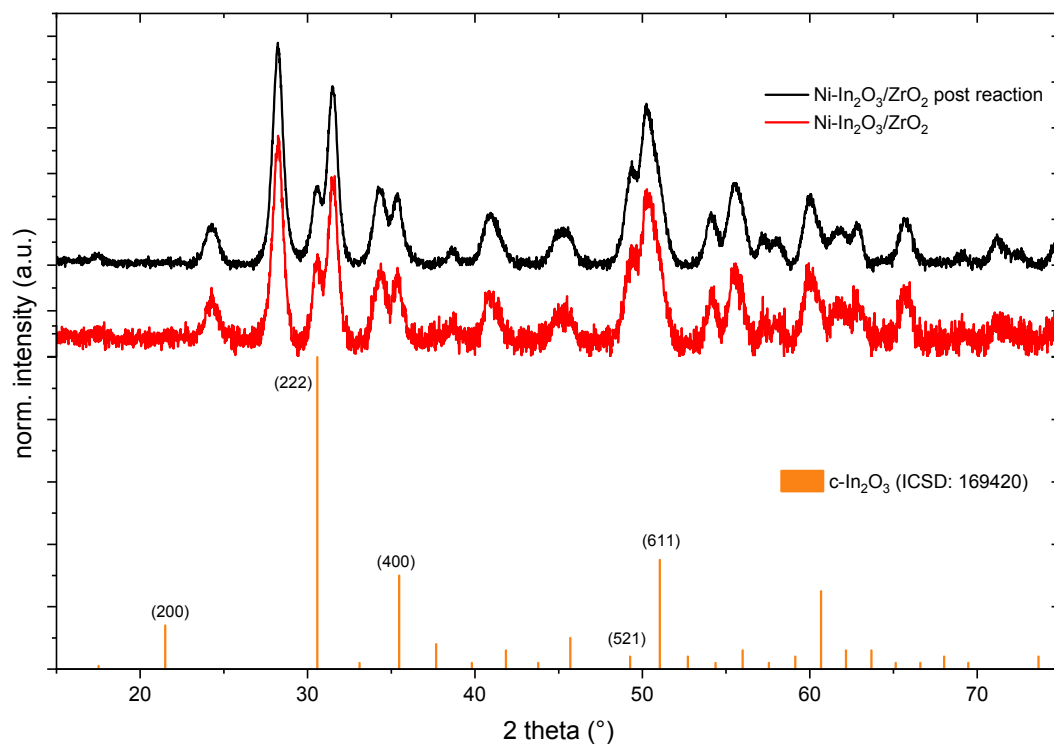


Figure S 7. XRD patterns of the Ni-In₂O₃/ZrO₂ catalyst before (red) and after 90 h time-on-stream (black). Expected locations of the c-In₂O₃ (ICSD: 169420) are shown at the bottom.

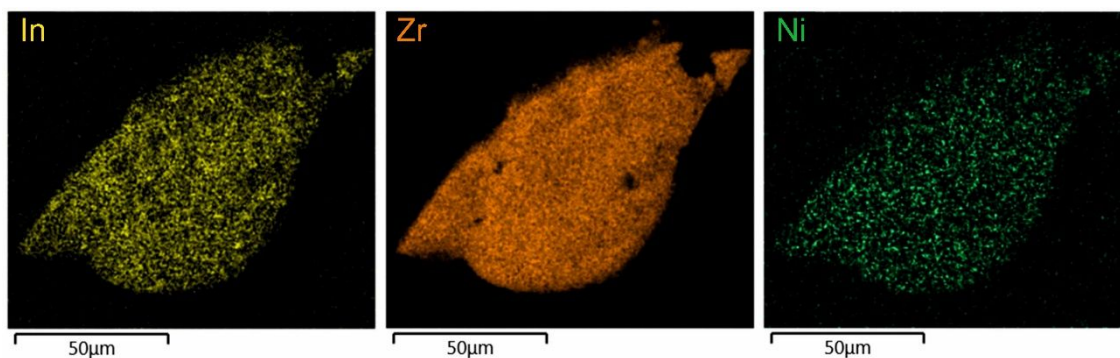


Figure S 8. SEM-EDX mapping analysis of indium (yellow), zircon (orange) and nickel (green) after 90 h time-on-stream.

References

- (1) Monshi, A.; Foroughi, M. R.; Monshi, M. R. Modified Scherrer Equation to Estimate More Accurately Nano-Crystallite Size Using XRD. *WJNSE* **2012**, *02*, 154–160.
- (2) Peng, Z.; Liu, X.; Li, S.; Li, Z.; Li, B.; Liu, Z.; Liu, S. Heterophase-structured nanocrystals as superior supports for Ru-based catalysts in selective hydrogenation of benzene. *Scientific reports* **2017**, *7*, 39847.
- (3) P. N. Dwivedi, S. N. Upadhyay. Particle-Fluid Mass Transfer in Fixed and Fluidized Beds.

- (4) G. Soave. Equilibrium constants from a modified Redlich-Kwong equation of state. *Chemical Engineering Science* **1972**, 1197–1203.
- (5) B. E. Poling, J. M. Prausnitz, J. P. O'Connell, Ed. *The Properties of Gases and Liquids*, Fifth Edition; McGraw-Hill Education: New York, 2001.
- (6) D. Friend, B. Poling, G. Thomson, T. Daubert and E. Buck, Ed. *Perry's Chemical Engineers' Handbook: Physical and chemical data*; McGraw-Hill: New York, 2007.
- (7) Poto, S.; van Vico Berkel, D.; Gallucci, F.; Fernanda Neira d'Angelo, M. Kinetic modelling of the methanol synthesis from CO₂ and H₂ over a CuO/CeO₂/ZrO₂ catalyst: The role of CO₂ and CO hydrogenation. *Chemical Engineering Journal* **2022**, *435*, 134946.
- (8) Falco, M. de; Capocelli, M.; Basile, A. Selective membrane application for the industrial one-step DME production process fed by CO₂ rich streams: Modeling and simulation. *International Journal of Hydrogen Energy* **2017**, *42*, 6771–6786.
- (9) Martin, O.; Martín, A. J.; Mondelli, C.; Mitchell, S.; Segawa, T. F.; Hauert, R.; Drouilly, C.; Curulla-Ferré, D.; Pérez-Ramírez, J. Indium Oxide as a Superior Catalyst for Methanol Synthesis by CO₂ Hydrogenation. *Angewandte Chemie (International ed. in English)* **2016**, *55*, 6261–6265.
- (10) Kampe, P.; Herrmann, N.; Wesner, A.; Ruhmlieb, C.; Albert, J. Catalyst and Parameter Optimization Study for Slurry-Phase Methanol Synthesis Using Ni-Doped Indium-Based Catalysts. *ACS Sustainable Chem. Eng.* **2023**, *11*, 14633–14644.
- (11) Frei, M. S.; Mondelli, C.; Cesarini, A.; Krumeich, F.; Hauert, R.; Stewart, J. A.; Curulla Ferré, D.; Pérez-Ramírez, J. Role of Zirconia in Indium Oxide-Catalyzed CO₂ Hydrogenation to Methanol. *ACS Catal.* **2020**, *10*, 1133–1145.

9.6 Supporting Information of 4th publication (available online)

Supporting Information for

Catalyst and parameter optimization study for slurry phase methanol synthesis using Ni-doped indium-based catalysts

Philipp Kampe^a, Nick Herrmann^a, Anne Wesner^a, Charlotte Ruhmlieb^b and Jakob Albert^{a*}

^a Institute of Technical and Macromolecular Chemistry, Universität Hamburg, Bundesstraße 45, 20146 Hamburg, Germany

^b Institute of Physical Chemistry, Universität Hamburg, Grindelallee 117, 20146 Hamburg, Germany

* E-Mail: jakob.albert@uni-hamburg.de

This document contains 5 Tables and 15 Figures on 15 pages.

Calculations

The error bars are calculated with the following formula:

$$\sigma = \sqrt{\frac{\sum(x-\bar{x})^2}{(z-1)}} \quad (\text{S1})$$

where \bar{x} is the sample average value and the sample size z .

The average particle size of the InOx catalysts are estimated by the Scherrer equation:¹

$$d = \frac{k\lambda}{\beta \cos\theta} \quad (\text{S2})$$

where k is the shape factor (0.89), λ is the wavelength of the X-ray, β is the Full width at half maximum (FWHM) of the reflection and θ is the Bragg angle.

Catalyst preparation according to known literature

F-Ni/In₂O₃-WI was synthesized according to Frei *et al.*² Ni(NO₃)₂·6 H₂O (7.93 g) was dissolved in 50 mL of dest. water. 13.5 g of In₂O₃ were added to the solution and the suspension was stirred for 14 h in a rotary evaporator (111 rpm, room temperature, 800 mbar). Afterwards the temperature was raised to 75 °C to remove the solvent. The residue was then calcinated for 3 h at 350 °C (heating rate = 2 K/min).

J-Ni/In₂O₃-CR was synthesized according to Jia *et al.*³ Ni(NO₃)₃·6 H₂O (5.29 g) was dissolved in 340 mL of dest. water. 9.00 g of In₂O₃ were added to the solution and the suspension further dispersed by ultra-sonication for 30 min. Afterwards the suspension was aged for 1 h at 80 °C. A 0.02 M NaBH₄ solution with 0.01 M NaOH was prepared and added dropwise to the suspension under constant stirring. The reaction mixture was then further aged for 2 h at 80 °C. The suspension was filtered and washed with 3·500 mL of dest. water. The residue was dried at 65°C for 12 h.

F-Ni/In₂O₃-CP was synthesized according to Frei *et al.*⁴ Ni(NO₃)₂·6 H₂O (7.93 g) and In(NO₃)₃·1.8 H₂O (32.4 g) were dissolved in 590 mL of dest. water. The pH of the solution was raised to 9.2 by the dropwise addition of a 1 M Na₂CO₃ solution under stirring. The suspension was aged for 1 h and 590 mL of dest. water was added afterwards. The suspension was filtered and the precipitate washed with dest. water until a pH of 7 for the filtrate was reached. The residue was dried (65°C, 12 h) and calcinated for 3 h at 300 °C (heating rate = 2 K/min).

The reference NiO material was prepared by calcination of Ni(NO₃)₂·6 H₂O (10.0 g) for 3 h at 350 °C (heating rate = 2 K/min).

In₂O₃/ZrO₂ catalysts have been prepared via impregnation according Martin *et al.* (M-In₂O₃-ZrO₂)⁵ or Schühle *et al.* (S-In₂O₃-ZrO₂).⁶ Martin *et al.* dissolved In(NO₃)₃·1.8 H₂O (6.84 g) in 630 mL

of ethanol and 216 mL of dest. water. Then 18 g of granulated ZrO₂ pellets with a particle size of 32-80 µm was added to the solution. The suspension was stirred for 5 h in a rotatory evaporator (111 rpm, room temperature, 800 mbar) to remove the solvent. After the impregnated powder was dried (65°C, 12 h), heated with 5 K/min to 300 °C and calcinated for 3 h. Schühle *et al.* prepared a stock solution due to dissolving 10 g of In(NO₃)₃·1.8 H₂O in 25 mL of dest. water. Then 17.1 g of granulated ZrO₂ pellets with a particle size of 32-80 µm was added to the solution. A rotary evaporator removed the aqueous supernatant followed by drying (65°C, 12 h). The generated powder was heated with 5 K/min to 300 °C and calcinated for 3 h.

Z-InZrO was synthesized according to Zhang *et al.*⁷ ZrO(NO₃)₂ (6.18 g) and In(NO₃)₃·1.8 H₂O (40.1 g) were dissolved in 100 mL of dest. water and heated to 80 °C. A 0.2 M Na₂CO₃ solution was added dropwise to the solution until a pH of 10 was reached. The solution was aged for 3 h at 80 °C and filtered afterwards. The residue was washed with 3·500 mL of dest. water and dried at 80 °C for 12 h and calcinated for 3 h at 300 °C (heating rate = 2 K/min).

Z-Ni-InZrO-CR was synthesized according to Zhang *et al.*⁷ Ni(NO₃)₂·6 H₂O (7.93 g) was dissolved in 200 mL of dest. water and stirred for 1 h at room temperature and heated to 80 °C afterwards. A second solution of NaOH and NaBH₄ in water was prepared. It was prepared to contain three times the molar mass of NaOH and four times the molar mass of NaBH₄ compared to the molar mass of Ni in the first solution. The second solution was added dropwise to the first solution and subsequently aged for 2 h at 80 °C. The resulting suspension was filtered and washed with dest. water until a pH of 7 for the filtrate was reached. The residue was dried at 65°C for 12 h.

Online GC analysis conditions

For each measurement 10 µL of the sample was injected by a sample loop. The valve and the sample loop are held at a constant temperature of 200 °C. First, in the nonpolar RT-Q-Bond column CO₂ and CH₄ were separated from CO. The polar RT-U-Bond column and the BR-Molsieve 5 A improved the peak shape, accuracy with sharp and symmetrical peaks for CO, CO₂ and CH₄. The polar BRSwax optimized the separation between methanol, i-butane and dimethyl ether (see Figure S 1.) The front thermal conductivity detector (TCD) with a temperature of 175 °C detects CO and CO₂. The Methanizer converts CO and CO₂ into CH₄ which is quantified by the middle flame ionization detector (FID, 250 °C). The rear FID with a temperature of 250 °C quantifies methanol. The initial temperature of the column oven was 50 °C. After 5 min the column oven is heated to 115 °C (5 °C min⁻¹).

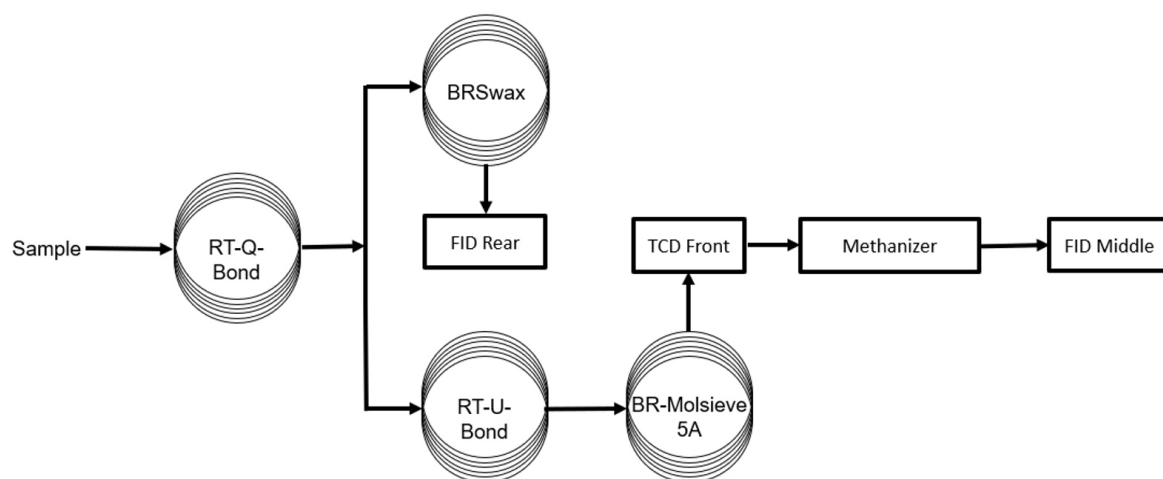


Figure S 1. Schematic setup for the online GC analysis with the four columns, three detectors and one methanizer in between.

List of all catalysts used with elementary composition

Table S 1. Elemental composition of all catalysts used determined by ICP-OES.

Catalyst	Indium content [wt%]	Promotor content [wt%]
F-Ni/In ₂ O ₃ -WI	72.26 %	Ni: 9.51 %
J-Ni/In ₂ O ₃ -CR	65.56 %	Ni: 11.95 %
F-Ni/In ₂ O ₃ -CP	66.85 %	Ni: 9.08
Z-InZrO	69.22 %	-
S-In ₂ O ₃ /ZrO ₂	11.09 %	-
M-In ₂ O ₃ -ZrO ₂	11.08 %	-
In(OH) ₃ /ZrO ₂	7.25 %	-
Z-Ni-InZrO-CR	56.45 %	Ni: 7.67 %
Ni-In ₂ O ₃ /ZrO ₂ -CP	3.55 %	Ni: 0.41 %
Ce-In ₂ O ₃ /ZrO ₂ -CP	8.10 %	Ce: 0.99 %
Mg-In ₂ O ₃ /ZrO ₂ -CP	2.84 %	Mg: 0.26 %
Ni-In ₂ O ₃ /ZrO ₂ -CP	7.44 %	Ni: 0.75 %
Ce-In ₂ O ₃ /ZrO ₂ -CP	7.62 %	Ce: 0.70 %

Blind activity of reactor setup and reference materials

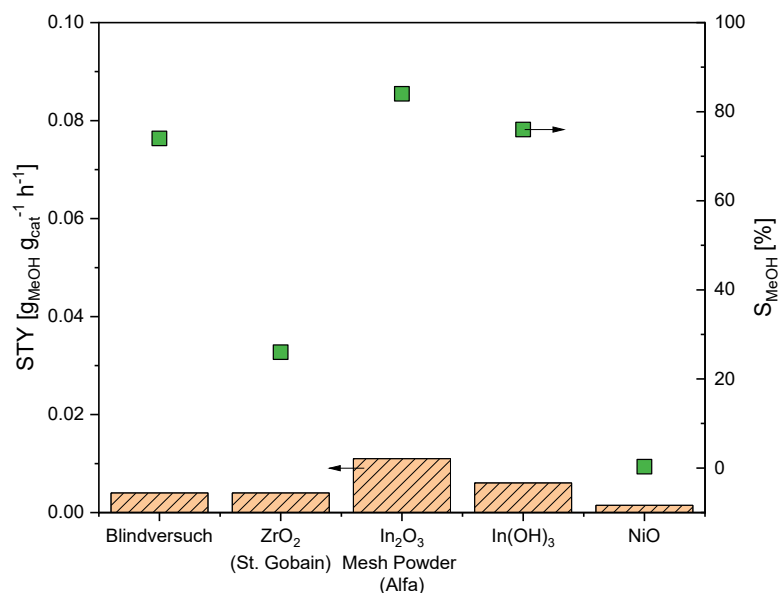


Figure S 2. Blind activity for the empty reactor setup and reference materials. Comparison of STY and selectivity. Reaction conditions: $T = 300\text{ }^{\circ}\text{C}$, $p = 75\text{ bar}$, $\text{H}_2/\text{CO}_2 = 4/1$, $m_{\text{ref}} = 2.0\text{ g}$, $N = 1200\text{ rpm}$, $V_{\text{oil}} = 100\text{ mL}$, $t_{\text{R}} = 3\text{ h}$.

Ni distribution on the In_2O_3 surface with different preparation methods

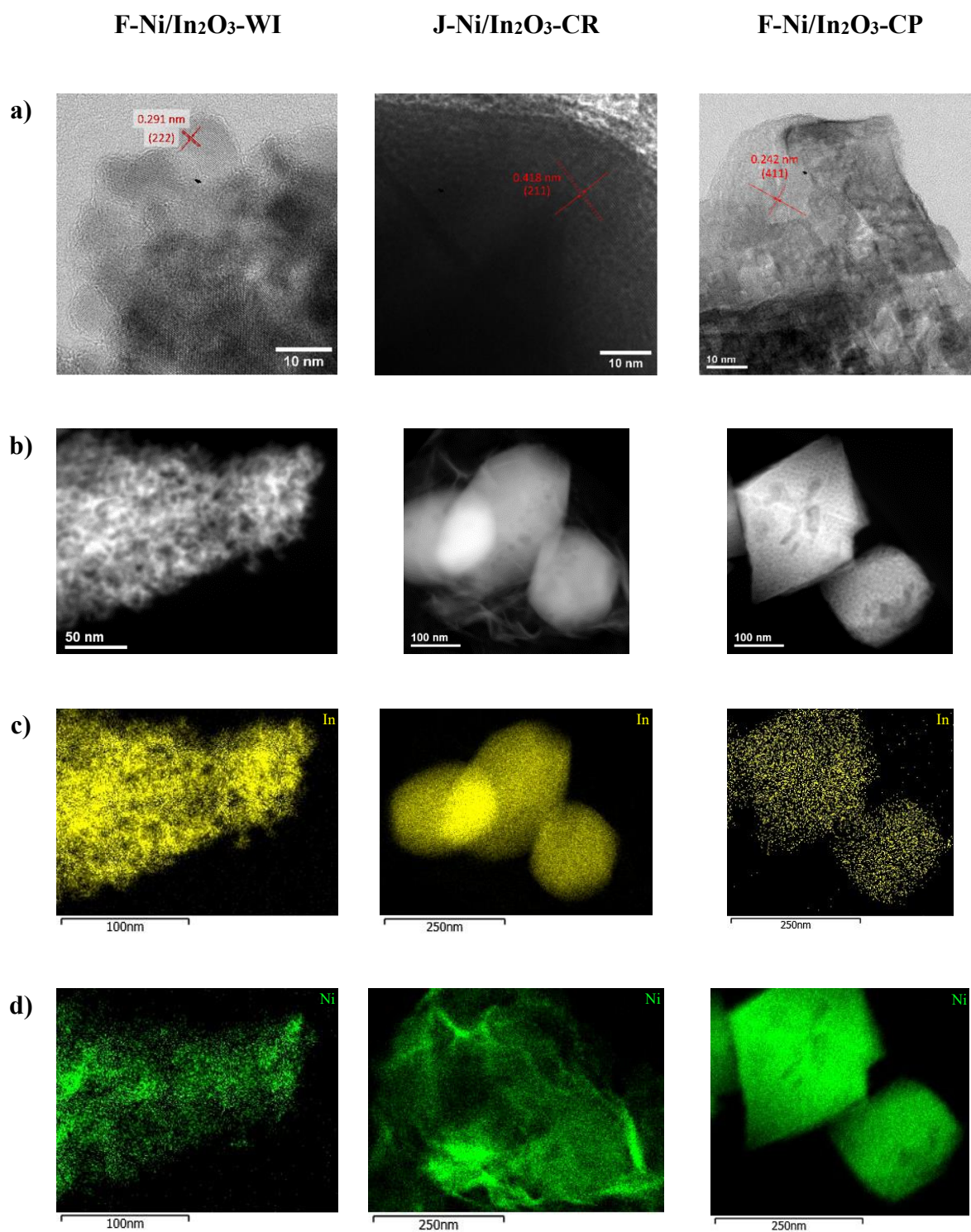


Figure S 3. Morphological and compositional analysis of nickel-doped In_2O_3 catalysts. a) HRTEM images, with d-spacing analysis. b) HAADF-STEM images. STEM-EDX maps of Ni- In_2O_3 catalysts c) Indium and d) Nickel distribution.

Reproduction experiments using the $\text{In}_2\text{O}_3/\text{ZrO}_2$ reference catalyst

Table S 2. Mean value and standard deviation of the reaction parameters yield (Y), selectivity (S), STY and conversion (X) for the reproduction experiments using the $\text{In}_2\text{O}_3/\text{ZrO}_2$ catalyst.

	\bar{x} $\text{In}_2\text{O}_3/\text{ZrO}_2$	σ $\text{In}_2\text{O}_3/\text{ZrO}_2$
$Y_{\text{MeOH, CO}_2}$	7.8 %	0.28 %
$S_{\text{MeOH, CO}_2}$	34 %	1.1 %
STY_t	0.066	0.0025
X_{CO_2}	22.5 %	1.62 %
$Y_{\text{CO, CO}_2}$	14.8 %	1.29 %

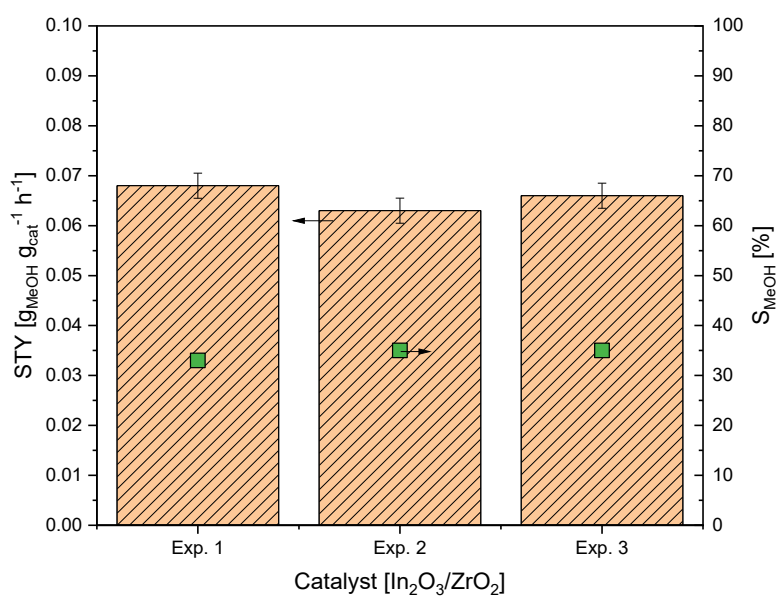


Figure S 4. Comparison of STY and selectivity for three reproduction experiments using a reference $\text{In}_2\text{O}_3/\text{ZrO}_2$ catalyst. Reaction conditions: $T = 300$ °C, $p = 75$ bar, $\text{H}_2/\text{CO}_2 = 4/1$, $m_{\text{ref}} = 2.0$ g, $N = 1200$ rpm, $V_{\text{Oil}} = 100$ mL, $t_{\text{R}} = 3$ h.

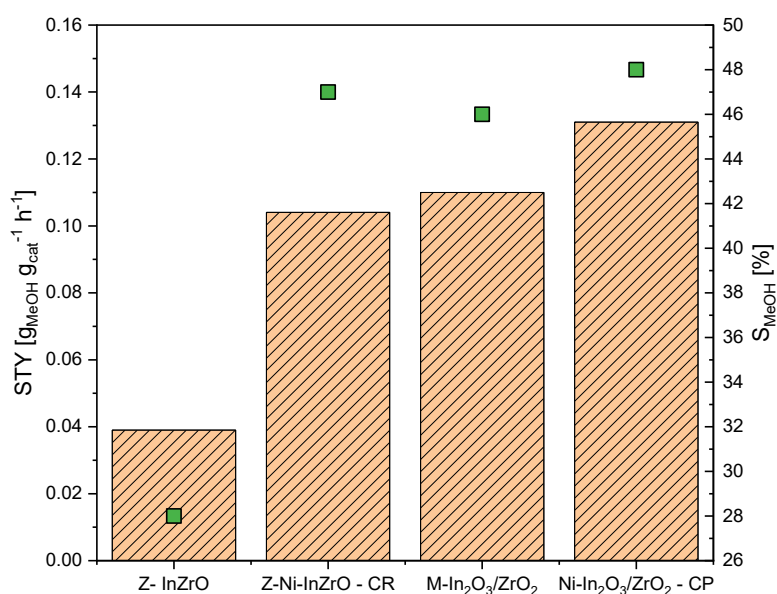


Figure S 5. Influence of nickel doping on the catalytic activity of Z-InZrO and M- $\text{In}_2\text{O}_3/\text{ZrO}_2$. Reaction conditions: $T = 300$ °C, $p = 75$ bar, $\text{H}_2/\text{CO}_2 = 4/1$, $m_{\text{ref}} = 2.0$ g, $N = 1200$ rpm, $V_{\text{Oil}} = 100$ mL, $t_{\text{R}} = 3$ h.

Conditions for the CO₂ TPD and H₂ TPR measurements

Table S 3. Conditions for the CO₂ TPD and H₂ TPR measurements performed with the ChemBET Pulsar by Quantachrome Instruments.

CO ₂ TPD	H ₂ TPR
Change Gas to Helium	Change Gas to Nitrogen
Ramp Temp to 200 °C at 10 °C/min	Ramp Temp to 180 °C at 10 °C/min
Wait until setpoint	Wait until setpoint
Wait for 60 min	Wait for 60 min
Change Gas to Carbon dioxide	Switch Fan On
Wait for 30 min	Ramp Temp to 40 °C in 30 min
Switch Fan On	Wait until setpoint
Ramp Temp to 40 °C in 30 min	Wait for 40 °C min
Wait until setpoint	Switch Fan Off
Wait for 10 min	Change Gas to Hydrogen
Change Gas to Helium	Wait for 10 min
Wait for 30 min	Perform TPR Analysis until completed
Switch Fan Off	Ramp Temp to 850 °C at 10 °C/min
Perform TPD Analysis until completed	Wait until setpoint
Ramp Temp to 700 °C at 10 °C/min	End Analysis
Wait until setpoint	Change Gas to Nitrogen
End Analysis	

CO₂ TPD curves for M- and S-In₂O₃/ZrO₂ catalysts compared to different types of ZrO₂

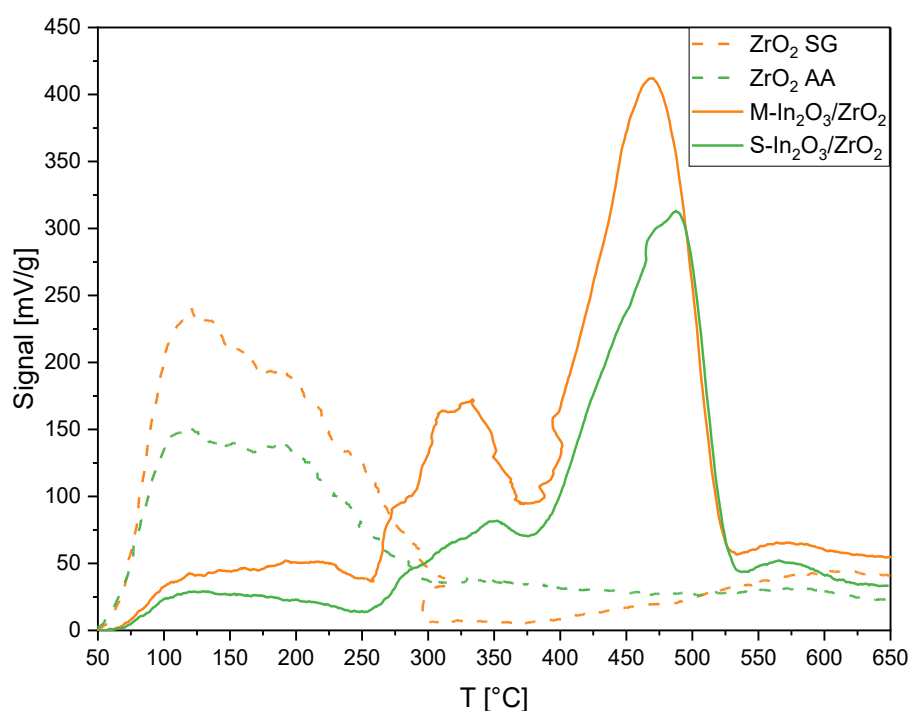


Figure S 6. CO₂ TPD curves for the prepared In₂O₃/ZrO₂ catalyst by Martin et al. and Schühle et al. with the corresponding ZrO₂ from St. Gobain (SG) and Alfa Aesar (AA).

CO₂ TPD curves for Ni- In₂O₃/ZrO₂ and Ce-In₂O₃/ZrO₂

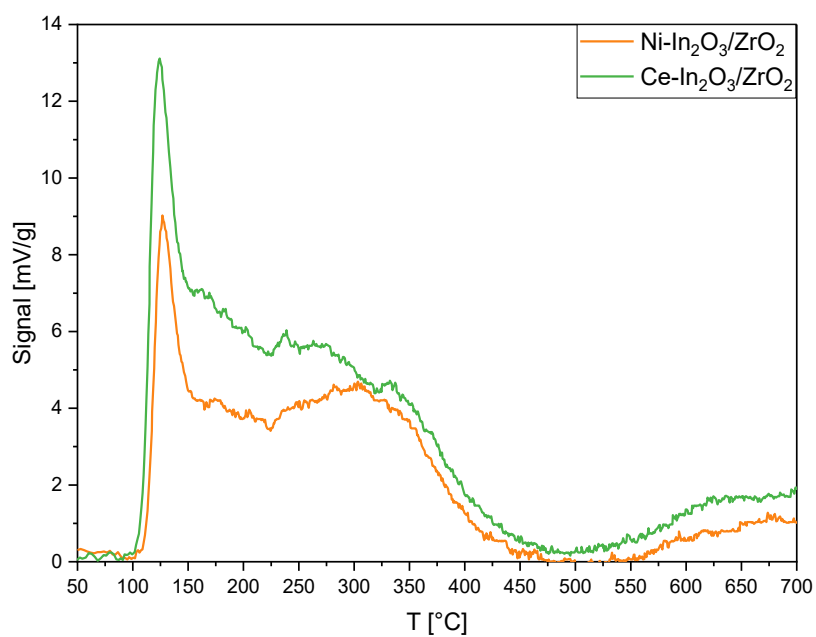


Figure S 7. CO₂ TPD curves for the prepared In₂O₃/ZrO₂ catalyst with nickel and cerium as a promotor.

H₂ TPR curves for various catalysts

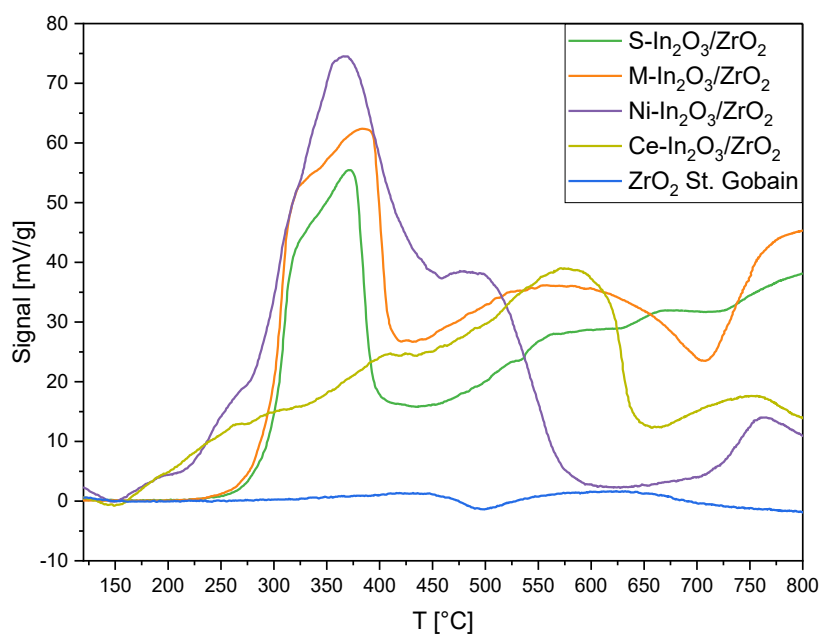


Figure S 8. Comparison of surface reducibility of various catalysts by H₂ TPR.

Batch comparison of Ni-In₂O₃/ZrO₂ catalysts

Table S 4. Metal loading of different batches of Ni-In₂O₃/ZrO₂-CP catalyst determined with ICP-OES.

Catalyst composition	Batch	Abbreviation	Indium content (ICP-OES)	Nickel content (ICP-OES)
Ni-In ₂ O ₃ /ZrO ₂ -CP	1	AW66SB	3,55 %	0,41 %
Ni-In ₂ O ₃ /ZrO ₂ -CP	2	AW69SB	4,74 %	0,51 %
Ni-In ₂ O ₃ /ZrO ₂ -CP	3	AW78NH	7,44 %	0,75 %

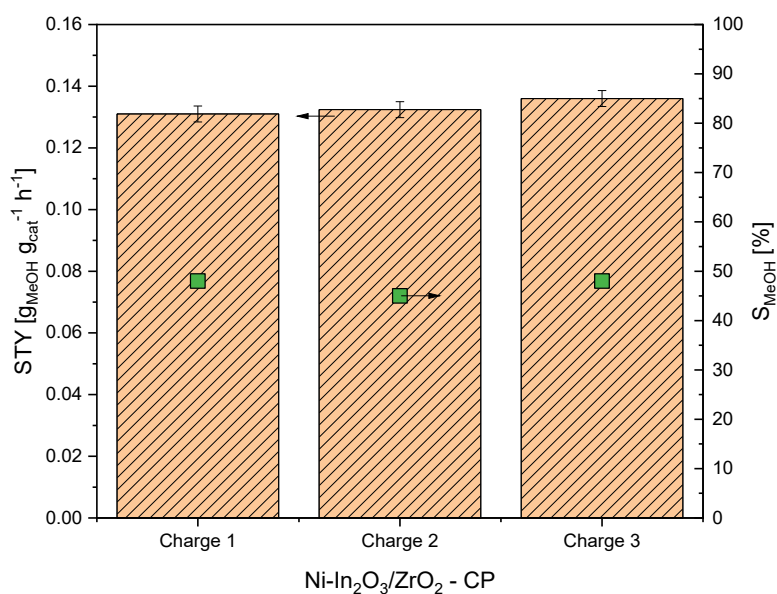


Figure S 9. Comparison of STY and selectivity for the Ni-In₂O₃/ZrO₂-CP catalyst. Reaction conditions: $T = 300\text{ }^{\circ}\text{C}$, $p = 75\text{ bar}$, $\text{H}_2/\text{CO}_2 = 4/1$, $m_{\text{ref}} = 2.0\text{ g}$, $N = 1200\text{ rpm}$, $V_{\text{Oil}} = 100\text{ mL}$, $t_{\text{R}} = 3\text{ h}$.

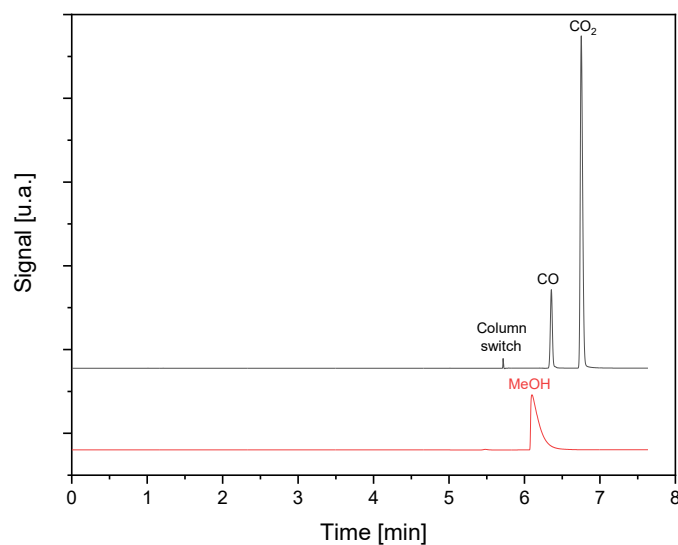


Figure S 10. FID chromatograms for Ni-In₂O₃/ZrO₂ (CP) with assigned peaks.

Post-mortem investigations of catalyst selection for DoE study

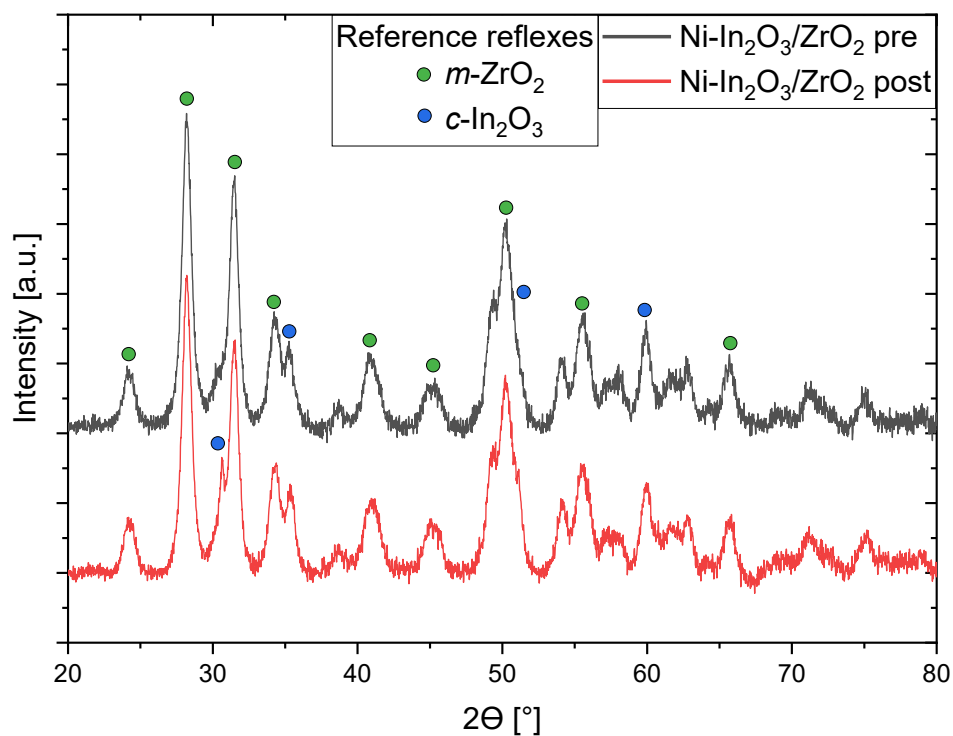


Figure S 11. X-Ray diffractograms of Ni-In₂O₃/ZrO₂-CP catalyst before (pre) and after (post) reaction. The reference reflexes are marked. Reaction conditions: $T = 300\text{ }^{\circ}\text{C}$, $p = 75\text{ bar}$, $\text{H}_2/\text{CO}_2 = 4/1$, $m_{\text{ref}} = 2.0\text{ g}$, $N = 1200\text{ rpm}$, $V_{\text{oil}} = 100\text{ mL}$, $t_R = 3\text{ h}$.

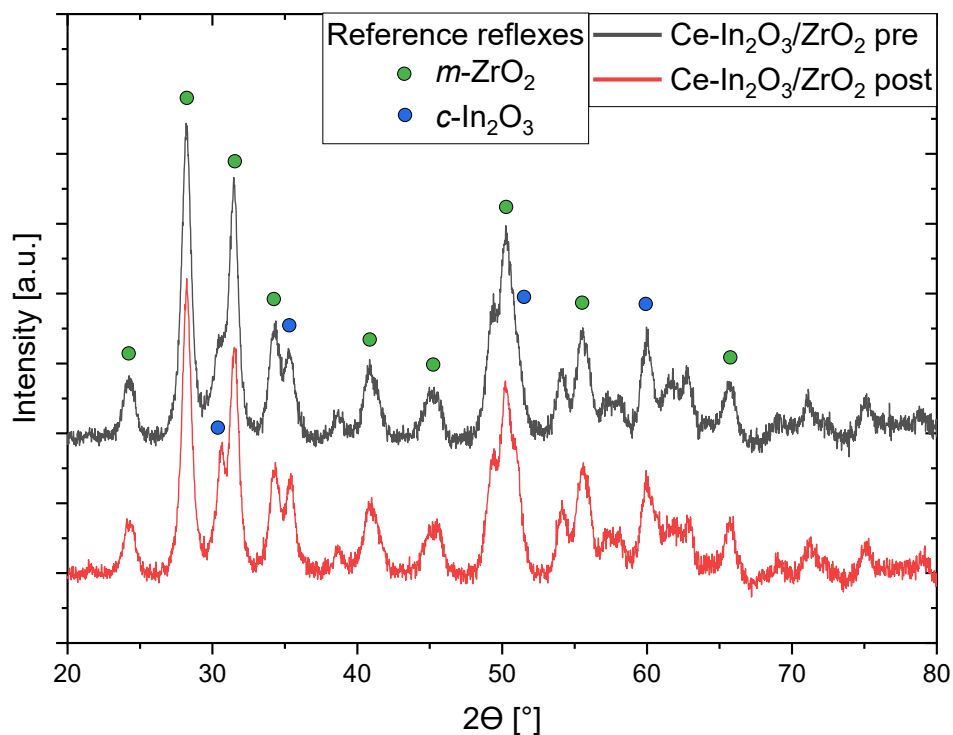


Figure S 12. X-Ray diffractograms of Ce-In₂O₃/ZrO₂-CP catalyst before (pre) and after (post) reaction. The reference reflexes are marked. Reaction conditions: $T = 300\text{ }^{\circ}\text{C}$, $p = 75\text{ bar}$, $\text{H}_2/\text{CO}_2 = 4/1$, $m_{\text{ref}} = 2.0\text{ g}$, $N = 1200\text{ rpm}$, $V_{\text{oil}} = 100\text{ mL}$, $t_R = 3\text{ h}$.

Stability of mineral oil as a carrier liquid

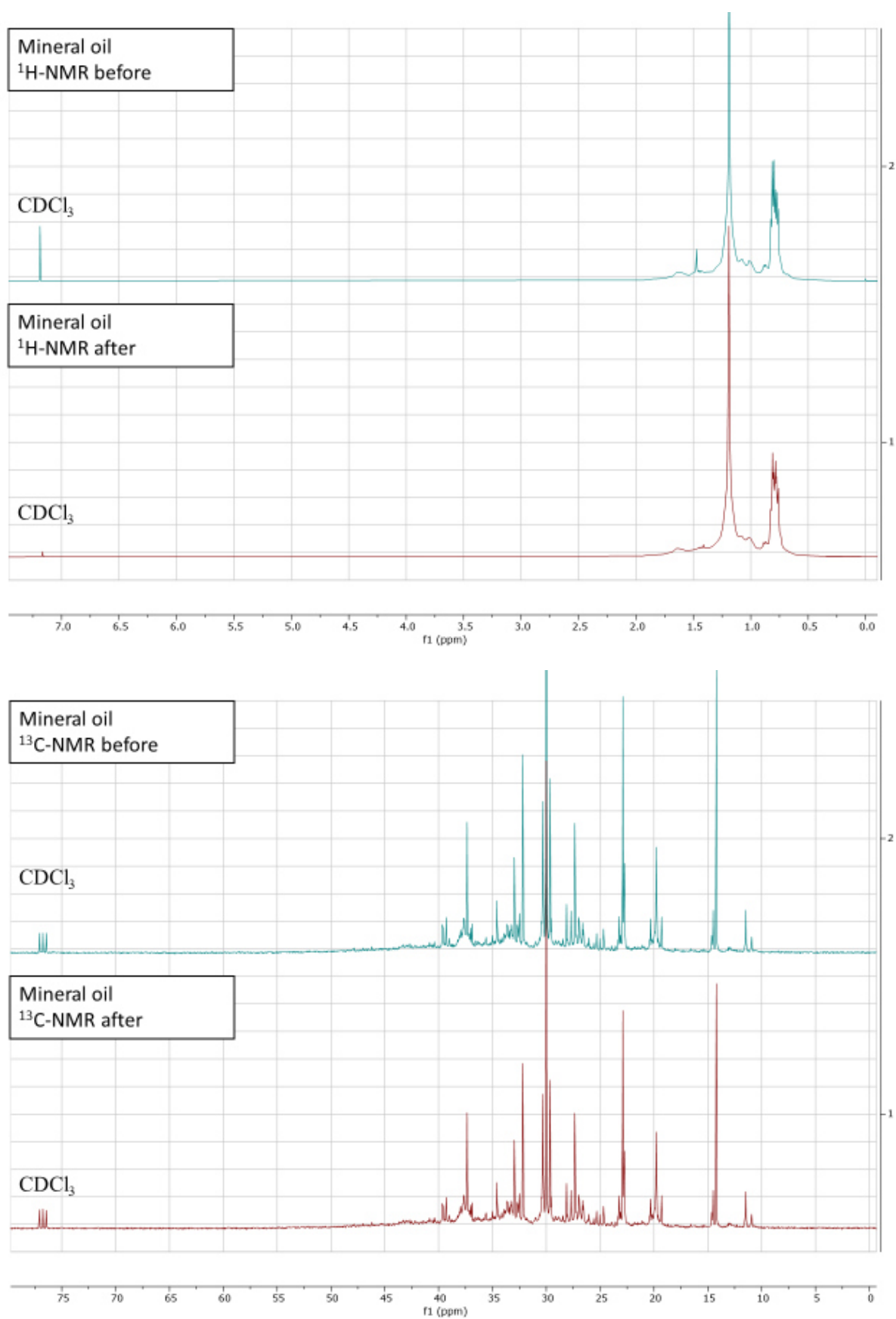


Figure S 13. ^1H and ^{13}C -NMR of the mineral oil before (blue) and after a total reaction time of 12 h (red).

Influence of different carrier liquids on the catalytic performance

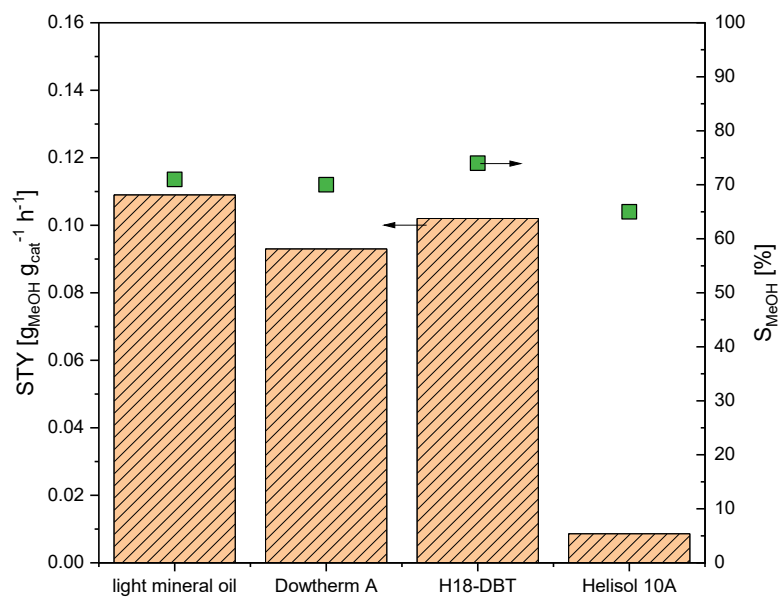


Figure S 14. Influence of different carrier liquids on the catalytic performance of the Ni-In₂O₃/ZrO₂-CP catalyst. Reaction conditions: $T = 300 \text{ }^\circ\text{C}$, $p = 75 \text{ bar}$, $\text{H}_2/\text{CO}_2 = 4/1$, $m_{\text{ref}} = 2.0 \text{ g}$, $N = 1200 \text{ rpm}$, $V_{\text{Oil}} = 100 \text{ mL}$, $t_{\text{R}} = 3 \text{ h}$.

Implementation plan of the statistical design of experiments

Table S 5. Implementation plan of the design of experiment study.

Run	Factor 1 A: Pressure [bar]	Factor 2 B: Temperature [°C]	Factor 3 C: Catalyst mass [g]	Factor 4 D: Stirrer speed [rpm]
1	50	250	2	1600
2	62.5	275	1.5	1400
3	75	300	1	1200
4	50	300	1	1600
5	62.5	275	1.5	1400
6	75	250	2	1200
7	75	250	1	1600
8	62.5	275	1.5	1400
9	50	300	2	1200
10	75	300	2	1600
11	62.5	275	1.5	1400
12	50	250	1	1200

Share of different influencing factors on the statistical design of experiments

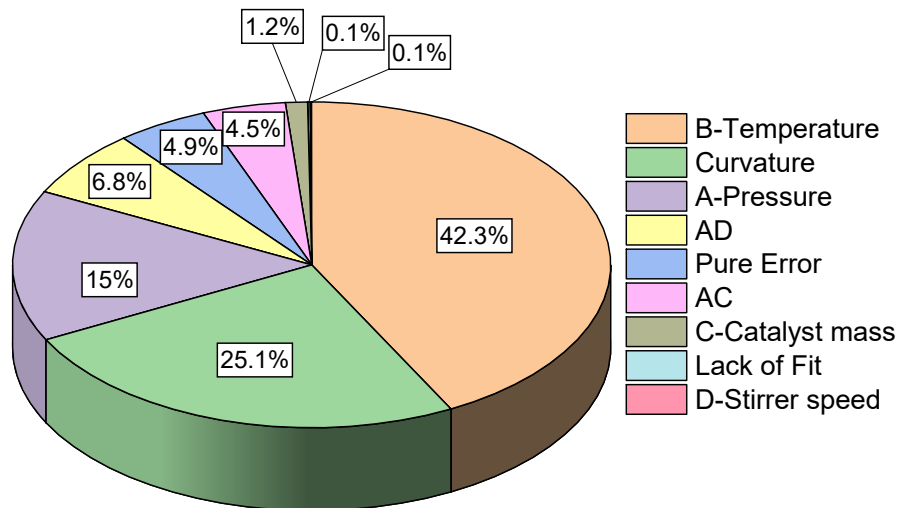


Figure S 15. Proportion of unknown influences on the statistical design of experiment.

Supporting References

- (1) Monshi, A.; Foroughi, M. R.; Monshi, M. R. Modified Scherrer Equation to Estimate More Accurately Nano-Crystallite Size Using XRD. *WJNSE* **2012**, *02*, 154–160.
- (2) Frei, M. S.; Mondelli, C.; García-Muelas, R.; Kley, K. S.; Puértolas, B.; López, N.; Safonova, O. V.; Stewart, J. A.; Curulla Ferré, D.; Pérez-Ramírez, J. Atomic-scale engineering of indium oxide promotion by palladium for methanol production via CO₂ hydrogenation. *Nature communications* **2019**, *10*, 3377.
- (3) Jia, X.; Sun, K.; Wang, J.; Shen, C.; Liu, C. Selective hydrogenation of CO₂ to methanol over Ni/In₂O₃ catalyst. *Journal of Energy Chemistry* **2020**, *50*, 409–415.
- (4) Frei, M. S.; Mondelli, C.; García-Muelas, R.; Morales-Vidal, J.; Philipp, M.; Safonova, O. V.; López, N.; Stewart, J. A.; Ferré, D. C.; Pérez-Ramírez, J. Nanostructure of nickel-promoted indium oxide catalysts drives selectivity in CO₂ hydrogenation. *Nature communications* **2021**, *12*, 1960.
- (5) Martín, O.; Martín, A. J.; Mondelli, C.; Mitchell, S.; Segawa, T. F.; Hauert, R.; Drouilly, C.; Curulla-Ferré, D.; Pérez-Ramírez, J. Indium Oxide as a Superior Catalyst for Methanol Synthesis by CO₂ Hydrogenation. *Angewandte Chemie (International ed. in English)* **2016**, *55*, 6261–6265.
- (6) Schühle, P.; Reichenberger, S.; Marzun, G.; Albert, J. Slurry Phase Hydrogenation of CO₂ to Methanol Using Supported In₂O₃ Catalysts as Promising Approach for Chemical Energy Storage. *Chemie Ingenieur Technik* **2021**, *93*, 585–593.
- (7) Zhang, Z.; Shen, C.; Sun, K.; Liu, C. Improvement in the activity of Ni/In₂O₃ with the addition of ZrO₂ for CO₂ hydrogenation to methanol. *Catalysis Communications* **2022**, *162*, 106386.

10 Danksagung

Die vorliegende Arbeit entstand am Institut für Technische und Makromolekulare Chemie der Universität Hamburg von Oktober 2020 bis September 2023.

Allen voran möchte ich mich bei meinem Doktorvater Prof. Dr.-Ing. Jakob Albert für die herausfordernde Themenstellung, die Unterstützung sowie die fachliche Betreuung dieser Arbeit bedanken. Danke für die Möglichkeit der Teilnahme an nationalen Konferenzen sowie die Kooperation mit Universitäten und Industriepartnern.

Herrn Prof. Dr. Raimund Horn danke ich herzlich für die Übernahme des Zweitgutachtens. Ich danke der Prüfungskommission Prof. Dr.-Ing. Jakob Albert, Prof. Dr. Michael Steiger und Dr. Charlotte Ruhmlieb für die Unterstützung und das Zustandekommen des Disputationstermins.

Danken möchte ich natürlich auch meiner Projektpartnerin, Anne Wesner. Ebenfalls geht mein besonderer Dank an die Kooperationspartner:innen Prof. Dr. Franziska Heß, Dr. Patrick Schühle, Dr. Charlotte Ruhmlieb, Dr. Maik Finsel und Oliver Korup für die erfolgreiche Zusammenarbeit, das Mitwirken in verschiedenen Veröffentlichungen und den fachlichen Austausch. Dem gesamten Team der Reacnostics GmbH möchte ich besonders für die fachliche und materielle Unterstützung danken, ganz besonders an Maik, für die schnelle und unkomplizierte Kommunikation und Hilfe während unserer Zusammenarbeit!

Herrn Dr. Michael Pabel von Saint-Gobain NorPro danke ich herzlich für die zeitnahe Bereitstellung von ZrO_2 .

Ich danke vielmals den Serviceeinrichtungen der Universität Hamburg, insbesondere der Elektronenmikroskopie, Röntgenstrukturanalyse, der Zentralen Element-Analytik, der NMR-Abteilung und der Forschungswerkstatt für die tolle Zusammenarbeit. Besonders Andrea Köppen, Robert Schön, Isabelle Nevoigt, Claudia Wontorra, Ansgar Weidner und Matthias Oswald Biermann danke ich für den lieben Austausch und die schnelle Bearbeitung meiner Anliegen. Des Weiteren danke ich allen zusätzlichen Kollegen die mir in irgendeiner Weise behilflich waren.

Ein großes Dankeschön geht an Michi Gröger. Du warst meine erste Anlaufstelle bei allen mechanischen Herausforderungen, wie Halterungen, Gestelle, Bohrungen und vieles mehr rund um die Anlagen. Danke für deine Geduld, dein offenes Ohr und deine humorvolle Art.

Ein riesiges DANKESCHÖN geht an meine Kollegen und Freunde Max und Nick. Ihr habt mich zu jeder Zeit aufgefangen und musstet meine Jammereien ertragen. Danke für die letzten Jahre, die

Danksagung

schönen und lustigen Momente, die gemeinsamen Feierabendbierchen, die gute Laune, die Hilfe bei „typisch Philipp“-Problemen, die mentale Unterstützung, die motivierenden Worte und natürlich auch für die tolle Zusammenarbeit, die fachlichen Gespräche und das Korrekturlesen verschiedener Texte. Lieber Nick, besonders danke ich dir für deine herausragende Unterstützung während deiner Masterarbeit.

Die Studierenden Simon Bisse und Leon Bacanli, die gemeinsam einen Beitrag zu dieser Arbeit geleistet haben, möchte ich sehr danken.

Ein weiteres dickes Dankeschön geht an die liebe Doro. Deine aufbauenden und motivierenden Worte, dein offenes Ohr, deine persönliche und fachliche Hingabe und deine leckeren Kuchen haben mich stets ermutigt weiter zu machen. Vielen Dank für deine Ratschläge und Ideen zur Bewältigung und Lösung von Herausforderungen. Danke für das Korrekturlesen meiner Arbeit. Ich habe sehr viel von dir lernen dürfen und die Zusammenarbeit mit dir genossen.

Für die ausgesprochen schöne und fröhliche Zeit im Büro am Institut bedanke ich mich bei Anna, Magdy, Max Poller, Jan und Sebi. Es hat viel Spaß gemacht, mit euch zu arbeiten und sich fachlich auszutauschen. Danke auch an alle weiteren Kollegen, die der guten Arbeitsatmosphäre beigetragen haben und mir mit Rat und Tat zur Seite standen.

Danke an meine Freunde Jan, Marie und Scott, die trotz der Entfernung immer für mich da waren und mir Zugesprochen haben.

Ich danke auch diejenigen, dir mir das nicht zugetraut haben. Euch das Gegenteil zu beweisen, hat mich extrem motiviert.

Meiner Freundin, Lea, bin ich sehr dankbar dafür, dass sie mich stets motiviert, ermutigt und aufgefangen hat. Danke für all deine Geduld, dein Verständnis, deine Zusprüche und deine Unterstützung während dieser intensiven Zeit. Du hast mich sehr bestärkt!

Abschließend einen besonderen Dank an meine Mama. Vielen, vielen lieben Dank für deine Unterstützung und dein offenes Ohr. Du hast mich bestärkt, motiviert und getröstet. Danke für deine Geduld und Verständnis in dieser anspruchsvollen Zeit!

11 Curriculum Vitae

PERSONAL INFORMATION

Name	Philipp Kampe
Date of birth	18/12/1995
Place of birth	Magdeburg, Germany



WORK EXPERIENCE

- Since 06/2024 **Process Engineer** – Cyclize GmbH, Stuttgart
- 10/2023–04/2024 **Postdoctoral researcher** – Institute of Technical and Macromolecular Chemistry, University of Hamburg, Hamburg
- 10/2020–09/2023 **Scientific researcher** – Institute of Technical and Macromolecular Chemistry, University of Hamburg, Hamburg

EDUCATIONAL BACKGROUND

- 10/2020–09/2023 **PhD student** – Institute of Technical and Macromolecular Chemistry, University of Hamburg, Hamburg
- 03/2019–09/2020 **Master of Science** in Applied Chemistry, dual study program
Faculty of Applied Chemistry, Technische Hochschule Nürnberg Georg Simon Ohm, Nürnberg
Nabu Oberflächentechnik GmbH, Stulln
- 10/2015–03/2019 **Bachelor of Science** in Applied Chemistry, dual study program
Faculty of Applied Chemistry, Technische Hochschule Nürnberg Georg Simon Ohm, Nürnberg
Nabu Oberflächentechnik GmbH, Stulln
- 09/2014–07/2017 Laboratory chemist – Städtische Berufsschule II Regensburg. Regensburg

12 Declaration on oath

Hiermit versichere ich an Eides statt, die vorliegende Dissertationsschrift selbst verfasst und keine anderen als die angegebenen Quellen und Hilfsmittel benutzt zu haben. Sofern im Zuge der Erstellung der vorliegenden Dissertationsschrift generative Künstliche Intelligenz (gKI) basierte elektronische Hilfsmittel verwendet wurden, versichere ich, dass meine eigene Leistung im Vordergrund stand und dass eine vollständige Dokumentation aller verwendeten Hilfsmittel gemäß der Guten wissenschaftlichen Praxis vorliegt. Ich trage die Verantwortung für eventuell durch die gKI generierte fehlerhafte oder verzerrte Inhalte, fehlerhafte Referenzen, Verstöße gegen das Datenschutz- und Urheberrecht oder Plagiate.



Philipp Kampe

I hereby declare on oath that I have written this dissertation myself and have not used any sources and aids other than those specified. If electronic resources based on generative artificial intelligence (GAI) were used in the course of writing this dissertation, I hereby declare that my own work was the main focus and that all resources used are fully documented in accordance with good scientific practice. I am responsible for any erroneous or distorted content, incorrect references, violations of data protection and copyright law or plagiarism that may have been generated by the GAI.



Philipp Kampe